

Computational Modelling of Brain Shift in Stereotactic Neurosurgery



Nicholas James Bennion

A thesis submitted for the degree of
Doctor of Philosophy

Supervisors

Prof. S. L. Evans

Prof. D. Marshall

2020

Abstract

Navigation in stereotactic neurosurgery relies solely on preoperative images, with the location of anatomical targets defined relative to the skull. Displacement of the anatomical target from its expected position is a common complication during surgery; however, the magnitude of this deviation is currently unpredictable. One potential source of this error occurs with reorientation of the head alone and is known as positional brain shift (PBS). PBS is the focus of this thesis, which aims to better understand the phenomenon through computational methods.

A finite element (FE) model was generated in FEBio, incorporating a novel spring element/fluid structure-interaction representation of the pia-arachnoid complex (PAC). The model was loaded to represent gravity in the prone and supine positions. Material parameter identification and sensitivity analysis were performed using statistical software, comparing the FE results to human in-vivo measurements.

Results for the brain Ogden parameters, μ , α and k yielded values of 675 Pa, -16.9 and 127,000 Pa, supporting previous values reported in the literature. Values in the order of 250,000 Pa and 480 Pa were obtained for stiffness of the pia mater and out-of-plane tensile stiffness of the PAC respectively. The PAC was found to be orders of magnitude less than what is currently accepted; a finding potentially significant for this and other areas of modelling. PBS was found to be non-rigid, with a magnitude of 1 mm in deep structures; driven by redistribution of fluid. Surface movement resulted from compression of the PAC, with trabecular elements in tension experiencing limited strain.

This is the first study focussed specifically on PBS using computational methods. In-vivo data was used to identify material parameters specific to PBS, yielding an improved understanding of the mechanical process. This method could now be developed into a meaningful tool to reduce the impact of PBS in stereotactic neurosurgery.

To Mum and Dad

Acknowledgements

I would like to acknowledge the following people for their encouragement, support and guidance over the last four years of this study.

Firstly, I would like to thank Prof. Sam Evans and Prof. David Marshall for invaluable contributions as my academic supervisors. I will always be grateful for your dedication in helping me develop academically, but also in a much broader sense. This sentiment extends to Matthew Potts and Stefano Zappalá, whom I have worked alongside throughout the majority of this project. Your direct contributions have enabled this work, and I wish you the best with your own submissions. Finally, to everyone in the School of Engineering who make it and fun and exciting place to work, thank you.

I would also like to thank those outside of the department, whose assistance has been instrumental in completing this project. Firstly, to Prof. Derek Jones and all those at Cardiff University Brain Research Imaging Centre (CUBRIC), for your assistance and guidance in acquiring human data. Computation of the final model was performed on the Hawk system at Advanced Research Computing at Cardiff (ARCCA). I would like to thank Thomas Green in particular, for his extensive help and support in making this possible. Considerable simplification of the model would have been necessary without it. Finally, to Rob Harrison, Dr Stephen Anderson and Renishaw Plc, along with the Engineering and Physical Sciences Research Council (EPSRC) for the financial support and industrial guidance offered.

On a personal note, much gratitude must go to all of my family and friends. In particular, to my Mum and Dad for amongst many other things, bravely tackling my illiteracy in proofreading this thesis. I promise that's University done, for now. On a more recreational front, I must acknowledge expert magnet fisherman Alex Bennion and expert skier (forwards and backwards) John Goldingham for providing some high-quality mischief around the world. To the Cardiff boys, Dr Nicholas Burnley-Hall, Dr Nicholas Hargreaves, Dr Oliver Post and Dr Hugo Trevelyan Thomas – many thanks for making this such a fun place to live, at least until you all found better places to go. Last but (not least), big thanks Dr Jennifer Gough, for keeping me sane and entertained throughout, with much appreciated encouragement to stay committed to the glorious house of gains.

One last huge shout out must also go to Carl Cox, Hot Since 82 and their merry entourage of disc spinners for providing some truly majestic tunes to enjoy during long hours of writing and beyond.

Contents

Chapter 1 : Introduction.....	1
Summary of novel contributions	5
Chapter 2 : Clinical Considerations.....	6
Anatomy and Physiology	6
Brain Shift in Neurosurgery.....	11
Conclusions	34
Influence of Findings.....	36
Chapter 3 : Computational Modelling of Brain Shift.....	38
Continuum Mechanics.....	39
Constitutive Modelling	44
Finite Element Modelling	55
Material Sensitivity Analysis.....	62
Influence of Findings.....	67
Chapter 4 : Methods	68
Human study.....	68
Phantom study.....	69
FE Model Development	70
Data analysis.....	85
Surgical Prediction Test Case	88
Chapter 5 : Results.....	90
In-vivo measurement.....	90
Material Parameter Identification	95
Biomechanical Analysis of the Final Model.....	119
Surgical Prediction Test Case	125
Chapter 6 : Discussion	127
Development of the model.....	127
Kinematics of Positional Brain Shift.....	129

Material Parameters and Sensitivity.....	138
Model Derived Mechanics of Positional Brain Shift.....	147
Implications for Modelling.....	149
Surgical Prediction Test Case.....	151
Limitations.....	153
Chapter 7 : Conclusions.....	155
Future work.....	158
References.....	160
Model parameter values.....	173
Solution parameters used in FEBio.....	175

List of Figures

Figure 1 – Example target definition (coloured regions) and device implantation trajectory (yellow device) for DBS surgery using the ‘neuroinspire™’ surgical planning software. Adapted from promotional material (3).	2
Figure 2 – The ‘neuromate™’ surgical robot utilises multiple degrees of freedom to attain the precise insertion location and trajectory as determined in the surgical plan. Adapted from promotional material (3).	2
Figure 3 – The falx cerebri and tentorium cerebelli of the dural septa (highlighted here in purple) in context within the cranial vault. Note that the dura mater continues over the inner surface of the cranium but is not shown here. Reproduced from (16).....	6
Figure 4 – Detailed schematic of the microstructure of the meninges. Of particular interest is the subarachnoid space (SAS) a region populated by cerebrospinal fluid, arachnoid trabeculae and smaller vessels. Reproduced from (17).....	7
Figure 5 – Coronal section detailing how the dural septa, sinuses, PAC and brain interact to form the complex brain-skull interface. Reproduced from (19).	8
Figure 6 – Anatomy of the brain from [A] a view of the cortical surface and [B] a midsagittal section, where the meninges are removed. Reproduced from (19).	9
Figure 7 – Annotated MRI depiction of the mid-sagittal AC-PC line on MRI. Case courtesy of A.Prof Frank Gaillard, Radiopaedia.org, rID: 50730.....	10
Figure 8 – Left – Five MER electrodes are used concurrently to identify the optimum positioning in the target. Right – zoomed view of the 5-electrode collet. The guide tube has been left in position 3 to allow insertion of the permanent electrode. Images reproduced from (44).	13
Figure 9 – Schematic of the potential sources of error in each step of the traditional frame-based, frameless and iMRI based stereotactic workflows. Reproduced from (6).....	15
Figure 10 – Sign convention for brain shift values reported in the literature. X = lateral, Y = anteroposterior and Z= dorsoventral.....	17
Figure 11 – Comparison of the scalar and Y vector component position change in the AC reported by each group, plotted against publication year of the study.	20
Figure 12 – The relationship between post-operative (one day after surgery) ICA volume and deviation of the AC from its original position ($r = 0.569$). Adapted from (5).....	22
Figure 13 – Box and whisker plots comparing the orthogonal components of AC and PC shift in semi-sitting and supine surgical positions, suggesting greater displacement in the former. Reproduced from Miyagi et al. 2015 (30).....	27
Figure 14 – Schematic illustration of unilateral air invasion and the subsequent midline shift. Adapted from (24).	30
Figure 15 – Schematic representation of displacement representation by Monea et al. (93).	33
Figure 16 – Schematic representation of the deformation field.....	40

Figure 17 – Example of a stress/strain plot depicting a region of energy loss as described by the Mullins effect	43
Figure 18 – Above axis – strain rates reported in a range of real-world impact/blast scenarios. Below axis – strain rates used in the mechanical characterisation of brain tissue in some of the most commonly cited studies.....	46
Figure 19 – Average stress relaxation behaviour obtained from cortex (C), basal ganglia (BG), corona radiata (CR) and corpus callosum (CC) samples of human brain tissue with shear strain of 0.2. Reproduced from (119).	48
Figure 20 – Comparison of experimental data to optimised theoretical prediction, obtained through oedometric testing of cylindrical brain samples. Reproduced from (115).....	49
Figure 21 – Example of experimental set-up, demonstrating the use of BioRakes and the dimension <i>dii</i> used to calculate the undeformed area. Image reproduced from (14).	54
Figure 22 – The KTH model geometry as presented in (161).	57
Figure 23 – Examples of the high biofidelity finite element models for traumatic brain injury used in (109, 160) [top] and (169) [bottom].....	58
Figure 24 – Representation of the bridging vein pairs by means of spring elements with linear elastic stiffness (171). Reproduced from (18) for improved clarity.	59
Figure 25 – The finite element representation of the cranial sinuses and selected bridging veins, reproduced from (173), showing greatly improved biofidelity.....	59
Figure 26 – [left] Example of the randomly generated PAC geometry reproduced from (133) - [right] local model geometry reproduced from (180).....	61
Figure 27 – Gaussian process regression plots, depicting the simulation code function (red dotted line), sparse observation indicating points at which the simulation had been computed and the posterior distribution after considering the observations. Note the posterior function is the mean of the 95% prediction interval. The left figure depicts deterministic data whilst the right contains numerical error, or noisy data and as such has no regions with a variance of zero. Reproduced from (189).	65
Figure 28 – Demonstration of the phantom held in a right semi-decubitus position for scanning in this orientation [left] and MR image of an axial section, highlighting the skull and falx cerebri (black), brain (dark grey) and ventricles/subarachnoid space (light grey) [right].	70
Figure 29 - Example of the ScanIP™ interface displaying the unsegmented MNI dataset.	71
Figure 30 – Regional segmentation of the MNI dataset – coloured regions represent the brain (beige), CSF spaces (blue), dura/dural septa (dark grey) and skull (light grey).....	72
Figure 31 – Off midline sagittal section of the dura mater and dural septa.	74
Figure 32 – Lateral view of the external surface of the PAC.....	75
Figure 33 – Lateral view of the lateral, third and fourth ventricles and cerebral aqueduct removed from the subarachnoid space for visualisation.....	75

Figure 34 – Lateral view of the brain/pia mater with arachnoid trabeculae springs removed....	76
Figure 35 – Superior view of the brain/pia mater with arachnoid trabeculae removed.	76
Figure 36 – Lateral view of the brain/pia mater with arachnoid trabeculae shown in pink.....	77
Figure 37 – Transverse section of the anterior brain and dura mater with CSF regions removed, highlighting the spanning of the subarachnoid space with the spring representation of the arachnoid trabeculae (pink).	77
Figure 38 – Transverse section of the brain (green), CSF regions (purple) and dura mater (blue).	78
Figure 39 – Midsagittal section of the brain, CSF regions and dura mater.	78
Figure 40 – Coronal section of the dura (dark blue), CSF region (light blue) and brain (beige) as used in the final model.....	79
Figure 41 – Anteroinferior view of the foramen magnum.....	80
Figure 42 – Schematic representation of head repositioning with respect to gravity.....	81
Figure 43 – Schematic of a two-element model, to aid the explanation of the displacement calculation methods used.....	87
Figure 44 – Input display and settings used for initial sensitivity analysis in GEM-SA.	87
Figure 45 – Schematic of the 6 head orientations chosen to investigate the potential for PBS in surgery.....	88
Figure 46 – Lateral view of the cerebral nodes, highlighting the region used to illustrate the subject displacement fields (orange).....	91
Figure 47 – Nodal displacement of subject 1 over the 10 mm transverse section. Displacement vectors have been scaled by a factor of 5 relative to the brain.....	92
Figure 48 – Nodal displacement of subject 2 over the 10 mm transverse section. Displacement vectors have been scaled by a factor of 5 relative to the brain.....	93
Figure 49 – Nodal displacement of subject 3 over the 10 mm transverse section. Displacement vectors have been scaled by a factor of 5 relative to the brain.....	94
Figure 50 – Main effect plots for each material parameter and each subject, displaying the impact of parameter variation against the EM for each FE model. The ME plot for each parameter is generated at the average value of all other parameters. If joint effects exist between parameters, change of the range and therefore of the mean value can impact the main effect output. Error bars indicate one standard deviation in the normally distributed predictions, indicating statistical confidence in the prediction at each point.....	98
Figure 51 – Percentage variance of the main effect data for each material parameter and each test subject. The variance not reaching a total of 100% indicates that other sources of variance in the data exists outside the 5 material parameters.	99

Figure 52 – Joint effect for each material parameter and each test subject. Total effect values include joint effects between variables - as such total effect can be counted twice and the patient total may be greater than 100..... 99

Figure 53 – Total effect (accounting for variance and joint effects) - between each of the material parameters for each test subject. 100

Figure 54 – Main effect plots generated from the 200 parameter sets which yielded the lowest error values of the 1000 generated with the simulator. With the range significantly reduced for the bulk modulus and spring constant, the shear modulus now exhibits a minima within the plot range. The Young’s modulus was plotted on a logarithmic axis due to the large range of values which remained. Error bars were removed for clarity. 102

Figure 55 – Variance results for the 2nd iteration. The parameter x4 now yielded a higher variance than the other variables for every subject, however the range of values used was still comparatively large. 103

Figure 56 – Joint effect results for the 2nd iteration. This time, the highest joint effects are seen with x2. Conversely to the variance, x4 has low joint effects with all variables, including x2... 103

Figure 57 – Total effect results for the 2nd iteration. On average x4 still shows the greatest total effect. 104

Figure 58 – Surface plots showing the EM change resulting from variation of the bulk modulus and shear modulus over the ranges defined in Table 5-4 for subjects 1, 2 and 3 [top, middle and bottom respectively]. The parameter range shown was fixed for all subjects for ease of comparison..... 106

Figure 59 – Surface plots showing the EM change resulting from variation of the bulk modulus and spring constant over the ranges defined in Table 5-4 for subjects 1, 2 and 3 [top, middle and bottom respectively]. The parameter range shown was fixed for all subjects for ease of comparison..... 107

Figure 60 – Surface plots showing the EM change resulting from variation of the shear modulus and spring constant over the ranges defined in Table 5-4 for subjects 1, 2 and 3 [top, middle and bottom respectively]. The parameter range was fixed for all subjects for ease of comparison. 108

Figure 61 – Displacement fields generated by the final FE model and average subject data taken through a 10 mm section at the same point as Figure 46. Displacement vectors have been scaled by a factor of 5 relative to the brain..... 111

Figure 62 – Colour plot proportional to: [Left] the magnitude of the displacement field (in mm) in the original averaged subject data and [Right] after correction of the subject data with the optimised FE result – highlighting resulting error. 112

Figure 63 – Main effect plots for each material parameter within the averaged subject data in elements greater than 10 mm from the dural surface. Note that the error value for the bulk modulus at 1 MPa is approximately equivalent to the zero-deformation EM..... 113

Figure 64 – Main effect plots generated from the 200 parameter sets which yielded the lowest error values of the 1000 generated with the simulator. The Young’s modulus was plotted on a logarithmic axis due to the large range of values which remained, and error bars were removed for clarity.	114
Figure 65 – Surface plot of the bulk modulus and exponential coefficient, m1 . Red points indicate the value at which the minima occurs.....	115
Figure 66 – FE displacement field (showing elements >10 mm from the boundary) generated from calibration 2, compared to the full region of the average subject field. Whilst there is still deviation towards the boundary, the central structures show considerable improvement compared to the results of calibration 1. Displacement vectors have been scaled by a factor of 5 relative to the brain.....	116
Figure 67 – Marker distribution throughout the brain, as used in the phantom study. The top image shows only the right-hand side for clarity. The bottom image shows a transverse view of both sides. The marker designation was based on the approximate anatomical location: C - Cerebellum, O - Occipital, P - Parietal, T - Temporal, F - Frontal, SN - Substantia nigra. Green regions show structures of the basal ganglia, clinically relevant to Parkinson’s disease. Left images reproduced from doctoral thesis of Matthew Potts; currently unpublished. Displacement vectors have been scaled by a factor of 10 relative to the brain.....	117
Figure 68 – Stress plots from the prone FE model, arranged such that the image occupies the location in the stress tensor which it represents. The x, y and z components range from -927 to 847, -930 to 853 and -928 to 846 Pa respectively. Colour plots for the shear components were fixed at -8 to 8 Pa for ease of comparison. The similarity between the x, y and z components and low shear stresses indicate that hydrostatic stress dominates the mechanical process.....	119
Figure 69 – Stress plots from the supine FE model, arranged such that the image occupies the location in the stress tensor which it represents. The x, y and z components range from -838 to 946, -840 to 951 and -838 to 945 Pa respectively. Colour plots for the shear components were again fixed at -8 to 8 Pa for ease of comparison.....	120
Figure 70 – Zoomed imaged of the anterior midline region of the supine model, where the PAC region is shown in solid blue. The colour scale shows σ_{xy} component of the Cauchy stress, highlighting a peak near the external boundary of the PAC.....	121
Figure 71 – 1 st deviatoric principle stress for the prone [left] and supine [right] FE models....	121
Figure 72 – Sections of the final FE model showing 1st principle strain [top] in the prone [left] and supine [right] positions, elemental Jacobian [bottom] respectively.....	122
Figure 73 – Neutral to prone [top], neutral to supine [middle] and prone to supine [bottom] displacement fields (scaled by a factor of 10), superimposed with the Jacobian of fluid regions (shown in colour). The prone to supine image treats the prone elemental volume as the starting point rather than calculating J from the neutral position.	123

Figure 74 – Prone [top] and supine [bottom] images of the pia mater, where the colour represents the reaction force (mN) in each spring element of the arachnoid trabeculae, averaged over the three nodes of each surface element, not accounting for elemental area.	124
Figure 75 – 1 st Principle stress (kPa) in the pia mater, in supine [left] and prone [right] loading.	125
Figure 76 – Modified schematic of the prediction test case positions.	125
Figure 77 – Sagittal (left) and axial (right) plots illustrating the vector displacements between the supine and other orientations as predicted by the final parameter sets.	126
Figure 78 – Cortical and ventricular surface displacement due to reorientation from supine to prone in the sagittal plane. Gross displacement is indicated by the red arrows, with local change corresponding to the colour code. Reproduced from (93).	130
Figure 79 – Surface displacement colour plot resulting from supine-to-prone repositioning. Adapted from (94).	130
Figure 80 – Anterior transverse section, highlighting the variation in cortical surface displacement in the subject data obtained as part of the accompanying human study.	131
Figure 81 – 2D CSF area measurement in the prone and supine positions, identified by manual tracing of the bright CSF filled region. Reproduced from (141).	132
Figure 82 – Midsagittal deformation field with supine to prone repositioning presented by Schnaudigel et al. (4).	132
Figure 83 – Subject displacement field from a sagittal plane just off midline (as midline has no limited brain nodes), presented as comparison to Figure 82. Note the displacements depict prone-supine reorientation as opposed to supine-prone. Midbrain/cerebellum is also not shown due to poor results. The black line indicates the approximate inferior boundary of the falx cerebri. Scaled by a factor of 10.	133
Figure 84 – Histogram of the gravitational component of the nodal displacements in the entire cerebrum vs the reduced cerebral area of the averaged human data set. For reference, Schnaudigel et al. (4) reported displacements between 0.6-1.3 mm.	133
Figure 85 – Sagittal component of the vectors in the reduced ‘middle cerebrum’ nodeset, for both optimisations of the FE model and the human data. Change of the material parameters led to significant change in magnitude of displacement but had little impact on the distribution. Again, for reference, Schnaudigel et al. (4) reported displacements between 0.6-1.3 mm.	134
Figure 86 – Surface displacement magnitude in mm from the calibration 2 final FE model. ..	136
Figure 87 – Vector plot of displacement induced with prone-to-supine reorientation across the volume of the cerebrum, shown from superior [left] and lateral [right] viewpoints. Arrows are intended to show the displacement pattern and have been scaled by a factor of 10 for clarity.	137

Figure 88 – Plot demonstrating the effect of exponential coefficient variation on the instantaneous deviatoric stiffness, using a realistic corresponding shear modulus. 141

Figure 89 – Schematic of the experimental set-up used by Mazumder et al., adapted from (136).
..... 144

Figure 90 – Schematic representation of the extension and compression of the PAC in neutral – prone/supine and the resulting supine – prone displacement. 148

Figure 91 – Interior view along the midline of the falx cerebri and cranial dura mater, showing the displacement (peak 0.35 mm) induced from neutral to right decubitus reorientation..... 152

List of Tables

Table 2-1 – Typical movement disorders treated with DBS, the associated anatomical targets, and approximate proportion of all DBS procedures: Subthalamic nucleus (STN), globus pallidus internus (GPi), ventral intermediate thalamus (VIM), pedunculopontine nucleus (PPN), zona incerta (ZI).....	12
Table 2-2 – Scalar and vector brain shift values reported in the literature regarding DBS patients. Beige cells indicate a value that has not been reported directly but calculated from those reported. Blue cells indicate a reported statistically significance to either preoperative values or comparative subject group	18
Table 2-3 – Weighted average values for brain shift reported in DBS procedures.....	19
Table 2-4 – Summary table of the influential and controllable factors relevant to stereotactic neurosurgical brain shift.....	34
Table 3-1 – Values of bulk modulus or Poisson’s ratio in the literature derived from experimentation.....	51
Table 3-2 – Material parameters obtained for mechanical testing reported in the literature. *Values reported for simultaneous fit of all loading conditions.	52
Table 3-3 – Mechanical properties of the bovine PAC as presented in (97).	52
Table 3-4 – Stiffness values for the cranial pia mater in the literature.	53
Table 4-1 – Number and type of elements in each regions of the final geometry.....	79
Table 4-2 – Geometric details of the final model.....	80
Table 4-3 – Constitutive model and parameter settings used for the parametric analysis. Where parameters were not varied only a high value is included.	83
Table 5-1 – Global displacements within the cerebrum of the initial training data subject group (n=3).	90
Table 5-2 – Minimum and maximum values of models that converged in the FE study.....	97
Table 5-3 – Material parameters used in the first two iterations of processing. The minimum and maximum parameter values for iteration 1 are as presented in Table 5-2. Here the parameter value which yielded the minimum EM is included. Iteration 2 – 1000 refers to the range over which the 1000 prediction sets were generated. Iteration 2 – 200 refers to the range found in the parameter sets which predicted the lowest EMs. Minima values in italics indicate this value came at one extreme of the initially defined range. Grey lines indicate values from the previous iteration.	101
Table 5-4 – Updated parameter values, included the minima from iteration two and the finalised ranges for iteration 3.	105
Table 5-5 – Parameter values found from the surface plots, generated with one parameter held (grey) whilst the remaining two were varied. The percentage values indicate the similarity of the refined 2D simulations to the initial estimate (grey) which was used when not being varied. ...	109

Table 5-6 – Mean parameter values found in calibration 1.....	109
Table 5-7 – Original global displacement and EM data, along with the reduced EM calculated after subtraction of the final FE displacement field. Pre-avg refers to values calculated from the three averaged displacement fields, as opposed to the average of the values obtained from each subject field as in Table 5-1.....	110
Table 5-8 – Parameter ranges resulting from 200 best sets from the 1 st simulation.....	113
Table 5-9 – Optimised values from the second calibration	115
Table 5-10 – Components of the marker displacement in the phantom, FE and subject data.....	118
Table 6-1 – Material parameters identified after calibration with the entire cerebrum and reduced volume.	138
Table 6-2 – Literature values for material parameters of the time-independent, one-term, Ogden strain energy density function.	140
Table 6-3 – Parameter values used in the calculation of the layer stiffness of the PAC.....	143
Table 6-4 – Comparison of the difference between value found for the tensile stiffness of the PAC found in the present study and the literature.....	144

Abbreviations

DBS	Deep brain stimulation
SEEG	Stereoelectroencephalography
MRI	Magnetic resonance imaging
CT	Computed tomography
PBS	Positional brain shift
CSF	Cerebrospinal fluid
SAS	Subarachnoid space
PAC	Pia-arachnoid complex
AC	Anterior commissure
PC	Posterior commissure
ISF	Interstitial fluid
ICA	Intracranial air
ET	Essential tremor
PD	Parkinson's disease
STN	Subthalamic nucleus
GPi	Globus pallidus internus
VIM	Ventral intermediate thalamus
PPN	Pedunculopontine nucleus
ZI	Zona incerta
MER	Microelectrode recording
FE	Finite element
UTS	Ultimate tensile strength
NH	Neo-Hookean
GOH	Gasser-Ogden-Holtzapfel
FEA	Finite element analysis
KTH	Kungliga Tekniska Hogskolan
FSI	Fluid structure interaction
YEAHM	Yet Another Head Model
VF	Volume fraction
TBI	Traumatic brain injury
GEM-SA	Guassian Emulation Machine for Sensitivity Analysis
CUBRIC	Cardiff University Brain Imaging Research Centre
MNI	ICBM152 Average Brain Stereotaxic Registration Model
iMRI	Interoperative magnetic resonance imaging
ME	Main effect
EM	Error magnitude
ZD	Zero displacement

Nomenclature

Continuum mechanics

Ω_0	Reference configuration
Ω	Current configuration
t	Time
\mathbf{X}	Material coordinates
\mathbf{x}	Spatial coordinates
χ	Deformation mapping function
\mathbf{F}	Deformation gradient tensor
\mathbf{u}	Displacement tensor
\mathbf{R}	Rotational tensor
\mathbf{U}	Right stretch tensor
\mathbf{C}	Right Cauchy-Green tensor
\mathbf{I}	Identity matrix
J	Jacobian determinant
$\tilde{\mathbf{F}}$	Deviatoric deformation gradient tensor
$\tilde{\mathbf{C}}$	Deviatoric right Cauchy-Green tensor
\mathbf{E}	Green-Lagrange tensor
$\boldsymbol{\sigma}$	Cauchy stress tensor
\mathbf{t}	Cauchy traction vector
\mathbf{n}	Infinitesimal normal tensor
\mathbf{T}	Piola-Kirchoff traction vector
\mathbf{N}	Reference configuration infinitesimal normal tensor
\mathbf{P}	First Piola-Kirchoff stress
σ_{hyd}	Hydrostatic stress
$\tilde{\boldsymbol{\sigma}}$	Deviatoric stress tensor
λ	Stretch
$\tilde{\lambda}$	Deviatoric stretch
p	Pressure
V	Volume
ψ	Strain energy density function
U	Internal energy
T	Temperature
S	Entropy
$\boldsymbol{\varepsilon}$	Green strain tensor

I_1, I_2, I_3	1 st , 2 nd and 3 rd invariants
\mathbf{S}	Second Piola-Kirchoff stress tensor
$\tilde{\psi}$	Deviatoric strain energy density function
$U(J)$	Volumetric energy
<u>Constitutive modelling</u>	Hyperelastic materials
k	Bulk modulus
ν	Poisson's ratio
E	Young's modulus
C_{10}	Neo-Hookean material constant
μ_i or c_1	Ogden material coefficient
α_i or m_1	Ogden exponential stiffening coefficient
μ	Classical shear modulus
	Prony series
μ_0	Initial shear modulus
τ_k	Relaxation time
g_k	Material coefficient
	Consolidation theory
C_v	Consolidation coefficient
k	Permeability
M	Oedometric coefficient
γ_w	Specific weight of fluid phase
<u>Data processing</u>	
W_n	Volumetric weight
Vol_n	Element volume
Vol_{region}	Total regional volume
d_n	Orthogonal elemental displacement
\mathbf{D}	Orthogonal global displacement

Chapter 1: Introduction

The brain is one of the most recognisable organs in the body. It is also arguably the most important, being responsible for almost all our conscious and unconscious being. Function of the brain is made possible through a complex network of billions of nerve cells which communicate through the generation and transmission of electrical charges. Given this complexity, clinical dysfunction can stem from number of different sources. Typical examples include the growth of cancerous tissues or problems with the transmission of these electrical signals (1). In some cases, surgical intervention is required to better understand or treat the problem.

The umbrella term of ‘Stereotactic and Functional Neurosurgery’ refers to a wide range of neurosurgical procedures, including deep brain stimulation (DBS), stereoelectroencephalography (SEEG), neuroendoscopy, biopsy and drug delivery. These procedures all rely on identifying anatomical targets within the brain relative to an external frame or reference system. Stereotactic methods are unique as they allow for neuro-navigation with no direct visual field, giving access to structures which are otherwise unreachable (2).

Although precise protocols vary, the general workflow is as follows. A detailed map of the brain is first obtained preoperatively, using magnetic resonance imaging (MRI), typically in the supine position. Next, the patient’s head is registered to a stereotactic reference frame, usually using computed tomography (CT). In frameless procedures, fiducial markers are fixed directly to the skull. Crucially, head orientation of the patient at this stage is at the surgeon’s discretion, chosen to help facilitate the surgery.

Specialist surgical planning software such as ‘neuroinspire™’ (Renishaw Plc., New Mills, United Kingdom) is used to register the CT and MRI images together, allowing for a detailed image of the brain within the surgical reference frame. From this, anatomical targets can be identified by the neurosurgeon – these are displayed as the coloured regions in Figure 1.

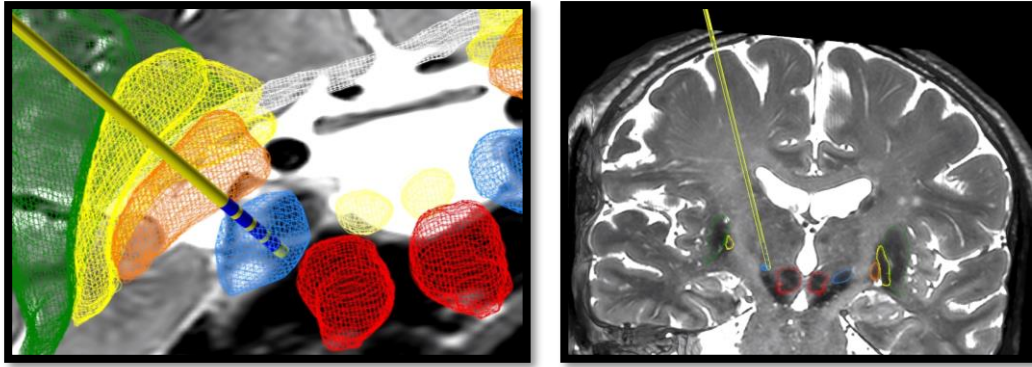


Figure 1 – Example target definition (coloured regions) and device implantation trajectory (yellow device) for DBS surgery using the ‘neuroinspire™’ surgical planning software. Adapted from promotional material (3).

Finally, an implantation trajectory is determined, taking care to avoid key features such as blood vessels. A stereotactic frame or surgical robot is used to locate the pre-planned insertion site and trajectory for insertion of the surgical device. An example of the ‘neuromate™’ (Renishaw Plc., New Mills, United Kingdom) surgical robot positioned ready to receive a surgical device for implantation is shown in Figure 2. The device to be inserted depends entirely on the type of procedure. Electrodes, needles and catheters are common, with all conforming broadly to the same long, thin, cylindrical shape.



Figure 2 – The ‘neuromate™’ surgical robot utilises multiple degrees of freedom to attain the precise insertion location and trajectory as determined in the surgical plan. Adapted from promotional material (3).

After alignment of the frame or robot, the device is then inserted along the trajectory to the planned depth, reaching the desired coordinates within the reference frame. The ability to reach these pre-planned coordinates relies upon the accuracy of the surgical system itself. However, due to the navigational methods used in stereotactic procedures it is also critical that the anatomy itself does not move within the reference frame. Movement of the brain relative to the skull, is known as brain shift. It is a well-recognised, but currently unpredictable source of error in stereotactic procedures. The study of brain shift forms the primary motivation for this thesis.

Two components of brain shift can be defined when considering stereotactic procedures (4, 5):

1. Positional brain shift (PBS) occurs when the orientation of the patient during MRI and surgery differs and is due to gravity alone. Being a non-uniform deformation of brain tissue, it is not accounted for in surgical planning as the pre-operative MRI and peri-operative registration CT are rigidly aligned.
2. Surgical brain shift occurs on the perforation of the meninges. Deformation can be directly induced by the surgical device but also by changes to the mechanical support structure of the brain as a result of surgery.

Without correction, brain shift can lead to improper placement of the surgical instrument. Depending on the type of procedure being carried out, this can have a significant impact on clinical effectiveness. State of the art systems now operate to an accuracy in the order of 0.6 mm (6). There are a number of methods currently in use to account for brain shift (6) and ensure that proper positioning has been achieved; however, these all have varying levels of invasiveness and expense.

An approach devoid of these associated costs would be beneficial to both the patient and surgeons. One possible solution could employ computational methods to preoperatively predict brain shift and use this prediction to adjust the surgical plan, effectively moving the target coordinates to the expected final position of the anatomical target.

In the long term, it is our intention to develop a system capable of generating reliable predictions of this nature. Patient specific modelling would likely be prohibitively time-consuming, but meaningful improvements could still be made for many patients using average values. In either case, this clinical implementation falls outside the intended scope of the current work. Instead, this thesis presents one of three distinct, but complimentary Ph.D. studies aimed at providing the necessary fundamental understanding to facilitate this in future.

The precise focus of each accompanying project evolved over the initial stages of work, much of which is explained in more detail later in this thesis. With these initial findings in mind, the following topics of study were established:

1. Human measurement and quantification of brain shift using image-based methods.
2. The design, construction and testing of a biofidelic head phantom.

Stefano Zappalá and Matthew Potts are acknowledged as the authors of these works respectively. The knowledge obtained from these projects was invaluable in supporting the work presented here.

With the accompanying studies addressing in-vivo measurement of brain shift and improved physical modelling of the head, it was decided that this work would focus on investigating the phenomenon through computational methods, as captured by the following aim:

Aim

Use a computational model to better understand the mechanics of brain shift relevant to a stereotactic neurosurgical setting.

Finite element (FE) modelling is a branch of computational modelling that has been used to study the brain for many years in many areas (7). These range from use in helmet design (8) to helping actively define tumour margins in resection cases with large craniotomies (9). A core requirement in each case is having a material representation, or constitutive model, that effectively captures the mechanical characteristics of the brain (10). Many authors have reported increasingly complex methods of doing this with promising success (11). However, the level of precision required within stereotactic neurosurgery requires a refined representation of both the anatomical structures of the intracranial cavity and the constitutive models used to describe them.

An improved understanding of the biomechanical process of brain shift in neurosurgery was critical to the development of this project. It was also hoped that the findings would add to the body of knowledge in a broader sense. Key areas of potential for improvement included the material properties of the intracranial tissues, modelling techniques and the mechanics of brain-skull movement in general. With this in mind, a set of objectives were defined to act both as a workflow for achieving the project aim and focus the tangential areas of investigation.

Objectives

1. Understand the key factors involved in brain shift, and which should be considered in the FE model.
2. Develop a FE model incorporating key anatomical structures (which can also be used for the phantom model).
3. Investigate the material sensitivity of brain shift and the mechanics of the process using human data and the FE model.
4. Predict a test-case of displacements in a clinically relevant region that could be used as a pre-operative adjustment.

Summary of novel contributions

This thesis details the design considerations and development of a new computational head model, applied to the mechanical analysis of brain shift. These constitute several novel contributions to the body of knowledge, with relevance to both stereotactic procedures and a wide range of other applications. In summary:

- A review of the literature was carried out, identifying brain shift in stereotactic procedures to consist of three phases: positional brain shift brought on by reorientation of the patient's head with respect to gravity, brain shift linked to the loss of the CSF on penetration of the meninges and brain shift linked to advancement of the surgical device. It was concluded that PBS should first be studied and accounted for before considering later phases of brain shift in stereotactic procedures.
- To the best of the author's knowledge, there has been no previous attempt to computationally model PBS. This novel application required implementation of various state-of-the-art methods from adjacent fields to achieve an acceptable level of accuracy. Namely, these were a combination of fluid structure-interactions and spring element arachnoid trabeculae to yield a biofidelic representation of the brain-skull interface.
- The developed FE model was used in conjunction with in-vivo human data and statistical modelling software to identify both material parameters of the intracranial soft tissues and the sensitivity of PBS to change of these parameters. It is believed that the method developed and values obtained represent important contributions to the literature.
- The mechanics of the PBS process were assessed using the material parameters derived as part of this study. This suggested that even with a stiffness considerably lower than is typically reported in the literature, the pia-arachnoid complex undergoes little extension from its initial length but is readily compressed. This informed the conclusion that PBS is a process of subarachnoid space compression and sagging of the central brain structures due to fluid redistribution induced volume change.
- A test case was computed, comparing displacement of the brain in a clinically relevant region in a number of typical surgical positions, of which direct measurement would not be possible. The results confirmed that PBS was of a surgically significant magnitude and that the developed model could be used for this function in the near future.

Chapter 2: Clinical Considerations

Anatomy and Physiology

More than any other organ, the complexity of the human brain is what makes us unique as a species. It forms the central part of our nervous system and is responsible for controlling almost all functions in our bodies. Given the importance of its function, the brain is one of the most protected organs in the body, lying within multiple layers of soft and hard tissues. This section will offer a brief introduction to the anatomy of the brain and surrounding structures and is largely based on Fitzgerald's Clinical Neuroanatomy and Neuroscience (1) with additions from other sources.

The cranium

The brain lies within a spheroid cavity known as the cranial vault. The cranium is a layer of bone which varies in thickness between 4-7mm, depending on the region. In children, some measurements of growth are correlated with skull thickness. In adults, correlation to factors such as gender, age and ethnicity is weak (12, 13). The skull is many orders of magnitude stiffer than other tissues concerned (14, 15) and as such can be considered a rigid body.

The cranial meninges

Surrounding the central nervous system are three distinct layers of collagenous tissue: the dura mater, arachnoid mater and pia mater, together known as the meninges. The meninges can be further subdivided into cranial and spinal regions; the cranial meninges are considered here.

The dura mater is the tough, outermost membrane which provides mechanical support and protection for the delicate brain below. It follows the surface of the cranium with additional large folds known as the dural septa which offer structural support to the brain (Figure 3).

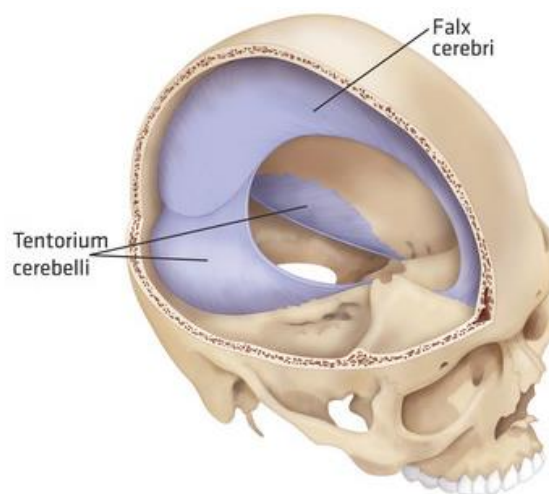


Figure 3 – The falx cerebri and tentorium cerebelli of the dural septa (highlighted here in purple) in context within the cranial vault. Note that the dura mater continues over the inner surface of the cranium but is not shown here. Reproduced from (16).

The cerebral hemispheres are separated by the falx cerebri which runs along the midline of the brain and extends to just above the corpus callosum. The tentorium cerebelli separates the cerebrum and the cerebellum in a lateral plane towards the posterior of the cranial vault. The falx cerebelli also follows the midline, separating the cerebellum laterally, but is considerably less prominent than the other two structures.

Figure 4 highlights the microstructure of further distinct regions of the dura: the periosteal layer is fused directly to the endosteum on the inner cranial surface, while the meningeal layer is fused to the arachnoid mater by a relatively weak layer of dural border cells. The arachnoid mater is a thinner fibrocellular layer which lies in direct contact with the dura, whilst the pia mater is thinner yet, and follows the contours of the brain closely. A cavity is formed between the contoured pia and relatively smooth arachnoid, known as the subarachnoid space. This space is maintained by a combination of cerebrospinal fluid (CSF) and finger like projections known as arachnoid trabeculae. Together, this will be referred to as the pia-arachnoid complex (PAC). Whilst the PAC refers to the distinct anatomical structure, the brain-skull interface in general is a key area of later discussion.

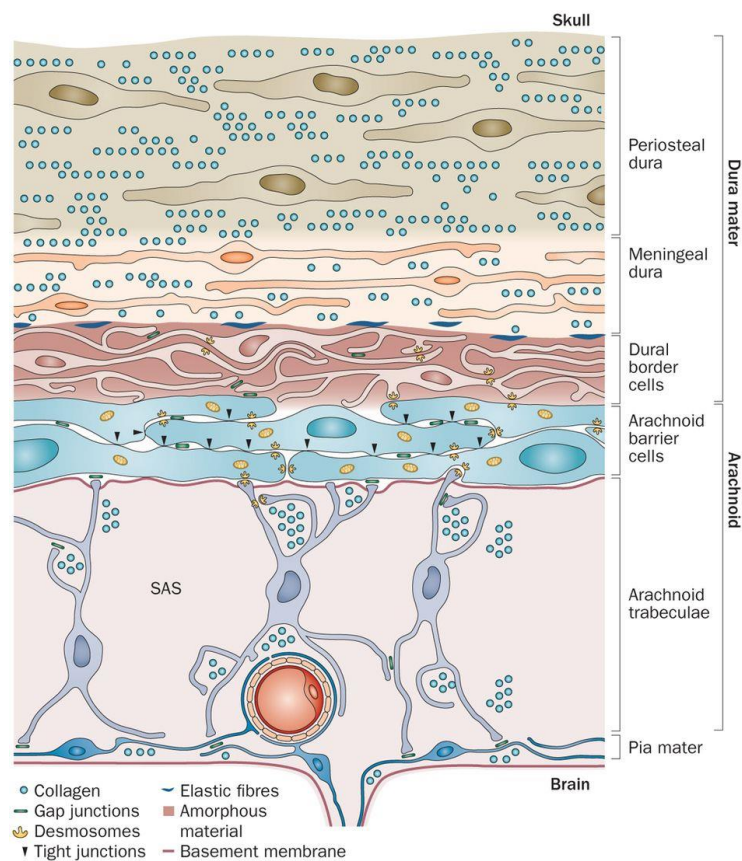


Figure 4 – Detailed schematic of the microstructure of the meninges. Of particular interest is the subarachnoid space (SAS) a region populated by cerebrospinal fluid, arachnoid trabeculae and smaller vessels. Reproduced from (17).

The brain is perfused by a complex vascular network. Deoxygenated blood passes through a series of bridging veins which span the meninges (18), in places running along the undulating

surface of the brain through the subarachnoid space. The bridging veins collect in large sinuses which follow the boundary of the dural septa and the skull before passing back to the heart. Figure 5 shows a coronal section of the superior sagittal sinus. This sinus is significant as it not only collects blood, but also allows for diffusion of CSF to the venous system through arachnoid granulations.

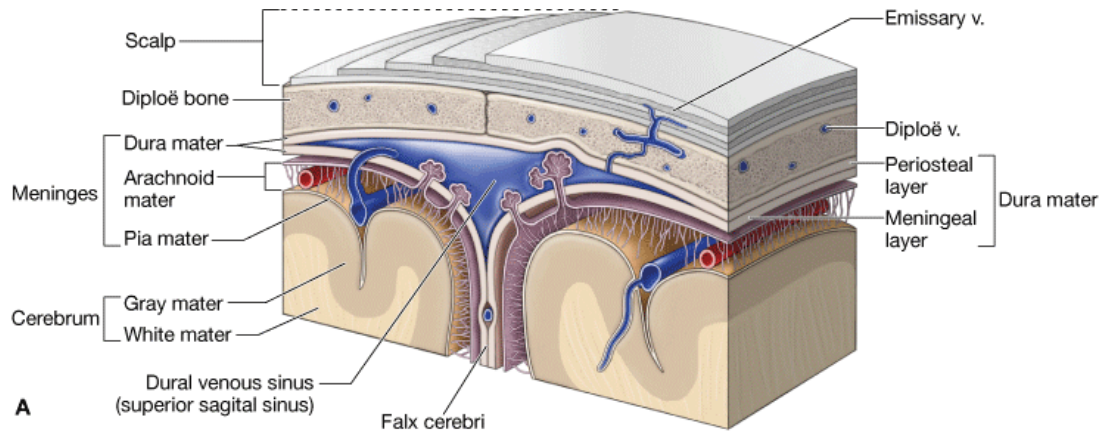


Figure 5 – Coronal section detailing how the dural septa, sinuses, PAC and brain interact to form the complex brain-skull interface. Reproduced from (19).

The brain

The brain itself has a mass of approximately 1.4 kg, although this can vary greatly with height, weight and age (20, 21). The density of brain tissue varies between the white and grey matter, however the specific gravity can be approximated to 1.040 (22), whilst the surrounding CSF has a specific gravity of 1.007 (23). The undulating surface of the brain consists of multiple dips known as sulci and ridges known as gyri. Although generally shallow, the prominent central sulcus (Rolandic fissure) and lateral sulcus (Sylvian fissure) help define the different regions of the cerebrum. In total, there are 5 such regions, or lobes: the frontal lobe, parietal lobe, occipital lobe, temporal lobe and limbic lobe.

The brain can be split more generally into the forebrain, midbrain and hindbrain. The forebrain largely contains the structures of the cerebrum. The hindbrain is made of the pons, medulla oblongata and cerebellum. The midbrain connects the forebrain to the hindbrain, as is labelled in Figure 6–B. The structures proximate to the forebrain/midbrain boundary are of particular importance to deep brain stimulation, which will be discussed further in the next section.

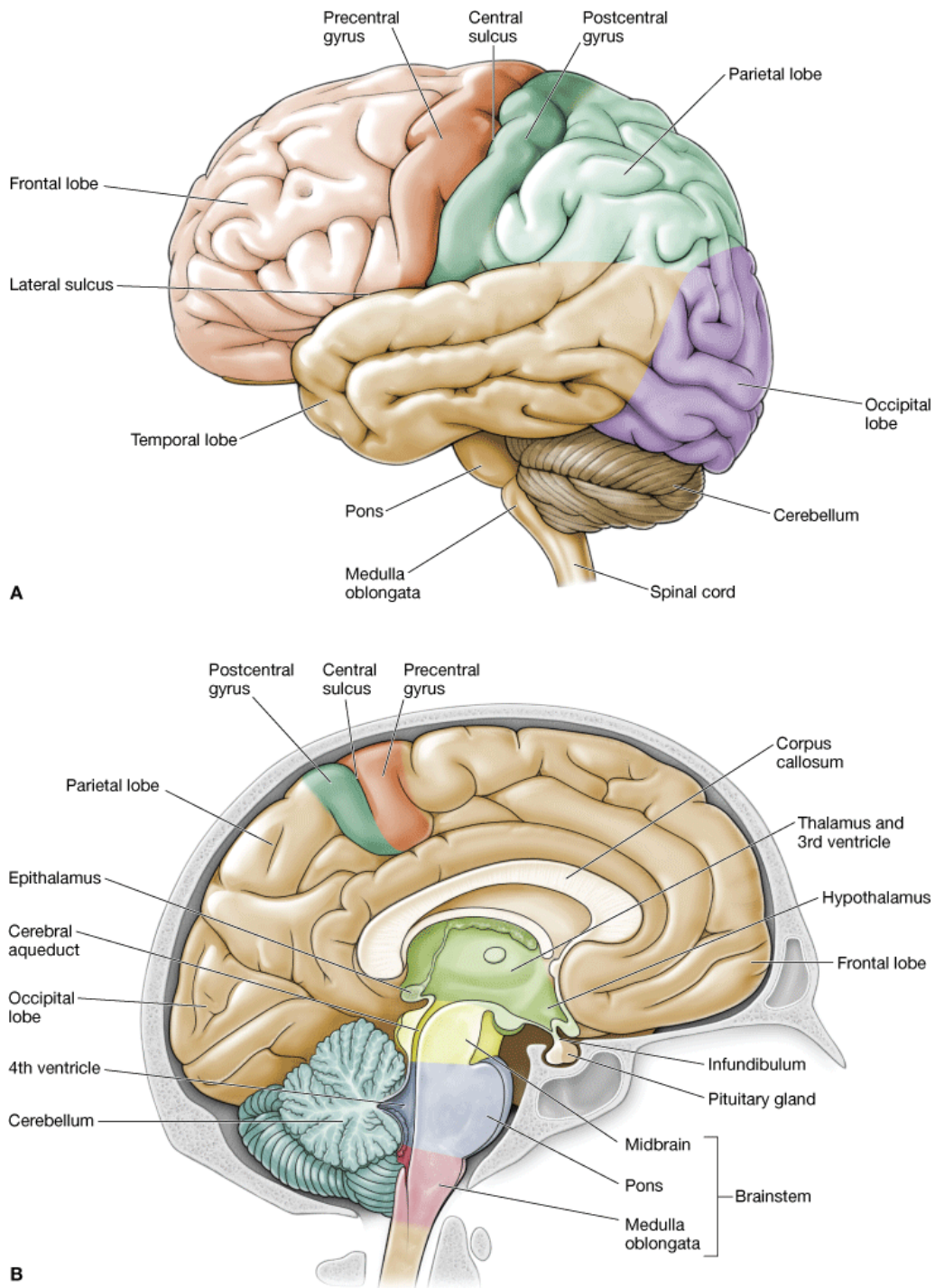


Figure 6 – Anatomy of the brain from [A] a view of the cortical surface and [B] a midsagittal section, where the meninges are removed. Reproduced from (19).

In a surgical setting it is often important to determine reference points within the brain to aid navigation. Due to their ease of identification on images and clinically relevant location, the most commonly used features are the anterior and posterior commissures, or AC and PC. They lie along the midline of the sagittal plane, spanning the cerebral hemispheres. The structures are most often not used alone, but to define an imaginary AC-PC line for navigation or analysis of brain deformation (5, 24).

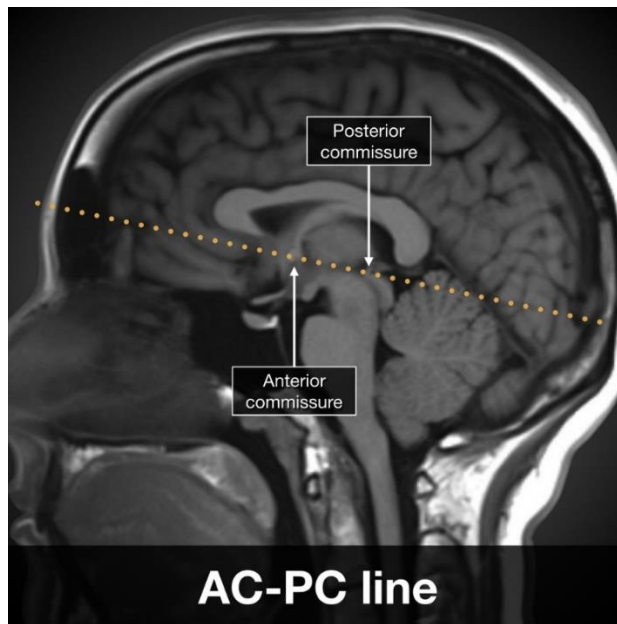


Figure 7 – Annotated MRI depiction of the mid-sagittal AC-PC line on MRI. Case courtesy of A.Prof Frank Gaillard, Radiopaedia.org, rID: 50730.

Fluid mechanics

Whilst the intracranial volume is generally considered to be fixed, the precise volumes of the constituent parts within it undergo constant change. When considering the fluid dynamics of the brain, three fluid networks are identified: vasculature, cerebrospinal fluid and interstitial fluid (ISF). Though classified as distinct networks, they are highly interdependent (25). The flow of blood and CSF within the brain is relatively well understood. Blood flows into the brain through the carotid arteries, perfuses the parenchyma through an incredibly dense vascular network and drains through the venous sinuses. CSF is made in the choroid plexus of the cerebral ventricles, before circulating around the brain and spinal cord. CSF returns to the venous system through the arachnoid granulations of the superior sagittal sinus (1). In contrast, there is still uncertainty about the sites of generation and mechanism of transport of ISF. A summary of experimental data in (26) found evidence of bulk flow of ISF in rats at a rate of $\sim 0.1\text{-}0.3 \mu\text{g}^{-1}\text{min}^{-1}$, highlighting considerably lower flow rates than blood or CSF. This likely stems from ISF flow through the tissue body itself as opposed to distinct macroscopic vessels and cavities.

Brain Shift in Neurosurgery

At the current time, brain shift is a largely unavoidable feature of almost all neurosurgical procedures. Stereotactic operations such as deep brain stimulation require precise targeting of specific structures. In the case of DBS, inaccurate placement of electrodes leads to increased morbidity, unwanted side effects and reduced efficacy (27). As a result, brain shift in stereotactic procedures has been the focus of study since at least 2005 (28).

Brain shift is most commonly attributed to loss of CSF and the subsequent influx of air. With sufficient volumes of intracranial air, brain shift of more than 10mm in the cortex and 5mm in the midbrain has been reported (5). The magnitude of total intracranial air (ICA) and brain shift does show some correlation (5), but it is clear that ICA is just one of many important variables and cannot be used to predict brain shift alone. Evidence for this comes from studies specifically designed to limit the loss of CSF. Some of these appear successful, with significant reductions in ICA being attributed to a supine position and the use of meningeal sealants (29, 30). However, even in cases where negligible levels of intracranial air are reported, surgically significant brain shift is still seen (5, 31).

This thesis details the development of methods to better understand brain shift, studying both the factors and mechanisms involved. Whilst it is hoped that the findings are applicable to all stereotactic cases, DBS specifically was chosen for further investigation, as the high levels of accuracy required for successful outcomes has led to significant interest in the literature. The following section introduces DBS in more detail, the current methods employed to account for brain shift and most importantly, assessment of how much each pre-operatively known variable is thought to impact brain shift. Whilst DBS was chosen as the main area of focus, it is important to highlight that the findings are relevant to a wide range of procedures. At the end of this section, this information is used to help define the scope for next stage of computational analysis.

Deep Brain Stimulation

Deep brain stimulation is a branch of stereotactic neurosurgery for the treatment of movement disorders which do not respond to medication. These conditions include essential tremor (ET), Parkinson's disease (PD) and dystonia, with Food & Drug Administration approval being granted in 1997, 2002 and 2003 respectively (32). In that time over 100,000 DBS procedures have been performed (33) leading to continuous advances in the procedure.

Table 2-1 – Typical movement disorders treated with DBS, the associated anatomical targets, and approximate proportion of all DBS procedures: Subthalamic nucleus (STN), globus pallidus internus (GPi), ventral intermediate thalamus (VIM), pedunculopontine nucleus (PPN), zona incerta (ZI).

Movement disorder	Target (33)	Proportion of procedures (32, 34)
Parkinson's disease	STN, GPi, VIM, PPN	58-65%
Essential tremor	VIM, ZI, dorsal STN	16-24.8%
Dystonia	GPi	7.8-31%
Other		5%

The basal ganglia are a group of structures in the basal forebrain and midbrain which are involved in controlling movement (1). Areas within the basal ganglia form circuits with the cerebral cortex responsible for movement. The structures identified in Table 2-1 do not induce movement directly, but instead modulate activity in other regions of the brain such as the motor cortex. Although the exact mechanism of action is still debated, the electrical signals generated in DBS act upon these electrical pathways to return more normal movement (35). Selection of which region to target is carried out by an experienced neurosurgeon and depends on the specifics of each case.

The exact size and position of these target structures vary between patients. The STN is approximately 5.9 mm x 3.7 mm x 5 mm (36), and split into limbic, associative and motor regions (37). Given their size and similarity to surrounding tissue, structures such as the STN are difficult to visualise with traditional medical imaging (38). Adding further complexity, debate continues over which specific region of the STN yields optimal clinical results (39). Anatomical atlases have been produced to aid identification of such deep structures by defining vector displacements of the targets from easily identifiable structures. However, patient-to-patient variations in position similar in size to the STN (36) mean that these atlases cannot always be relied upon. With increasingly powerful MRI systems, direct identification of structures may become less difficult. However, even with correct identification of the target, accurate placement can still be compromised by brain shift.

The unpredictability of brain shift has led to the use of additional measures to ensure acceptable device placement. Some have attempted to develop methods to predict pneumocephalus from specific characteristics seen on preoperative scans, although these require further refinement (40). Others simply adjust stereotactic coordinates with a fixed shift across all patients with unacceptable initial device positioning (41). In general, more reliable outcomes are obtained with microelectrode recording (MER) (42) and interoperative magnetic resonance imaging (iMRI) (43).

Microelectrode recording is a technique often used to confirm acceptable placement of the electrode in the target structure. Each region of the basal ganglia is identifiable by the electrical signals it emits. By measuring these signals along the predefined tract, surgeons are able to identify

if they are in the correct anatomical target before inserting the permanent electrode. A five-bore collet allows the use of up to five MER electrodes without movement of the stereotactic frame. Some groups take recordings with all electrodes and decide a permanent location based on the results, as is shown in Figure 8 (44). Others start with the centre hole, and simply change to the posterior option if initial placement is unsatisfactory (41). Whilst MER is an incredibly popular tool, the method has associated costs: financial expense, increased duration of surgery, risk of haemorrhage and neurological deterioration (45).

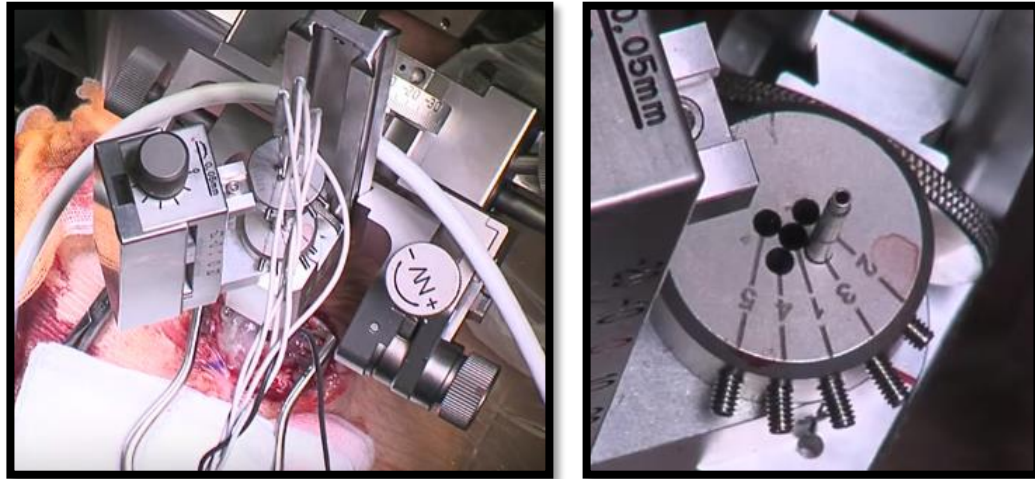


Figure 8 – Left – Five MER electrodes are used concurrently to identify the optimum positioning in the target. Right – zoomed view of the 5-electrode collet. The guide tube has been left in position 3 to allow insertion of the permanent electrode. Images reproduced from (44).

As the name suggests, iMRI uses modified stereotactic equipment to allow for anatomical MR imaging during the procedure. Often used in conjunction with MER, this allows for real time visualisation of electrode position (46). The impact of stereotactic error or brain shift is reduced by updating the implantation trajectory during surgery. If it develops that the electrode placement is still unsatisfactory, this can be easily identified and the electrode re-implanted (43). Whilst iMRI based systems offer excellent accuracy they are expensive and therefore not commonly used at present (46). Although they represent the state-of-the-art, risks associated with re-implantation highlight that even the best technology has limitations.

These techniques are currently being implemented around the world, with varying levels of success; however, they are not always available. Developing a surgical method that is reliable enough to reduce the need for assessment of electrode position would offer a great improvement to surgical time, expense and potential radiation exposure.

Complications

Complications associated with DBS procedures are relatively well understood. Although not always directly harming the patient, misplaced electrodes occur in approximately 5% of procedures (47) and would likely require revision. It should be noted that rates of electrode

misplacement are likely to vary greatly between institutions and methods. Intracranial haemorrhage is infrequent (2.1% of procedures) and normally associated with postoperative confusion or seizures. Severe haemorrhage is more uncommon still but can require emergency intervention and lead to permanent hemiparesis (47). Intracerebral infection is rare but possible, requiring antibiotic treatment and the removal of implanted devices (48).

Given the confines of brain surgery, implantable devices are limited in size. As a result, hardware-based complications are in the region of 5-9% (34, 49, 50). The design of electrode leads may predispose them to fatigue failure (51). Electrode breakage, seen in up to 2.5% of cases (34), leads to an open electrical circuit, presenting an immediate and obvious end to clinical improvement. More frequently, degradation of insulation can lead to a short circuit and diminishing clinical effect over time. To prevent this impedance testing of implantable devices should be carried out regularly (52). Other complications include electrode migration or stricture formation (49). Given the very low mortality and morbidity rates and vast clinical improvement often seen, good post-operative monitoring enables DBS procedures to be a relatively safe and worthwhile intervention (34, 50).

Components of targeting error

As stated in the introduction, the accuracy of placement is related to both the accuracy of the surgical equipment/imaging and movement of the anatomical target within the reference frame due to brain shift. Stereotactic systems can broadly be split into three subsets: frame-based, frameless and iMRI guided operations. As the focus of this thesis is on brain shift, a phenomenon common to all methodologies, the specifics of each is not critical. However, it is useful to cover some key aspects of common approaches to provide context for further points of discussion.

Stereotactic systems have improved dramatically over recent years with the most advanced systems achieving accuracy in the order of 1 mm, as opposed to 2-3 mm when originally introduced (6). In an extensive review, Li et al. (6) presented the workflow shown here in Figure 9, highlighting sources of error at each step of the process.

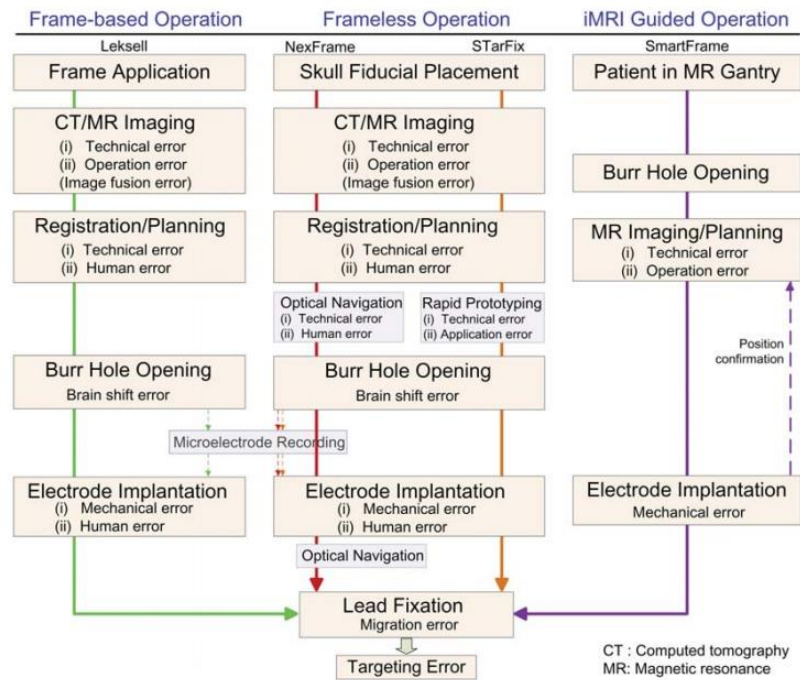


Figure 9 – Schematic of the potential sources of error in each step of the traditional frame-based, frameless and iMRI based stereotactic workflows. Reproduced from (6).

Currently, most methods rigidly fuse MR and CT data, the MR providing excellent anatomical distinction within the parenchyma, and CT highlighting the vessels and skull. This can induce error in a number of distinct ways: 1) misidentification of the anatomical target, 2) misalignment of the CT and MR images, 3) misalignment of subject and surgical device within the stereotactic reference frame and 4) geometric distortion of the MR image itself. MR image distortion is likely the most significant of these, arising from non-linearity of the gradient fields leading to a morphing of the compiled image. The level of distortion can be significant, increasing with Euclidean distance from the isocentre to a typical maximum of around 5mm. Whilst distortions can be corrected computationally, this is not applied universally leading to a significant source of error (53).

Studies using iMRI have reported displacements in the order of 0.6 - 0.7mm (43, 54), compared to robotic systems such as ‘neuromate™’, where an accuracy of 0.86 ± 0.32 mm has been reported (55). Whilst this suggests an improvement of around 0.2 mm using iMRI, the same robotic system achieved an accuracy of 0.44 ± 0.23 mm when tested in robot space with no patient. This remaining inaccuracy is attributed to deformation of the stereotactic head-frame, the mechanical accuracy of the arm and the microdrive system, in addition to errors associated with the registration process (55).

With iMRI, trajectory adjustment is commonly made with the patient’s head in the operative position and after cranial perforation to reduce the impact of brain shift (43). It is inferred that the discrepancy between the levels of error between iMRI and traditional methods are therefore due to this adjustment. However, reduced accuracy compared to the ex-vivo testing suggests that

the process of device insertion is still influential. Most importantly in the context of this study, this suggests that submillimetre accuracy is the new standard within the field. These levels of improvement seen by using iMRI methods, which only account for the effects of brain shift, are sufficiently valuable in the eyes of the clinician to warrant the expense, when available. Furthermore, a future model capable of capturing penetration of the device may have the potential to offer more accurate results than even iMRI methods, at least on the first attempt.

With this in mind, the following section focusses not on the total accuracy of stereotactic systems, but on quantifying brain shift in DBS procedures and understanding which variables are most influential.

Magnitude of brain shift in DBS surgery

A considerable amount of work has focussed on assessing the levels of brain shift in neurosurgery. Whilst precise methods vary, the general approach involves comparing pre and post-operative position of the relevant structures relative to either an external or anatomical reference point. In cases of craniotomy and tumour removal, cortical shifts in the region of 20 mm are reported (56). In stereotactic procedures this is considerably less in magnitude, although arguably more impactful as there is no visual field of the target structures. Different groups have reported brain shift in a variety of different ways. The AC and PC are regularly used as an indicator of deep brain shift as they are readily identifiable on medical images and positioned along the midline of the brain.

The sign convention adopted in this section is show in Figure 10. The values reported in Table 2-2 have been adapted to fit this convention for comparability. As sign convention used to define shift in the frontal (X) plane is not consistent between authors, these are defined individually as follows:

- Miyagi et al. 2007 (24) – Positive X displacement is defined as lateral movement on the side contralateral to the first electrode placement (in unilateral and bilateral procedures).
- Elias et al. 2007 (5) – Positive X displacement is defined as a lateral shift in either direction for each patient.
- Petersen et al. 2010 (57) – Positive X displacement is defined as shift laterally to the left.
- Miyagi et al. 2015 (30) – Not defined – assumed to be the same as previous method (24).

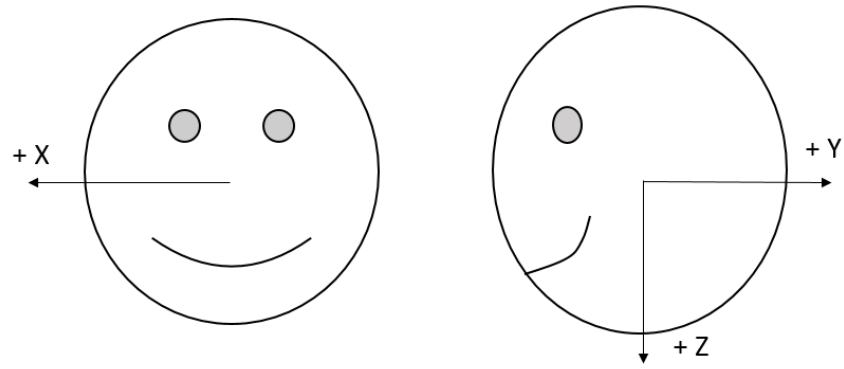


Figure 10 – Sign convention for brain shift values reported in the literature. X = lateral, Y = anteroposterior and Z= dorsoventral.

Table 2-2 – Scalar and vector brain shift values reported in the literature regarding DBS patients. Beige cells indicate a value that has not been reported directly but calculated from those reported. Blue cells indicate a reported statistically significance to either preoperative values or comparative subject group

		Miyagi et al. 2007 (24)		Halpern et al. 2008 (41)		Elias et al. 2007 (5)	Khan et al. 2008 (38)	Petersen et al. 2010 (57)	Ivan et al. 2014 (58)	Hunsche et al. 2009 (31)			Miyagi et al. 2015 (30)	
Group		Unilateral	Bilateral	Group A	Group B					Group 1	Group 2	Group 3		
Patients (Leads)		8(8)	10(20)	33 (66)	17 (34)	66 (104)	25 (32)	135 (254)	36 (44)	16(16)	8(8)	1(1)	28(56)	
Scalar Shifts	Δ AC position/ mm	1.46	2.28			0.98 ± 0.8 (0.21 to 5.67)	1.8 ± 0.7	1.0 ± 0.5 (max 2.5)		0.5 ± 0.3 (max 0.8)	0.6 ± 0.3 (max 1.3)	1.2	0.49	
	Δ PC position/ mm	0.88	1.10			0.74 ± 0.48 (0.03 to 2.75)	1.6 ± 0.8	1.0 ± 0.5 (max 2.8)		0.6 ± 0.3 (max 0.9)	0.5 ± 0.3(0.9)	0.5	0.26	
	Pre-op ACPC length/ mm	23.60 ± 1.72	23.96 ± 1.50					24.6 ± 1.5						
	Post-op ACPC length/ mm	23.14 ± 1.57	22.77 ± 2.09					24.4 ± 1.5						
	Δ ACPC length	-0.46	-1.19			-0.22 ± 0.85 (-4.28 to 1.66)		-0.2						
Vector Shifts	Δ Y ACPC length	-0.43	-1.2	-0.04 ± 0.76	-0.41 ± 0.68	-0.23		0.2						-0.24
	Δ Y AC/ mm	1.15 ± 0.91	2.23 ± 0.93	1.45 ± 2.67	1.54 ± 1.74	0.56 ± 0.9 (-0.97 to 5.59)		0.4 ± 0.6 (-1.0 to 2.4)	0.43					0.48 ± 0.29
	Δ Y PC/ mm	0.72 ± 0.56	1.03 ± 0.90	1.18 ± 2.39	0.99 ± 1.61	0.33 ± 0.45 (-0.50 to 1.70)		0.2 ± 0.7 (-1.8 to 2.8)	0.3					0.24 ± 0.25
	Δ X AC/ mm	0.69 ± 0.45	0.27 ± 0.22			0.04 ± 0.38 (-0.89 to 1.95)		-0.1 ± 0.3 (-0.8 to 1.0)						-0.02 ± 0.16
	Δ X PC/ mm	0.35 ± 0.26	0.13 ± 0.18			0.08 ± 0.45 (-0.89 to 2.34)		-0.1 ± 0.3 (-0.8 to 0.8)						-0.02 ± 0.13
	Δ Z AC/ mm	0.58 ± 0.77	0.39 ± 0.68			-0.14 ± 0.57 (-1.68 to 1.47)		-0.1 ± 0.7 (-1.8 to 1.5)						0.11 ± 0.19
	Δ Z PC/ mm	0.37 ± 0.47	0.37 ± 0.30			0.11 ± 0.51 (-0.97 to 1.63)		0.0 ± 0.7 (-1.9 to 1.7)						0.11 ± 0.18
	Δ Y Frontal Cortex/ mm			0.56 ± 1.15	4.80 ± 1.52	2.66 ± 2.10(-0.56 to 10.42)		6.2 ± 3.0 (1.6 to 12.8)	1.4 ± (0.00 to 10.1)					

To assess the meaning of the values shown in Table 2-2, average values for each parameter were calculated. Over all the procedures, 67% of 384 patients were bilateral. Some groups who carried out bilateral procedures but reported values found after placement of the first electrode have been treated as unilateral (31). Therefore, it can be suggested that bilateral procedures are by far the norm. Reported values were weighted by study sample size and averaged over the total sample size for that variable. As the values reported in Table 2-3 are calculated with results from a number of different groups it is likely that they offer a good approximation of what is usually seen in the field.

Table 2-3 – Weighted average values for brain shift reported in DBS procedures.

	Variable	Weighted average (mm)
Scalar Shifts	Δ AC position	1.03
	Δ PC position	0.88
	Pre-op ACPC length	24.53
	Post-op ACPC length	24.25
	Δ ACPC length	-0.26
Vector Shifts	Δ Y ACPC length	-0.24
	Δ Y AC	0.70
	Δ Y PC	0.43
	Δ X AC	-0.03
	Δ X PC	-0.03
	Δ Z AC	-0.05
	Δ Z PC	0.06
	Δ Y Frontal Cortex	4.48

As expected with a semi-supine/supine patient, the AC and PC shift posteriorly with a magnitude of 1.03mm and 0.88mm, respectively. Importantly this discrepancy confirms the non-rigid nature of brain shift; a factor overlooked in some registration methods and a possible source of error. This is supported by a shortening of the AC-PC distance which is predominantly in the anteroposterior direction.

Due to the different sign conventions used between groups, the X component of the vector shifts average to a negligible value of 0.03 mm. Averaging the total magnitude found by each group leads to a value of approximately 0.09 mm for both AC and PC. More interesting than the average magnitude is the finding from Miyagi et al. 2007 (24) which suggests greater lateral movement in unilateral procedures.

When considering the vector shifts, this averaging of non-sagittal components gives the impression that displacement is almost exclusively in the sagittal plane. Whilst this is likely to be an accurate representation on average, it is important to remember that significant lateral and anterior/inferior displacements can be found in individual cases.

Variation in patient orientation which occurs across the groups studied is likely to be seen in the Y-Z planes. Interestingly, on average, the AC experiences a superior shift contrary to the inferior shift reported by some in the PC, suggesting an element of rotation. With this data the statistical significance is not known.

The average value found for each group varied significantly. The same applies to sample size. Although the averages which have been calculated are weighted for sample size, this cannot avoid the fact that one group with particularly high or low results and large sample size could bias the averages. As a result, the data provides an interesting approximation but cannot be used, for example, to determine a direct adjustment that could be applied in theatre.

It is apparent from the literature that surgical technique is constantly evolving. As shown in Figure 11, there appears to be a reduction in brain shift over recent years. This is likely due to the discovery, and adoption of improved techniques. As such, more insight can be gained from studying methodological improvements than the absolute values which are seen in historical data.

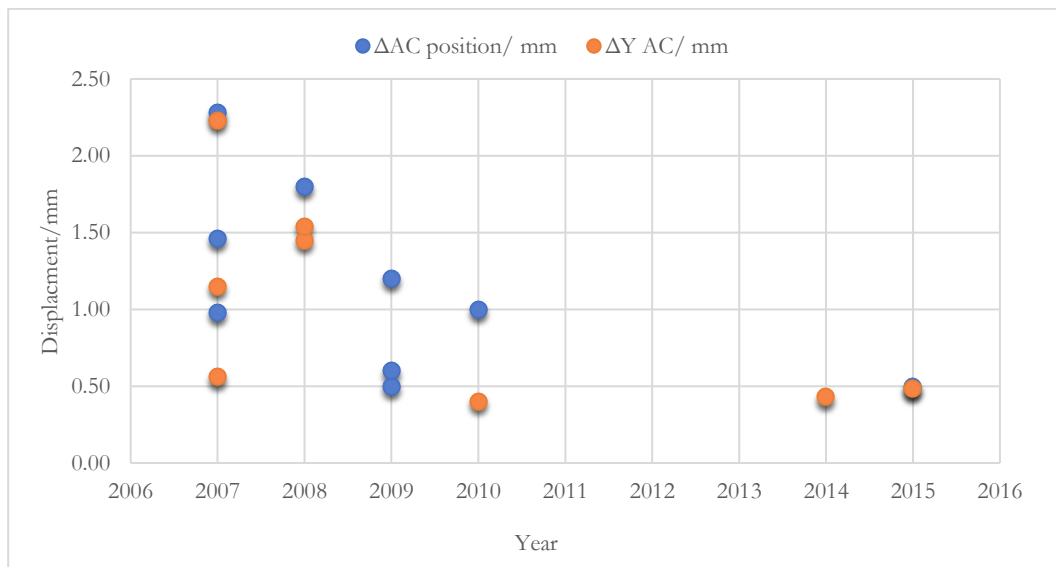


Figure 11 – Comparison of the scalar and Y vector component position change in the AC reported by each group, plotted against publication year of the study.

It can be concluded that brain shift varies significantly between patients and in different regions of the brain. Movement is predominantly in the direction of gravity, but shifts in the other principle axes are likely, and dependant on the specific methods used. Even in DBS procedures, cortical shifts of over 10 mm are possible (5, 57). Although the deep brain target is unlikely to move this much, it is still important to consider as avoiding rupture of vessels and other structures is critical (59). Most importantly, even with AC shift in the order of 0.5 mm, this is still a clinically relevant phenomenon.

What factors influence brain shift, and by how much?

The literature suggests that certain factors are more influential in leading to brain shift than others. In the following section, these factors are individually analysed with the aim of assessing which should be considered when developing this study further.

The influence of pneumocephalus on brain shift

In order to insert the electrode into the brain the meninges must be penetrated. This is normally done in advance to allow insertion of a guide tube or MER device. As the arachnoid is perforated, the CSF contained within it can leak out of the cranial cavity. This loss in intracranial CSF volume causes a reduction in the effective buoyancy of the brain and is the main source of brain shift (5). With firm attachments to the pia and arachnoid, cortical movement leads to detachment of the arachnoid from the dura along the relatively weak dural border cells and air invasion of the subdural space (60).

Increasing numbers of researchers are focussing on methods of reducing the loss of CSF and subsequent pneumocephalus. This is based on the accepted association between pneumocephalus and brain shift. This was first demonstrated by Elias et al. (5) and is still one of the few reports measuring both ICA and brain shift in various parts of the brain. A relationship was found between ICA and AC shift, and was shown to be statistically significant, with a similar correlation existing with cortical shift (5). However, others have failed to find similar statistical significance. This is likely due to the influence of many other variables (58). The complexity is highlighted in Figure 12, which clearly illustrates that AC shift of 0-2 mm is common with little to no measurable intracranial air. Consistent shift under 1 mm can occur with ICA up to approximately 10 ml, with a significant impact only becoming clear at approximately 15 ml (31). In fact, the unpredictable nature of brain shift is such that pneumocephalus has been shown to have no statistically significant correlation to the deviation of the electrode from the intended position in some cases (61).

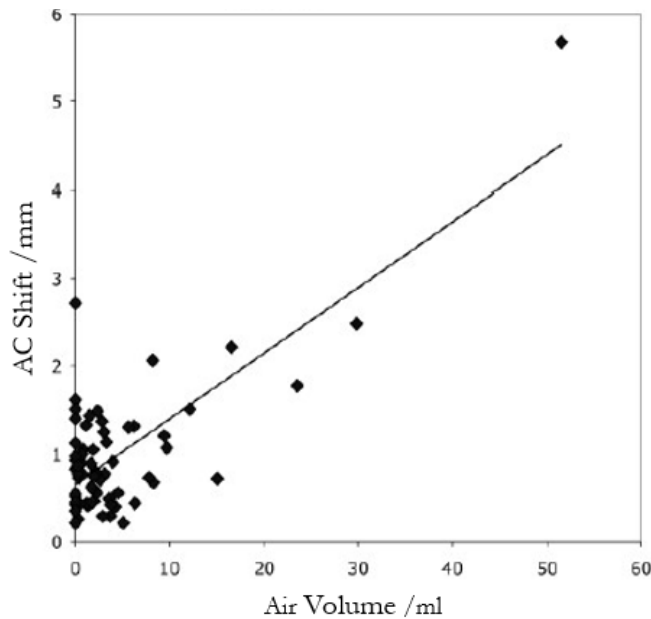


Figure 12 – The relationship between post-operative (one day after surgery) ICA volume and deviation of the AC from its original position ($r = 0.569$). Adapted from (5).

That said, pneumocephalus is clearly a prominent source of brain shift, especially if intracranial air volumes are high (5, 31, 61, 62). It is also clear that the usefulness of this information is in knowing that it should be kept as close to zero as possible so that the other contributing factors can be readily identified. Aspects affecting brain shift such as orientation of the patient with respect to gravity (42) and sealing of the meninges (29) amongst other things are thought to have a significant impact on levels of pneumocephalus. These are discussed further in the following section.

The cranial burr-hole

In order to access the meninges and brain the cranium must be perforated. In locations used for DBS procedures, skull thickness can be as much as 10mm (63). Most authors report using ‘large’ 11mm or 14mm burr-holes (5, 41, 42, 57, 58, 61), with burr-holes as small as 4mm also reported (24, 64). As most studies include participants with only one size of burr-hole, the effect of burr-hole size cannot be determined from these.

Sharim et al. (65) proposed that CSF loss leading to pneumocephalus may be related to both burr hole and the size of the opening in the dura, known as the durotomy. To investigate this, patients with either small (4mm twist drill), or large (14mm cranial perforator) cranial holes (78 and 87 implantations, respectively) were assessed. Patients were elevated at 20-30° to the floor, with bone wax applied after completing the cranial perforation and Tisseel™ sealant applied to the dura directly after opening. Eight hours after the operation, CT scans were used to assess pneumocephalus. For both unilateral and bilateral procedures, no significant correlation between diameter of burr-hole and volume of pneumocephalus was found. However, extrapolating this finding to brain shift must be done with caution.

Creation of the burr hole can be done by hand at the approximate location. Introducing devices into the brain sometimes requires increasing the size of the burr hole to prevent interference with the cranium. Stereotactic burr hole drilling can lead to significant reduction in additional drilling and decrease the size of the burr hole compared to freehand techniques (63).

With the suggestion that cranial window diameter is insignificant in relation to intracranial air intake, safety and personal preference become the most important factors when deciding which technique to use. A 14 mm burr hole is compatible with a wide range of anchoring systems and gives a better view of the cortical surface potentially minimising the risk of damaging cortical vessels (65). However, advanced surgical planning software enables avoidance of major vessels and structures before the procedure even begins. The use of a stereotactic burr hole technique raises new surgical challenges; whether these are offset by the reduced need for expansion of the cranial window is unclear. The incidence of accidental perforation of the dura or parenchyma using the conventional automatic-releasing perforator reported to be 0.54% (66). As the equivalent rates with the stereotactic system unknown, comments on safety also cannot be made.

Attempting to model any protrusion of the brain through a 4 mm vs 14 mm cranial window would be unreliable, due to the use of various sealants and surgical adaptors. Considering the literature, the method of creating the cranial window did not appear to influence brain shift and was not considered further.

Duration of surgery

It is largely accepted that the majority of CSF loss, and therefore intracranial air intake occurs during perforation of the cranium and meninges at the beginning of surgery (61, 67). This is supported by many studies which fail to find a correlation between surgical duration on intracranial air volume or brain shift (5, 38, 57, 61, 65, 68).

Azmi et al. (69) found a weak correlation between surgical time and total intracranial air. However, they also found a stronger correlation between surgical time and the number of microelectrode recordings required. It is therefore likely that the increased number of perforations was responsible for this increased intracranial air rather than the duration of surgery itself.

More significantly, a study by Halpern et al. (41) found that in a group of subjects with cortical shift >2 mm, AC-PC shortening correlated with surgical duration [$r=0.43$; $p<0.04$]. This correlation was not found in the patient group with <2 mm of cortical shift. In addition, there was no statistically significant difference in procedure duration between the two groups. This may suggest that surgical duration may only have an impact if a certain amount of CSF is lost before adequate burr hole sealing, although the levels of intracranial air are not reported.

Other studies with significant mean volumes of intracranial air found no correlation with duration of surgery (65). As a similar patient position and method of dural sealing is used in these studies, it is unlikely that the CSF loss hypothesis is correct. It is therefore unclear what caused this correlation.

Perforation and sealing of the meninges

It is well understood that the release of CSF after meningeal penetration has a major influence on brain shift. A number of potential methods to prevent this have been suggested, with varying success. Flooding the burr hole with saline (70) was thought to replace any lost CSF, maintaining volume. However, as brain sinking is associated with redistribution of CSF from the third ventricle to the subdural space, this may not work (24). Similarly, filling the ventricles with air could counteract brain shift if done to the correct volumes, but this volume would be varied and unknown. This method also causes anterior movement of the commissures making navigation more complex (24). Finally, direct suction of the site is likely to cause the loss of more CSF and make the problem worse (24).

More promising methods include limiting the dural perforation to the size of the guide tube (42, 71), although this is still not commonly used (29, 57, 58, 61, 65). Another option is penetrating the meninges with the microelectrode itself (30), although there do not appear to be any studies assessing the method of opening the meninges specifically. More common is the use of monopolar/bipolar electrocautery of the meninges before the electrodes are inserted (24, 30, 57, 61, 65). Whilst normally used to prevent blood loss, the same process may inhibit loss of CSF from the subarachnoid space (72).

The real advancement in this area is in the use of various substances to ‘plug’ the burr hole, or seal the meninges preventing CSF loss. In 2007, this was limited to fibrin glue or melted bone wax (24). These are now consistently used as part of normal procedure (31, 42, 57, 61, 65, 69). Development of this idea was reported by Takumi et al. (29) with the use of a novel polyethylene glycol (PEG) hydrogel dural sealant. The dura and arachnoid were excised manually, with minimal parenchymal electrocautery. PEG hydrogel was then applied to the entire exposed surface before introduction of the guide tubes. On average, post-operative imaging revealed an ICA volume of 1.3 ± 1.5 ml (0.0 to 3.5 ml), compared to 32.3 ± 12.3 ml (19.1 to 42.5 ml) for a control group.

In a similar investigation Coenen et al. (72) compared ‘welding’ the arachnoid and pia together using blunt tip bipolar forceps, as opposed to simple coagulation as usual. Both Gelfoam™ padding and Tisseel™ fibrin sealant were also used in each group in an attempt to prevent CSF loss. ICA volume in the ‘welded’ group was 4.86 ± 4.35 ml (0.2 to 10.7 ml) compared to 27.59 ± 17.80 (0.3 to 55.4 ml) for the control. Although this is a marked improvement, a delay on average of almost 24 hours between surgery and follow-up imaging means the measured values will be

an underestimate of what actually occurred. With this in mind, PEG hydrogel currently appears to be the most effective method of controlling CSF loss.

Patient age and atrophy of the brain

As humans age, changes occur to the brain on a molecular and morphological scale. These changes are not consistent across all regions of the brain and are thought to be influenced by genetic and environmental factors (73). Atrophy, or shrinking of the brain, is one age-related change frequently assessed in the literature. Quantification of brain atrophy requires analysis of preoperative images; multiple methods to do so are available (5, 24, 69). Changes specific to DBS procedures include lateralisation of the STN relating to aging (74). This should not be overlooked if an atlas-based targeting approach is relied upon.

Patient age has been shown by many to have no impact on pneumocephalus (5, 65, 75) or brain shift (57, 58, 76, 77). This finding is once again contradicted by the results of Halpern et al. (41) reporting a link between age and posterior shift of the AC. Although atrophy was not itself measured, they cite many possible explanations linked to aging. These include ventricular enlargement due to increased resistance to CSF outflow, and various causes of reduced or negative intracranial pressure.

Unlike age, quantifying atrophy of the brain can be undertaken in many ways. Some suggest the same trend follows, with no significant impact on pneumocephalus and brain shift (5, 24). Elias et al. (5) analysed the lateral and third ventricle volume. Miyagi et al. (24) reported assessing ventricular enlargement, measured by the width of the third ventricle and cerebroventricular index, a ratio of subdural area to intracranial area on a 2D segment. However, only a lack of correlation between ventricular width and AC shift was reported. Whether this infers the same finding with cerebroventricular index is unknown. Nazzaro et al. (42) do not report their method of quantifying atrophy.

This method of quantification is important according to the work of Azmi et al. (69). No relationship was found between ventricular volume and ICA supporting the work of the previous authors. However, a statistically significant correlation [$cc=0.47$] was found between the ratio of extra-axial CSF to total intracranial volume and ICA, when normalised for total intracranial volume. Similarly, Obuchi et al. (76) found no relationship between brain shift and third ventricle width, but did with cella media index, a ratio of lateral ventricle width and cranial window width at the cella media level.

Picking a trajectory so that the electrode enters a gyrus close to the cranium, and adopting a supine position, so that gravity packs the brain against the burr hole are both recommended on anecdotal evidence (24, 42). The theory for this is that a reduced subarachnoid space may limit CSF loss as a greater hydrostatic pressure is generated over smaller cross-sectional areas. Applying the same logic would suggest that atrophy of the cortical surface would increase the potential for

CSF loss. Interestingly, these ideas are presented by authors who reported no associations with atrophy and brain shift, highlighting a lack of proper understanding in the area.

The influence of age and atrophy on brain shift is not completely understood but potentially very important. The negative findings of many groups may be due to a reduction in sensitivity to atrophy as a result of the large range of other influential factors which are not consistent across patients. In order to improve our understanding of the potential mechanisms, more detailed analysis of the morphological changes to the brain are required.

Orientation with respect to gravity

Patient position during stereotactic procedures varies greatly between surgeons, and patients. Typically the patient is positioned so that the head and neck sit anywhere between 0 to 30° to the floor (5, 29, 38, 41, 42, 57, 58, 61, 65), although positions of up to around 40° have been reported (24). Personal preference of the surgeon is a large factor in determining orientation, with the need to achieve a safe trajectory through the brain contributing to this decision. In the personal experience of the author, some surgeons opt to operate with the patient in fully prone or lateral positions, in order to achieve what they feel to be the optimum trajectory; it is unclear why this positioning is relatively absent in the literature. The change in orientation impacts the perceived magnitude of brain shift in two distinct ways:

1. Repositioning the head with respect to gravity causes PBS of a surgically significant magnitude even in everyday life (4, 42, 78).
2. The orientation of the head may affect the distribution of CSF when this is not controlled otherwise.

Preoperative scans are usually performed in the supine position. If this orientation remains for surgery, PBS is not a contributing factor to the total level of brain shift seen. It follows that if scanning and operative orientation are not the same, PBS will have an impact. The magnitude of PBS is discussed later.

It is generally assumed that with total intracranial volume constrained by the skull, any ICA is equivalent in volume to the volume of CSF lost (61, 72). Others suggest that the total volume is not fixed, and an up-right position may lead to a reduction in brain volume due to increased venous return (30) and therefore introduce a negative hydrostatic pressure leading to air invasion (24). With few reports detailing both patient position and ICA volume, comparing most of the literature is difficult. The few articles specifically assessing this draw strong conclusions. Nazzaro et al. (42) studied 61 DBS patients where surgery was performed in the strict supine position. From this they suggested strict supine positioning results in “minimal intracranial air”, with mean levels 0.98 ± 1.42 ml (0 to 7.02 ml). However, other studies such as Takumi et al. (29) achieved similarly low ICA volumes with patients at 10-15° with the use of a novel sealant. In addition to supine positioning, Nazzaro et al. (42) also used a hole in the dura of only 1.5mm; the same size

as their guide cannula. Dural openings of this size are not often seen in the literature. In light of this, it is hard to conclude whether the low ICA volume reported here is a result of patient positioning alone.

The use of a supine position is supported by Miyagi et al. (30) with a direct comparison of AC and PC shift in previous results (24) showing a statistically significant reduction in brain shift when compared to a previous semi-sitting position. These results are shown in Figure 13. The direct measurement of brain shift allows a more reliable assessment of the effect of patient position than measuring ICA volume alone. It is likely that the supine position does have a positive impact on brain shift reduction; whether this is due to the mitigation of PBS or another reason is unknown. However, regardless of the efficacy of a supine position in reducing intracranial air intake, this technique alone cannot be relied upon entirely as patient specific discrepancies may prevent a supine position from being used (24).

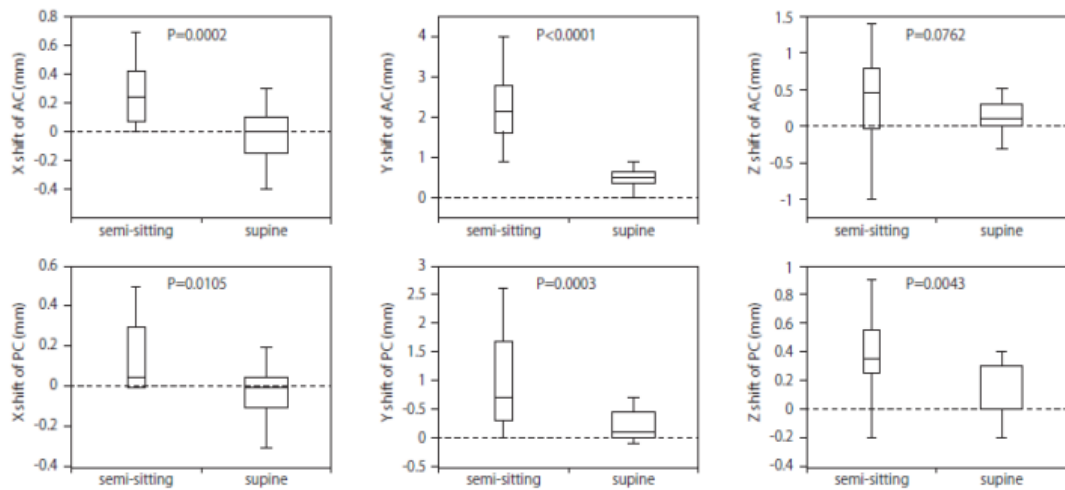


Figure 13 – Box and whisker plots comparing the orthogonal components of AC and PC shift in semi-sitting and supine surgical positions, suggesting greater displacement in the former. Reproduced from Miyagi et al. 2015 (30).

Deformation due to the advancing electrode

Inserting the guide tube and electrode into the brain is a critical phase in the procedure due to the risk of unintended injury to structures and vessels in the brain. Also, as an external force is being applied, electrode insertion may induce further brain shift, not necessarily in the direction of gravity. Testing on Agarose 0.6% brain phantom gel resulted in a peak insertion force of approximately 250 mN for a standard guide tube, although this dropped significantly after initial perforation (79). The significance and impact of electrode insertion force warrants further investigation. As peak force is achieved at the cortical surface, impact on the deep brain target is unclear. With constant application of force, electrode induced displacement is unlikely to recover properly. However, with an oscillatory insertion force this could potentially be avoided. It is also likely that tissue coaxial to the advancing electrode will be displaced away, but along the same path. By this reasoning, if the displacement from the intended region will be along the axis of the

electrode, clinical impact will be mitigated due to a choice of four active regions along the long axis of each device (80).

A typical guide tube causes disruption and haemorrhage to the surrounding tissue, potentially impacting proper neurological function (79). Peterson et al. (57) discuss how a sharper electrode with a lower coefficient of friction will impart less force onto the brain tissue and therefore reduce brain shift. However, avoiding movement of all brain structures is not always desired.

For instance, the displacement of tissue due to a blunt device displacing a vessel is favourable to piercing that vessel with a sharp instrument. Rather than reducing friction, some are investigating micro-textured surfaces to try and reduce post-operative brain shift (81). The risks associated with this, such as tissue damage, if removal is required, are still unknown.

Intraventricular approach

Although without the same risks to patient safety as blood vessel perforation, an intraventricular approach may still have implications on stereotactic accuracy. Zrinzo et al. (82) found a 36% reduction in mean targeting error in procedures that avoided the ventricle as opposed to those that did not. Ventricular penetration was also associated with increased MER tracks. It was suggested that this was likely to be ventricular penetration and target movement leading to multiple MER tracks, rather than multiple MER tracks leading to a higher chance of ventricular penetration. Although the exact mechanism of ventricle associated targeting error is not known, it is likely that the ventricles present a mechanical obstacle, inhomogeneous to the rest of the brain (46). Not only might this allow the application of more force and subsequent displacement of underlying structures, but also distortion of the electrode once inserted.

A study by Kramer et al. (27) found that intraventricular trajectories did not appear to be detrimental to safety or targeting accuracy; a position supported by others (5, 41). In fact, greater posterior subcortical shift was seen in the group with strict intraventricular routing. One explanation is that the frictional force of the guide tube on the surrounding tissue is reduced when travelling through the CSF filled ventricle compared to parenchyma. This hypothesis adds weight to the need for further understanding on the transition of forces on different structures within the brain.

Given the lack of consensus on the matter, the choice of whether to plan an intraventricular trajectory largely comes down to other factors. For instance, an intraventricular trajectory is preferable if avoiding the vessel-rich sulci is otherwise not possible. There are also a number of targets which, given their location within the brain, may require passing through a ventricle. That said, with the majority of institutions avoiding the ventricles if possible, it was decided that this convention would be followed here.

Multiple trajectories and micro electrode recording

Halpern et al. (41) found a trend between posterior cortical displacement over 2 mm and more than one electrode placement, although this was not statistically significant. It seems likely that increased cortical displacement would lead to the need for a second electrode placement, rather than vice versa. Khan et al. (38) found no link between number of MER tracks and brain shift or final accuracy. However, these results are likely to have been affected by a limited sample size, and relatively high levels/range of brain shift respectively. More parallel electrodes require a greater hole in the dura, increasing the apparent risk of CSF leakage. On the contrary, they may also offer improved mechanical support of the brain (68), although the effectiveness of this mechanical support will be limited by the rapid onset of brain shift regardless.

Unlike others (68), Azmi et al. found a slight correlation between the number of MER tracks on the second side of a bilateral procedure and ICA volume (69). This result was supported by the second side also needing more MER tracks to locate the target acceptably. Again, the causality in this relationship is hard to establish.

Rather than using MER, some groups check electrode positioning with intra-operative MRI and reposition if necessary. Ivan et al. (58) found this was required in about 10% of cases, with these leading to significantly more brain shift on both sides of the brain. Interestingly, multiple electrode passes also removed the difference in brain shift normally found between unilateral and bilateral procedures. Given the significance of these findings compared to the weak correlations of others, it seems likely that the number of electrode penetrations is less important than the number of times an electrode is inserted and withdrawn with no support remaining in the interim.

MER utilises parallel tracks which limit the possibility of interaction. If multiple stimulator leads are used ipsilaterally there is a risk of mechanical contact between the two, and displacement of the original lead. Although this may not impact brain shift directly, it should be kept in mind as a possible complication (83). The important thing to remember is that MER is a method used to account for brain shift which has taken place. The process of using MER may then make brain shift worse. If a system is developed such that MER is not required, a very circular dependence can be broken. Until then, multi-track MER will still be relied upon by many groups (84). Crucially, it has already been shown that CSF loss can be very successfully controlled even with multiple electrodes (29).

Unilateral/ bilateral placement

The effect of unilateral vs. bilateral placement on brain shift is important, as a significant impact would suggest any method of correction would not be able to assume symmetry. Furthermore, the loading and initial boundary conditions may need to be different on each side of the model, adding real complexity.

Generally, a unilateral procedure leads to air invasion on the side of the procedure. However, bilateral invasion in unilateral procedures is not rare, meaning this cannot be assumed (24, 31). As unilateral air invasion inevitably causes sinking of the brain predominantly on one side, this leads to a midline shift contralateral to the side of surgery as is shown in Figure 14 (24).

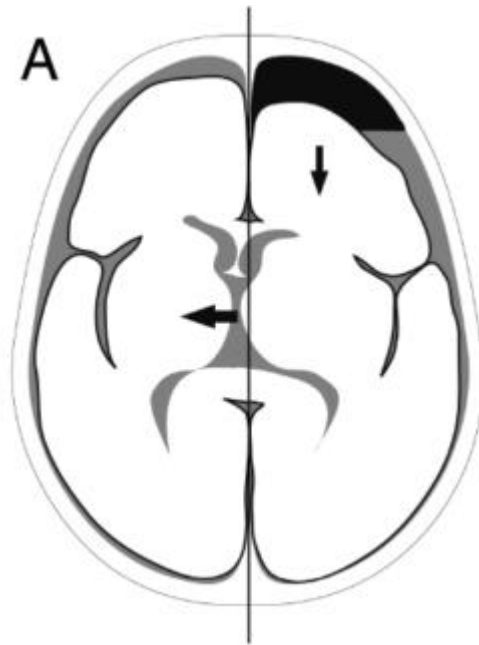


Figure 14 – Schematic illustration of unilateral air invasion and the subsequent midline shift.
Adapted from (24).

In the AC, differences between unilateral and bilateral procedures have been found in the X (lateral) and Y (posterior) axes. When considering positioning error of the surgical device, only the lateral shift remained significant (24). These results are not always supported, for example, Sadeghi et al. (84) found no significant difference in medio-lateral shift between uni/bilateral procedures. Interestingly, the lateral movement in both cases was similar to that found in the unilateral procedures in Miyagi et al. (24). As Sadeghi et al. do not fully explain their system of defining medio-lateral shift in bilateral procedures it is difficult to draw any further conclusions.

Ivan et al. (58) plotted lateral shift against anteroposterior position for structures not necessarily along the midline. These results showed that lateral shift was greatest in the anterior ipsilateral brain, but more importantly was not consistently 'away' from the side of surgery in these procedures. Although not discussed, it appears that brain shift leads to an unpredictable buckling of the brain based on patient specific factors. Whether this could affect certain electrode trajectories requires further investigation.

Azmi et al. (69) found just that more MER passes were required on the second side in bilateral procedures. This is not always the case though, as others find no negative impacts of bilateral procedures either during surgery (57) or when considering long term placement (68). It is interesting to note that it is very common for the average values of comparisons to be worse for

the bilateral procedure on the second side of surgery, but not to the level of statistical significance (68, 85, 86). Whether a large enough sample size could overcome the wide range of variation is unknown.

Although achieving statistical significance is ever difficult, it is logical that without complete elimination of CSF loss in all cases, bilateral procedures will induce greater levels of ICA and associated shift. However, ICA is consistently unreported. As midline shift is clearly associated with unilateral air, it would follow that in unilateral procedures with low levels of air invasion this effect would be minimised. With all results considered, in general it is likely that unilateral procedures are associated with greater lateral shift away from the side of implantation, although this may only be prominent in the deep brain. Bilateral procedures appear to be more stable in the X axis, although they result in greater posterior shift. Considering safety and cost, there appears to be no difference between bilateral or staged unilateral procedures (87) although any certainty regarding accuracy is lacking.

Other factors

Choice of anaesthetic has been shown to have no impact on brain shift (57, 61). Considerations in this regard are normally attributed to managing comorbidities or surgical complications (88). Traditionally patients have been taken off dopaminergic medicines before surgery, although it has recently been shown that this offers no improvement on surgical outcome and the practice is unlikely to be necessary (89).

Lalys et al. (77) found gender to have an effect on post-operative electrode deformation. They hypothesised that this was due to lower cerebral density in female patients compared to males. Other studies have shown no difference in brain density has been found between men and women (90), although gender may influence atrophy, which is likely to be found in patients of an age which typically require DBS treatment (91). As atrophy should be measured and considered rather than predicted, it is therefore unlikely that further consideration of gender is required. This is supported by the lack of any correlation found by other groups (58).

Air-reabsorption and post-operative electrode movement

After surgery, any air trapped within the skull slowly dissolves away and CSF is regenerated. This allows the brain to return to its original position and is known as inverse brain shift. Increasing amounts of work are being done on both quantifying and predicting (92) post-operative electrode curvature and displacement. Displacements as significant as 3.3 ± 2.5 mm along the electrode track have been reported (68). Not only does this displacement significantly correlate with post-operative ICA (68) but also with the method used to secure the electrode wire to the skull (75). Anatomical target structures lie in different parts of the brain and are associated with different conditions. As some of these conditions are linked with greater cerebral atrophy, the choice of

structure is also associated with varying levels of postoperative device curvature (77). As a result, two weeks should pass before confirmation of true electrode placement can be made (77).

It is also important to note the link between post-operative electrode displacement and the levels of brain shift in the first place. As a result, the work presented here will focus on quantifying and predicting initial brain shift, after which adaptations to account for any inverse shift can be made.

Brain shift within the intact cranium

Although patients undergoing DBS electrode placement are often supine/semi-supine, this is not the case for all surgeries. The density of brain tissue and CSF is very similar but not the same and hence a small resultant force acts on the brain regardless of orientation. Even with no perforation of the skull, this leads to non-negligible brain movement when oriented differently with respect to gravity (4, 78, 93). Patients are usually imaged in a flat supine position meaning any deviation from this in theatre leads to the brain resting in a slightly different position. As discussed previously, brain shift is dependent on a large number of surgical and non-surgical factors. Although there will always be some unavoidable variation between patients, investigation of brain shift within the intact skull removes a large proportion of the surgical variation such as CSF loss.

To date, the study of PBS has been limited. A study by Hill et al. (78) is itself limited by image quality and sample size, but suggests a cortical brain shift of less than 1mm. Schnaudigel et al. (4) used magnetic resonance morphometry to assess the displacement and deformation of the brain under gravity in 13 patients. Transferring patients from a supine to prone position led to a posterior-anterior shift in the brain of between 0.6-1.3 mm, concentrated in frontal parts of the brain. Moving from left side to right side caused a greater shift, with deformations of up to 1.8 mm this time in central parts of the brain.

In a similar study concerned with traumatic brain injury, Monea et al. (93) scanned 30 patients in 4 positions using 3T MRI. Their method involved calculating the normal displacement at points on the cortical and ventricular surfaces induced by reorientation of the head. An outward shift is taken as positive, and an inward shift is taken as negative. Many of the results of this deformation are given as mean values across the whole brain. In the case shown in Figure 15, the shape is displaced by a magnitude X, however if the values of all faces are averaged the mean result would be a displacement of zero.

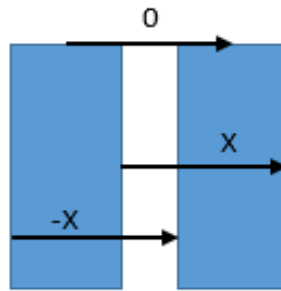


Figure 15 – Schematic representation of displacement representation by Monea et al. (93).

Through this analysis it was shown that sagittal reorientation from supine to prone did not yield rigid body translation but rather a complex deformation, predominantly in the direction of gravity. Displacements were predominately found to be negative, indicating a trend of ‘inward’ movement of the surfaces. This appears to suggest greater displacement in the gravitational direction of the posterior surface than the anterior. However, the methodology used is prone to high local variation due to the gyri and sulci, as the values presented are not vector components but displacement magnitudes normal to the surface. Histograms presented more potentially meaningful information, with clear peaks in the 0.000 to 1.150 mm and -0.1740 to -0.0300 mm bins. In contrast to Schnaudigel et al. (4), the data indicates greater displacement of the cortex than the ventricles. Furthermore, whilst the majority of displacements appears plausible, significant numbers of points are reported to move by a magnitude similar to, or greater than the thickness of the PAC itself. For example, the peak negative and positive displacements with sagittal reorientation are -7.86 and 5.71 mm, with coronal peaks greater still. With inwards displacement away from the skull this is unlikely, but with outwards displacement towards to skull, movement greater than the thickness of the PAC would not be possible. It is rightly mentioned that these results support previously reported levels of brain shift seen in mild impacts but contradict other reports on PBS (4, 78). Most recently, Mikkonen and Laakso (94) also measured surface displacement in a study concerned with the impact of brain shift on transcranial direct current and magnetic stimulation. Their results indicated anterior and inferior surface shift with supine to prone reorientation.

Brain settling

When conducting magnetic resonance morphometry within the enclosed cranium, Schnaudigel et al. (4) left one set of patients in the same position between scans at 12 and 24 minutes. Results indicated that brain shift continued between the 12 and 24 minute scans, contrary to what might have been expected. With no further information on this found in the literature, it seems an experiment to establish the average time for brain settling would be extremely useful. This is especially the case as DBS procedures rely on the patient being in position for considerably longer than they are during pre-operative imaging.

Conclusions

Brain shift is an unavoidable part of neurosurgery, with movements of over 5 mm possible in the midbrain. There is an established relationship between brain shift and pneumocephalus, while useful to keep in mind, is not strong enough to predict brain shift alone. To consider how best to move forward, each variable discussed in the literature was assessed in terms of its understood impact on brain shift and whether it can actually be controlled. Table 2-4 summarises this information, into what are thought by the author to be controllable and influential factors in the levels of brain shift experienced.

Table 2-4 – Summary table of the influential and controllable factors relevant to stereotactic neurosurgical brain shift.

	Controllable	Not controllable
Influential	<ul style="list-style-type: none"> • Patient position • Use of PEG hydrogel/Tisseel (Fibrin glue)/bone wax • Meningeal incision • Intraventricular route 	<ul style="list-style-type: none"> • Deformation due to the advancing electrode • Atrophy – general brain geometry • Target position
Not influential	<ul style="list-style-type: none"> • Burr hole size • Duration of surgery 	<ul style="list-style-type: none"> • Patient age • Gender

Controllable - Influential

A supine patient position and occlusion of the burr hole have proven to be the best methods of reducing CSF loss and subsequent intracranial air intake. Although not compared directly, electrocautery of the meninges such that local ‘welding’ takes place, and minimising the arachnoid opening also seem promising. The risks associated with a poor visual field of the cortical surface can be minimised by good preoperative imaging. Although there is some debate over the impact of an intraventricular trajectory, it is commonly avoided and there is not enough evidence to say that this should change.

Controllable - Not influential

The size of the cranial burr hole is normally considerably larger than the underlying incision and is not influential at the diameters normally seen in stereotactic procedures. If the burr hole was considerably larger, or in a position that allowed the brain to protrude from its normal anatomical position this may no longer be the case. A considerably smaller cranial window may itself prevent CSF outflow. Even in cases where large ICA volumes were measured, the duration of surgery is unlikely to impact brain shift. It is largely accepted that this is due to most CSF loss occurring in the early stages of surgery. In addition to this, time-dependant brain settling is likely to stabilise long before post-operative scanning, although once again data to prove this is not currently available.

Uncontrollable - Influential

The advancing electrode imparts a force onto the brain which inevitably results in movement. The extent of this is likely to be influenced by geometry, friction and rate of insertion. An implanted electrode also has a tethering effect on the brain, which is likely to increase with multiple MER electrodes in place. The impact of both aspects requires further investigation.

Atrophy of the brain is an unavoidable part of aging and varies greatly from patient to patient. Relationships between brain shift and cerebral atrophy have been identified, although this is largely dependent on the system of measurement used.

Finally, the anatomical target is determined largely by the patient's condition; however, there is still debate regarding which offers the best clinical results.

Uncontrollable – Not influential

Patient age and gender are likely to affect brain shift as a result of cerebral atrophy. As this is already accounted for, there is no direct influence that needs further consideration.

Limitations of this interpretation

The surgeon must sometimes make choices which have a significant impact on brain shift. Although time consuming and more invasive, techniques such as MER allow for the effects of brain shift to be minimised. It is also critical to avoid penetrating vessels and some other structures, meaning the choice of a cranial window location may be limited. On a practical level it will not be possible to rely entirely on the previously discussed methods of limiting brain shift, as they will not be feasible for all patients.

This review is also limited by the variation that is seen across all sample groups. This often means that the impact of any one variable is lost within uncontrollable variation between test and control groups. Many groups have suggested correlations which failed to reach statistical significance due to sample size with high levels of baseline variability. Although this means there are likely to be false negatives, it is reassuring that the factors identified to be important are unlikely to be false positives. In the case of pneumocephalus, median and mean averages are often different due to a small number of significant outliers which could frequently not be explained, again complicating analysis.

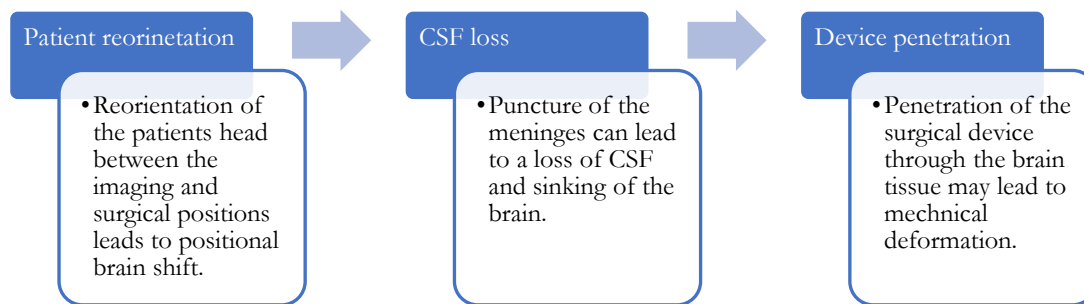
Brain shift affects not only the initial stereotactic placement of electrodes, but also induces deviation from the initial position in the days following surgery. This 'inverse shift' is a problem currently subject to much study. At this time, this is acknowledged but not studied further as the main aim is in measuring and understanding brain shift in the first place.

It is also worth considering that many of the values of brain shift reported fall within the resolution of the imaging systems commonly being used. CT slice thicknesses of 2.5 mm (95) approach the dimensions of the STN itself (36). There is also debate over what constitutes

‘clinically significant’ brain shift, with some saying movement in the relevant areas under 1 mm (31) or even 2mm could be inconsequential (75) depending on the direction. Regardless, this work assumes that electrode placement of considerably higher accuracy is something that is sought after in the field; a view that is supported by the increasing use of iMRI.

Influence of Findings

The objective of this review was to better understand brain shift and determine potentially predictive factors. If it was identified that such a factor existed and was measurable preoperatively, it may have been possible to incorporate a level of patient specific adjustment into the model. Sufficient debate remains in the literature to conclude that preoperative prediction is simply not possible on a patient specific basis. However, on balance of all the reports considered, it is proposed that surgical brain shift should not be considered a continuous process but one of three distinct stages.



The stage given most significance in the literature is brain shift due to CSF loss. However, prediction of CSF loss is simply not possible at the current time. That said, it is possible to effectively eliminate CSF loss, which is already widely advocated amongst the community. With these factors in mind, it was decided that modelling of CSF loss would be excluded from the scope of the computational study. The impact of device penetration has received relatively little study. Whilst potentially important, it was felt that a modelling approach to understanding brain shift should progress in a chronological order to include the potential impact of process interactions. As such device penetration was also not considered.

The specifics are discussed in greater detail later; however, computational modelling of biological structures is complicated by the complex material properties of the tissues involved. In-vivo material testing is, in general, very uncommon in the field due to practical constraints. Modelling results can be highly dependent on the material properties used and the material properties obtained are also dependant on the test scenario. The circular nature of the problem dictates that material properties should be obtained with boundary conditions similar to those found in the computation model in which they are utilised. PBS is unique in that it can be induced and measured in an ethically conducive manner, simply with reorientation of the head.

This considered, it was concluded that developing a model for PBS alone had two distinct benefits:

1. PBS alone is still a significant component of brain shift seen in stereotactic neurosurgery.
2. Improved understanding of the material response of the intracranial tissues under this type of loading could facilitate more complex future modelling related to neurosurgery and the wider field in general.

As such, the focus of this study moved from brain shift induced throughout the entirety of a stereotactic procedure to the modelling, material parameter identification and prediction of positional brain shift.

Recap: Objectives

1. Understand the key factors involved in brain shift, and which should be considered in the FE model.
 - i. Neurosurgical brain shift is currently so unpredictable that a simplified approach is required.
 - ii. Due to the unique combination of clinical relevance and ability to induce it for academic study alone, PBS has been chosen as the focus of further work.
 - iii. Once developed, a computational model of PBS can offer insight into the material sensitivity of brain shift and can also be adapted to study geometric differences and more complicated surgical cases.
2. Develop a FE model incorporating key anatomical structures (which can also be used for the phantom model).
3. Investigate the material sensitivity of brain shift and the mechanics of the process using human data and the FE model.
4. Predict a test-case of displacements in a clinically relevant region that could be used as a pre-operative adjustment.

Chapter 3: Computational Modelling of Brain Shift

In the previous chapter it was identified that brain shift in stereotactic neurosurgery is a complex process, with many potentially influential factors. However, the number of variables is sufficiently large that determining the contribution to brain shift of any one is not possible. As such, it was decided that this study would focus on positional brain shift, which results from reorientation of the head alone.

To develop a successful computational model of this phenomenon, an understanding of the theoretical basis of modelling and previous implementations was required. To address this, the following chapter consists of four main areas:

- The theoretical basis of continuum mechanics.
- Constitutive modelling of the soft tissues of the head.
- Previous applications and methods in head modelling.
- The theoretical basis of material sensitivity analysis.

Many groups in the past have proposed new constitutive models of the brain (10) capturing the material response of increasingly complex loading regimes. Others have focussed on finite element (FE) algorithms themselves, to make more computational efficient processes (96). Whilst implementation of these methods is critical, the work presented here was not intended to advance these aspects directly, but instead to utilise what is accepted to be the state-of-the-art in this regard.

With the intention instead to develop a FE model of PBS, this section was intended to examine previous attempts at this. To the best of the author's knowledge, no such studies exist in the literature. Within any FE analysis, the stress/strain response of the body in question is a function of the geometry, material properties and boundary conditions. In the case of PBS, the boundary conditions are relatively simple, as structures of the intracranial cavity are only subjected to load arising from gravity. As such, accurate results in this case are dependent on the material properties of the intracranial structures and their geometric representations. Given this novel application, the material parameters and geometric representations used in adjacent fields were considered. In this section, these aspects are examined more closely.

It will be shown that the literature provides many estimates for some material parameters, but for others, such as the bulk modulus of the brain, there is little consensus. The same can be said for the meninges, where this stiffness of the PAC is often cited to one ex-vivo mechanical test (97). Geometrically, the brain-skull interface is equally important; however, there is still debate about how best to represent it. State-of-the-art implementations involve spring representations

of the arachnoid trabeculae and bridging veins. Although the impact of the material and geometric representations is highly sensitive to the specific application, these topics constitute a significant deficit in the body of knowledge.

Continuum Mechanics

This work employs the theory of continuum mechanics; the study of the mechanical behaviour of materials where it is considered that no spaces exists throughout the material body. Taking a continuum approach involves studying the material at a macroscopic level, using constitutive models to capture the general behaviour. Continuum mechanics has long been used in the study and characterisation of a wide range of materials; notably rubber and metals. The specialised study of soft tissues involves the implementation of traditional theory with a number of key adaptations and assumptions to capture complex material behaviour. A detailed account of the theoretical basis of continuum mechanics can be found in the book of Holzapfel (98). The following section offers a summary of the principles and quantities discussed in (98) and (99) providing relevant context to the present work.

Material deformation

Consider a body in 3D Euclidian space. The *initial* or *reference configuration* Ω_0 undergoes deformation to a *deformed* or *current configuration*, Ω , over a given time, t . The location of any point within the reference configuration is described by the material coordinates, \mathbf{X} . Likewise, the spatial coordinates of the current configuration are defined by \mathbf{x} . The deformation of the reference configuration to deformed configuration is described by the deformation map, χ . In the interests of relevance for the analysis to come, this explanation will focus mainly on the material (Lagrangian) reference frame.

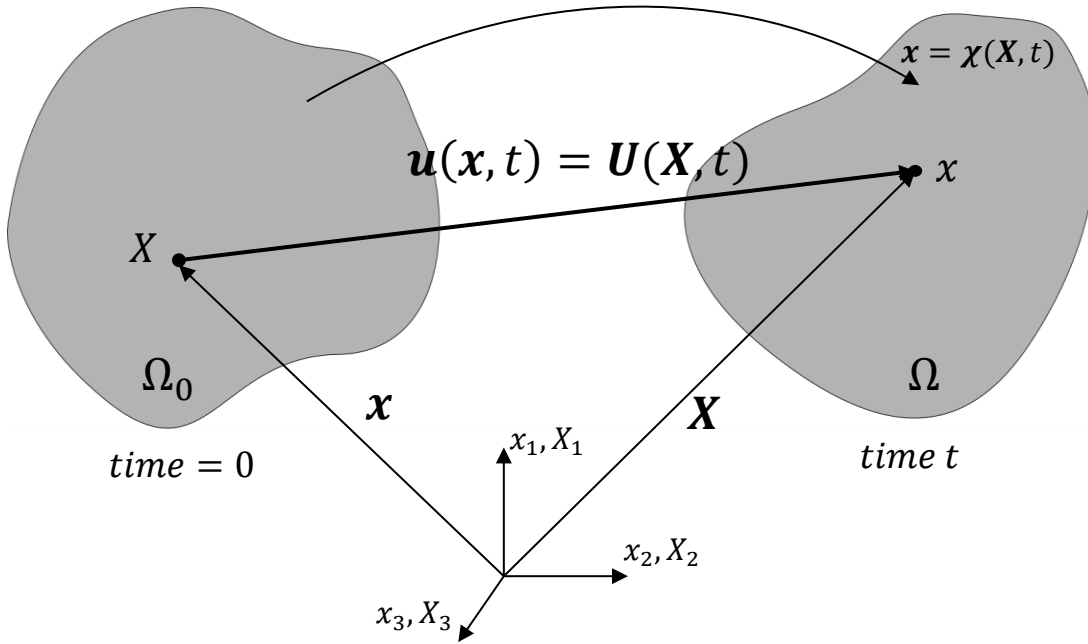


Figure 16 – Schematic representation of the deformation field.

The displacement field \mathbf{u} describes the relation of the spatial and material coordinates with respect to time, such that:

$$\mathbf{u}(\mathbf{x}, t) = \mathbf{x}(\mathbf{X}, t) - \mathbf{X} \quad 1$$

For further analysis, we must not only consider the displacement of a single point, but also those immediately around it. To do this, we take the derivative of each component of the deformed vector with respect to the initial reference vector. This quantity contains nine components and is known as the deformation gradient tensor, \mathbf{F} . This is most easily visualised in tensor notation where:

$$F_{ij} = \begin{bmatrix} \frac{\partial x_1}{\partial X_1} & \frac{\partial x_1}{\partial X_2} & \frac{\partial x_1}{\partial X_3} \\ \frac{\partial x_2}{\partial X_1} & \frac{\partial x_2}{\partial X_2} & \frac{\partial x_2}{\partial X_3} \\ \frac{\partial x_3}{\partial X_1} & \frac{\partial x_3}{\partial X_2} & \frac{\partial x_3}{\partial X_3} \end{bmatrix} \quad 2$$

At a given time step, Equation 1 can be simplified such that:

$$\mathbf{x} = \mathbf{X} + \mathbf{u} \quad 3$$

and as such:

$$\mathbf{F} = \frac{d\mathbf{x}}{d\mathbf{X}} = \frac{d(\mathbf{X} + \mathbf{u})}{d\mathbf{X}} = \frac{d\mathbf{X}}{d\mathbf{X}} + \frac{d\mathbf{u}}{d\mathbf{X}} = \mathbf{I} + \frac{d\mathbf{u}}{d\mathbf{X}} \quad 4$$

where \mathbf{I} is the identity matrix. In cases where there is rigid body displacement, all particles move by an identical distance and direction over time, therefore being independent of \mathbf{X} , such that $\mathbf{F} = \mathbf{I}$. From the deformation gradient tensor we can define a number of useful quantities, which describe the process of deformation. To do this we must first decompose \mathbf{F} into components of pure stretch and pure rotation. Within the reference configuration this is termed the right polar decomposition and is defined such that:

$$\mathbf{F} = \mathbf{R}\mathbf{U} \quad 5$$

where \mathbf{R} is the rotational tensor and \mathbf{U} is the right stretch tensor. The right stretch tensor measures local stretching or contraction along orthogonal eigenvectors in the material configuration. The rotational tensor captures the change in local orientation. As such, in rigid body rotation $\mathbf{F} = \mathbf{R}$ and conversely in pure stretch $\mathbf{F} = \mathbf{U}$.

The right Cauchy-Green tensor \mathbf{C} is now introduced and defined such that:

$$\mathbf{C} = \mathbf{F}^T \mathbf{F} \quad 6$$

where \mathbf{C} is a positive, symmetric tensor. In the derivation of Equation 6 through manipulation of Equation 5, it can be shown that $\mathbf{R}^T \mathbf{R} = \mathbf{I}$. As such, rotational components are removed from right Cauchy-Green tensor, which becomes important in the calculation of strain within the material coordinates moving forward.

Volume change as a result of deformation equates to the product of the orthogonal components of the deformation gradient tensor, otherwise defined as $J = \det \mathbf{F}$. When considering compressible materials, both volumetric and deviatoric components of the deformation gradient must be considered. The deviatoric deformation gradient $\tilde{\mathbf{F}}$ represents pure shape change in the body. By definition, it must satisfy Equation 7:

$$\det \tilde{\mathbf{F}} = 1 \quad 7$$

In order to satisfy this, $\tilde{\mathbf{F}}$ is calculated using Equation 8:

$$\tilde{\mathbf{F}} = J^{-\frac{1}{3}} \mathbf{F} \quad 8$$

The deviatoric right Cauchy-Green tensor, $\tilde{\mathbf{C}}$ is defined similarly to Equation 6:

$$\tilde{\mathbf{C}} = J^{-\frac{2}{3}} \mathbf{C} \quad 9$$

The symmetric, second order, Green-Lagrange strain tensor is defined as:

$$\mathbf{E} = \frac{1}{2}(\mathbf{C} - \mathbf{I}) \quad 10$$

Such a definition evaluates strain, removing components of rotation and rigid body displacement. It is noted that similar quantities can be defined in the spatial form. Material and spatial measures remain approximately equivalent at small strains.

The internal forces within the body are expressed through the quantity of stress. The Cauchy traction vector \mathbf{t} is defined as the force per unit area acting along the normal \mathbf{n} , for every infinitesimal surface within the body. The similar first Piola-Kirchoff traction vector \mathbf{T} is defined in the reference configuration (with \mathbf{N} , the corresponding normal vector). Cauchy's stress theorem proposes the existence of unique second-order tensor fields $\boldsymbol{\sigma}$ and \mathbf{P} , such that:

$$\mathbf{t} = \boldsymbol{\sigma} \cdot \mathbf{n} \quad 11$$

$$\mathbf{T} = \mathbf{P} \cdot \mathbf{N} \quad 12$$

Where $\boldsymbol{\sigma}$ and \mathbf{P} are the Cauchy stress and first Piola-Kirchoff stress tensors respectively. These tensors are further defined as:

$$\boldsymbol{\sigma} = J^{-1} \mathbf{P} \mathbf{T}^T \quad 13$$

$$\mathbf{P} = J \boldsymbol{\sigma} \mathbf{F}^{-T} \quad 14$$

The Cauchy stress can be decomposed into deviatoric and hydrostatic components. The hydrostatic stress is defined as:

$$\boldsymbol{\sigma}_{hyd} = -\frac{1}{3} tr(\boldsymbol{\sigma}) \mathbf{I} \quad 15$$

and is equal and opposite to the pressure, p . As such, the deviatoric stress of the Cauchy stress tensor $\tilde{\boldsymbol{\sigma}}$ is defined:

$$\tilde{\boldsymbol{\sigma}} = \boldsymbol{\sigma} - \boldsymbol{\sigma}_{hyd} = \boldsymbol{\sigma} - p \mathbf{I} \quad 16$$

As such, it holds that $tr \tilde{\boldsymbol{\sigma}} = 0$.

Hyperelasticity

Hyperelastic (Green elastic) materials have a Helmholtz free energy function ψ defined per unit volume. The Helmholtz free energy is a thermodynamic measure of the energy within a closed system such that:

$$\psi = U - TS \quad 17$$

Where U is the internal energy, T is the temperature of the surrounding environment and S is the entropy within the system. The internal energy is taken as the total energy within system at

constant temperature and volume. The Helmholtz energy therefore describes the energy required to create the system when the product of temperature and surrounding entropy is also taken into account.

In general, rubber-like solids and soft tissues dissipate energy through loading and un-loading, such that the stress-strain curve does not follow the same path. Figure 17 demonstrates this phenomenon, known as the Mullins effect (100).

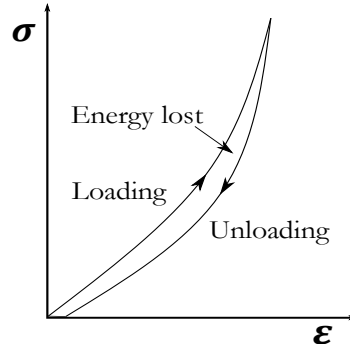


Figure 17 – Example of a stress/strain plot depicting a region of energy loss as described by the Mullins effect.

It can be defined that the Helmholtz free energy is a function of a given strain tensor, such as \mathbf{F} alone. When $\psi = \psi(\mathbf{F})$, it is termed the strain energy density function. In such cases where work done by stresses in the material are path independent, the material is termed hyperelastic. Whilst hyperelasticity is theoretically impossible, it is a necessary assumption for much real-world material characterisation. The assumption of hyperelasticity and fitting of a strain energy function to experimental data is the basic premise of constitutive modelling of soft tissues.

Material isotropy exists when constitutive behaviour is independent of the material axis. Truly isotropic biological materials rarely exist. However, this assumption is often necessary, or at least convenient. In such cases ψ is simply a function of the invariants of \mathbf{C} :

$$\psi(\mathbf{C}(\mathbf{X}), \mathbf{X}) = \psi(I_1, I_2, I_3, \mathbf{X}) \quad 18$$

where the invariants themselves are:

$$I_1 = \text{tr } \mathbf{C} \quad 19$$

$$I_2 = \frac{1}{2} [(\text{tr } \mathbf{C})^2 - \text{tr } \mathbf{C}^2] \quad 20$$

$$I_3 = \det \mathbf{C} = J^2 \quad 21$$

When it is given that $\psi_1 = \frac{\partial \psi}{\partial I_1}$, $\psi_2 = \frac{\partial \psi}{\partial I_2}$ and $\psi_3 = \frac{\partial \psi}{\partial I_3}$, the second Piola-Kirchoff stress, \mathbf{S} , can be evaluated as:

$$\mathbf{S} = 2\{(\psi_1 + I_1\psi_2 + I_2\psi_3)\mathbf{I} - (\psi_2 + I_1\psi_3)\mathbf{C}\} + \psi_3\mathbf{C}^2 \quad 22$$

and the Cauchy stress can now be derived in terms of the defined strain energy function and the deformation dependant invariants of \mathbf{C} :

$$\boldsymbol{\sigma} = \frac{2}{J} \{(\psi_1 + I_1\psi_2 + I_2\psi_3)\mathbf{C} - (\psi_2 + I_1\psi_3)\mathbf{C}^2\} + \frac{1}{J}\psi_3\mathbf{C}^3 \quad 23$$

In practical terms, we can consider that many soft tissues are comprised of water-based fluid held within a solid scaffold. At the stresses seen in soft tissue modelling, it is generally accepted that the fluid phase can be considered incompressible. This incompressibility, or near-incompressibility is often inferred onto the entire tissue. In true incompressibility $J = 1$ and there would be no energy change resulting from volume change. Instead, near-incompressibility is often assumed and the hyperelastic constitutive equation can be rewritten with the distortional and volumetric energy components:

$$\psi(\mathbf{C}) = \tilde{\psi}(\mathbf{C}) + U(J) \quad 24$$

Here $\tilde{\psi}$, the deviatoric strain energy density function, is derived from the deviatoric right Cauchy-Green tensor $\tilde{\psi} = \psi(\tilde{\mathbf{C}})$. Different formulations of the volumetric energy component $U(J)$ are defined by different authors and hence used in different finite element implementations. One such example (101) defines:

$$U(J) = \frac{1}{2}k(\ln J)^2 \quad 25$$

where k is a material parameter of compressibility; the bulk modulus. With the pressure, p given as:

$$p = \frac{dU}{dJ} \quad 26$$

The second Piola-Kirchoff stress can be reformed as Equation 27:

$$\mathbf{S} = \frac{\partial \tilde{\psi}}{\partial \mathbf{C}} + pJ\mathbf{C}^{-1} \quad 27$$

incorporating the discussed distortional and volumetric components.

Constitutive Modelling

Constitutive modelling is the mathematical description of a materials stress strain response, using a parameterised representation of the strain energy function given in Equation 18. Incorporation of constitutive models in FE software allows for the analysis of non-linear materials in complex geometries and loading regimes. The constitutive models used for soft tissues today, were first developed for the study of soft rubbers, as both derived non-linear elasticity from long chain molecules with notable works coming from Treloar (102-104). Since then, the development of new models capable of capturing the behaviour of a wide range of soft tissues has been the focus of much work.

The neo-Hookean model proposed by Treloar (103) is one of the simplest and most commonly used examples. Not considering the volumetric component, the neo-Hookean strain energy function is given as:

$$\psi = C_{10}(I_1 - 3) \quad 28$$

Where I_1 is as defined in Equation 19 and C_{10} is a material constant to be determined experimentally. Generally, more highly parameterised equations allow for better fit to experimental data. As such, the neo-Hookean model often struggles to describe complex material behaviour at large strains. This section will introduce the experimental characterisation of relevant soft tissues and the popular constitutive models used to describe their behaviour in the context of brain shift.

Brain

The complexity of the brain makes it one of the most interesting and challenging organs to mechanically characterise. Many decades of study have led to the current description of brain mechanics, consisting of solid, fluid, electrochemical and electromechanical components (25). Each of these components may certainly play a role in any mechanical analysis; however, it is accepted that with the complexity of current constitutive models, material properties found in one loading condition may not necessarily replicate the material response in another (25). As such, one must carefully consider the suitability of a constitutive model to the specific application (10).

At high strain rates, relative brain/skull movement can be analogised as a mass tethered by springs to a rigid container (105). Biological tissues can exhibit equivalency between short-time biphasic and incompressible material responses (106). As a result, highly-incompressible or volume preserving material formulations for the brain are often used (107-109). However, the viscous nature of brain tissue exhibits pronounced strain rate dependency (110-112) which must still be accounted for. On the contrary, slower rate scenarios often consider Biot's theory of consolidation in their representation of brain tissue; analogised as a fluid-soaked sponge, where loading drains fluid from the underlying material matrix over time (113, 114). A poroelastic material model is often used to capture the time dependency of this process. Each case adds complexity to the mathematical representation and requires identification of additional material properties (114).

The point at which the predominant mechanism changes from viscoelasticity to poroelasticity is by no means fixed and is highly dependent on many factors. Figure 18 gives a broad indication of typical strain rates seen in various brain interactions.

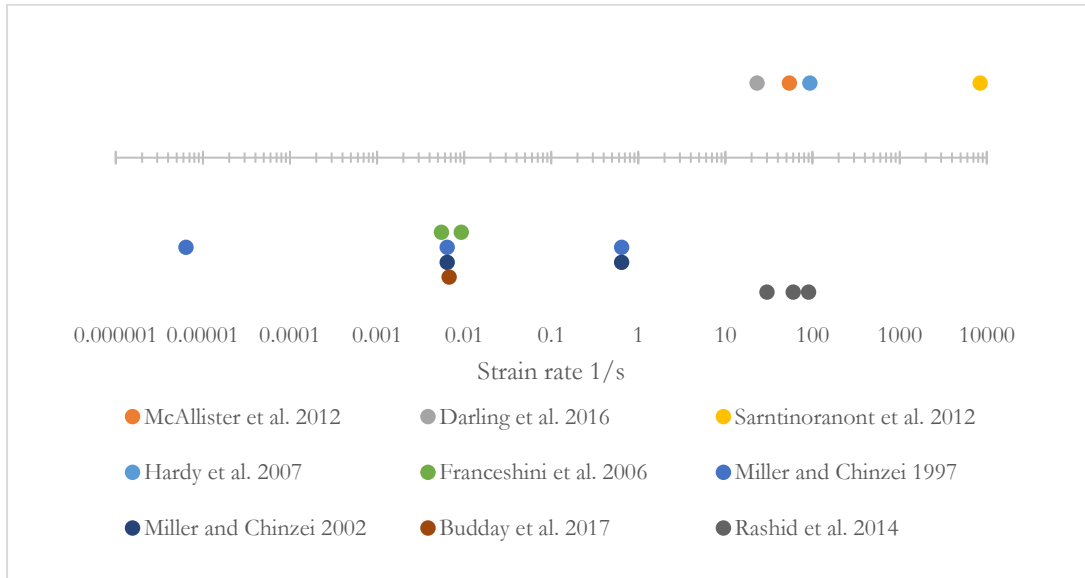


Figure 18 – Above axis – strain rates reported in a range of real-world impact/blast scenarios. Below axis – strain rates used in the mechanical characterisation of brain tissue in some of the most commonly cited studies.

As a general rule, low and high strain rates in the order of magnitude shown are best represented by porohyperelastic and viscohyperelastic formulations respectively (110, 115). Neurosurgical applications fall into an interesting middle ground where both methods are often used (108, 113) and there is evidence to suggest some scenarios are insensitive to constitutive model choice altogether (9).

Constitutive models

A number of constitutive models have been developed over the years each with a unique area of application. A comprehensive review by de Rooij and Kuhl (10) offers more detail for the interested reader. In studying the literature, it becomes apparent that the majority of groups use the Ogden (116) hyperelastic model, adding or altering to it to capture particular behaviour (11, 110, 112, 115, 117-121). With such clear adoption within the community and direct evidence to support the use of the Ogden model over others, such as neo-Hookean, Mooney-Rivlin, Fung and Gent (118), it seems an appropriate choice for this work.

In the generalised Ogden model (116) given in Equation 29, α_i represents the “strain-magnitude sensitive nonlinear characteristics of the tissue” (119).

$$\psi = \sum_{i=1}^N \frac{\mu_i}{\alpha_i} (\lambda_1^{\alpha_i} + \lambda_2^{\alpha_i} + \lambda_3^{\alpha_i} - 3) \quad 29$$

In a typical one-term reformulation (112, 119) where $N = 1$ and $\alpha = \alpha_1$, the classical shear modulus μ is defined:

$$\mu = \frac{\mu_1 \alpha}{2} \quad 30$$

and Equation 29 is modified to take a new form:

$$\psi = \frac{2\mu}{\alpha^2} (\lambda_1^\alpha + \lambda_2^\alpha + \lambda_3^\alpha - 3) \quad 31$$

More complex versions of up to eight terms have been implemented (11, 118), but this one term model is simple to implement and has been shown to yield acceptable results (119), particularly with small strains (116).

Viscoelasticity

If the relaxation response induced by viscoelastic effects are to be considered, one typical approach is to scale the time dependant shear modulus $\mu(t)$ using a Prony series:

$$\mu = \mu_0 \left[1 - \sum_{k=1}^N g_k (1 - e^{-\frac{t}{\tau_k}}) \right] \quad 32$$

where μ_0 is the initial shear modulus, and τ_k and g_k are the experimentally determinable relaxation time and coefficient respectively (110). Inclusion of Equation 32 in Equation 31 leads to the new form:

$$\psi = \frac{2}{\alpha^2} \int_0^t \left[\mu(t - \tau) \frac{d}{d\tau} (\lambda_1^\alpha + \lambda_2^\alpha + \lambda_3^\alpha - 3) \right] d\tau \quad 33$$

The time-dependency of the tissue can be assessed using a stress relaxation test; a technique that has been employed for many years (117). In such tests, significant stress relaxation is seen even with moderate strains. Budday et al. (119) reported stress relaxation of up to 80% within 5 minutes. More importantly, the exponential decay, as can be seen in Figure 19 and captured within Equation 33, suggests whether these effects should be considered within the modelling scenario of interest. Note that Equation 33 converges with the time-independent response of Equation 31 as t tends to infinity.

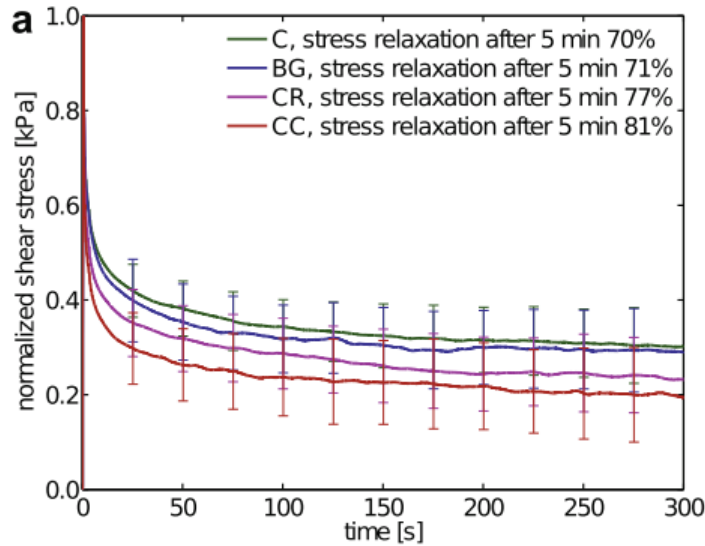


Figure 19 – Average stress relaxation behaviour obtained from cortex (C), basal ganglia (BG), corona radiata (CR) and corpus callosum (CC) samples of human brain tissue with shear strain of 0.2. Reproduced from (119).

On this basis it can be assumed that the viscous response occurs over a sufficiently short timescale to be insignificant in the case of PBS (122). Whilst the viscoelastic formulation is popular, it is not implemented in this work.

Porosity and consolidation

In other areas of engineering, particularly soil mechanics, the mechanical response to load is derived from the squeezing of fluid from an elastic porous medium. This general theory of three-dimensional consolidation is described by Biot (123) with notable contribution from Terzaghi (25, 124) who offered a simplified one term consolidation coefficient. This coefficient C_v is defined such that $C_v = \frac{kM}{\gamma_w}$, where, in this case k is the permeability (not to be confused with bulk modulus), M is the oedometric coefficient and γ_w is the specific weight of the fluid phase (115).

The link to brain tissue was first made by Hakim (125) in the study of hydrocephalus; work most notably built upon by Franceschini et al. (115). Figure 20 is an example of oedometric testing data obtained by Franceschini et al. on human brain tissue.

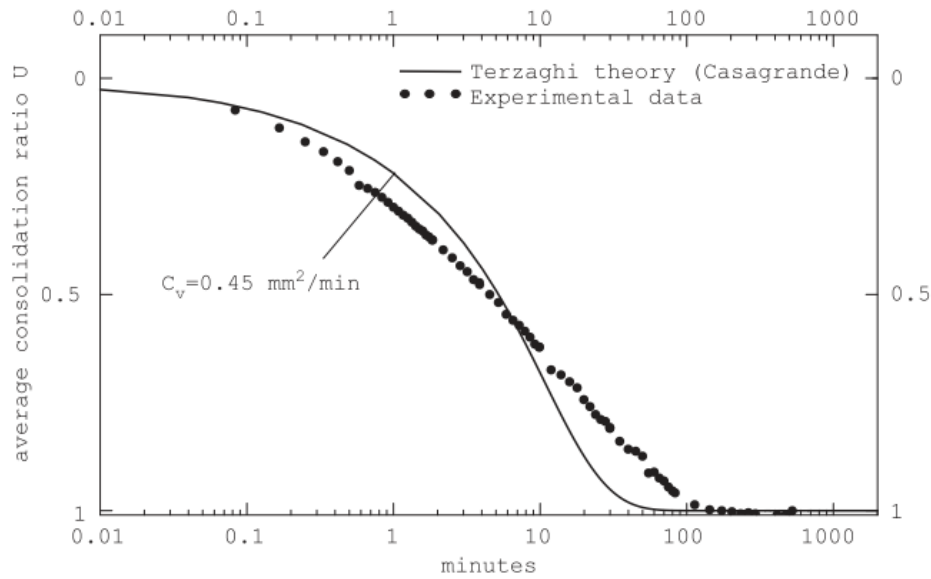


Figure 20 – Comparison of experimental data to optimised theoretical prediction, obtained through oedometric testing of cylindrical brain samples. Reproduced from (115).

In this experiment, cylindrical tissue samples were subjected to uniaxial loading with free-flowing top and bottom surfaces. In this case, the sample reached equilibrium in approximately 100 minutes, however this value is highly sensitive to sample thickness. This study is arguably most notable for providing the first direct evidence that brain tissue obeys consolidation theory; however, they report a number of key findings equally pertinent to the current study, namely:

- The solid (drained) phase of brain tissue exhibits low compressibility with an equivalent Poisson’s ratio of approximately 0.496.
- Full consolidation was achieved with axial strains in the order of 3%.
- The solid phase of brain tissue is likely to exhibit viscous properties, but consolidation is primary mechanism of delayed volumetric deformation.
- Consolidation is the dominant mechanical process when high mean stresses are applied over time but offers a “correction” to single phase theory when considering large deviatoric deformations.

The ultimate implication is that some volumetric compression of brain tissue is possible through the redistribution of fluid. Consolidation theory has been applied to neurosurgical finite element models in the past with positive effects (126), suggesting that the effects are relevant in a neurosurgical time scale. However, capturing the time dependant response requires consideration of hydraulic conductivity and associated adaptations to the constitutive relations.

In general, studies aimed at material characterisation and constitutive modelling assume brain tissue to be incompressible and define this mathematically (118, 119). In FE analysis, incompressibility is not enforced mathematically and the volumetric material response is

described using the bulk modulus or Poisson's ratio (ν). The bulk modulus is defined as the rate of volume metric change under a given pressure change, Δp , such that:

$$k = -V \frac{\Delta p}{\Delta V} \quad 34$$

where V is the volume of material being considered (127). With linear elasticity or small strains, the bulk modulus and Poisson's ratio can be related according to Equation 35:

$$k = \frac{2\mu(1 + \nu)}{3(1 - 2\nu)} \quad 35$$

where μ is the shear modulus (128). These relations offer rough approximation for non-linear responses at small strains.

When considering PBS, the transient state between load and equilibrium is unimportant as the process has now been shown to occur over a short time scale (122). As such, apparent compressibility associated with fluid redistribution can be captured within a single-phase material by defining a suitable bulk modulus. Whilst almost every FE study will report the bulk modulus used, these often vary wildly with little evidence (129). It is likely that this stems from an assumption that the value of bulk modulus used will have a limited impact on results. With this in mind, reporting the commonly used values is somewhat meaningless, though for completeness, an in depth review of the literature in (130) reports values for the Poisson's ratio to be $0.4 \leq \nu \leq 0.495$.

Table 3-1 details the few identified experimental studies which have offered values for the bulk modulus or Poisson's ratio. Each involved direct testing and measurement in-vivo, or used ex-vivo tissue.

Table 3-1 – Values of bulk modulus or Poisson’s ratio in the literature derived from experimentation.

Bulk modulus /kPa	Poisson’s ratio	Comments	Source
37.8 – 46.3	-	<ul style="list-style-type: none"> • Dog • In vivo • Based on pressure change with tilting • Concerns contents of ‘dural sac’ • Value decreased with increasing age 	Flexner et al. 1932 (131)
38.4 ± 7.9	-	<ul style="list-style-type: none"> • Cat • In vivo • Based on induced hydrocephalus • Approx. 30 min timescale 	Sahar et al. 1969 (127)
-	~0.4	<ul style="list-style-type: none"> • Calculated based on the bulk modulus given by Sahar et al. (127) 	Tenti et al. 1999 (132)
-	0.496	<ul style="list-style-type: none"> • ‘Drained’ Poisson’s ratio • Human • Post-mortem • Based on oedometric testing 	Franceschini et al. 2006 (115)

The value reported by Franceschini et al. is notably higher than the others. One possible explanation for this, is that it seems Flexner et al. and Sahar et al. considered an increase in ventricular volume to be equivalent to decrease in brain volume. In reality, redistribution of fluid from the cerebral vasculature or subarachnoid space may have been the cause of this. Regardless, these values offer a good starting point for further investigation.

Reported Ogden parameters

Characterisation of the brain is still far from complete. There is debate in the literature about the effect of age, regional property variation as well local anisotropy (119). Whilst it is certainly safe to assume the brain is not one isotropic, homogenous mass, the impact of this variation is again likely to vary with the specifics of each case. With such disagreement yet unresolved, these aspects were deemed to fall outside of the scope of this project and were left for future investigation. It is important to consider some of the previous reported material parameters. Table 3-2 highlights mechanical characterisation and constitutive modelling using the forms presented in Equations 31 and 33 as a point of comparison.

Table 3-2 – Material parameters obtained for mechanical testing reported in the literature.
*Values reported for simultaneous fit of all loading conditions.

μ / Pa	α	τ_k / s	g_k	Species	Source
842	-4.7	0.5	0.450	Porcine	Miller and Chinzei
		50	0.365		2002 (112)
296	0.0323	2.40	0.335	Human	Prange and
		0.146	0.461		Margulies 2002
					(117)
350 – 1,430	-25.3 – -19.0	–	–	Human	Budday et al. 2017
					(119)*

Other groups using different constitutive models or higher order Ogden models have found similar results. Considering the expected high variation, the initial shear modulus of adult human brain tissue is likely to be in the order of 1 kPa (119).

Pia-arachnoid complex (PAC)

Compared to the brain itself, the PAC has received relatively little attention in the literature. In the context of this research, the arachnoid mater is considered to be bonded to the dura mater, with the stiffness of the dura mater alone being approximately equivalent to the two structures combined. This leaves the subarachnoid space-spanning arachnoid trabeculae (97), bridging veins (18) and cranial pia mater.

Arachnoid trabeculae

The PAC is thought to play an important role in brain mechanics, especially in impact scenarios (133). Mechanical testing of the PAC is almost exclusive to a series by Jin et al. (60, 97, 134, 135) where in-plane tension, shear and out-of-plane tension loading were investigated. Stiffness of the PAC was found to be highly sensitive to strain rate, with clear structural anisotropy.

Table 3-3 – Mechanical properties of the bovine PAC as presented in (97).

	In-plane tension	Traction [out-of-plane]	Shear
Modulus	6-40 MPa	61-148 kPa	11-22 kPa
Ultimate stress	1-4 MPa	21-126 kPa	9-22 kPa
Ultimate strain	0.21	0.35-0.93	1.5-1.8

In the final paper (97), a non-linear viscoelastic constitutive model was developed, capturing the unusual behaviour of zero compressive stiffness. However, direct implementation of this model is limited by it being unavailable in finite element software and by the use of solid elements eliminating the potential to define a fluid-filled subarachnoid space.

Indirect methods have also been implemented to determine PAC stiffness. Mazumder et al. (136) introduced an L-shaped indenter through a hole in the decapitated head of a sheep, measuring the force and displacement with X-ray. A corresponding FE model was developed where the

PAC was modelled with numerous individual springs. Inverse modelling found agreement of the data sources with a PAC spring stiffness density of 11.45 N/mm/mm².

A study by Zhang et al. (137) is often referred to as reporting a Young’s modulus of 21.5 MPa for the arachnoid trabeculae (138, 139); however, upon reading the paper it appears this is likely referring to vasculature, as the trabeculae are not discussed.

Bridging veins

For its size, the brain receives a considerable volume of blood, accounting for 15-20% of cardiac output (140). Supporting this level of perfusion requires a complex network of veins and arteries. The cerebral cortex is drained of blood by bridging veins, which emerge from the cortical tissue, pass through the subarachnoid space, emptying into the major sinuses (18). In passing through multiple structures, the bridging veins are immobile and as such present a risk for subdural haemorrhage in cases of head trauma (141). It is in this context that they have received the most study (18). Numerous constitutive models have been proposed to study bridging veins. Using linear theory, the Young’s modulus has been reported to be in the order of 6-30 MPa (18). In the present study, rupture of the bridging vessels was not under investigation. They were assumed to contribute to the tensile stiffness of the PAC layer and as such were not considered alone.

Pia mater

Within the theme of spinal cord injury, the pia mater has received some attention (142), and has been shown to significantly contribute to the elastic and viscous response of the entire construct. Whilst it is understood that the pia mater is likely to exhibit non-linear behaviour (143), it is expected that strains will be small, and a linear elastic representation sufficient. Table 3-4 details the limited information available from which a range of variation was determined.

Table 3-4 – Stiffness values for the cranial pia mater in the literature.

Region	Modulus (E) /MPa	Thickness / μ m	Comments	Source
Pia and arachnoid	6-40	Unclear	Bovine PAC, in-plane tension.	(134) in (97)
Pia	1.8	15	Bovine cranial pia mater – approx. tangent modulus at 2.5%, assuming thickness of 15 μ m – this is unstated in the article.	(143)
Pia	1.1	400	Unclear where values are derived from.	(144)

Dura mater

The dura mater lines the inside surface of the skull and forms the great folds of the dural septa. It encapsulates cerebrospinal fluid and provides important protection and support for the underlying brain (14). With this critical mechanical role, accurate representation of the dura mater

is necessary for improved computational modelling of both head impact (14) and neurosurgical brain shift (145).

1970 saw the initial attempts to mechanically characterise the dura (146, 147), in particular demonstrating a viscoelastic behaviour. The ultimate tensile strength (UTS) is not particularly relevant to most modelling works and can be affected by factors such as patient age, storage media and time post-mortem (148, 149). UTS is reported to be in the region of 3-13 MPa at 13-32 % strains (149-152) in tests studying dura mater for use as allografts or prosthetic valves.

With the advent of new modelling methods, characterising stiffness has become the primary area of interest. The stress strain behaviour is directly related to the thickness of the sample and intra-sample variation in thickness cannot be accounted for. In (14), average thickness was found to be 1.05 ± 0.22 mm; in line with previous studies. However, it is established that dural thickness varies considerably by region and probably with age, in this case with a range of 0.53 – 1.88 mm. Galford and McElhaney (147) suggested that a linear viscoelastic model was sufficient to capture the behaviour of the dura mater. Linear elastic material models have since proven popular (153), but parameters are often estimated from previous publications. A Young's modulus of 31.5 MPa and Poisson's ratio of 0.45 is frequently used in linear elastic representations (14), although maximum tangent moduli have been reported anywhere from approximately 20-190MPa (151), highlighting the importance of using a more complex constitutive model if one expects high strains.

One recent and comprehensive work by De Kegel et al. (14) studied the more applicable case of biaxial tension. In brief, 5 human cadavers yielded a total of 53 10x10 mm test samples across the dura mater of the cranial vault. The samples were mounted in a biaxial testing device Figure 21 by means of BioRakes on each side.

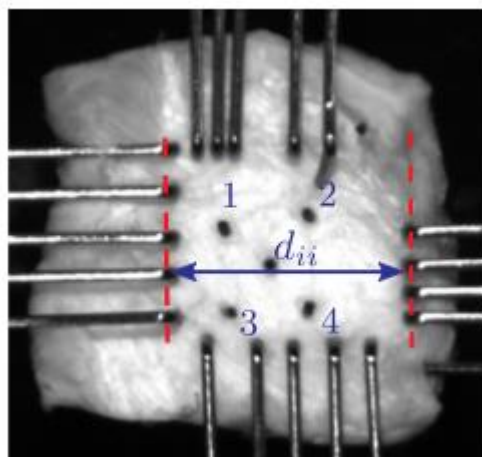


Figure 21 – Example of experimental set-up, demonstrating the use of BioRakes and the dimension d_{ii} used to calculate the undeformed area. Image reproduced from (14).

Material incompressibility was assumed for constitutive modelling. Neo-Hookean (NH), one term Ogden and Gasser-Ogden-Holtzapfel (GOH) constitutive models were fitted to the data by comparing forces calculated using the strain energy density function of each to the output of the mechanical testing. A reduced version of the GOH model assuming isotropy within the imbedded fibre families was also considered.

On balance it appears safe to consider the dura mater to be isotropic across a large sample (14, 149, 152); however, anisotropic fibre distribution can be found if the sample size is relatively small (151). De Kegel et al. showed a highly non-linear stress-strain response even at low strains, with a large amount of inter and intra specimen variability. No location or subject dependency could be shown.

It is difficult to apply individually determined parameters to an FE representation as non-linear parameters cannot simply be averaged. From (14) it is also clear that one parameter set will not adequately describe the stress-strain response of all human subjects. The GOH model was shown to be optimum, although this comes with increased computational cost. This cost must be considered against the predicted improvement in the accuracy in a simulation result when using 'better' constitutive representation.

Using the results presented in (14), an equivalent Young's modulus of approximate 1 MPa was calculated. On this basis, it can be said for certain that the modulus of dura mater is many orders of magnitude higher than that of the brain at any realistic strain. Considering the case of PBS, the weight of intracranial tissues in the prone and supine positions act in a direction where the dural septa are most geometrically stiff. It is possible that the strains in the dural septa in this loading are so small that differences between material representations are negligible. This was investigated before full parametric testing.

Finite Element Modelling

Finite element analysis (FEA) is a tried and tested method used in a wide range of engineering scenarios, allowing for the analysis of complex, multi-material structures without the need for mechanical testing. The geometry concerned is divided into numerous elements known as a mesh. Mesh optimisation is important in FEA and numerous software packages exist to aid with this. With the material properties and loading conditions defined, stress, strains and displacements are then calculated throughout the mesh.

FEBio is an implicit, non-linear finite element solver specifically designed to enable biomechanical simulations. It contains a wide range of constitutive models typically used for soft tissues. When mechanically characterising soft tissues, incompressibility is often defined mathematically. In FE implementation, constitutive models have 'coupled' and 'uncoupled' formulations, used in the modelling of compressible and nearly-incompressible materials,

respectively. For example, the strain energy density function ψ of the ‘nearly-incompressible’ hyperelastic Ogden material as found in FEBio is ‘uncoupled’, as it contains separate volumetric and deviation components. It takes the form shown in Equation 36:

$$\psi = \sum_{i=1}^N \frac{c_i}{m_i^2} (\tilde{\lambda}_1^{m_i} + \tilde{\lambda}_2^{m_i} + \tilde{\lambda}_3^{m_i} - 3) + U(J) \quad 36$$

Where $\tilde{\lambda}_k$ ($k = 1,2,3$) are the deviatoric stretch components, c_i is an instantaneous stiffness coefficient and m_i the exponential stiffening coefficient, each with up to 6 terms. Compared to classic linear theory with a one term model ($i = 1$), the FEBio representation defines that $c_1 = 2\mu$, where μ is the shear modulus (at small strains). $U(J)$ is the volumetric component defined in Equation 25.

A comment on the bulk modulus

The parameter k is normally used as a penalty factor to enforce the incompressibility constraint; however, in compressible, hyperelastic materials it can represent a true material parameter. As a rule of thumb, when the bulk modulus is not known, it is estimated at approximately 100-1000 times the shear stiffness defined in the model. In fact, validity of such an uncoupled formulation is only thought to remain when a near-isochoric response results from the simulation concerned. On a practical front, enforced volume preservation is not always possible due to convergence issues in the solver.

Existing models of the head and brain

Computational modelling of the head is common in the literature across a broad range of themes.

These include but are not limited to:

- Neurosurgery
 - Craniotomy and tumour resection (113, 145, 154-156)
 - Stereotactic procedures (59, 92, 157, 158)
 - Infusion (159)
- Impacts
 - Crashes (137, 160)
 - Blast (129)
 - Sports (7, 8, 109, 161)
- Understanding pathological conditions
 - Normal pressure hydrocephalus (162, 163)
 - Plagiocephaly (164)

A computational model that perfectly captured all geometry and material properties of the head, would in theory be able to model any loading scenario. Currently we, as a collective, are some way off this. Material properties, in particular, are often only applicable to the set of boundary

conditions in which they were derived. To the best of the author's knowledge, there is currently no computation model specifically designed to study PBS. With this in mind, we offer a brief review into methods used in adjacent modelling scenarios, with the hope of identifying modelling techniques which are equally relevant to the present.

High strain rate models

High strain rate injury is probably the oldest implementation of FE head modelling and given the applicability to the whole population, remains immensely popular. As such, the area is a subject of frequent review (107, 165, 166). Several FE models are the product of many years of development. For example, the well-known Kungliga Tekniska Hogskolan (KTH) model shown in Figure 22, was first presented in 2002 (7). Since then, improvements have included the addition of anisotropy within the brain (167) and most recently fluid structure-interactions (FSI) between the brain and cerebrospinal fluid (168). Whilst the load rate is very different to the case of PBS, this area of modelling is probably most similar, as it still concerns the intact cranium and no loss of CSF.

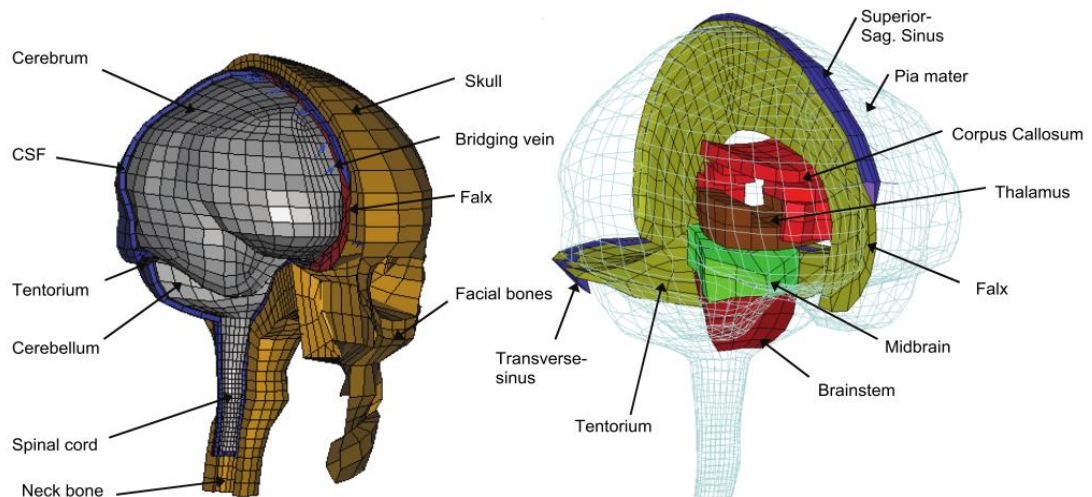


Figure 22 – The KTH model geometry as presented in (161).

With increasing computational power, geometric biofidelity of models is improving greatly. Automated geometry generation methods are able to create FE meshes containing millions of elements (109, 160, 169). This improved geometry has led directly to some key findings, such as the involvement of the sulci in chronic traumatic encephalopathy (109). However, without appropriate smoothing, jagged edges can lead to numerical artefacts (169).

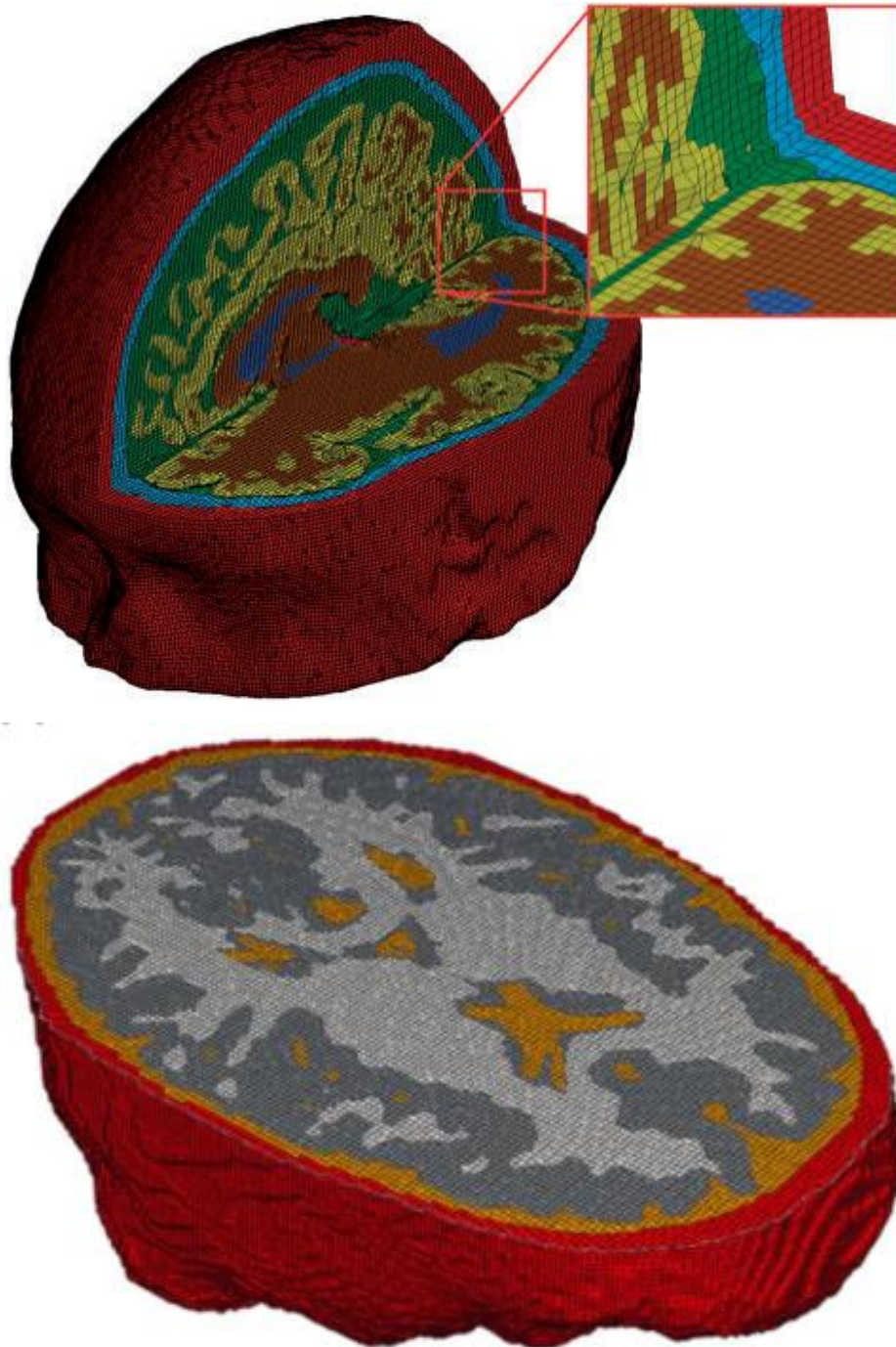


Figure 23 – Examples of the high biofidelity finite element models for traumatic brain injury used in (109, 160) [top] and (169) [bottom].

One of the main risks with significant head impact is subdural haemorrhage, commonly caused by the rupture of bridging veins. As such, the bridging veins are a key component of many head impact finite element models (18). In some cases they are defined with no mechanical stiffness and only strain is assessed (170). More commonly they are defined as springs or beam elements with linear elastic stiffness (7, 161, 171, 172). An example of this linear representation can be seen in Figure 24 below.

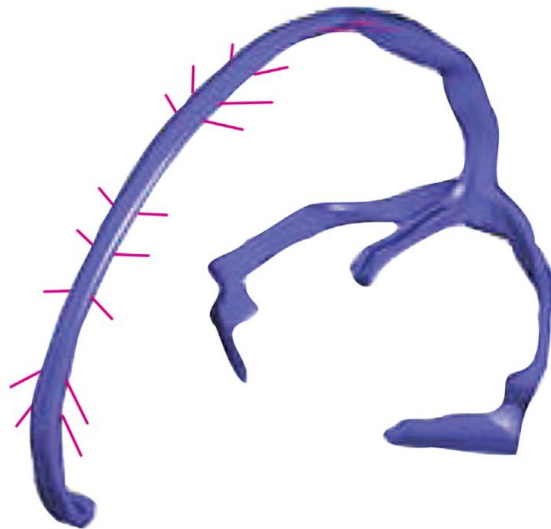


Figure 24 – Representation of the bridging vein pairs by means of spring elements with linear elastic stiffness (171). Reproduced from (18) for improved clarity.

More recently, Migeuis et al. (173) used a more realistic geometry and damage model to investigate the rupture of bridging veins. Vessels were defined with linear elastic properties and a plastic representation to capture vessel failure. In this case, these improvements led to more accurate prediction of kinematic parameters involved in vessel tearing.

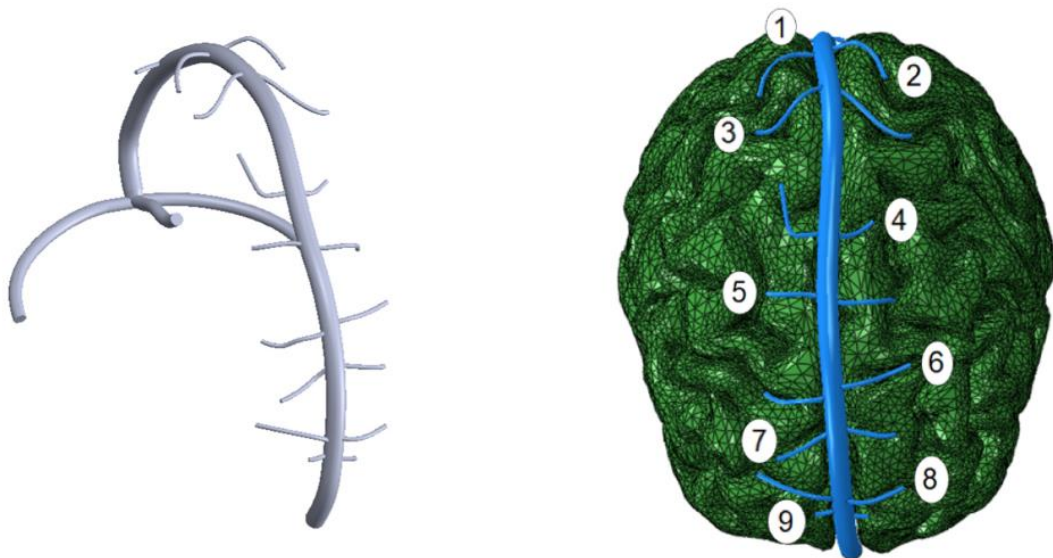


Figure 25 – The finite element representation of the cranial sinuses and selected bridging veins, reproduced from (173), showing greatly improved biofidelity.

Even in some of the latest models, such as the Yet Another Head Model (YEAHM) (174) from which Figure 25 was based, there are still some significant simplifications and debate in the literature. Foremost of these is the PAC (133, 153), often referred to as the brain-skull interface.

There are a number of methods used in modelling this region (153):

1. Tied contact between the brain surface and skull (175).
2. Brain/skull sliding with a coefficient of friction of 0.2 (or similar) (171).

3. Brain/skull free sliding (176).
4. Connection of brain and skull surface nodes with two-dimensional connectors/springs (136, 153).
5. High bulk modulus/low shear stiffness solid element representation of CSF/PAC combined (7, 161, 167, 172, 174, 177).
6. Various combinations of the above.

In general, the CSF layer is well recognised to be important and most approaches use solid elements with varying degrees of sliding allowed between the CSF region and the skull. Some studies have compared these methods directly. Coats et al. (153) modelled five contact conditions separately: conditions 1, 2, 3 and 4 (with vasculature) from the above list, and solid elements with fluid properties. Impact testing on immature piglets was undertaken to validate the FE models. Results showed the use of spring connectors or solid elements gave the greatest agreement with experimental data. Saboori et al. (138) compared soft solid, viscous fluid and porous elastic material representations of the subarachnoid space. The results of all three material representations were very similar, meaning one method was not advocated over any others. Most recently, Wang et al (178) considered four representations:

1. The approach used in the THUMS model (179) where CSF, dura, arachnoid and pia are all modelled separately as solid elements.
2. Rigid connection of the pia and skull through tied contacts.
3. Frictionless sliding between the brain and skull.
4. A cohesive layer between the brain and skull connected by spring elements.

Once again, the original solid element representation was found to best match validation data. However, it is acknowledged that a better understanding of the cohesive material properties may improve the results.

Multiscale models are the next logical step in investigating the role of the PAC more closely. Zoghi-Moghadam et al. (180) calculated loads in head impact using separate global solid and global fluid models. These were then applied to a detailed local model (Figure 26 [right]) to assess the chance of vessel rupture. Scott et al. (133) assessed the local geometry of the PAC and also regional changes in volume fraction (VF) of solid components. Figure 26 [left] shows the result of random generation of chords (blue), narrow sheets (green), broad sheets (red) and combined sheets and vessels (grey).

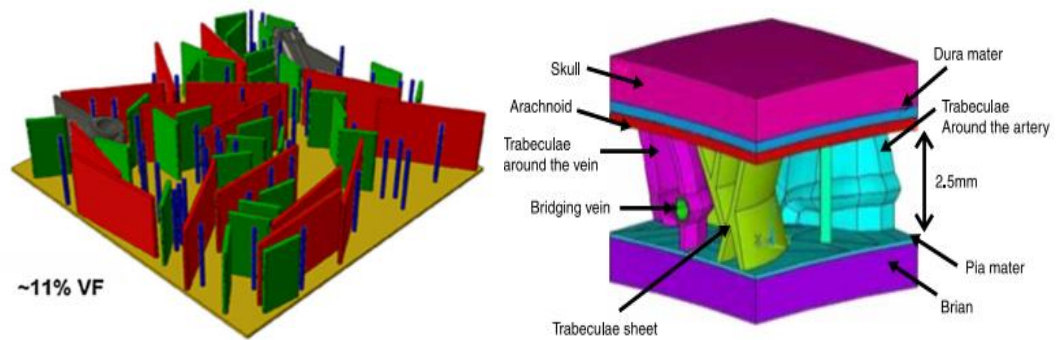


Figure 26 – [left] Example of the randomly generated PAC geometry reproduced from (133) - [right] local model geometry reproduced from (180).

This technique suggested significantly different cortical stress compared to a uniform representation of the PAC, with excellent regional prediction of haemorrhage. From these studies it can be concluded that on a global scale, a biofidelic representation of the PAC is essential for the continued improvement of computational models, although implementation is still challenging.

Fluid structure-interactions

One of the main limitations of many previous investigations of traumatic brain injury (TBI) has been the absence of FSI in the model (178). CSF has generally been modelled with incompressibility and low shear stiffness; crucially not considering potential fluid redistribution. Zhou et al. (168) developed the KTH model to overcome this problem, using a Lagrangian-Eulerian multi-material formulation to capture FSI. Firstly, the cortical boundary was defined as a void mesh, where CSF could flow under deformation. Then, in a two-step process, the Lagrangian deformation of the FE mesh was computed followed by transportation of element state variables to the reference frame. Bridging veins were included in the model, which was found to achieve improved validation performance on solid CSF representations. However, even with FSI considered, this is still an over-simplification of the brain-skull interface. A better solution would be a model which incorporates fluid CSF with FSI and the tethering arachnoid trabeculae together (168).

Neurosurgery

Computational modelling of neurosurgery is also prolific in the literature. Focus is mainly on the model-driven update of navigational neuroimages in craniotomy and tumour resection (156), where computational speed is the main concern (96, 181). As such, non-commercial computational software is often developed for this purpose, and used with significant geometric simplification. For example, some authors advocate the generation of FE models with a physical gap, no PAC and a sliding interface between the brain and skull (108). Craniotomy causes the loss of large volumes of CSF with subsequent displacements in the order of 10 mm (182). This method may be acceptable in such cases; however, in PBS this is not likely to be the case.

Loading of other neurosurgical models is somewhat unique in that it is often displacement driven, with measurements taken from the cortical surface of the patient during surgery (9, 108, 183). In these cases, it is suggested that the displacements throughout the remaining domain are only weakly dependant on the mechanical properties (9, 184). However, this property is mathematically driven and again is almost certainly not applicable in PBS.

Some studies have investigated brain shift in the context of stereotactic neurosurgery (59, 92, 157, 158, 185). In the initial works, it was considered that CSF loss was both unavoidable and unpredictable. Instead, the authors employed worse case boundary conditions to generate a risk volume that must be avoided to ensure safe insertion of the electrode. Subsequent focus turned to automation of this process and intra-operative registration of the computational model to a deformed image. These works utilised a physics-based approach, in which the loss in CSF was accounted for by a reduction in force applied directly to the surface of brain itself, calculated as a function of the fluid head above each point. Fixation of the brain stem, and a non-penetrating contact algorithm between the brain and skull/falx cerebri contained the brain within the intracranial cavity when equilibrium was lost. Whilst potentially improving surgical safety, these works do not address PBS directly.

Material Sensitivity Analysis

One of the primary points of interest in this work is to understand the impact of material parameter variation on PBS. This is done with two outputs in mind:

1. To determine material properties for each of the human data sets.
2. To determine the sensitivity of PBS to property change; in other words to show which material properties most influence the process.

Investigating both thoroughly would require computing the model (in the context of this section, the simulation) in increments over the desired range for each parameter, as well as for every combination of parameters to capture joint effects. For a meaningful analysis this would require many thousands of simulations. This is completely unfeasible given the complexity and computational time.

This section discusses the background theory and software used to overcome this problem, and the subsequent methodology which employed these techniques.

Material sensitivity study: Theory

The Gaussian Emulation Machine for Sensitivity Analysis (GEM-SA) is software designed to tackle such problems. It is free to use for non-commercial purposes and can be found at www.tonyohagan.co.uk/academic/GEM. When using this software, an understanding of the theory from which it is based is useful, but a deep mathematical understanding is not necessary. As such, a basic account of the theory follows. This explanation is based predominantly on

publications of the software developers' (186, 187) and the original theory of Bayes, first published in 1763 and republished in (188).

Bayesian and frequentist statistics

Bayesian methods are becoming increasingly vital in a wide range of statistical applications, the most relevant of these being the development of complex statistical models designed to simulate real-world systems. In order to understand the more complex statistical models one must first understand the underlying theory.

Most people are familiar with the frequentist definition of probability. This considers probability as the frequency of a given outcome in an infinite number of trials. There is uncertainty in the result which stems from randomness or unpredictability. Although useful in some cases, this method is limited when considering one-off occurrences that are not repeatable. An example of such a one-off case could be an intrinsic material property of a given sample of soft tissue. In these cases, the uncertainty does not stem from randomness, but from a lack of knowledge about that sample. These distinct types of uncertainty are known as *aleatory* and *epistemic* respectively. The Bayesian statistical framework allows for quantification of all uncertainty, and hence gives potential for a more accurate mathematic representation of a process.

Bayes' theorem

To understand the statistical basis of emulators we must first introduce some concepts of probability theory and in particular, *Bayes' theorem*.

Considering an event or proposition A , we denote the *marginal probability* of A being true as $P(A)$. Introducing another proposition B , we denote the *joint probability* of both A and B being true as $P(A \cap B)$. When the two events are independent, this is calculated as the product of $P(A)$ and $P(B)$. As joint probability concerns the product of two marginal probabilities, it holds that $P(A \cap B) = P(B \cap A)$. This is not the case for conditional probability.

The *conditional probability* can be defined as the probability one event occurring given that another already has. This is written as $P(A|B)$ and defined as:

$$P(A|B) = \frac{P(A \cap B)}{P(B)}, \text{ if } P(B) \neq 0$$

If we also consider that:

$$P(A \cap B) = P(A|B) \cdot P(B) = P(B|A) \cdot P(A)$$

Bayes' theorem can be derived to state:

$$P(A|B) = \frac{P(B|A)}{P(B)} P(A), \text{ if } P(B) \neq 0$$

Whilst simple, Bayes' theorem can be powerful, particularly when considering the probabilities A and B to be a hypothesis and an observation, respectively. $P(A)$ is termed the *prior probability* and now represents the probability of the hypothesis being true before the observation of evidence. The 'informed' output $P(A|B)$ is termed the *posterior probability*. These are related by the *likelihood ratio* $\frac{P(B|A)}{P(B)}$ such that the posterior probability is the product of the prior probability and the likelihood ratio.

Simulators and emulators

The implementation of a mathematical model into a computer program results in what is known as a *simulator*. Simulators have two main subclassifications: deterministic simulators always produce the same output for a given input, whereas stochastic simulators involve a random-number seed. Monte Carlo simulation methods are some of the most popular and easy to implement. A mathematical model of the process under consideration is first developed incorporating the necessary range of variables. This model is then computed many times, randomly selecting values for any uncertain variables at each step of the simulation. With enough data points, the outcomes can be plotted as a probability distribution curve. The probability distribution can then be used to find the likelihood of any deterministic outcome.

To achieve a meaningful probability distribution, simulators must be computed many thousands of times. For complex models, the level of code runs required to yield accurate probability estimates may be prohibitive. Bayesian methods provide a solution to this problem in the form of statistical *emulators*. A meaningful emulator relies on two main properties of the function in question:

1. There is a smooth relationship between inputs and outputs with no sharp changes. i.e. information about one point yields information about surrounding points.
2. Output variation can be described by a small number of inputs, even if the simulator code has many.

In cases where these conditions are satisfied and the output is deterministic, Bayesian methods can be employed and the outputs of a simulator can be modelled as an unknown function of inputs using a Gaussian process.

Implementation in GEM-SA

In the explanation of Bayes' theorem we considered a simple case of two probabilities. Gaussian processes build on this theory to describe probabilistically the output of a function over an infinite range of input values. Suppose that the simulation output is a function of p inputs such that $y = f(x)$, where $x = (x_1, \dots, x_p)$. In the context of this work, the function output y describes the deviation between FE data and human data over the defined range of values of a material parameter x .

Within the software, the prior expectation can either be linear such that $E(f(x)) = 1$ or a linear function of each of the inputs with unknown coefficients β , where:

$$E(f(x)) = \beta_0 + \beta_1 x_1 + \dots + \beta_p x_p$$

The inaccuracy of this initial estimate is not consequential, as the processes iteratively adapts even in cases of nonlinearity.

Covariance is a measure of the of correlation between sets of points. Recalling that in Gaussian processes, a smooth transition of inputs and outputs is required, a covariance function is applied to characterise this smoothness:

$$Cov(f(x), f(x')) = \sigma^2 \prod_{i=1}^p \exp\{-r_i(x_i - x'_i)^2\}$$

Here, r_i is a scaling parameter used to define function roughness. This roughness infers the expected rate of change of an output with distance from a known point, and therefore the probability distribution of outputs between points; this is assumed to be Gaussian. The key aspect to be noted here is that roughness is related to the distance between them, not their location. The parameter σ^2 determines the predicted variation around the response.

The posterior distribution is found after training the emulator with observed outputs $d = (f(s_1), \dots, f(s_N))$ of the simulator at input points (s_1, \dots, s_N) . The emulator is fit by iterative estimation of the prior variables (β, σ^2, r) . Bayes theorem and the fitted emulator parameters are used to derive a Gaussian probability distribution of the all input points between the training data points. The mean of this probability distribution at any input describes the posterior mean function; the emulator approximation of the simulator code. By design this passes exactly through all known points, unless numerical error is known to exist in the training data (i.e. it is not deterministic).

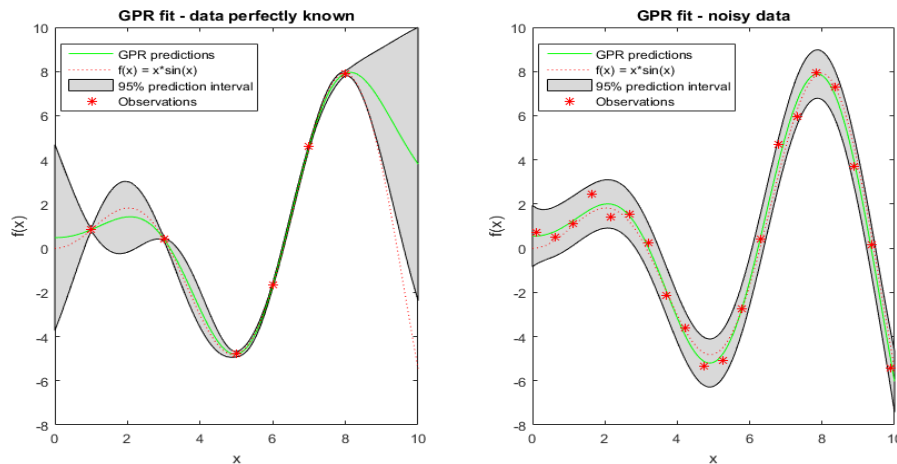


Figure 27 – Gaussian process regression plots, depicting the simulation code function (red dotted line), sparse observation indicating points at which the simulation had been computed

and the posterior distribution after considering the observations. Note the posterior function is the mean of the 95% prediction interval. The left figure depicts deterministic data whilst the right contains numerical error, or noisy data and as such has no regions with a variance of zero. Reproduced from (189).

The example of Gaussian process posterior predictions in Figure 27, reproduced from the MathWorks documentation (189), demonstrates some of the key principles discussed. In regions where there is considerable linearity between observation points, the prediction has an extremely small confidence interval. In the perfect data set, the most significant deviation from the true value occurs in the region where $x > 8$, due to the lack of observation points. This highlights the need for effective design of input distribution in simulator runs and leads onto the practical aspects of using GEM-SA.

User considerations

Appropriate space-filling input design is necessary for optimal emulator fitting. GEM-SA has two functions for this: the LP-tau algorithm and maximin Latin hypercube algorithm. The LP-tau method is preferred when the number of required computations is not known, as it sequentially fills space in the existing distribution with each iteration. The Latin hypercube method uniformly covers the input space with an iterative process that achieves the largest minimum distance between points.

Quoting directly from (186), the GEM-SA emulator has the following outputs:

“

- *Prediction* of the code output at any untried inputs.
- *Main effect* of each individual input, showing the degree and nature of the influence of the input, averaged over the variations due to all other inputs.
- *Joint effect* of each pair of inputs, showing the joint influence of inputs again after averaging.
- *Total effect* of each input, which is a measure of influence that includes higher order interactions to which the input contributes.

”

In summary, GEM-SA can be trained with a relatively small set of well-chosen data points and subsequently predict the output of any future combination, dramatically reducing computational time. In the context of a biomechanical analysis, the impact of both individual material properties and joint effect interactions between pairs of properties can be considered. This allows the user to objectively determine the influence of each property on the measured output, greatly improving the ability to understand the mechanical process at hand.

Influence of Findings

The objective of this section was to gain insight into commonly used methods in constitutive modelling of soft tissues and previous FE models of the head. Some of the techniques used are not entirely applicable to PBS but understanding the state-of-the-art in other areas can still inform the development of new models.

In terms of material representations, an Ogden constitutive model appears to be the optimal choice for brain tissue. In PBS, strain rates are expected to fall between those seen in pathological conditions and impacts. As such, a single phase, time-independent model, in which the bulk modulus represents a true material parameter as surrogate for fluid redistribution, appears appropriate.

In terms of modelling techniques, the brain-skull boundary has been identified as an important structure that has often been over-simplified in the past. State-of-the-art implementations model this structure as either a fluid layer using FSI, or through a layer of numerous discrete springs. Each of these components of the PAC is expected to play an important role in the mechanics of deformation, but to the best of the author's knowledge, no model has yet implemented a combined FSI/spring representation.

In a highly constrained process such as DBS, it is expected that the prescribed material response will have a significant impact on the generated displacement field. As the material parameters available in the literature have not in general been obtained under this type of loading, it is possible that the values presented are not applicable to the current study. To understand the impact of material variation on the result with the time and resources available, a typical parametric study was not feasible. The GEM-SA software package was introduced, offering easy generation of a statistical emulator based on relatively few model runs. No previous uses of this software in head tissue material sensitivity analysis have been identified in the literature.

With the findings of this chapter in mind, the following section details the development of the head model and methodology of its implementation in the study of PBS.

Chapter 4: Methods

Previous chapters have assessed the literature in order to guide this study to most effectively add to the body of knowledge. It was identified that positional brain shift should be the focus of computational analysis, with the model requiring a realistic representation of the PAC to yield accurate results. As the material parameters found through ex-vivo mechanical testing are not necessarily applicable to other loading scenarios, a parametric study was planned, allowing calibration of the parameters to in-vivo displacement fields of the same loading. The following section outlines the methods used by this and the adjacent Ph.D. projects to make this possible.

Human study

One of the underlying premises of this study was to use inverse modelling techniques to determine material properties from in-vivo displacement fields rather than generating such fields with material properties obtained from mechanical testing. Previous studies which focussed on PBS were discussed and estimates of what to expect were considered. These estimates are interesting, but they do not offer a high-resolution, volumetric description of brain shift. With the intention to understand the deformation pattern across the entire brain, it is important that the computational model is also calibrated across its whole volume rather than at sparse points, or with average global measurements. With this, it was decided that a new, concurrent study, would focus on the acquisition and analysis of PBS in a group of healthy volunteers.

This was carried out by Stefano Zappalá, in work to be submitted for his doctoral thesis.

Explanation of this study is included for completeness but should be accredited to him.

An extended abstract has presented some of the methods and processes (122); however, the majority of data used in this project has yet to be published. A brief summary of the methods can be found below.

Acquisition

The human study was carried out in conjunction with the Cardiff University Brain Imaging Research Centre (CUBRIC). The study was approved by the Ethical Committee of the Cardiff University School of Psychology and informed consent was obtained from all participants before scanning. This initial study consisted of three subjects (all male), aged 30, 20 and 60. Subjects were first placed in a prone position outside of the scanner for 30 minutes to ensure the brain had completely settled. One prone image was taken before transition to the supine position, in which 3 consecutive scans were undertaken over a period of approximately 30 minutes to assess the time dependency of brain shift. Structural T1 weighted scans of 1 mm³ resolution were obtained from the same Siemens 3T Prisma scanner for all subjects in all positions.

Data processing

To determine displacement within the soft tissue structures of the intracranial cavity, affine registration was first used to align the skulls of each patient in the prone and supine images. Elastic registration was then performed from the prone to each supine image, generating a vector displacement field over the entire volume. The displacement field was registered to the node space of the finite element model to allow for nodal displacement comparison.

Phantom study

It was quickly identified from the literature that the state-of-the-art in physical phantoms of the head and brain are falling far behind advancements in the rest of the field, especially in the sense of the geometry used. This is most likely due to the highly complex, multi-scale nature of the tissues surrounding the brain, presenting real challenges to its design and production. Should a more realistic phantom be developed it would have many potential uses. Firstly, phantoms do not have the same constraints as live patients and can therefore be imaged repeatedly, in any orientation and using technologies such as CT, which is usually unethical to use on non-clinical subjects. Secondly, a more realistic phantom would provide opportunities for surgeon training and testing of newly developing surgical techniques, at a stage before trial on human patients would be possible.

This was carried out by Matthew Potts, in work to be submitted for his doctoral thesis. Explanation of this study is included for completeness but should be accredited to him. This work is currently unpublished; however, the full doctoral thesis explaining the process will be submitted in a similar time frame to this.

Geometrical Development

The base geometry used for the phantom was directly based on that used for the FE study, which will be explained later. This was then modified to allow for a complex manufacturing process. Stiffer structures such as the dural septa and skull were produced using rapid prototyping techniques. Moulds for the brain were fabricated to facilitate casting of a hydrogel, specifically tuned to match the mechanical properties of the brain. A novel method using similar techniques to investment casting was developed to form the hollow ventricles within the brain. The final phantom comprised the skull, dural septa, brain, ventricles and subarachnoid space. Attempts to recreate the tethering arachnoid trabeculae were made but could not be achieved due to limitations in the available technology.

A multi-axis cradle was developed to allow for reorientation of the phantom within clinical MRI/CT scanners. The phantom within its cradle and an MR image of the phantom are shown in Figure 28.

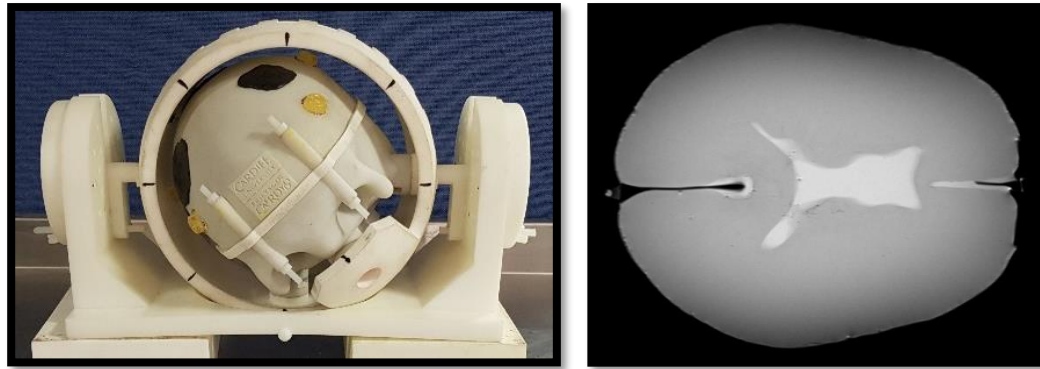


Figure 28 –Demonstration of the phantom held in a right semi-decubitus position for scanning in this orientation [left] and MR image of an axial section, highlighting the skull and falx cerebri (black), brain (dark grey) and ventricles/subarachnoid space (light grey) [right].

Orientation testing

As part of the experimental work, supine to prone brain shift was studied within the phantom. This provided a second source of validation data for the FE study. The inverse of the supine to prone data obtained was calculated for consistency with the prone to supine human study.

Displacement was tracked using rigid registration of the skull and a series of bead markers spaced throughout the brain. Imaging was performed with CT, meaning image distortion as is seen in MRI was not a concern. However, due to the non-inclusion of the arachnoid trabeculae it was expected that the displacement pattern may differ slightly from the human and FE results. Nonetheless, it was still expected that the displacement would be representative of the general magnitude and pattern of brain shift.

FE Model Development

The basis of the finite element method and implementations used in previous similar works have been discussed in the previous section. Whatever the application, the results of any finite element simulation are determined by three factors:

- Geometry
- Boundary conditions
- Materials

The accurate capture of each of these components within a computational model has a direct impact on the accuracy of the final model. However, this accuracy is not equally sensitive to each distinct input. As such, the careful consideration of biofidelity versus computational efficiency is required when developing a new model. This section details the development process of a new FE model within FEBio for the study of PBS with these considerations in mind.

Geometry generation

It was indicated in the literature that a relationship between certain geometrical features and the levels of brain shift is emerging; however, at this point a definitive correlation has not been found.

Although it is likely that the shape of one's brain will impact the level of brain shift that is seen, general morphometric variation was not considered in this initial part of the investigation. On the other hand, accurate representations of structures such as the PAC have been shown to be important in adjacent fields. As such, the PAC was considered a critical component to include.

The MNI dataset

The MNI ICBM152 Average Brain Stereotaxic Registration Model (McConnell Brain Imaging Centre, Montreal Neurological Institute, McGill University) was used as the geometric base structure. This data set is an average of 152 linearly registered T1 weighted images. Use of this averaged geometry removes aspects of intra-patient variability that could influence model validity across a wider population, while maintaining a high level of anatomical detail (Figure 29). On this basis, the MNI ICBM152 dataset has been used in a wide range of academic pursuits to date.

Image Segmentation

Automatic image segmentation algorithms are becoming increasingly powerful and offer true potential in certain modelling cases. In this instance, the requirements of this and the concurrent phantom study meant that automatic segmentation was not suitable. As such, segmentation was performed using Simpleware ScanIP™ (Synopsis, Mountain View, USA).

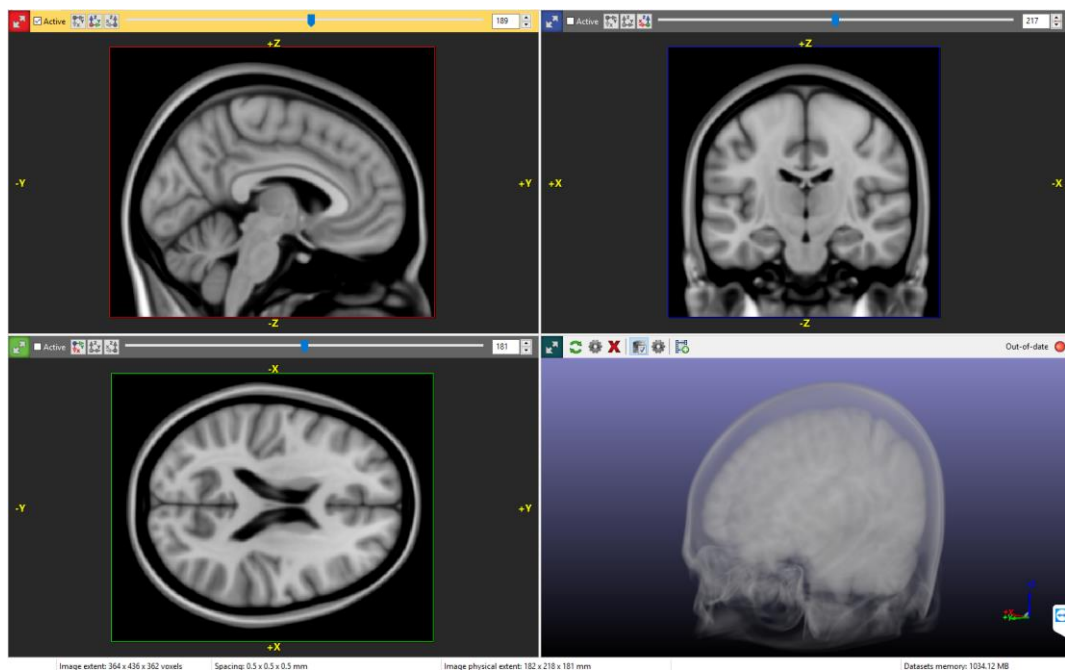


Figure 29 - Example of the ScanIP™ interface displaying the unsegmented MNI dataset.

Upon starting this study, it was expected that the fluid networks would play an important role in brain shift; however, directly modelling the interaction of these three networks would involve highly detailed geometries with single-phase/multi-phase fluid flows (25). This level of complexity is not possible and probably not necessary for the current study, so was not considered further. Instead, at this initial stage of geometry generation, the image was separated into three distinct regions:

- Brain
- Ventricles and subarachnoid space
- Dura and dural septa

Generating these 3D structures requires first applying a 2D mask covering each anatomical region on the MR image. Within ScanIP™ there are several tools to aid in this process. These include functions to bulk fill areas based on voxel intensity and various methods of image smoothing. Although these are useful for obtaining the general form of each region, a large amount of manual adjustment is inevitably required. Figure 30 shows sections similar to those seen in Figure 29, this time with transparent masks representing each anatomical region superimposed onto the image. Although not used in the FE analysis, the skull, shown in grey, was also segmented to provide an external boundary of the intracranial cavity and for the phantom model.

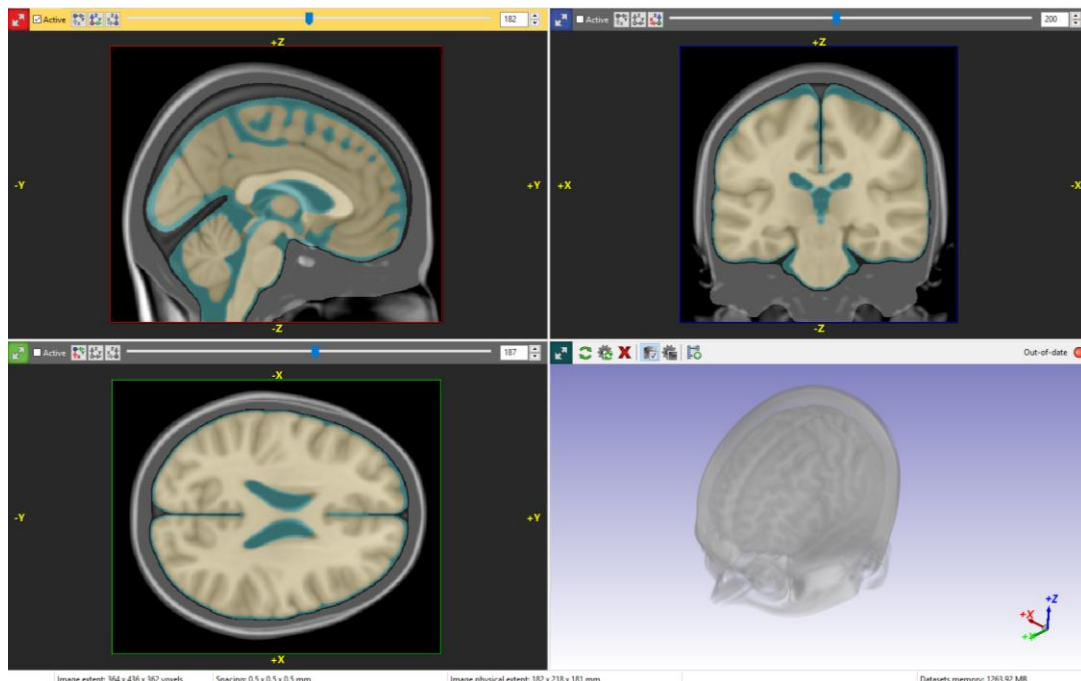


Figure 30 – Regional segmentation of the MNI dataset – coloured regions represent the brain (beige), CSF spaces (blue), dura/dural septa (dark grey) and skull (light grey).

Intentional deviation from the apparent geometry

Although great care was taken to produce a geometry that replicates the MNI data as accurately as possible, there were some situations in which this was either not possible or desired. Firstly, an irregular or malformed mesh can slow down the FEA solution dramatically. This can be caused by thin sections of a deforming structure or the intersection of multiple parts. For example, the intricate recesses and foramen of the ventricles could cause such instabilities. For this reason, some anatomical detail was intentionally removed from the segmentation.

Additionally, within the sulci and many other areas of the brain, regions of brain tissue are effectively adjacent, but separated by the pia and thin layers of CSF. Through regions such as the

Sylvian fissure it was possible to retain this separation. Within the images this region is shown as a dark, apparently CSF filled cavity; however, there are many strong vessels and connective tissues running through the region. For this reason, it was decided that areas such as this would be considered 'brain' for segmentation purposes.

Finally, as the development of a computational model of brain shift is being developed in conjunction with a physical phantom, it was deemed beneficial that the geometry of both models would be the same. For practical reasons, the phantom could not incorporate thin, membranous structures, such as the mid-sagittal separation of the lateral ventricles. All such structures were either removed or increased to a minimum thickness of 5mm, as can be seen in Figure 30.

Thickness of the subarachnoid space

It must be considered that the state of pre-stress in the intracranial tissues is not known. This is particularly relevant to the arachnoid trabeculae which span the subarachnoid space. In an attempt to overcome this, the model geometry was modified to maintain a uniform PAC thickness of approximately 2 mm (190). Whilst this is not the case in reality, it is considered to be a lesser assumption than accurate segmentation in the supine position and estimation of pre-stress.

Arachnoid trabeculae and pia mater

From the outset of this project it was expected that the PAC would play an integral role in the biomechanics of PBS. As previously discussed, the PAC can be thought of as a construct of four main features:

1. Arachnoid mater
2. Arachnoid trabeculae
3. Pia mater
4. CSF

The arachnoid mater is assumed to be attached to the dura mater and is unlikely to separate in this scenario, as such it was not considered. To utilise a fluid representation of the CSF, the region may not also be occupied by solid elastic elements as have been used in the past. Instead, the incorporation of discrete spring elements would offer the tensile stiffness of the arachnoid trabeculae whilst preserving the subarachnoid space to be defined as a fluid layer. The model was too complex to use the automatic spring spanning function within FEBio and as such the following methodology was developed:

1. The interior surface of the dura and exterior surface of the brain was defined within Preview and exported within a new '.feb' file.
2. The file was read into Matlab.

3. The node lists for each surface were compared such that the single closest pairs of points were identified.
4. All spring elements longer than 4mm were removed to prevent the spanning of unintended surfaces
5. The finalised spring set was written into a new '.feb' file.

The pia mater was simply defined as the exterior surface of the brain and generated through Matlab in a similar way.

Final Geometry

The following figures detail the finalised geometry used in all subsequent simulations. Figure 31 illustrates the stiff outer layer of protection for the brain. Key features retained in the segmentation were the cranial dura mater, falx cerebri, tentorium cerebelli, falx cerebelli, superior sagittal sinus and transverse sinus. It was assumed that the stiffness of sinuses was such that hollowing of these regions was unnecessary.

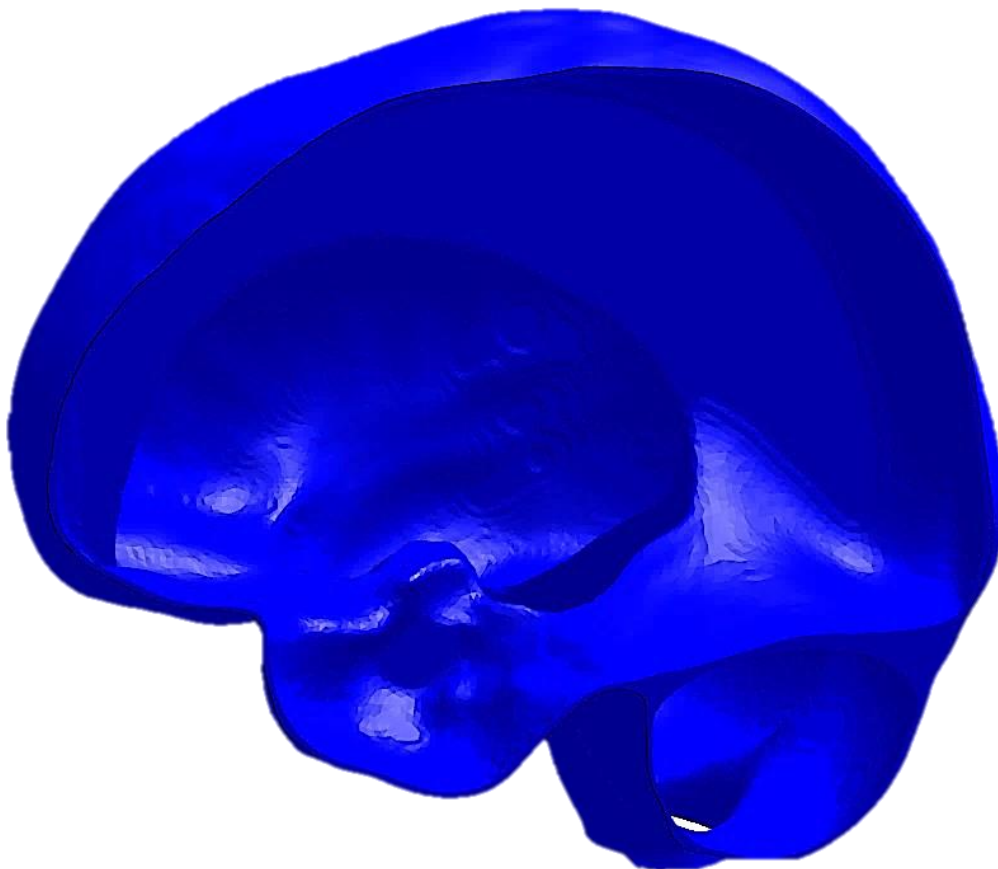


Figure 31 – Off midline sagittal section of the dura mater and dural septa.

The exterior surface of the combined CSF filled regions in Figure 32 shares nodes with the interior surface of the dura layer and as such no contact is required. The morphology of the lateral, third and fourth ventricles (Figure 33) was impacted by the MNI data itself and modelling considerations. Notably the inferior horns of the lateral ventricles were not included, and the

body of the lateral and third ventricles were combined. In the MNI dataset the interthalamic adhesion appeared to be enlarged, though this was carried through to the model.



Figure 32 – Lateral view of the external surface of the PAC.



Figure 33 – Lateral view of the lateral, third and fourth ventricles and cerebral aqueduct removed from the subarachnoid space for visualisation.

The gyri and sulci of the brain surface were retained as much as possible (Figure 34 and Figure 35). Smoothing of the original MNI dataset along with intentional smoothing in model generation did lead to a smoother surface than expected. However, it was taken that the surface of the brain was to include vessels which often track sulci, mitigating the impact.

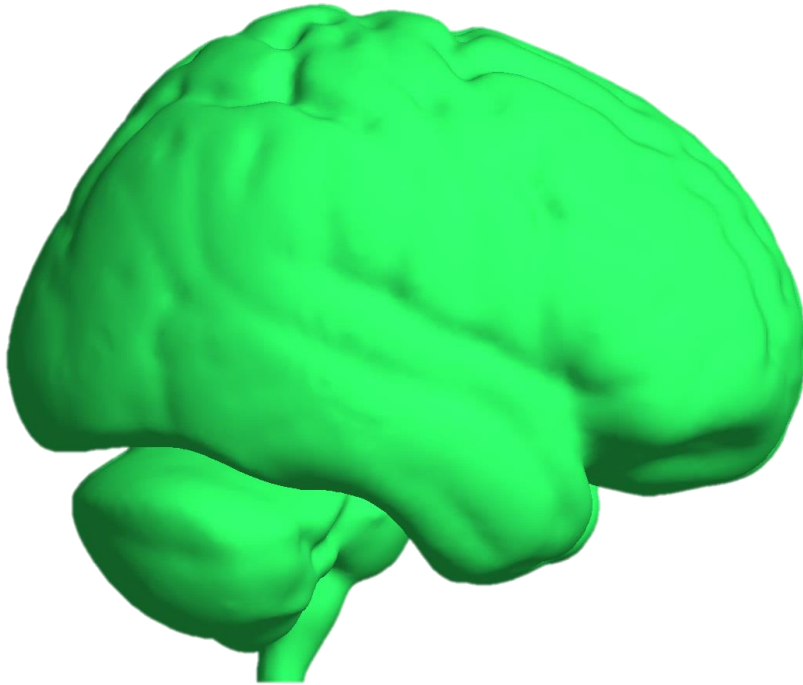


Figure 34 – Lateral view of the brain/pia mater with arachnoid trabeculae springs removed.

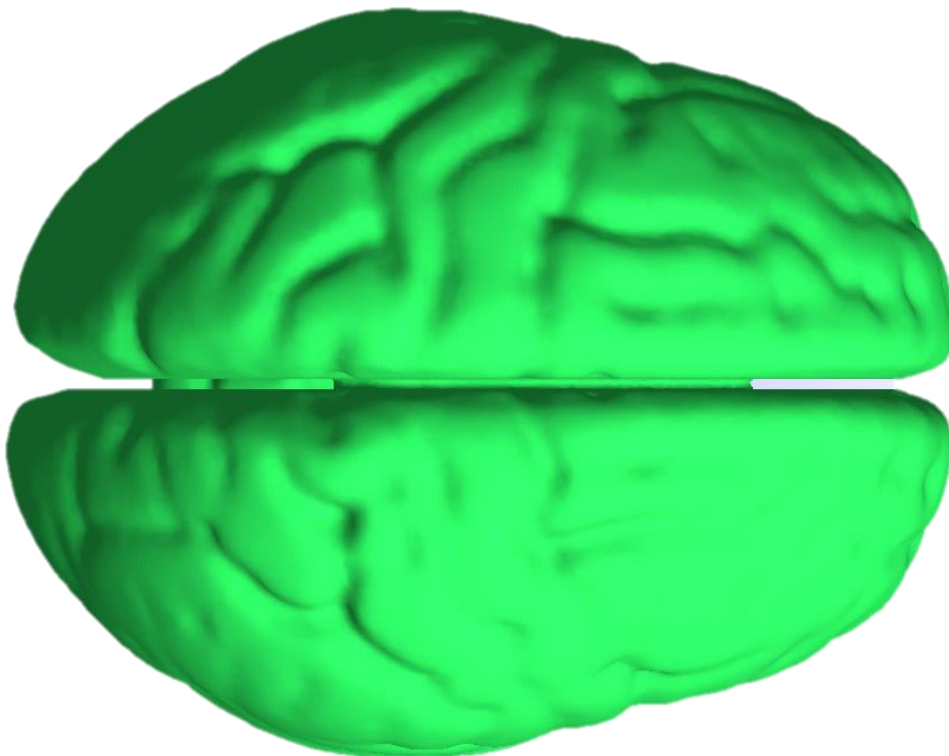


Figure 35 – Superior view of the brain/pia mater with arachnoid trabeculae removed.

The arachnoid trabeculae shown in Figure 36 were regularly distributed across the surface due to the high-quality mesh obtained through ScanIP™. The sparse, stiff bridging vessels of the subarachnoid space were not included at this stage although this is feasible in future. The distribution of the arachnoid trabeculae is further detailed in Figure 37, where the CSF is not visualised.

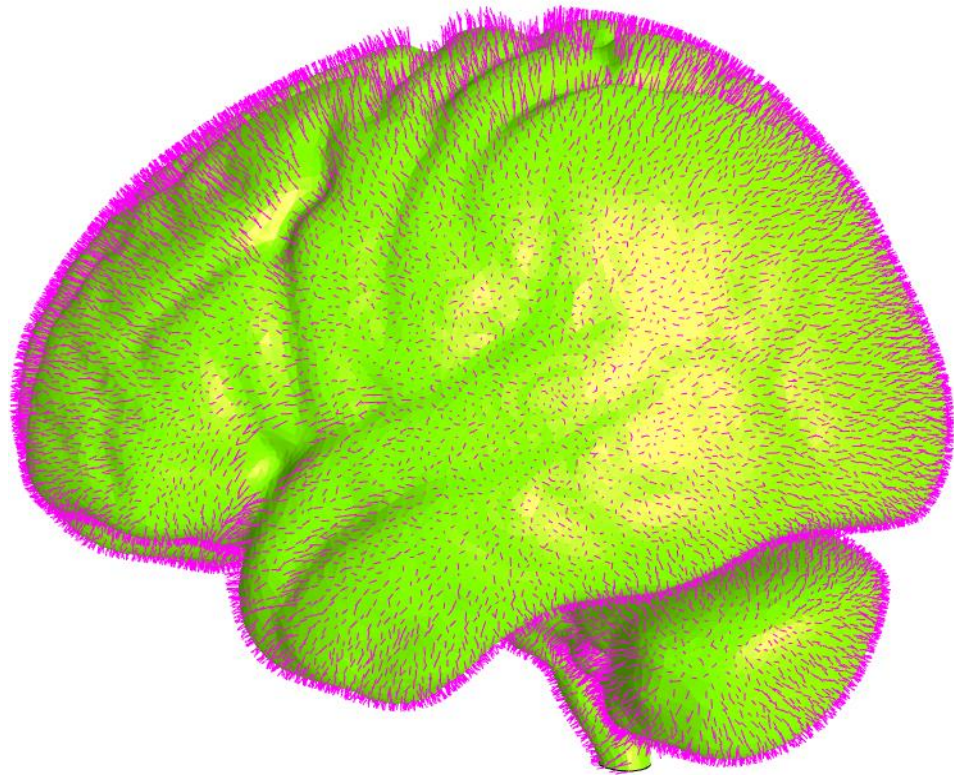


Figure 36 – Lateral view of the brain/pia mater with arachnoid trabeculae shown in pink.

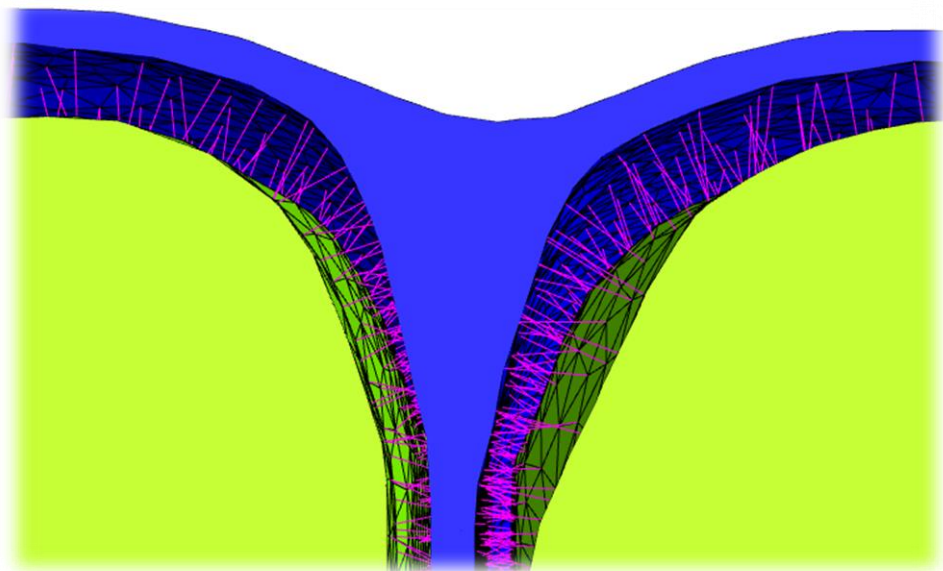


Figure 37 – Transverse section of the anterior brain and dura mater with CSF regions removed, highlighting the spanning of the subarachnoid space with the spring representation of the arachnoid trabeculae (pink).

The sectioned views in Figure 38 and Figure 39 illustrate the largely uniform subarachnoid space achieved in segmentation, retaining some undulation of the gyri and sulci.

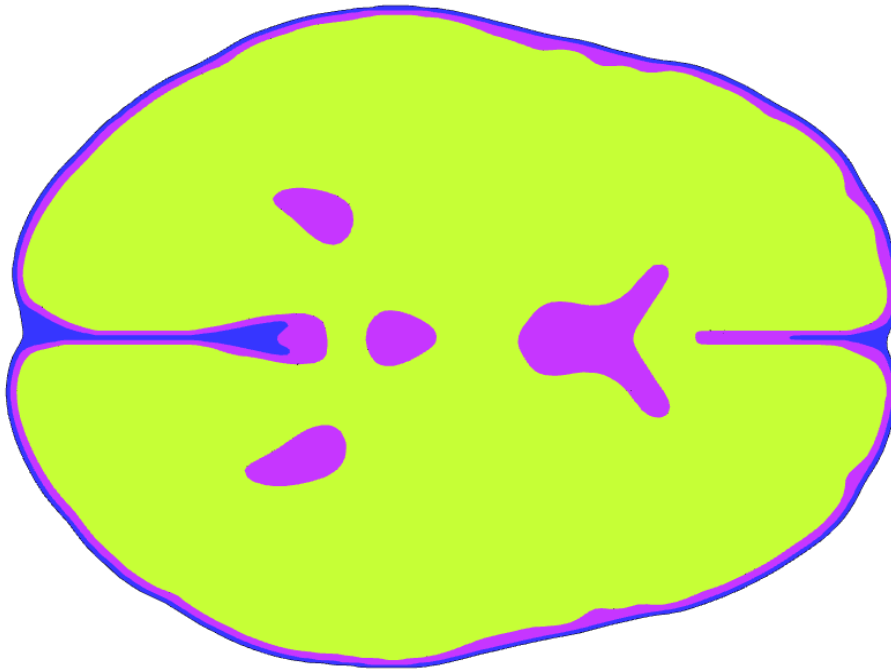


Figure 38 – Transverse section of the brain (green), CSF regions (purple) and dura mater (blue).

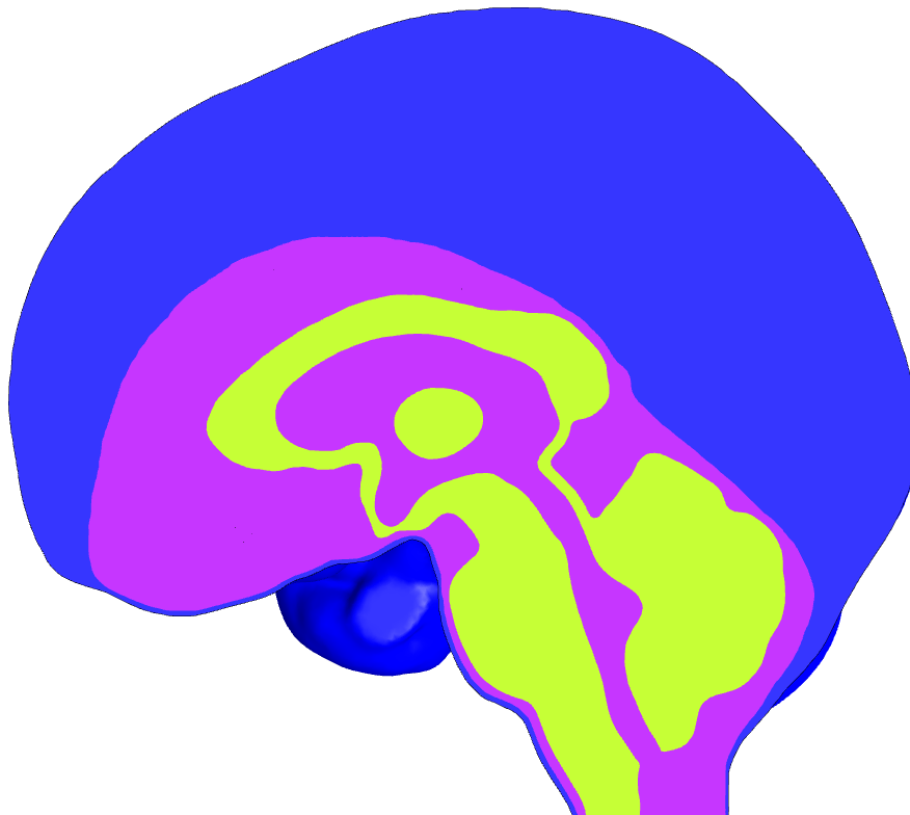


Figure 39 – Midsagittal section of the brain, CSF regions and dura mater.

Mesh Generation

The segmented geometry was meshed using the in-built meshing capabilities of ScanIP™. Free form linear tetrahedral elements were selected, with the meshed geometry exported to FEBio Preview in the form of an ‘.inp’ file. The geometry contained large regions of relatively thin material layers, such as the dura mater. Mesh density was high in these regions, even though the most coarse meshing settings were chosen. Automatic refinement was performed to remove low quality elements. Details of the final mesh are given in Table 4-1.

Table 4-1 – Number and type of elements in each regions of the final geometry.

Region	Elements	Element type
Brain	432,059	Tet4
CSF combined	367,751	Tet4
Dura/dural septa	376,309	Tet4
Pia mater	100,574	Tri3
Arachnoid trabeculae	37,838	Spring

An example of the mesh along a coronal section of the base geometry is show in Figure 40. This highlights the increased density in regions of high geometric detail, with more coarse meshing in the bulk of the brain tissue. This variation in element size was necessary to generate a model which was not prohibitively large to compute but also had enough detail to provide meaningful results and be computationally stable.

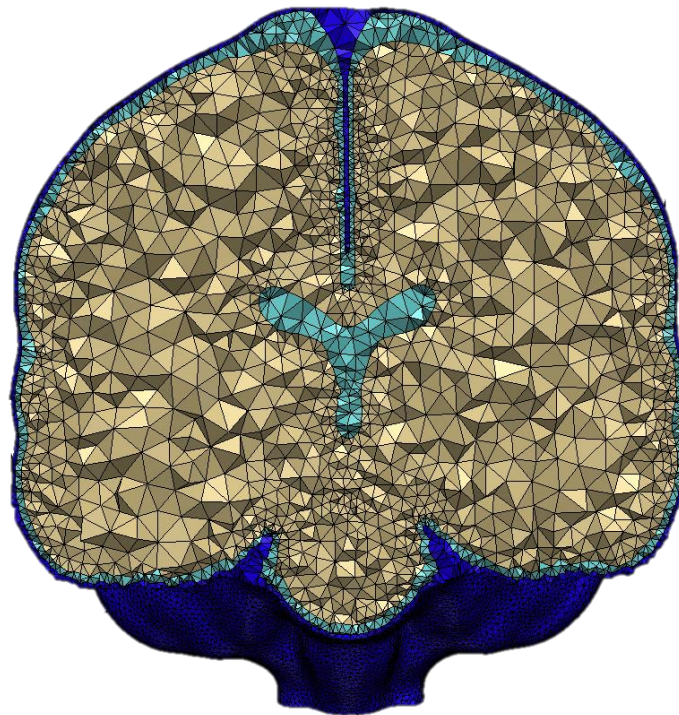


Figure 40 – Coronal section of the dura (dark blue), CSF region (light blue) and brain (beige) as used in the final model.

A traditional mesh sensitivity study was not feasible, given the already large number of elements and complexity in making the final model. However, considering the quality of the mesh used, it was expected that further refinement of the mesh would have made negligible impact on results.

The brain and ventricle surface areas were calculated in ScanIP™. The approximate surface area of the brain in contact with the PAC was found by subtracting the brain surface area with the ventricular surface area of 10,740 mm².

Table 4-2 – Geometric details of the final model.

Brain volume /mm ³	Brain surface area /mm ²	PAC volume /mm ³	PAC thickness /mm
1,581,100	101,170	209,100	2.1

The value of the average PAC thickness given in Table 4-2 should only be treated as approximate due to the method of calculation. For example, in the superior region of Figure 40 some anatomical variation in PAC thickness was retained.

The trabecular spring elements and pia mater were generated subsequently through manipulation of the ‘.feb’ text file using Matlab. Given the complexities of this process it was decided that one single model geometry would be used for this initial material study.

Boundary conditions

Constraints

As it is assumed that the skull remains rigid, and that the dura remains attached to the interior surface of the skull, the exterior surface of the dura was fixed in all dimensions at each node. The foramen magnum shown in Figure 41, is the only area where other materials form the exterior surface of the model. Here, the nodes were constrained such that no movement was possible in the direction normal to the face.

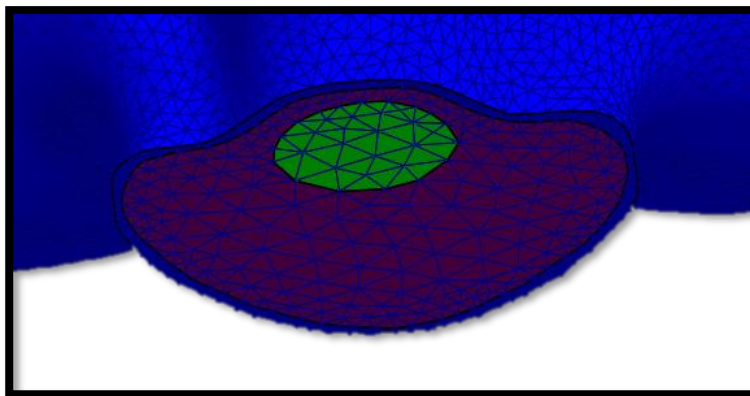


Figure 41 – Anteroinferior view of the foramen magnum.

Loads

One of the unique aspects of PBS investigation is the simple load case which exists with head reorientation. In this case, the only load change is the force generated on all structures within the intracranial cavity due to gravity in the prone and supine positions (Figure 42).

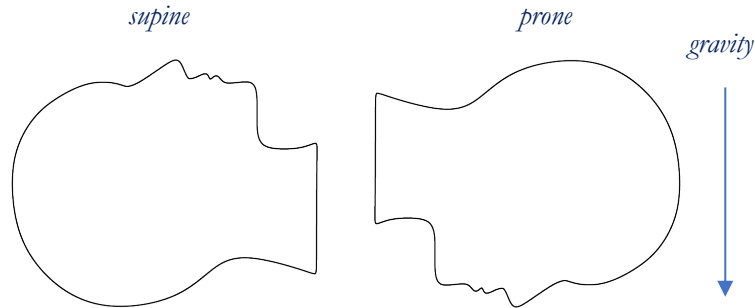


Figure 42 – Schematic representation of head repositioning with respect to gravity.

Within a body of fluid, a hydrostatic pressure head, P , is generated linearly with depth from the surface, h , according to Equation 37:

$$P = \rho gh + P_0 \quad 37$$

where ρ is the fluid density, P_0 is the atmospheric pressure and g is the gravitational constant. To maintain equilibrium within a body of fluid, this hydrostatic pressure acts equally in all directions at any single point. It should also be noted that aside from dynamic situations where geometry itself may introduce a hydrostatic pressure loss, the shape of the body does not influence the pressure generated by this fluid head. This relationship exists in all bulk materials. Within solids, this may be less apparent as the inherent rigidity of the material can redistribute stresses.

When this pressure acts upon the surface of an object submerged within the fluid, the variation in pressure over the height of the object generates a resultant force acting upwards upon the body. This is the basis of Archimedes' principle, which states that an object submerged in fluid experiences an upward buoyancy force equal to the weight of the fluid displaced. In the present case, the density of the brain is marginally higher than the surrounding CSF, at 1040 kg/m^3 and 1007 kg/m^3 respectively (22, 23). As such, the effective weight of the brain is considerably reduced.

If CSF is not represented in the model as a true fluid (92, 157), the pressure must be calculated and applied to the surface of the brain. In this study, the CSF is modelled using computational fluid dynamics and FSI functionality within FEBio and defined such that pressure generated within the fluid body acts upon the brain.

Within FEBio exists a 'body load' function. The defined constant represents an acceleration which generates an elemental force, equivalent to the product of the body load constant g ,

element volume and density. The sum of these forces over the body is analogous to its weight. As the simulation is assumed to be stationary relative to earth, the body load constant is equivalent to the gravitational constant and is defined as $g = 9.81 \text{ m/s}^2$.

Material representation

FEBio allows the use of a wide range of non-linear hyperelastic material representations, ideal for the modelling of soft tissues. The considerable body of knowledge concerning the mechanical testing and constitutive modelling of the intracranial soft tissues has been discussed in Chapter 3. The field is clearly advancing, with the development of constitutive models that capture increasingly complex material behaviour. It would be a significant achievement to develop a constitutive model capable of capturing all strain rates and types of loading, but this is not currently possible. As such the material characterisation carried out under one loading-boundary mode may not predict the material response of another.

During early stages of the associated human trial it was found that PBS occurred over a sufficiently short time frame that it could be considered complete, in the context of surgery. On this basis it was decided that the initial study would be based on time-independent, single phase representations of the soft tissues. It was not feasible to test every proposed constitutive model within the scope of this work. For structures like the arachnoid trabeculae, there is insufficient mechanical testing data to justify using a more complex non-linear representation. With this in mind, the material representations were selected based on information available in the literature and experience gained through early model development. Material parameters were varied over an estimated realistic range for the sensitivity analysis or fixed when well defined in the literature. A summary of the values used can be found in Table 4-3.

Table 4-3 – Constitutive model and parameter settings used for the parametric analysis. Where parameters were not varied only a high value is included.

Region	Constitutive model	Parameter	Low value	High value	Units	Source
Brain	Ogden (uncoupled)	Density	-	1,040	kg/m^3	(22)
		Bulk modulus k	5	1,000	kPa	(115)
		Coefficient c_1	1	3,000		(112, 118, 119)
		Coefficient m_1	-30	-1		(112, 118, 119)
CSF	Newtonian fluid	Density	-	1007	kg/m^3	(23)
		Bulk modulus	-	2.2	GPa	(191)
		Shear viscosity	-	*	$mPa \cdot s$	(192)
		Bulk viscosity	-	2	$mPa \cdot s$	(192)
Pia mater	Neo-Hookean	Density	-	-		
		Young's modulus	1	15,000,000	Pa	(143)
		Poisson's ratio	-	0.45		
Arachnoid trabeculae	See text	Spring constant	0.01	25	N/m	Preliminary testing
Dura mater	Linear elastic	Density	-	1000	kg/m^3	
		Young's modulus	-	1	MPa	(14)
		Poisson's ratio	0	0.45		

* The shear viscosity for the CSF was set at an arbitrarily low value, as the dynamic response is not desired, and the value does not affect the equilibrium response.

Brain

The brain has been studied considerably with a wide range of constitutive models reported. In recent work, Budday et al. (119) fit a simple one term Ogden model to mechanical testing results

of real human brain tissue. The formulation used in this and other similar works (112) was readily adaptable to the format used in FEBio making it a good choice.

CSF

As time dependence was intentionally not investigated, the shear viscosity was lowered by a factor of approximately 10 compared to realistic levels to save computational time reaching equilibrium. The bulk modulus was assumed to be equivalent to that of water.

Pia mater

The pia mater is the thin membrane which lies directly on the surface of the brain and is thought to offer important mechanical support. As strains were expected to be small and there is limited information in the literature, a complex non-linear model was not implemented. The range was defined based on the values given in Table 3-4.

Arachnoid trabeculae

It is assumed that the string-like arachnoid trabeculae offer no compressive stiffness. As such, the restorative response force F was defined according to Equation 38:

$$-F = \begin{cases} 0, & \Delta x \leq 0 \\ a\Delta x, & \Delta x > 0 \end{cases} \quad 38$$

where a is the spring constant and Δx is the scalar extension of the spring. In a similar sense to the pia mater, limited mechanical testing data meant little confidence was had in defining a non-linear tensile stiffness. Again, the impact of this is mitigated by what were expected to be relatively small strains.

Dura and dural septa

To reduce complexity in a region expected to undergo relatively small strains, a neo-Hookean material model was initially used for the dura mater. The values presented by de Kegel et al. (14) fell approximated within a range of $C_{10} = 0.05\text{-}3$ MPa, which when assuming incompressibility equates to a Youngs modulus of 0.3-1.8 MPa.

In preliminary testing with values in this range, peak displacements within the dura mater were found to be orders of magnitude less than in the rest of the model, leading to a negligible impact overall. To reduce computational time, the dura was defined to be a rigid body for the sensitivity analysis. For subsequent work where reorientation is not parallel to the falx cerebri this assumption was reassessed.

Material sensitivity study

GEM-SA was used to identify the optimum material parameters and understand output change to material property variation. The maximin Latin hypercube method was used to populate the initial parameter range effectively as defined in Table 4-3. A total of 60 unique combinations were generated. The values for these can be found in Appendix A. This number was chosen based on

previous experience and practicality in computing the models, as more FE input data leads to a better statistical model.

Computation

With the material sets determined, '.feb' files were generated with a custom Matlab script. As each model was to be run from 'neutral'-supine and 'neutral'-prone, a total of 120 models were generated, only differing by the respective body load. The control parameters used can be found in Appendix A. It should be noted that the majority of these were default settings. With the material definitions used, only CSF exhibits time-dependant properties. Preliminary testing over an arbitrary time period of 1 second showed the viscous properties of the fluid made an inconsequential impact to the overall result and this was therefore used moving forward.

Due to the large size and combined fluid/solid definitions, computation on a standard PC for 120 models would have taken many weeks or months. Instead, up to 15 models at a time were run simultaneously using the Advanced Research Computing at Cardiff University (ARCCA) Hawk supercomputer. This system contains a Linux cluster of 7000 cores of Intel Skylake Gold 6148 processors (2.4 GHz / 4.8 GB per core / 20 cores per processor).

Recap: Objectives

1. Understand the key factors involved in brain shift, and which should be considered in the FE model.
2. Develop a FE model incorporating key anatomical structures (which can also be used for the phantom model).
 - i. Upon studying the literature and through development of the model, it was determined that the subarachnoid space and arachnoid trabeculae play an important mechanical role in PBS.
 - ii. A finite element model incorporating state-of-the-art representations of these structures, along with a brain geometry, pia mater and dura mater conducive to physical modelling was developed.
3. Investigate the material sensitivity of brain shift and the mechanics of the process using human data and the FE model.
4. Predict a test-case of displacements in a clinically relevant region that could be used as a pre-operative adjustment.

Data analysis

All data processing was carried out in Matlab using custom processing scripts. Nodal displacement was generated automatically in text format for each FE model, with further geometric details parsed from the '.feb' file itself. Subject data was obtained and processed as part of the accompanying human analysis. A deformation field was generated from the prone and

supine images, and subsequently registered to the node space of the segmented MNI 152 geometry; the same as was used for FEA.

Some of the code used in this project, particularly in the generation of figures presented later, was adapted from the open source GIBBON toolbox (193).

Nodal displacement processing

Data points within the cerebellum were excluded due to clearly erroneous displacement resulting from poor MRI contrast in this region. For the remaining elements, representing the cerebrum, a volumetric weighting ratio W_n was first calculated for each element ($n=361031$), according to Equation 39:

$$W_n = Vol_n / Vol_{region} \quad 39$$

where Vol_n is the volume of each element and Vol_{region} is the total volume being considered, in this case the whole remaining brain. This was necessary to account for differences in regional elemental density. The displacement at the four nodes of each element were then averaged to give the elemental displacement vector $d_n = \begin{pmatrix} u_n \\ v_n \\ w_n \end{pmatrix}$, where u, v and w are the x, y and z components respectively. Each elemental vector was multiplied by the weighting ratio such that

$$D_n = W_n d_n \quad 40$$

and the orthogonal global displacement D_n was defined to be the sum of D_n in each axis. This represents the ‘average’ movement of the brain for each subject. These values are given later in Table 5-1.

Parametric study

For training of the statistical model within GEM-SA, a single input value was required to describe the likeness of the subject and FE data sets. To do this, Equation 41 was used to calculate a scalar error value D_{error} , referred to as the error magnitude (EM):

$$D_{error} = \sum_{i=1}^n \sqrt{\left(w_n(u_{n_{sub}} - u_{n_{FE}})\right)^2 + \left(w_n(v_{n_{sub}} - v_{n_{FE}})\right)^2 + \left(w_n(w_{n_{sub}} - w_{n_{FE}})\right)^2} \quad 41$$

This EM was calculated for each subject, with each FE generation. For clarity, a schematic representation of the meaning of the quantities D and D_{error} is given in Figure 43.

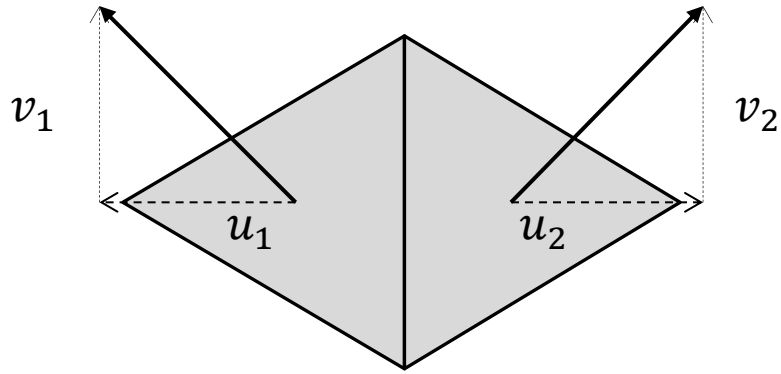


Figure 43 – Schematic of a two-element model, to aid the explanation of the displacement calculation methods used.

In this simplified 2D case, take $W_1, W_2 = 0.5$, $u_1 = -1$ and $u_2, v_1, v_2 = 1$ and the comparison displacement to be zero. Therefore, the global displacement, $\mathbf{D} = \begin{pmatrix} 0 \\ 1 \end{pmatrix}$, whilst according to Equation 41 the EM:

$$EM = D_{error} = \sqrt{(0.5(-1 - 0))^2 + (0.5(1 - 0))^2} + \sqrt{(0.5(-1 - 0))^2 + (0.5(1 - 0))^2} = 1.4$$

In essence, \mathbf{D} captures the general body movement, where opposite vectors can cancel and information is lost. On the contrary, D_{error} compares pointwise error across the whole body. As such, D_{error} is a more rigorous method of comparing subject and FE displacement fields and forms the basis of the material analysis.

The EM was calculated for each FE model, for each subject. This, paired with the material parameters defined for each model were inputted into GEM-SA for the material study.

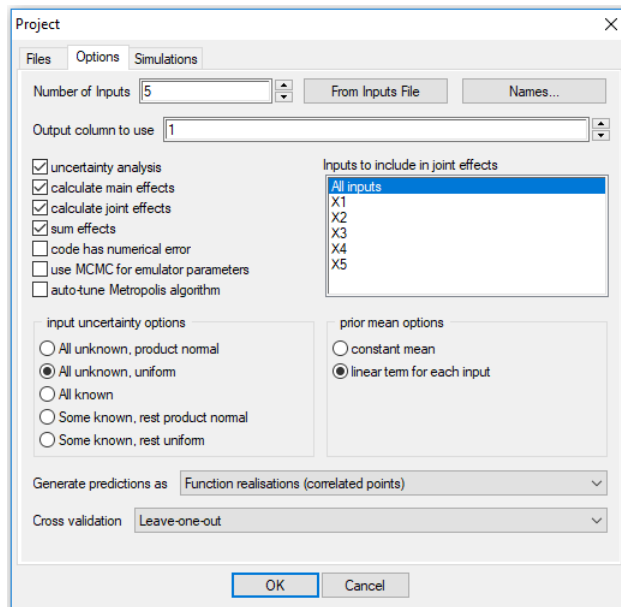


Figure 44 – Input display and settings used for initial sensitivity analysis in GEM-SA.

Figure 44 gives an example of the options selected within GEM-SA. The 5 inputs: x_1 , x_2 , x_3 , x_4 and x_5 , refer to the material parameters: the brain bulk modulus, brain c_1 coefficient, brain m_1 coefficient, pia Young's modulus and trabeculae spring constant, respectively. Due to the iterative nature of the process, further methodological details are given in the results section.

Surgical Prediction Test Case

Once final material parameters were identified, the model was used to generate predictions in positions which could not be measured as part of the human study but are seen in surgery. At this stage the aim was not to generate a full atlas, but to offer an initial estimate of what displacements might be likely in key positions relative to a supine imaging position. Figure 45 shows the six chosen orientations: 1) Supine 2) Semi-supine 3) Upright 4) Semi-prone 5) Prone 6) Lateral decubitus.

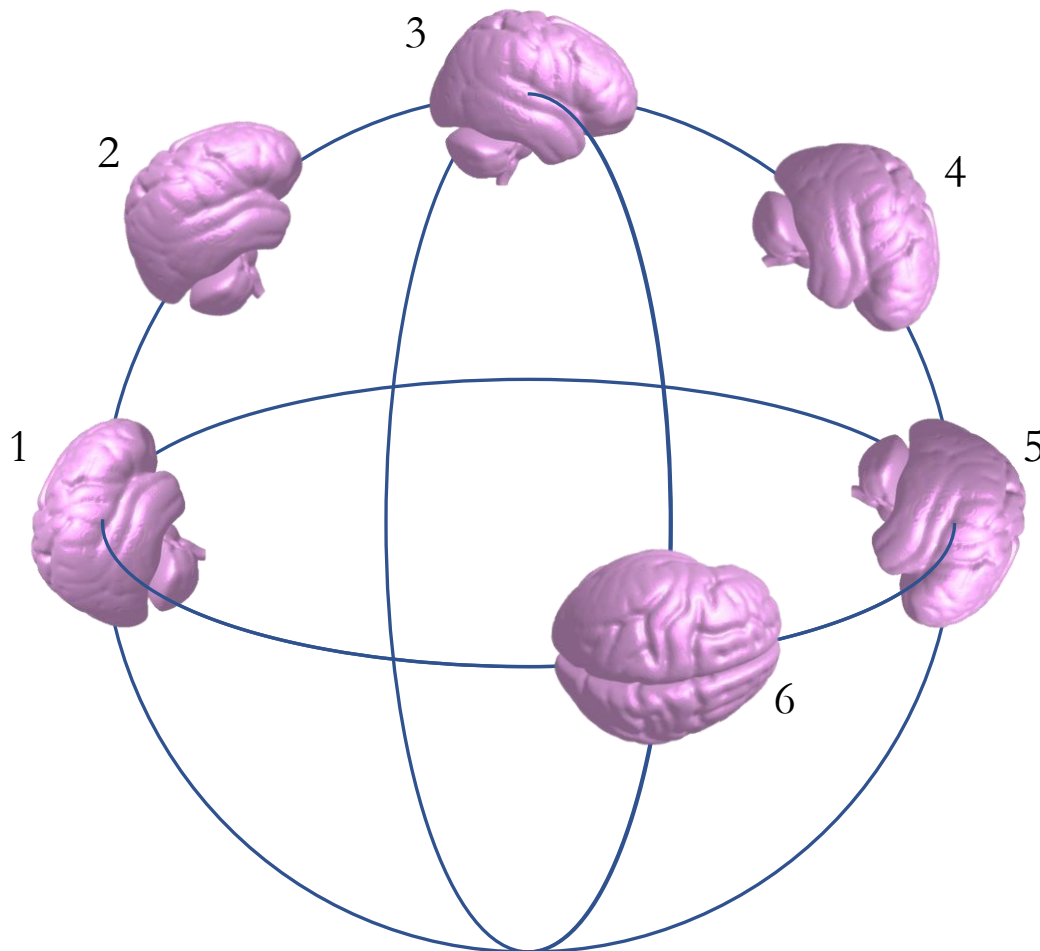


Figure 45 – Schematic of the 6 head orientations chosen to investigate the potential for PBS in surgery.

As with the initial prone-to-supine study, the model was left stationary in the FE space and the body load was adjusted to account for gravity in each position. Unlike the full sensitivity analysis, the dura layer was reintroduced in these final computations. This was to ensure that the

assumption the dura made a negligible impact in sagittal reorientation was valid and assess its role in lateral repositioning.

As this result is intended as proof of concept rather than to be used directly, one node in the region of the STN in the basal ganglia was chosen as an example. If required in future, extracting displacements from other regions within the brain would be trivial.

Chapter 5: Results

With the FE model developed and refined, each of the 60 parameter sets was computed with prone and supine loading. In this chapter, we report the results of the in-vivo testing in general terms but focus more on use of the full displacement field in the identification of material parameters. The iterative calibration process presented here utilised three sources of data: the prone-supine in-vivo testing, the computational model, and material analysis in GEM-SA. This is understood to be the first implementation of its kind in the literature. It will be shown that this method yielded remarkable results when compared to mechanical testing previously reported.

In-vivo measurement

Material parameter identification in soft tissues can be highly context dependant. Models run during the development of this project highlighted that some parameters of the material representations commonly used in the literature were unable to adequately capture PBS, supporting the use of human validation data obtained in the same loading regime. Early in the processing of the human data it became clear that poor tissue contrast in the cerebellum led to poor registration and clearly erroneous displacement fields. As a result, it was decided that the cerebellum would be excluded from this stage of analysis.

As an additional point of comparison, the EM was also calculated against an artificial displacement field of zero. This is now termed the zero-displacement error magnitude (ZDEM), which represents the total level of disorder in an uncorrected deformation field. It can be considered the baseline from which any improvement can be measured.

The global displacements and ZDEM are shown in Table 5-1, where positive X, Y and Z values represent right lateral, anterior and superior displacements respectively. As expected, the predominant displacement was in the gravitational axis. Averaging the individual results of the 3 subjects showed a global displacement magnitude of 0.22 ± 0.02 mm (mean \pm SD). This ZD yielded an average of 0.39 ± 0.02 mm, indicating a non-uniform displacement throughout the model.

Table 5-1 – Global displacements within the cerebrum of the initial training data subject group (n=3).

Subject	X disp. /mm	Y disp. /mm	Z disp. /mm	Magnitude /mm	ZDEM /mm
1	0.02	0.20	-0.05	0.20	0.38
2	0.01	0.26	-0.01	0.26	0.38
3	0.00	0.20	-0.05	0.20	0.41
Average	0.01 ± 0.01	0.22 ± 0.04	-0.04 ± 0.03	0.22 ± 0.03	0.39 ± 0.02

The displacement fields of each subject were also combined to form an average displacement field. In principle this should remove some noise from the data. As expected, the ZDEM was slightly reduced at 0.33 mm.

For illustration purposes, nodal displacements were extracted across a 10 mm region, highlighted in Figure 46, spanning the approximate widest point in the sagittal plane.

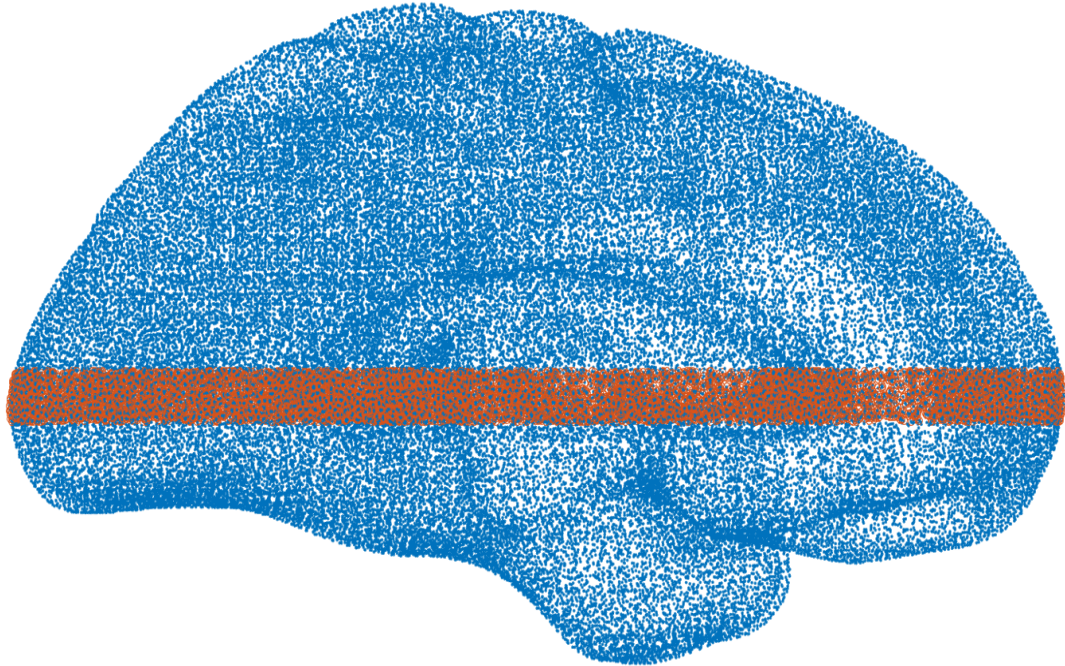


Figure 46 – Lateral view of the cerebral nodes, highlighting the region used to illustrate the subject displacement fields (orange).

Figure 47, Figure 48 and Figure 49 illustrate the trends reported in Table 5-1, showing nodal displacement across the brain. Displacement is generally concentrated in the deep structures of the brain with limited movement around the surface.

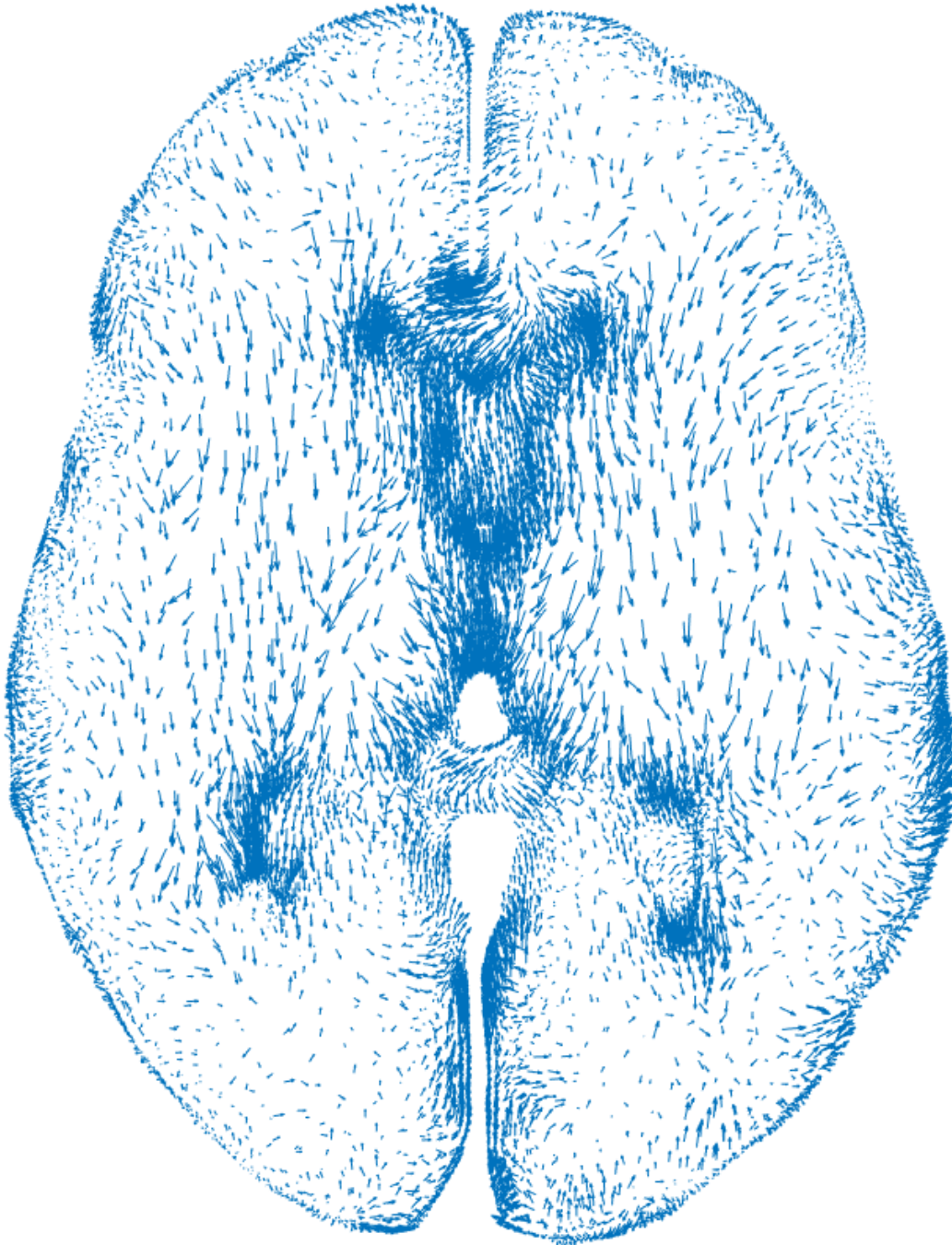


Figure 47 – Nodal displacement of subject 1 over the 10 mm transverse section. Displacement vectors have been scaled by a factor of 5 relative to the brain.

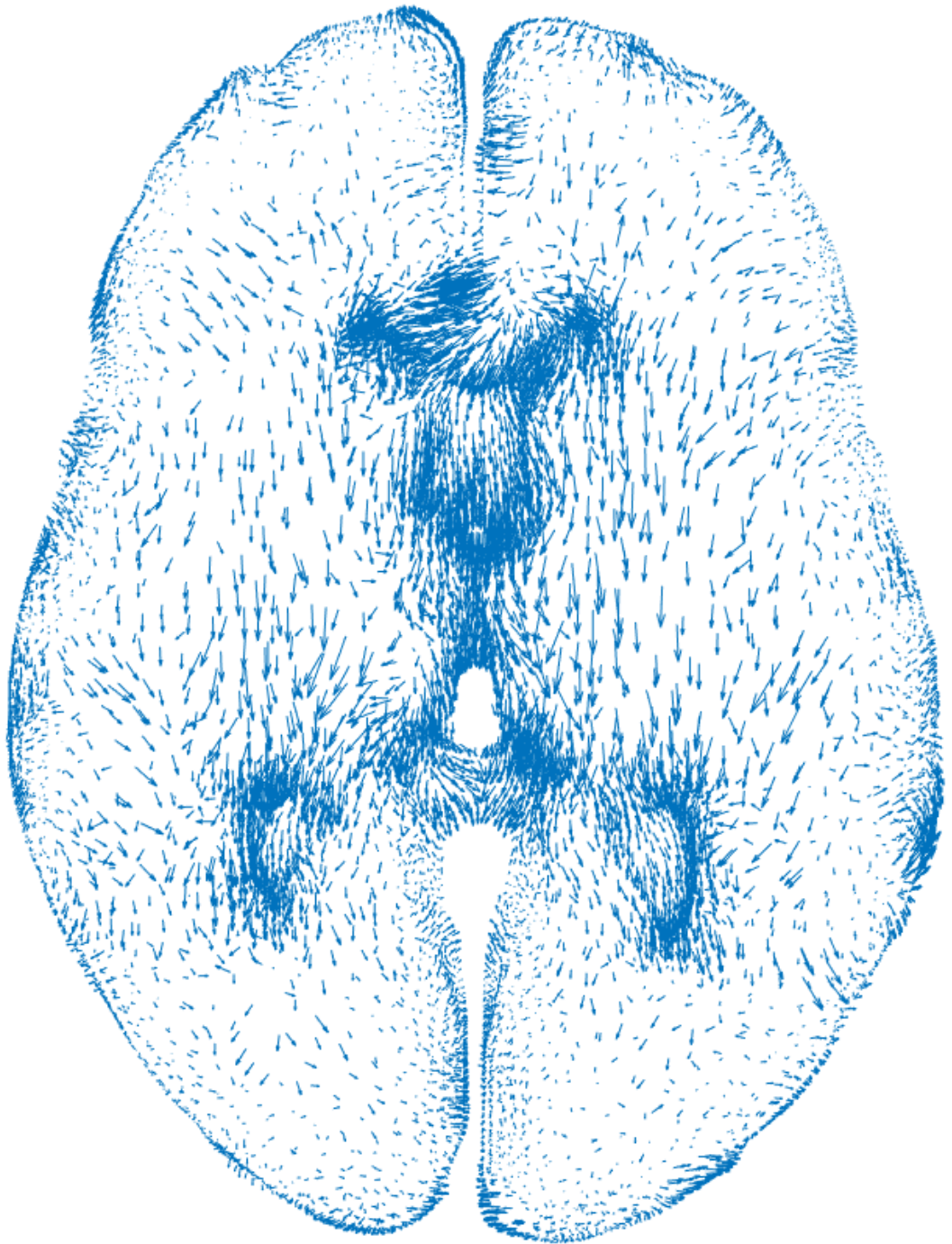


Figure 48 – Nodal displacement of subject 2 over the 10 mm transverse section. Displacement vectors have been scaled by a factor of 5 relative to the brain.

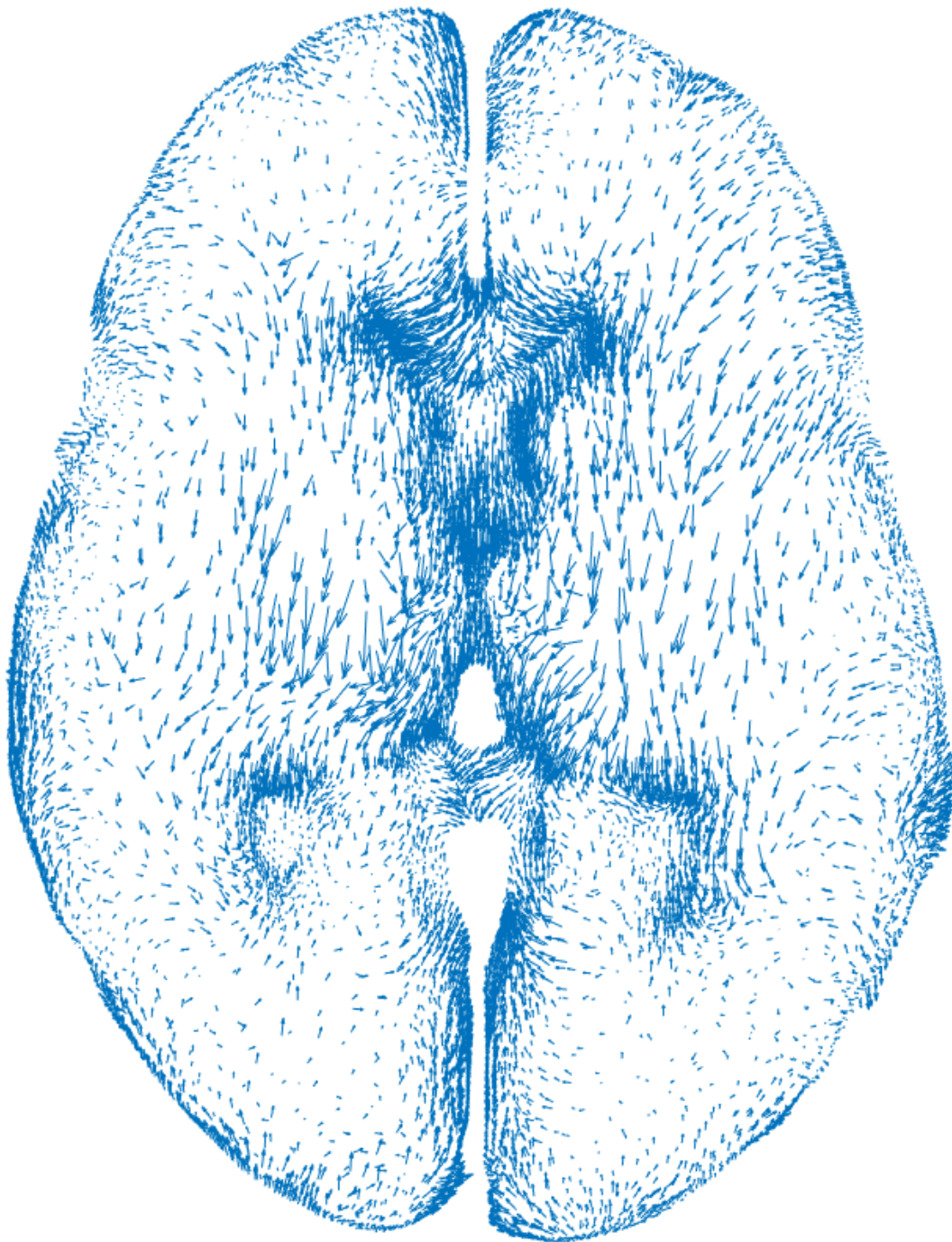


Figure 49 – Nodal displacement of subject 3 over the 10 mm transverse section. Displacement vectors have been scaled by a factor of 5 relative to the brain.

Regions displaying rapid changes in vector orientation are concentrated around the surface of the brain, potentially due to slight differences in boundary definition between the prone and supine images.

Material Parameter Identification

The subject data was next used in the direct validation of the FE model. This process required an iterative approach, as sequential processing steps were decided on consideration of the previous results. The following terms used frequently throughout this section are explained here for clarity:

1. Constitutive model parameters:
 - a. Brain – bulk modulus – k – x1.
 - b. Brain – shear modulus – c_1 – x2.
 - c. Brain – exponential coefficient – m_1 – x3.
 - d. Pia mater – Youngs modulus – E – x4.
 - e. PAC – spring constant – a – x5.
2. Terminology:
 - a. Calibration – Identification of material parameters most able to recreate a specific displacement field.
 - b. Error magnitude (EM) – Elemental sum of error between the FE and subject data field.
 - c. Emulator – The statistical model that is populated by known material parameters and the corresponding EM.
 - d. Main effect (ME) – Value generated for each material parameter, describing in this case how the EM varies with the value of said parameter at a mean value of each of the others. Generally presented graphically over the parameter range.
 - e. Simulation – Output generated by the emulator for a given set of untested material parameters. The output is not deterministic, but a normal distribution of the probability of the ME for a given parameter value.
 - f. Iteration – Process of training the emulator and simulating results with a refined range of material parameter values.

The occasional interchanging of material parameter names is largely due to practicality. The ‘shear modulus’ described here is actually the value of the c_1 material coefficient; two times the value that is defined as per linear theory, as explained on page 55. The term is used here to aid intuition of the results, with the true value recalculated when later comparing to the literature.

For reasons later discussed, two calibrations of model parameters were required. A summary of the process is as follows:

- Calibration 1 – Concerns the material parameter identification with the entire cerebrum and the three subject data sets individually.
 - The calibration consisted of three iterations:
 - 1 – Initial analysis of all parameters.
 - 2 – Reassessment of material sensitivity with intentionally reduced parameter ranges for the brain bulk modulus and spring constant.
 - 3 – Removed the m_1 coefficient and pia stiffness from analysis.
 - Final model 1 – Material parameters were identified, but comparison of the resulting displacement field to the subject data was unsatisfactory.
- Calibration 2 – Concerned the material parameter identification with cerebral elements near the surface removed and the subject data sets averaged together.
 - The calibration also consisted of three iterations:
 - 1 – Initial analysis of all parameters.
 - 2 – Reassessment of material sensitivity with intentionally reduced parameter range for the brain bulk modulus.
 - 3 – Considered only the bulk modulus and m_1 for final sensitivity.
 - Final model 2 – The identified material parameters lead to a significant improvement in error reduction across the subject data set.

The results of the sensitivity analysis are presented throughout this section in the form of ME plots. The ME plots which are generated represent error change in each variable assumed at the mean value of all other variables used. These ranges were based on some development testing, but largely what was available in the literature. The ME plots cannot be used to derive parameter values directly until the mean of each parameter is near the true value. However, all results are indicative of the potential variance which would be seen in the result displacement fields if parameters were poorly estimated. Variance, joint effect and total effect charts are also given. These were used in helping to define the iterative process, but as the parameter ranges were initially arbitrary, it should be remembered that latter values bear more significance to the true mechanical process at play. As such, only the most noteworthy initial results are highlighted in more detail.

Calibration 1

For calibration 1, individual processing was undertaken for each subject data set individually, considering all the material parameters.

Iteration 1

Of the 60 models generated, a total of 57 converged fully. The range of parameter values from the converged models is given in Table 5-2. It is notable that the initially defined range was considerably reduced in some cases due to this lack of convergence.

Table 5-2 – Minimum and maximum values of models that converged in the FE study.

Parameter	Minimum	Maximum
Brain bulk modulus /Pa	21,864	1,000,000
Brain c_1 coefficient /Pa	1	3000
Brain m_1 coefficient	-30	-1
Pia Youngs modulus /Pa	254,240	15,000,000
Spring constant /N/m	0.4336	25

ME plots were generated with these parameter sets and the corresponding EM, which was calculated in Matlab. These plots, shown in Figure 50, are the product of 100 simulations at 25 points spaced evenly over the range. A lower value indicates a lower EM and a greater alignment of the FE model and subject displacement field. Of the five parameters considered, the bulk modulus and spring constant exhibit minima within the range of variation for all subjects. These came at approximate values of: 185,000 Pa and 10.76 N/m, 185,000 Pa and 9.64 N/m and 185,000 Pa and 10.76 N/m, for subjects 1, 2 and 3, respectively. The results should not be interpreted as accurate to the number of significant figures presented as the value was one of 25 equally spaced points across the entire, very large, range.

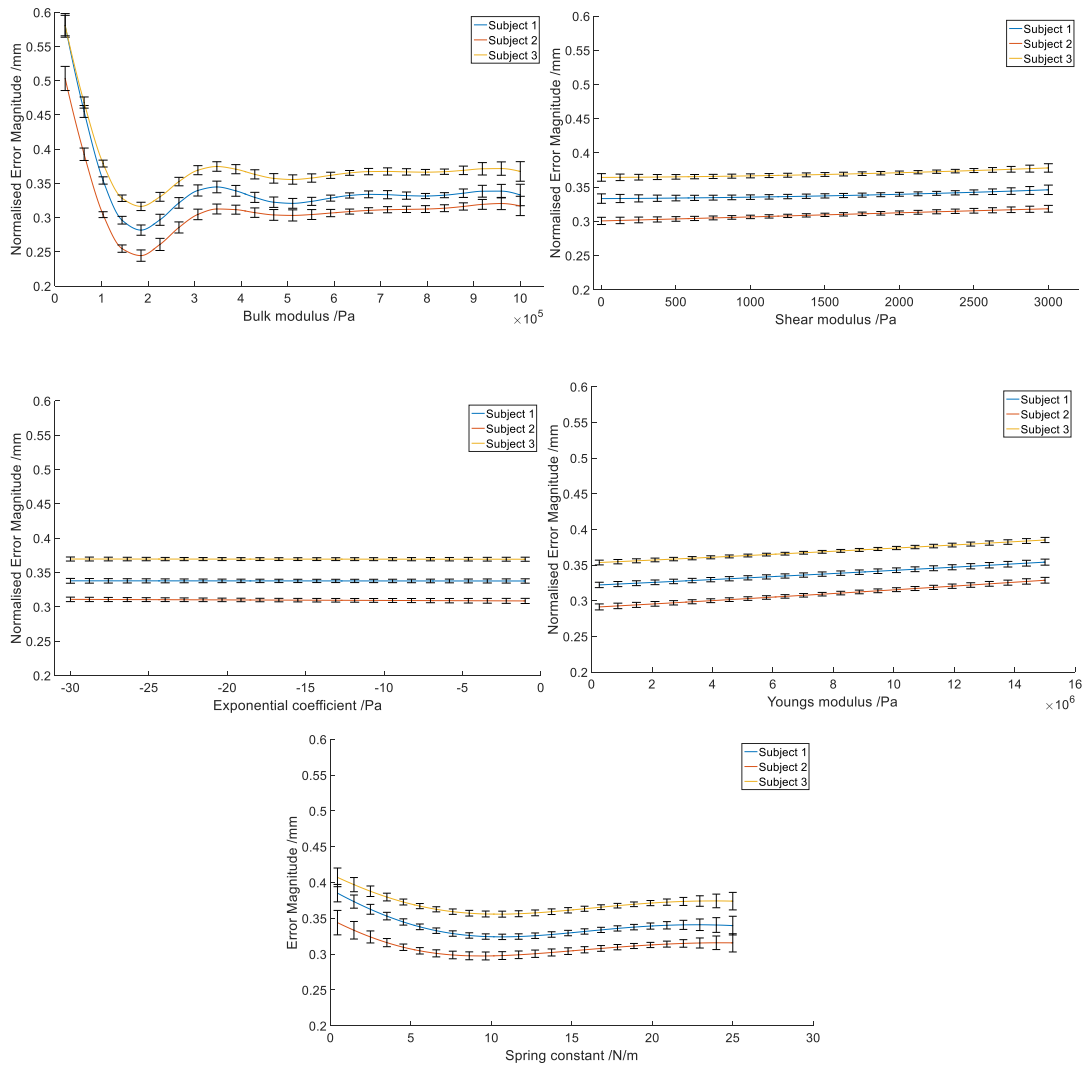


Figure 50 – Main effect plots for each material parameter and each subject, displaying the impact of parameter variation against the EM for each FE model. The ME plot for each parameter is generated at the average value of all other parameters. If joint effects exist between parameters, change of the range and therefore of the mean value can impact the main effect output. Error bars indicate one standard deviation in the normally distributed predictions, indicating statistical confidence in the prediction at each point.

The results of the sensitivity analysis are influenced by the defined parameter ranges. At this point these were somewhat arbitrary estimates based on the literature. With this in mind, Figure 51 demonstrates that the bulk modulus (x_1) is the driving factor, accounting for approximately 50% of the variance. The spring constant of the arachnoid trabeculae (x_5) follows, accounting for approximately 5% of variance, and stiffness of the pia mater (x_4) next with approximately 3%. The data variance resulting from the Ogden parameters c_1 (x_2) and m_1 (x_3) was effectively negligible compared to the others at this stage.

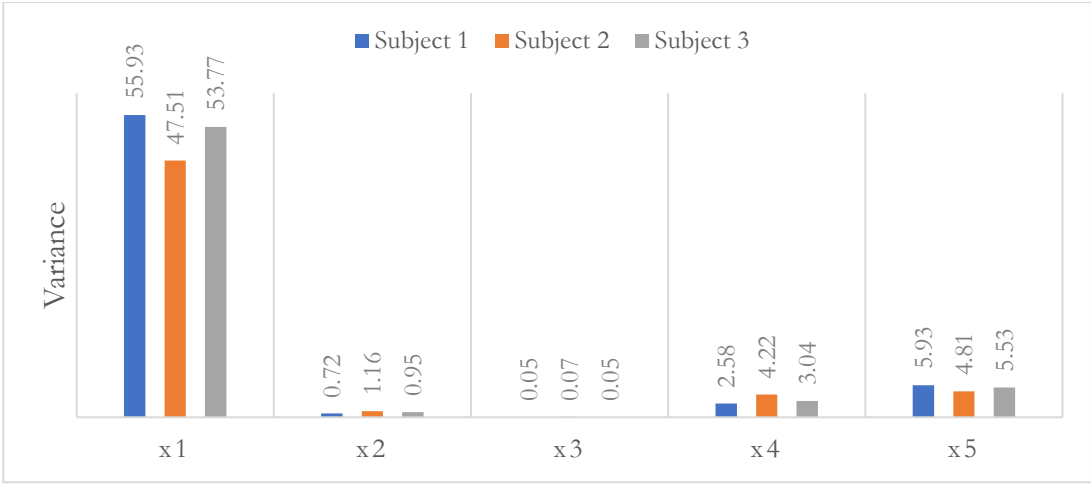


Figure 51 – Percentage variance of the main effect data for each material parameter and each test subject. The variance not reaching a total of 100% indicates that other sources of variance in the data exists outside the 5 material parameters.

Figure 52 shows that the most significant joint effect was with x1 and x5. It is also notable that contrary to the variance, x2 showed a minor contribution to joint effects, predominantly with x1. This suggests that alone x2 has little impact on the output but becomes more important when other parameters are within certain ranges. It will be shown later that strains throughout the brain in PBS are small. This explains the finding that the impact of x3 is almost negligible across all measures, as it functions to scale the non-linearity of the strain energy density function at larger strains.

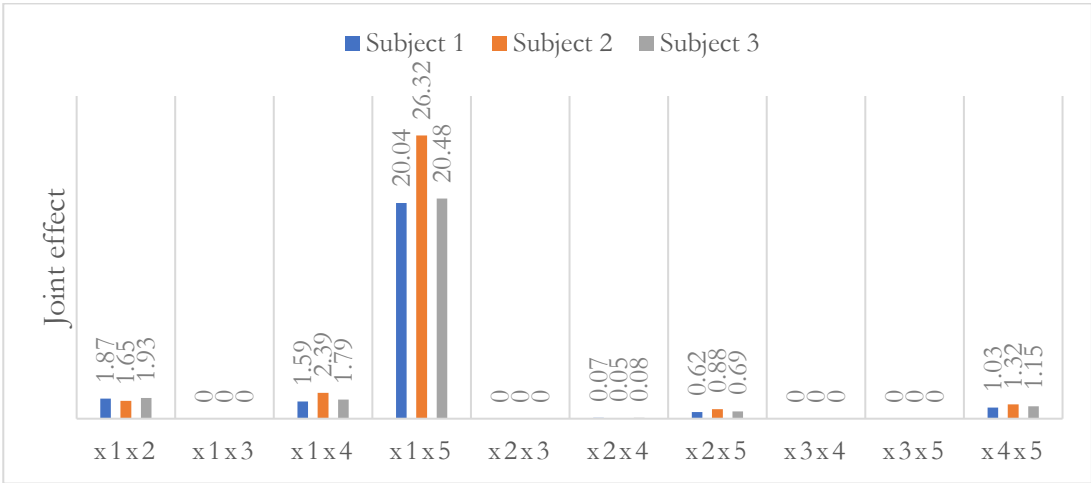


Figure 52 – Joint effect for each material parameter and each test subject. Total effect values include joint effects between variables - as such total effect can be counted twice and the patient total may be greater than 100.

The combined variance and joint effects for each parameter are displayed as the total effect shown in Figure 53. As the bulk modulus (x1) has a total effect of almost 90%, it is apparent that attributing an arbitrary value has a significant impact on the result of the model.

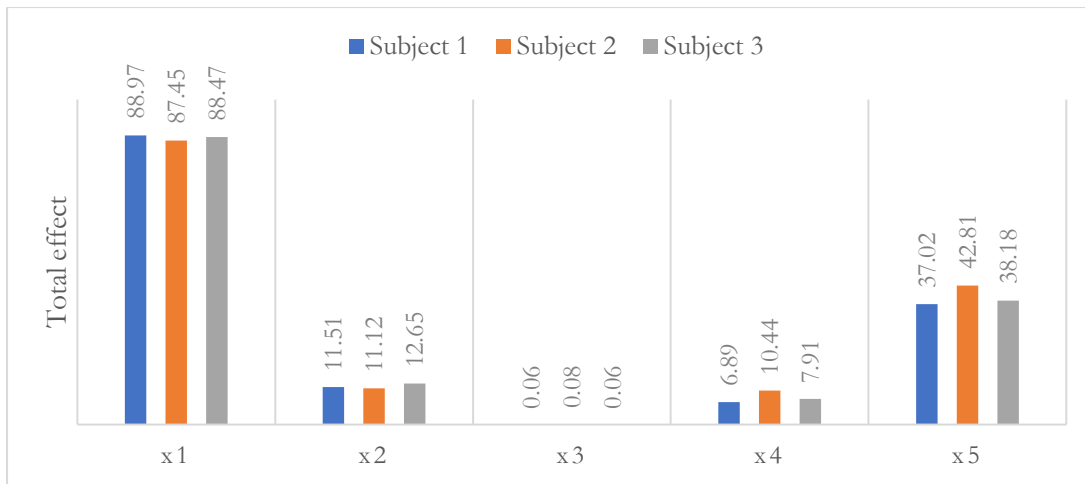


Figure 53 – Total effect (accounting for variance and joint effects) - between each of the material parameters for each test subject.

Finally, intrasubject variability, for each parameter, across each measure, was low. This suggests similar displacement patterns between subjects, dominated by similar mechanics of motion.

Iteration 2

Once the initial 57 parameter sets were used to train the statistical emulator in GEM-SA, an additional 1000 parameter sets were randomly generated in Matlab within refined ranges. As minima appeared in the main effect plots for the bulk modulus and spring constant, the new parameter sets for these were defined to contain values within a range of +/- 20% from the minima values found.

For the remaining parameters, the range was kept as the initial parameter set. The GEM-SA emulator was then used to run simulations for each of these sets, predicting the value which would have been generated as if they had been run in FEBio.

From the 1000 new parameters and simulated error value sets, the 200 with the lowest error values were found and inputted back into GEM-SA for sensitivity analysis and to retrain the emulator over a range closer to the expected value.

The range of input parameters from 1000 generations, and the 200 parameter sets which yielded the lowest EM in the simulation are given in Table 5-3. Notably, the brain coefficient c_1 showed a narrowing of the total range with this methodology. This suggests that this parameter may be more influential when the others (namely the bulk modulus and spring constant) are limited to a more realistic range.

Table 5-3 – Material parameters used in the first two iterations of processing. The minimum and maximum parameter values for iteration 1 are as presented in Table 5-2. Here the parameter value which yielded the minimum EM is included. Iteration 2 – 1000 refers to the range over which the 1000 prediction sets were generated. Iteration 2 – 200 refers to the range found in the parameter sets which predicted the lowest EMs. Minima values in italics indicate this value came at one extreme of the initially defined range. Grey lines indicate values from the previous iteration.

Parameter	Subject	Iteration	Minimum	Minima	Maximum
Brain bulk modulus /Pa	1,2,3	1	21,900	185,000	1,000,000
	1,2,3	2 – 1000	148,000	-	222,000
	1	2 – 200	153,000	-	220,000
	2	2 – 200	149,000	-	221,000
	3	2 – 200	153,000	-	220,000
Brain c_1 coefficient /Pa	1,2,3	1	1	<i>1</i>	3,000
	1,2,3	2 – 1000	1	-	3,000
	1	2 – 200	354	-	2,950
	2	2 – 200	15.9	-	2,990
	3	2 – 200	241	-	2,950
Brain m_1 coefficient	1,2,3	1	-30	<i>-1</i>	-1
	1,2,3	2 - 1000	-30.0	-	-1
	1	2 – 200	-29.9	-	-1.15
	2	2 – 200	-29.9	-	-1.06
	3	2 – 200	-30	-	-1.15
Pia Youngs modulus /Pa	1,2,3	1	254,000	<i>254,000</i>	15,000,000
	1,2,3	2 – 1000	254,000	-	15,000,000
	1	2 – 200	254,000	-	6,720,000
	2	2 – 200	277,000	-	5,100,000
	3	2 – 200	252,000	-	6,720,000
Spring constant /N/m	1,3	1	0.434	10.76	25
	2	1	0.434	9.64	25
	1,3	2 – 1000	8.53	-	12.8
	2	2 – 1000	7.72	-	11.6
	1	2 – 200	8.51	-	12.7
	2	2 – 200	7.84	-	11.5
	3	2 – 200	8.51	-	12.7

Main effect plots were regenerated using the simulation results of iteration 2. This time the ‘code has numerical error’ option was selected, as predicted values are the mean of 100 normally distributed simulations and therefore may not be perfectly deterministic. Figure 54 shows the

new main effect plots. With the mean value of the bulk modulus and spring constant now much closer to what is likely to be the optimum value, the result is considerably more sensitive to the shear modulus, which now displays a minima. The Young's modulus for the pia still does not display a minima, indicating the optimum value falls outside of the range of expected values.

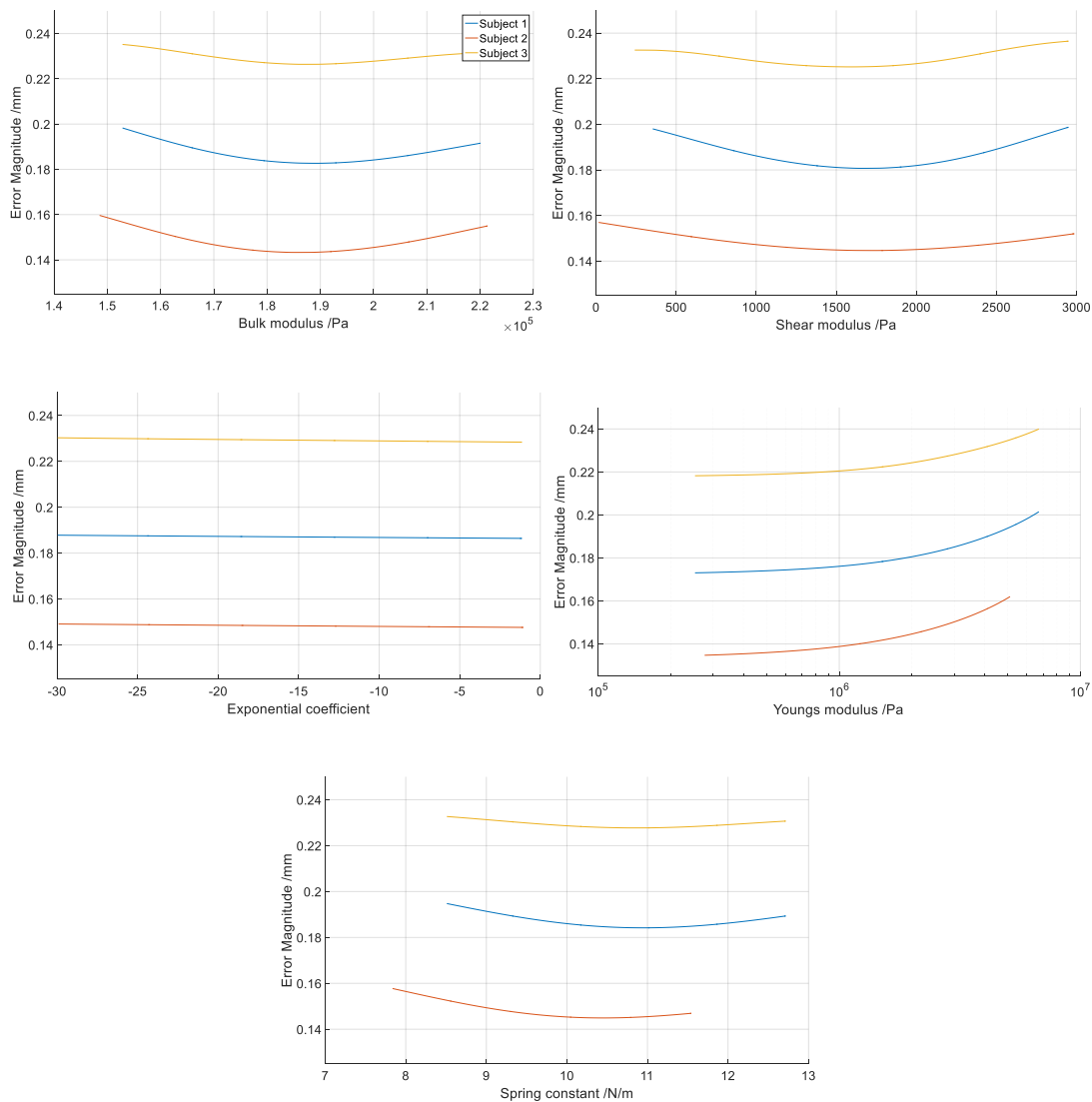


Figure 54 – Main effect plots generated from the 200 parameter sets which yielded the lowest error values of the 1000 generated with the simulator. With the range significantly reduced for the bulk modulus and spring constant, the shear modulus now exhibits a minima within the plot range. The Young's modulus was plotted on a logarithmic axis due to the large range of values which remained. Error bars were removed for clarity.

When considering the variance plots (Figure 55), the range of variation for x4 was still large, leading to a high degree of total effect. However, the low joint effects (Figure 56) suggest that the value chosen for x4 will have limited impact on the value at which the minimum EM occurs for the other variables. The main effect plot also flattens considerably around the expected value range according to the literature, suggesting a minima may not be significantly outside the range. Once again, x3 had almost no impact in any measure, the lowest error was found at the least

negative values used, -1. The most notable joint effects were found between x2 and x5, potentially suggesting that the stiffness of the brain and arachnoid trabeculae had more significant interactions now the bulk modulus was at a more realistic level. That said, joint effects were lower than the previous iteration. The total effect Figure 57 results broadly mirrored the variance, although contained an intriguing reduction in significance for subject 2, x2.

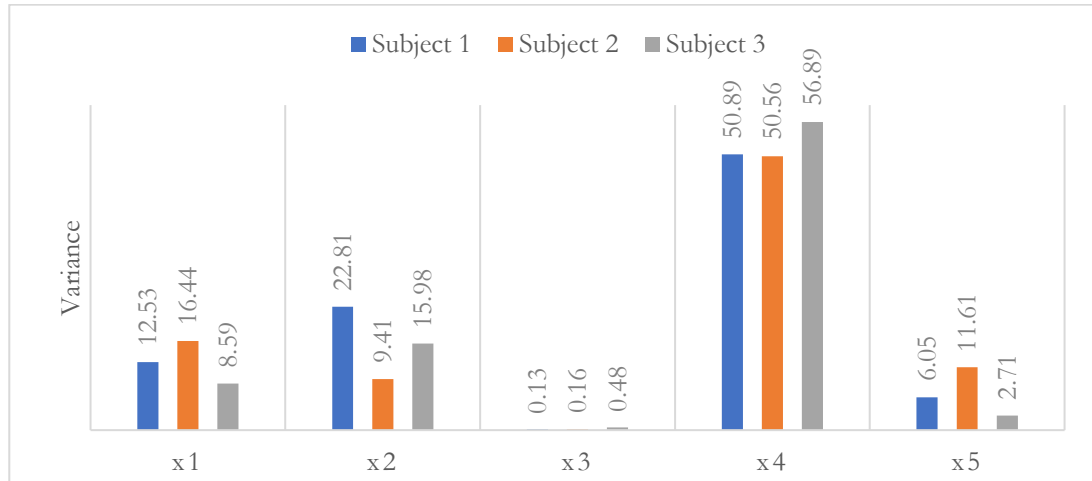


Figure 55 – Variance results for the 2nd iteration. The parameter x4 now yielded a higher variance than the other variables for every subject, however the range of values used was still comparatively large.

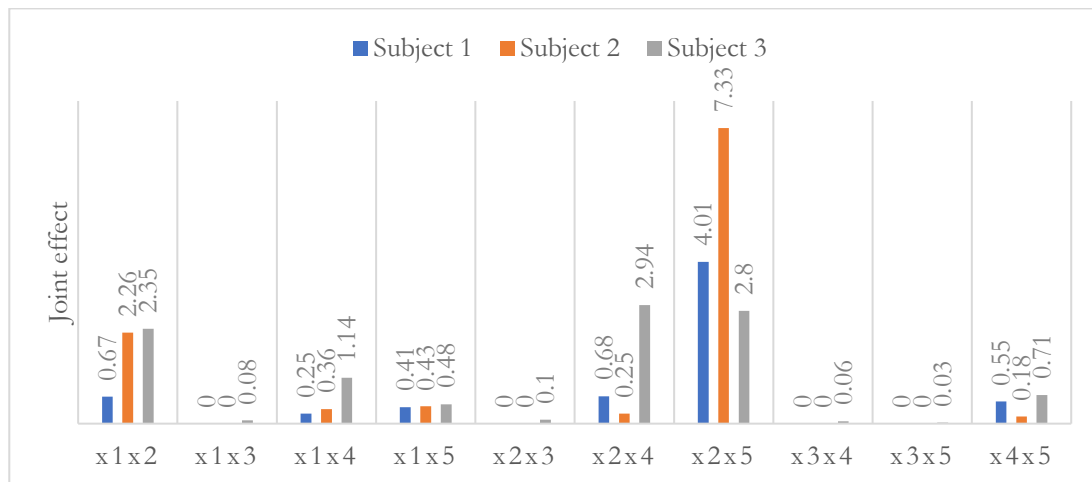


Figure 56 – Joint effect results for the 2nd iteration. This time, the highest joint effects are seen with x2. Conversely to the variance, x4 has low joint effects with all variables, including x2.

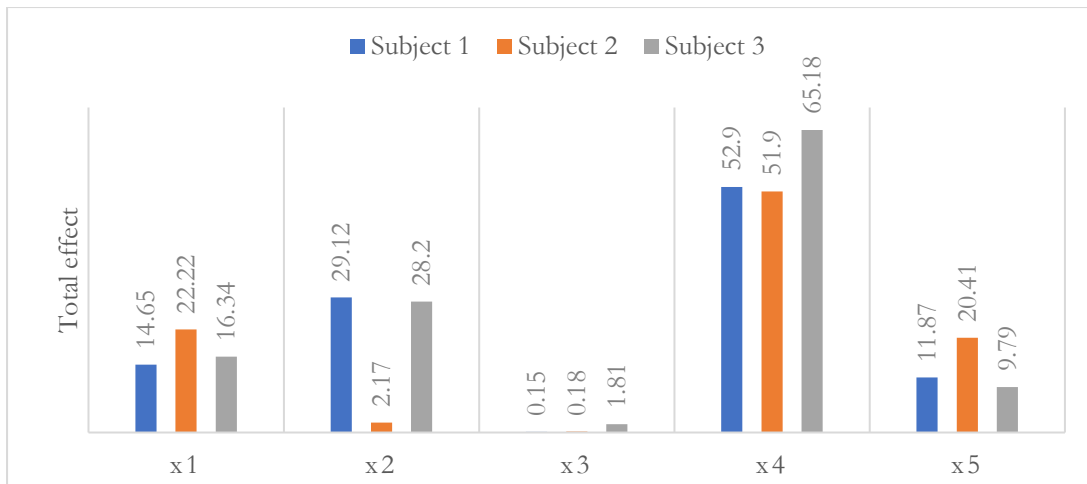


Figure 57 – Total effect results for the 2nd iteration. On average x4 still shows the greatest total effect.

Iteration 3

With the 2nd iteration using narrowed parameter ranges for the bulk modulus and spring stiffness, the shear modulus became more significant overall and an initial value was identified. Once again, the exponential coefficient and Young's modulus did not exhibit minima within the range of values defined. Moving forward, they were set at the range limits of -10 and 254,000 Pa respectively for the remainder of testing.

For the three remaining parameters, the bulk modulus, shear modulus and spring constant, three new parameter sets were made. In each case, one parameter was fixed at the minima value from the last set of main effect plots, whilst the others were generated as to evenly populate a 2-dimensional grid over the +/- 20% range from the minima found previously. The 200 best results from the first iteration were now used to train the statistical emulator in GEM-SA and predict the outputs for the new parameter sets.

Table 5-4 gives the minima values from iteration 2, which were used to define the final 2-dimensional distributions used to generate surface plots. The surface plots for each subject follow. As the parameter ranges are a proportion of the value, the shape of the surface indicates true material sensitivity.

Table 5-4 – Updated parameter values, included the minima from iteration two and the finalised ranges for iteration 3.

Parameter	Subject	Iteration	Minimum	Minima	Maximum
Brain bulk modulus /Pa	1,2,3	1	21,900	185,000	1,000,000
	1,2,3	2 – 1000	148,000	-	222,000
	1	2 – 200	153,000	189,000	220,000
	2	2 – 200	149,000	185,000	221,000
	3	2 – 200	153,000	186,000	220,000
	1	3	151,000	-	227,000
	2	3	148,000	-	222,000
	3	3	149,000	-	224,000
Brain c_1 coefficient /Pa	1,2,3	1	1	-	3,000
	1,2,3	2 – 1000	1	-	3,000
	1	2 – 200	354	1,650	2,950
	2	2 – 200	15.9	1,750	2,990
	3	2 – 200	241	1,600	2,950
	1	3	1,280	-	1,910
	2	3	1,400	-	2,100
	3	3	1,320	-	1,980
Brain m_1 coefficient	1,2,3	3	-1		
Pia Young's modulus /Pa	1,2,3	3	254,000		
Spring constant /N/m	1,3	1	0.434	10.76	25
	2	1	0.434	9.64	25
	1,3	2 – 1000	8.53	-	12.8
	2	2 – 1000	7.72	-	11.6
	1	2 – 200	8.51	11.0	12.7
	2	2 – 200	7.84	10.5	11.5
	3	2 – 200	8.51	10.8	12.7
	1	3	8.77	-	13.1
	2	3	8.37	-	12.6
	3	3	8.63	-	12.9

The surface plots shown in Figure 58 depict a trough, where the bulk modulus is considerably steeper sided than the shear modulus. This suggests that the error value is more sensitive to change in bulk modulus as a percentage change from the mean value. This feature is also found

in Figure 60, again with the shear modulus being the least influential of the two parameters. In contrast Figure 59, which plots bulk modulus against spring constant depicts more even sensitivity to the two variables.

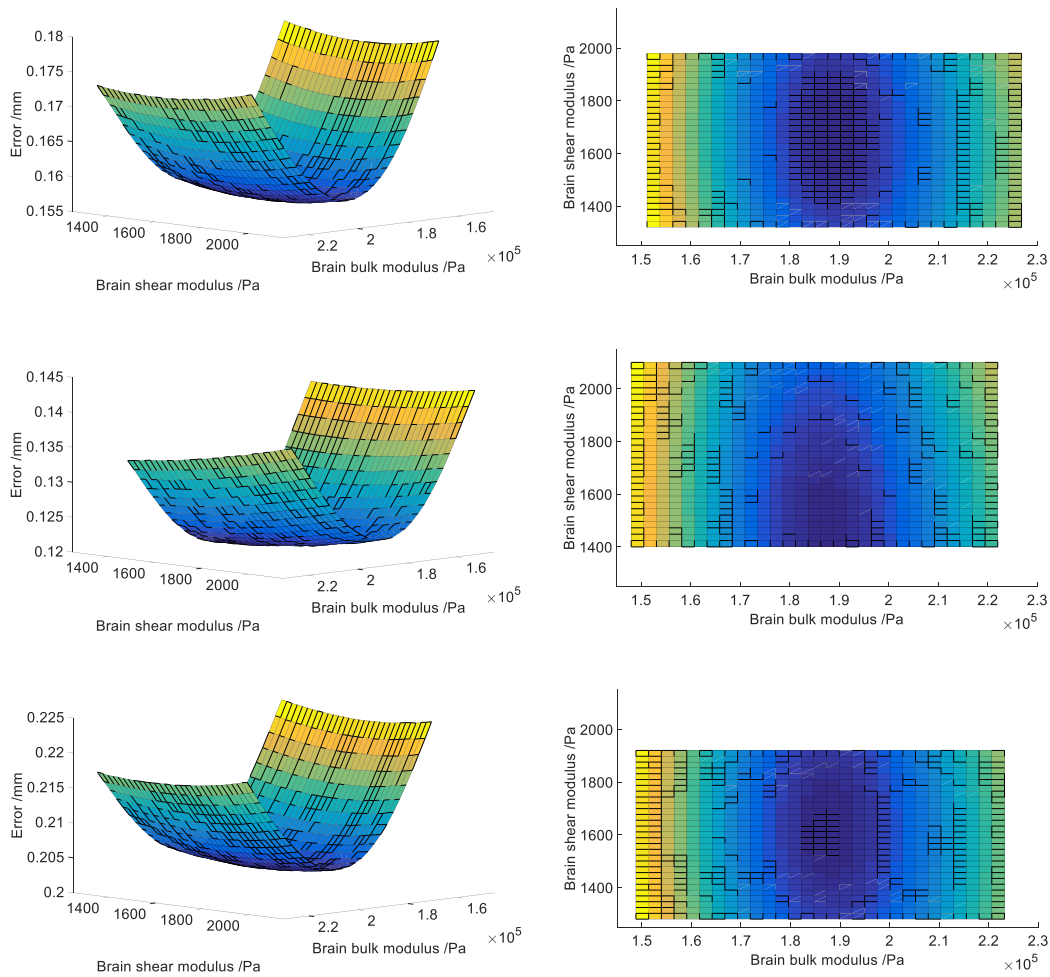


Figure 58 – Surface plots showing the EM change resulting from variation of the bulk modulus and shear modulus over the ranges defined in Table 5-4 for subjects 1, 2 and 3 [top, middle and bottom respectively]. The parameter range shown was fixed for all subjects for ease of comparison.

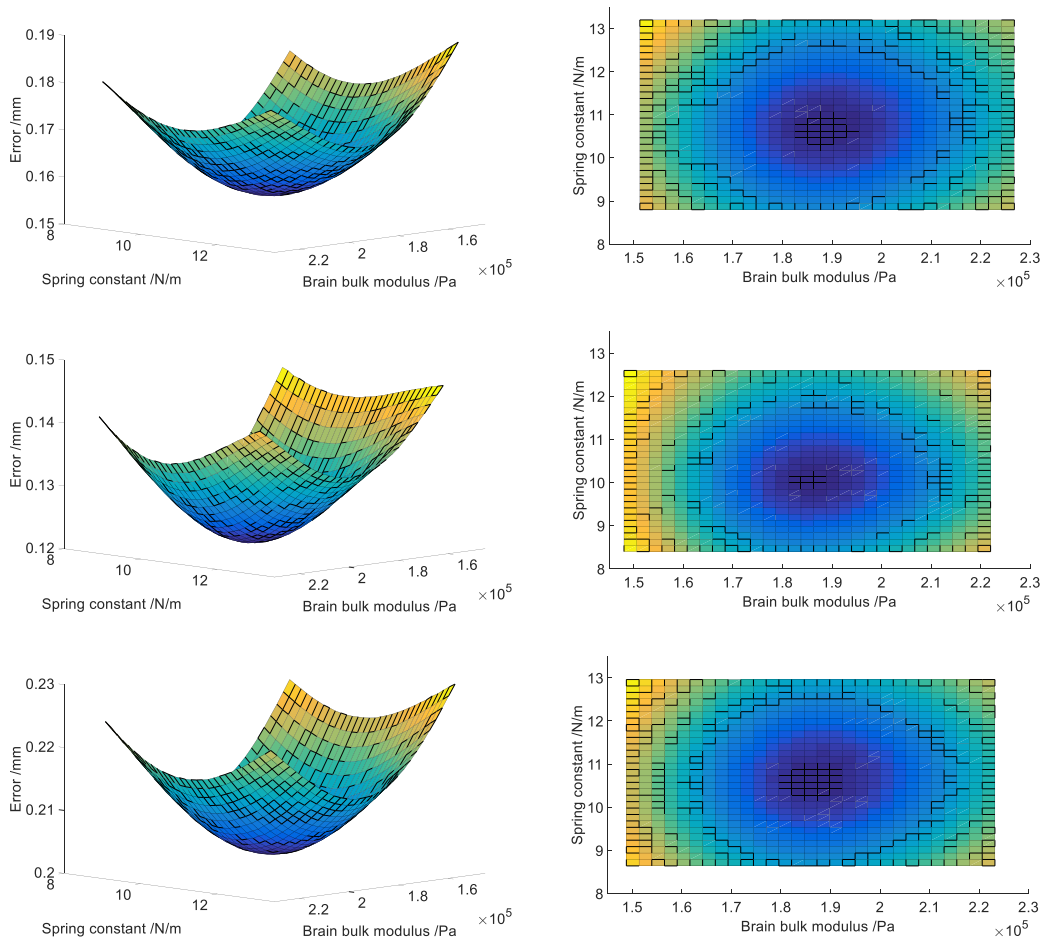


Figure 59 – Surface plots showing the EM change resulting from variation of the bulk modulus and spring constant over the ranges defined in Table 5-4 for subjects 1, 2 and 3 [top, middle and bottom respectively]. The parameter range shown was fixed for all subjects for ease of comparison.

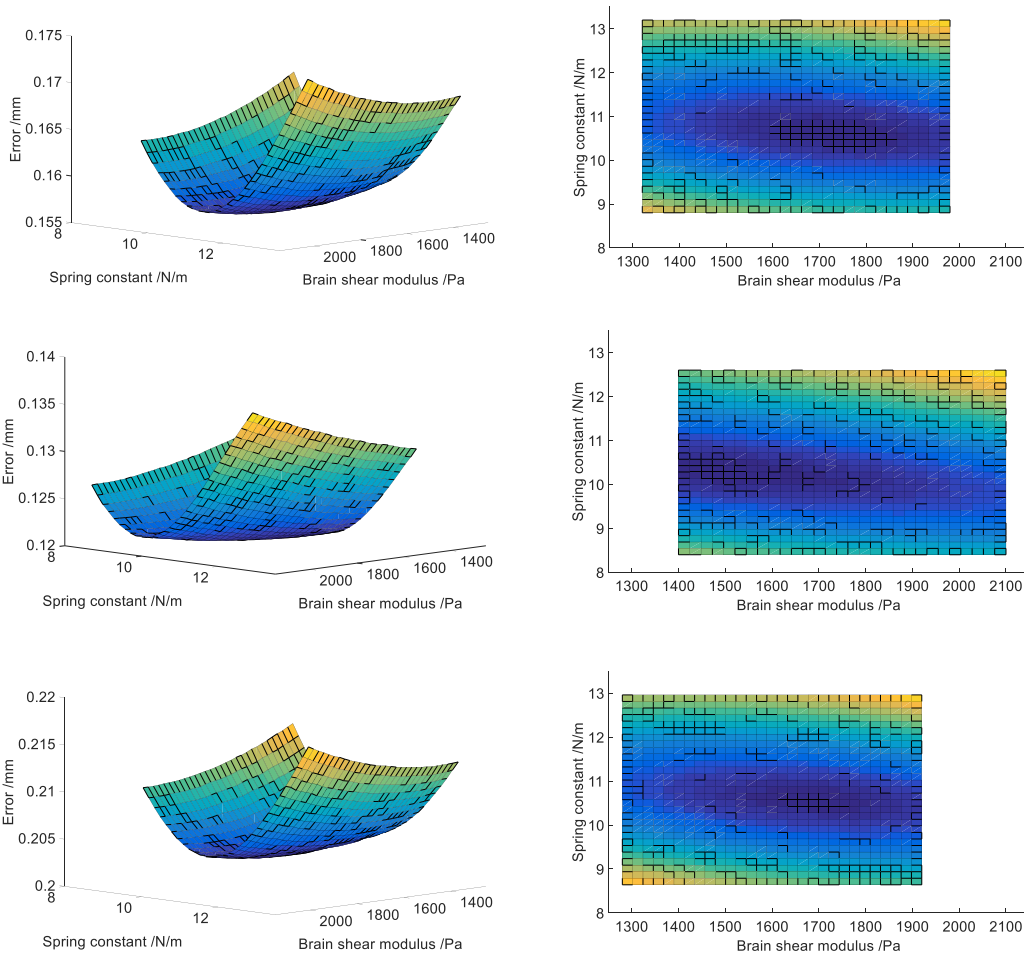


Figure 60 – Surface plots showing the EM change resulting from variation of the shear modulus and spring constant over the ranges defined in Table 5-4 for subjects 1, 2 and 3 [top, middle and bottom respectively]. The parameter range was fixed for all subjects for ease of comparison.

The shape of the surfaces shown above indicate some intersubject variability, but have a largely similar shape, showing similar sensitivity trends. The minimum values obtained indicate the optimum value for each subject. When compared to the previous estimates, these values, given in Table 5-5, indicate the improvement gained by this additional iteration. In each case, the refinement induced the least change in x_1 , and the most in x_2 , suggesting these parameters are the most and least sensitive respectively.

Table 5-5 – Parameter values found from the surface plots, generated with one parameter held (grey) whilst the remaining two were varied. The percentage values indicate the similarity of the refined 2D simulations to the initial estimate (grey) which was used when not being varied.

Subject 1							
	Error	x1	x2	x5	x1	x2	x5
x1x2	0.16	188,000	1,660	11.0	99%	101%	100%
x1x5	0.16	188,000	1,650	10.6	99%	100%	97%
x2x5	0.16	189,000	1,710	10.6	100%	104%	97%
Subject 2							
x1x2	0.12	186,000	1,400	10.5	101%	80%	100%
x1x5	0.12	186,000	1,750	10.0	101%	100%	95%
x2x5	0.12	185,000	1,500	10.1	100%	86%	97%
Subject 3							
x1x2	0.20	187,000	1,590	10.8	101%	99%	100%
x1x5	0.20	187,000	1,600	10.6	101%	100%	98%
x2x5	0.20	186,000	1,630	10.6	100%	102%	98%

Once the final values were found they were used to test the improvement gained by FE predicted correction to the subject data. Due to the lack of subject data and the similarity between results, leave-one-out style testing of the final parameters was not attempted. Whilst averaging of non-linear constitutive model parameters is not mathematically allowed, it is done here with the following justifications:

- The strain is small and as such occupies a relatively linear region of the stress strain curve.
- The exponential stiffening coefficient m_1 from which these values have been calculated has been fixed and is at a value where the effect is minimal.
- The values are close enough together that a more methodologically rigorous ‘average’ would be negligibly different than a simple average value.

These mean values over all subjects for each parameter are summarised in Table 5-6 below.

Table 5-6 – Mean parameter values found in calibration 1.

Parameter	Final value
Bulk modulus /Pa	187,000
‘Shear modulus’ /Pa	1,580
Exponential coefficient	-10
Pia Young’s modulus /Pa	254,000
Spring constant /N/m	10.4

Final model 1

The FE model was recomputed with the final parameter values and a new EM was calculated between the final FE displacement field and each subject data set. These values are summarised in Table 5-7.

Table 5-7 – Original global displacement and EM data, along with the reduced EM calculated after subtraction of the final FE displacement field. Pre-avg refers to values calculated from the three averaged displacement fields, as opposed to the average of the values obtained from each subject field as in Table 5-1.

Subject	X disp /mm	Y disp /mm	Z disp /mm	Magnitude /mm	ZDEM /mm	Final error mag /mm
1	0.02	-0.20	0.05	0.20	0.38	0.31
2	0.01	-0.26	0.01	0.26	0.38	0.27
3	0.00	-0.20	0.05	0.20	0.41	0.34
Pre-avg.	0.01	-0.22	0.04	0.22	0.33	0.25
FE	0.00	-0.22	0.01	0.22		

In all cases the EM was reduced after correction with the optimised FE model predictions, with improvements ranging from 0.07-0.11 mm. Comparison of the initial EM and the reduction in EM yielded a Pearson correlation coefficient of -0.13, although the sample size is admittedly small. This low correlation suggests that the ability of the FE model to correct the displacement field is relatively consistent, regardless of the initial level of non-uniformity in the displacement field. The global displacement found in the optimised FE model differed from the subject data by 0.01, 0.00 and 0.03 mm in the X, Y and Z axes respectively. This suggests that the parameter identification process was successful given the inputs used; however, achieving regional similarity was the goal here. Figure 61 compares the displacement fields of the FE and average subject data through a sagittal section.

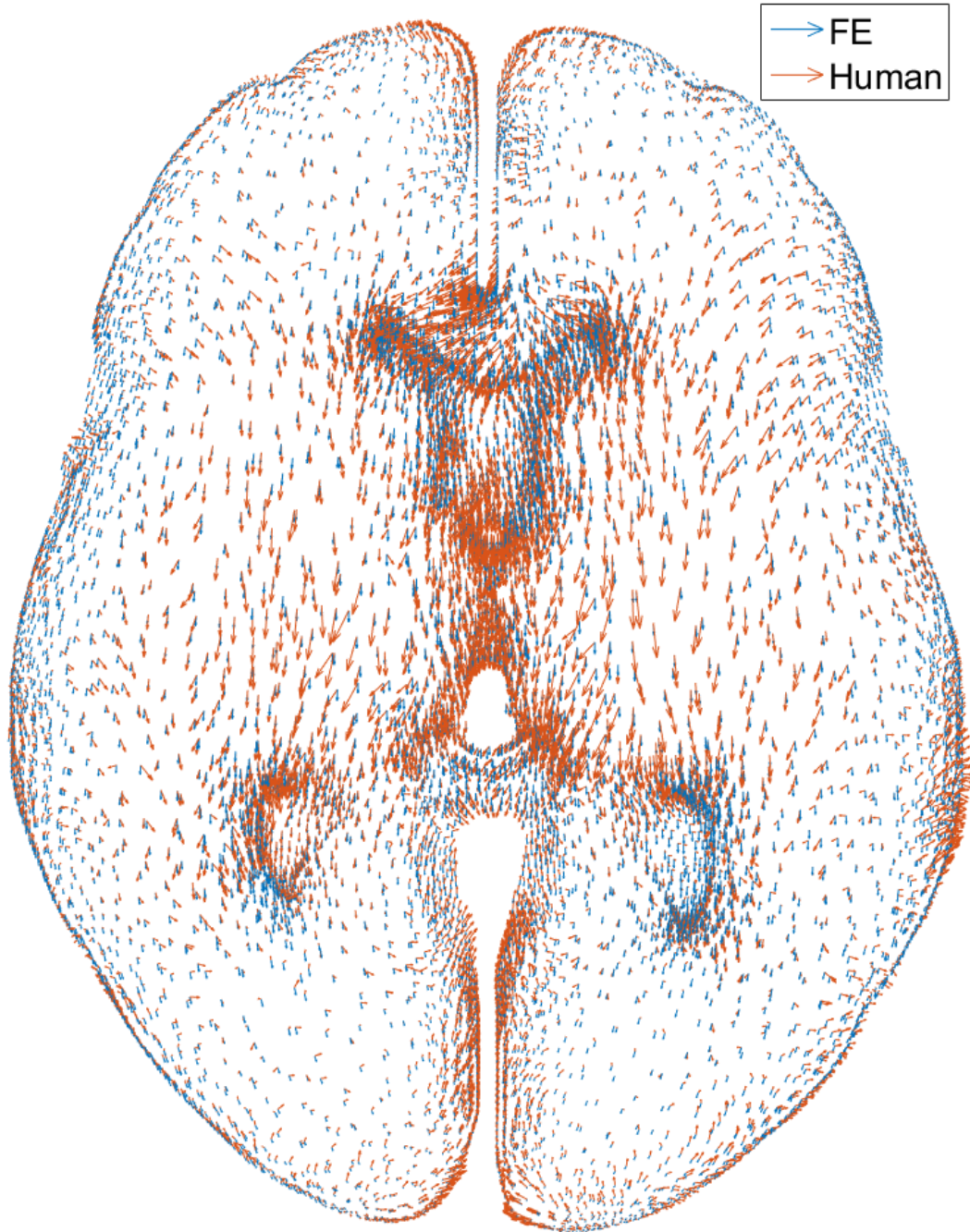


Figure 61 – Displacement fields generated by the final FE model and average subject data taken through a 10 mm section at the same point as Figure 46. Displacement vectors have been scaled by a factor of 5 relative to the brain.

It is highlighted in Figure 61 and Figure 62, that whilst the FE adjustment does improve the result, there is still some deviation between the data sets, focussed mostly towards the centre of the brain.

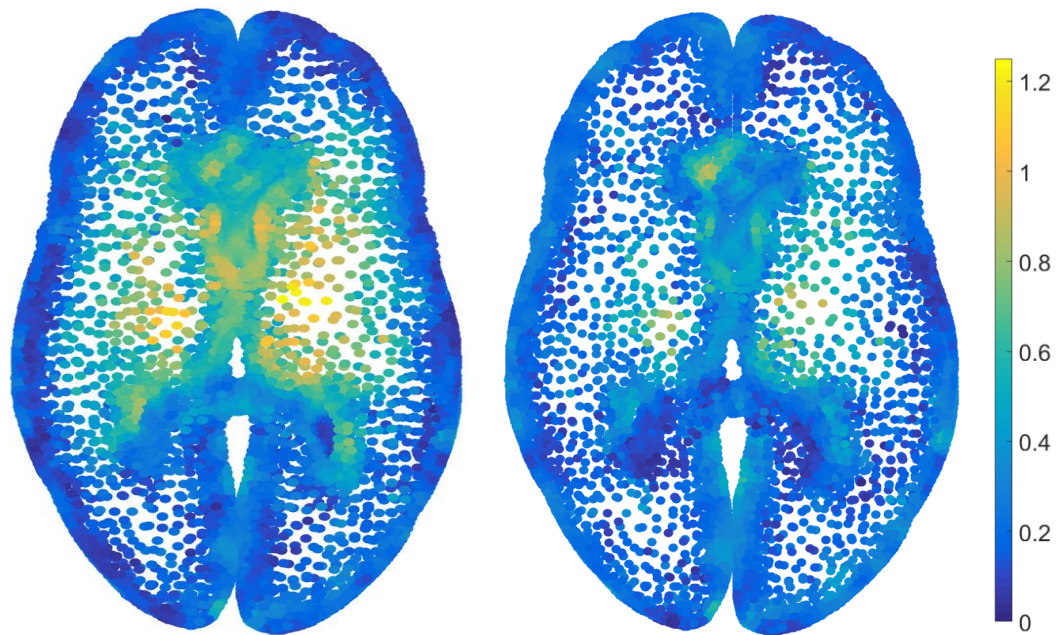


Figure 62 – Colour plot proportional to: [Left] the magnitude of the displacement field (in mm) in the original averaged subject data and [Right] after correction of the subject data with the optimised FE result – highlighting resulting error.

It was suspected that small variations in the automatically segmented skull region during image registration led to boundary artefact and erroneous displacements on the surface of the brain. An example of this can be found in Figure 61, where anterior movement is apparent in the posterior brain during prone to supine repositioning. As the FE optimisation process considered the entire brain equally, this boundary error led to central displacements which were lower than the MR data suggests.

Calibration 2

To overcome this problem, the parameter identification was repeated, this time considering elements >10 mm from the interior surface of the dura region. Given the similarity between data sets, the average subject displacement field was used moving forward. The same methodology used in iteration 1 was employed here. For brevity, details of this process are not repeated. The initial ME plots of the second calibration are shown in Figure 63.

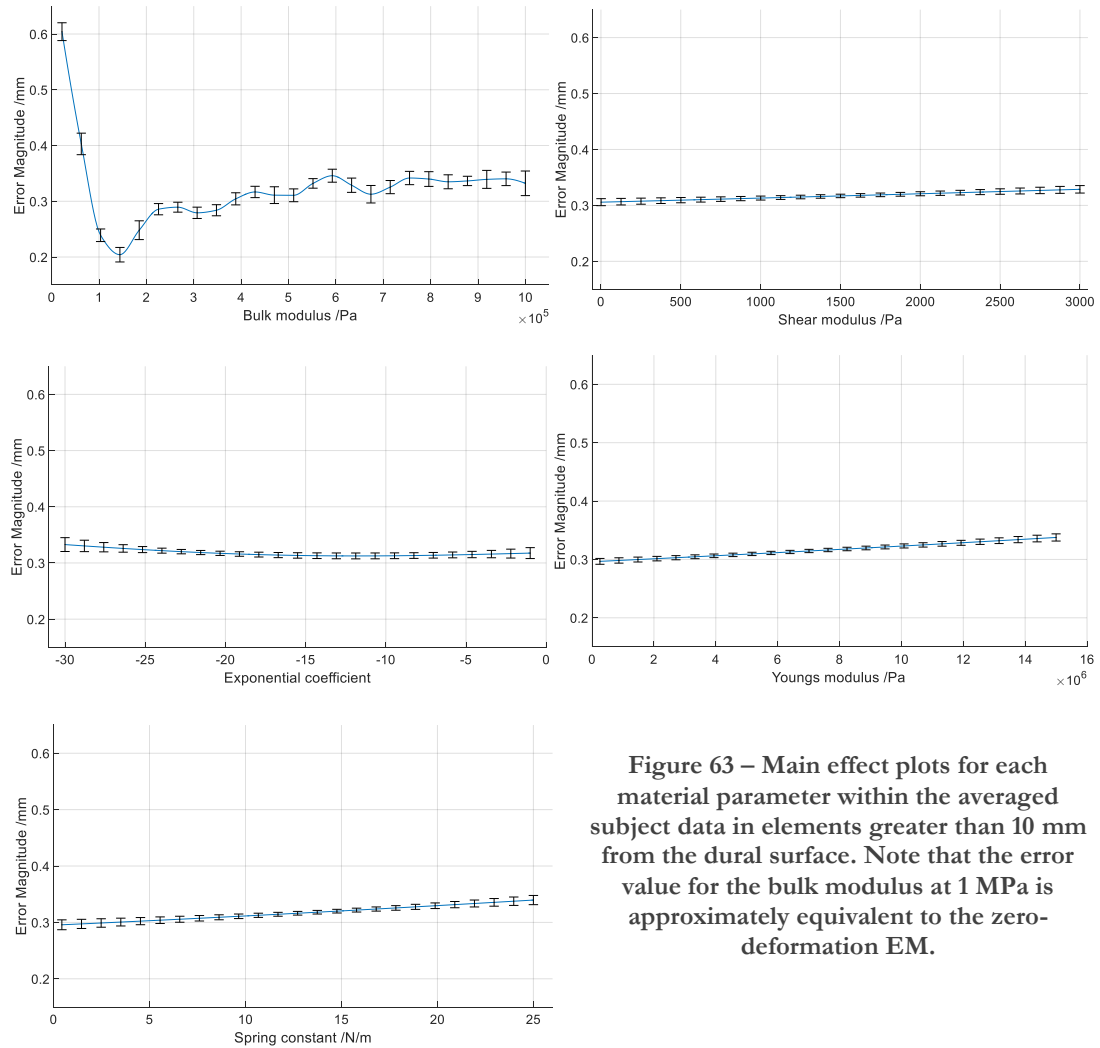


Figure 63 – Main effect plots for each material parameter within the averaged subject data in elements greater than 10 mm from the dural surface. Note that the error value for the bulk modulus at 1 MPa is approximately equivalent to the zero-deformation EM.

This time, in-range minimas were found with the bulk modulus and m_1 , at values of 144,000 Pa and -11.8 respectively. The only notable joint affect found was $x1x3$, with a variance of 10.5%, further suggesting the more important role of the exponential coefficient in this case. As done previously, parameters with in-range minimas were initially varied over a range of $\pm 20\%$ while the other were kept over the original range. 1000 random parameter sets were generated, with the resulting 200 best sets reprocessed in GEM-SA. This method led to m_1 falling outside of the range, and as such it was repeated with the original range instead. With this adjustment, the final parameter ranges are given in Table 5-8.

Table 5-8 – Parameter ranges resulting from 200 best sets from the 1st simulation.

Parameter	Minimum	Maximum
Brain bulk modulus /Pa	118,000	175,009
Brain c1 coefficient /Pa	5.01	2990
Brain m1 coefficient	-27.8	-5.03
Pia Youngs modulus /Pa	259,000	12,600,000
Spring constant /N/m	0.45	22.2

Iteration 2

The 2nd iteration ME plots are shown in Figure 64. It is interesting to note the increased apparent sensitivity of some parameters with the variation range reduced.

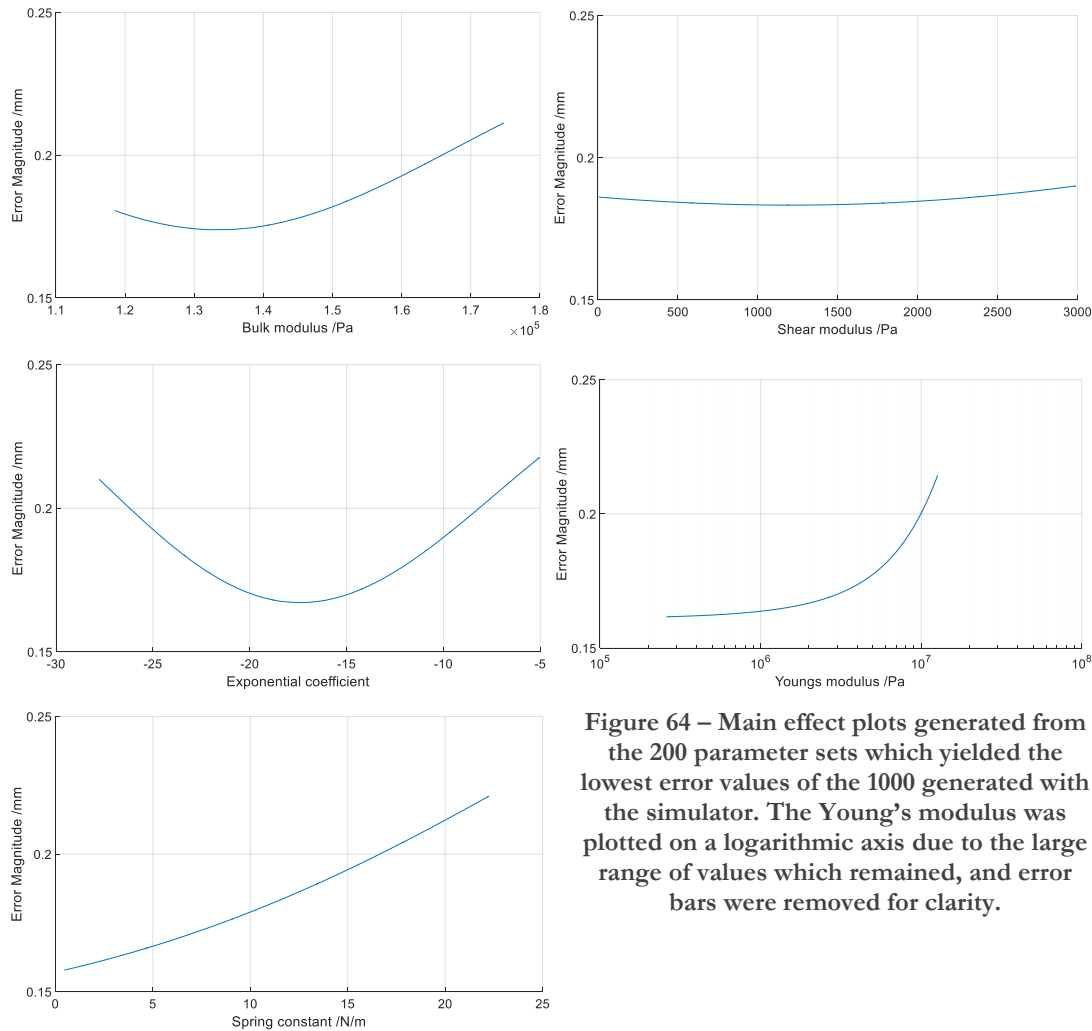


Figure 64 – Main effect plots generated from the 200 parameter sets which yielded the lowest error values of the 1000 generated with the simulator. The Young’s modulus was plotted on a logarithmic axis due to the large range of values which remained, and error bars were removed for clarity.

Results from the 2nd iteration yielded in-range minimas for three parameters, the bulk modulus, shear modulus and m_1 , with values of 133,000 Pa, 1,250 Pa and -17.3 respectively. Joint effects were reduced on the previous iteration; again $x1x3$ was the highest this time at 3.1%. Whilst the shear modulus displayed an in-range minima, it’s total effect was at least an order of magnitude less than the other parameters. The Young’s modulus displayed a similar trend to the full cerebrum analysis suggesting the range was too low; however, this was also the case this time for the spring constant. To continue, the shear modulus, Young’s modulus and spring constant were fixed at the minimum values from this iteration and surface plot points were generated for the bulk modulus and m_1 .

Iteration 3

Figure 65 shows that once again, error is most sensitive to the bulk modulus. Illustrated by the red points, the error value variation for m_1 at the optimum bulk modulus was 0.0862-0.0964 mm,

whilst the converse had a range of 0.0862-0.1345 mm. This indicates a sensitivity to the bulk modulus almost 5 times greater than m_1 , over the range used.

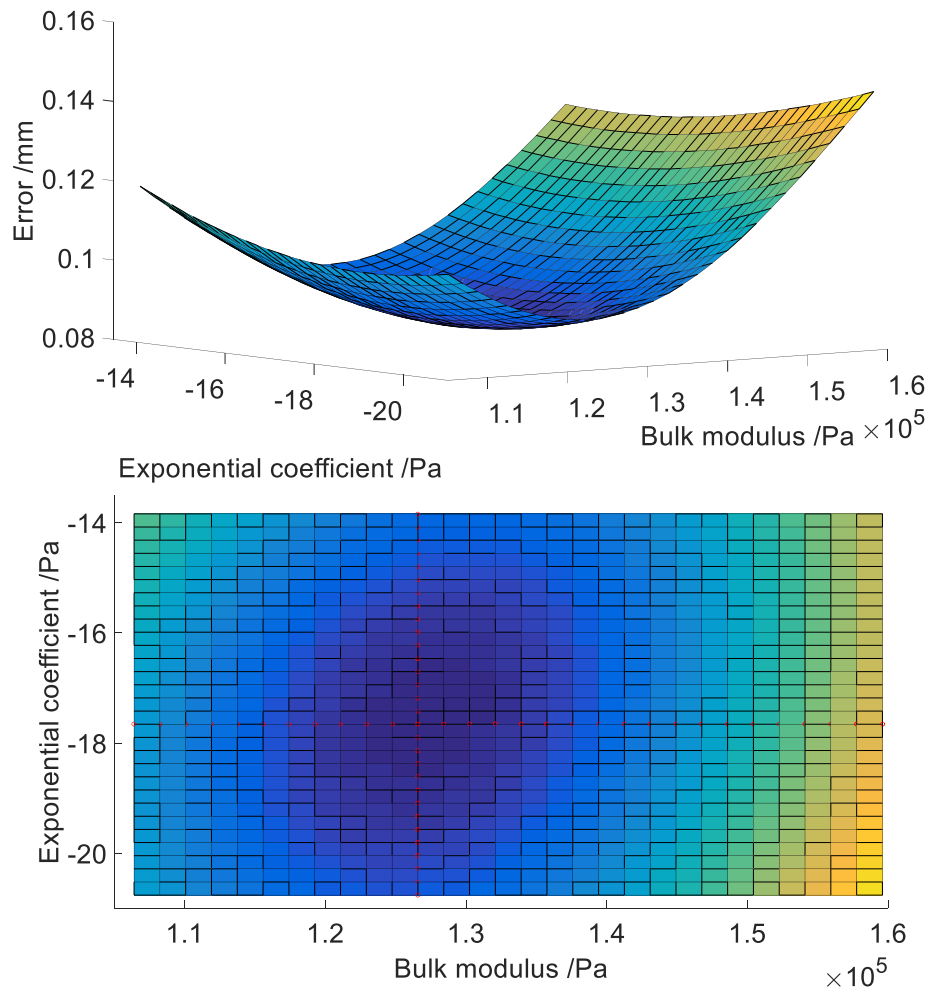


Figure 65 – Surface plot of the bulk modulus and exponential coefficient, m_1 . Red points indicate the value at which the minima occurs.

Final model 2

The new optimised parameters are given in Table 5-9 below.

Table 5-9 – Optimised values from the second calibration

Parameter	Final value
Bulk modulus /Pa	127,000
'Shear modulus' /Pa	1,250
Exponential coefficient	-16.9
Pia Young's modulus /Pa	250,000
Spring constant /N/m	0.5

Considering only the elements used in the second optimisation (>10 mm from the boundary), global displacements and EMs were recalculated for the average subject data, the FE results from the first set of optimised values and the FE results from the final set of optimised values. We recall that averaged subject displacement field had a ZDEM of 0.33 mm. When using the

optimised values found in calibration 1, the EM calculated from the reduced brain volume was 0.25 mm. With the new parameters from calibration 2, this was significantly improved to 0.05 mm.

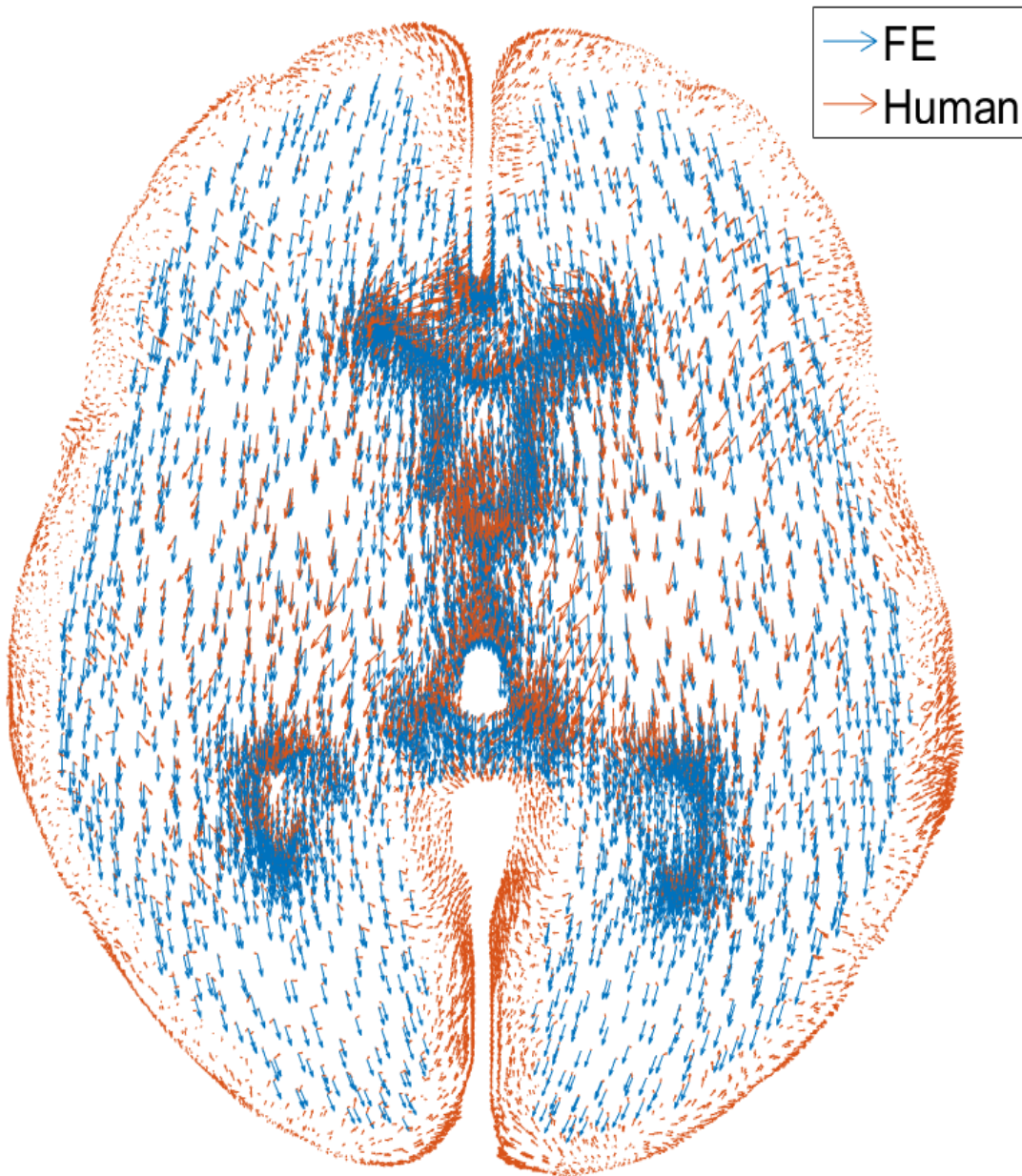


Figure 66 – FE displacement field (showing elements >10 mm from the boundary) generated from calibration 2, compared to the full region of the average subject field. Whilst there is still deviation towards the boundary, the central structures show considerable improvement compared to the results of calibration 1. Displacement vectors have been scaled by a factor of 5 relative to the brain.

Parameters identified from the calibration 2 have been shown to offer a significant reduction in error value compared to those obtained over the entire cerebrum. This is supported visually by the new displacement field. Further analysis was conducted at 44 points defined in the concurrent phantom study, which intentionally used the same segmentation. These points, shown in Figure

67, were chosen based on what was physically possible to achieve in the phantom whilst offering a good coverage of the brain area.

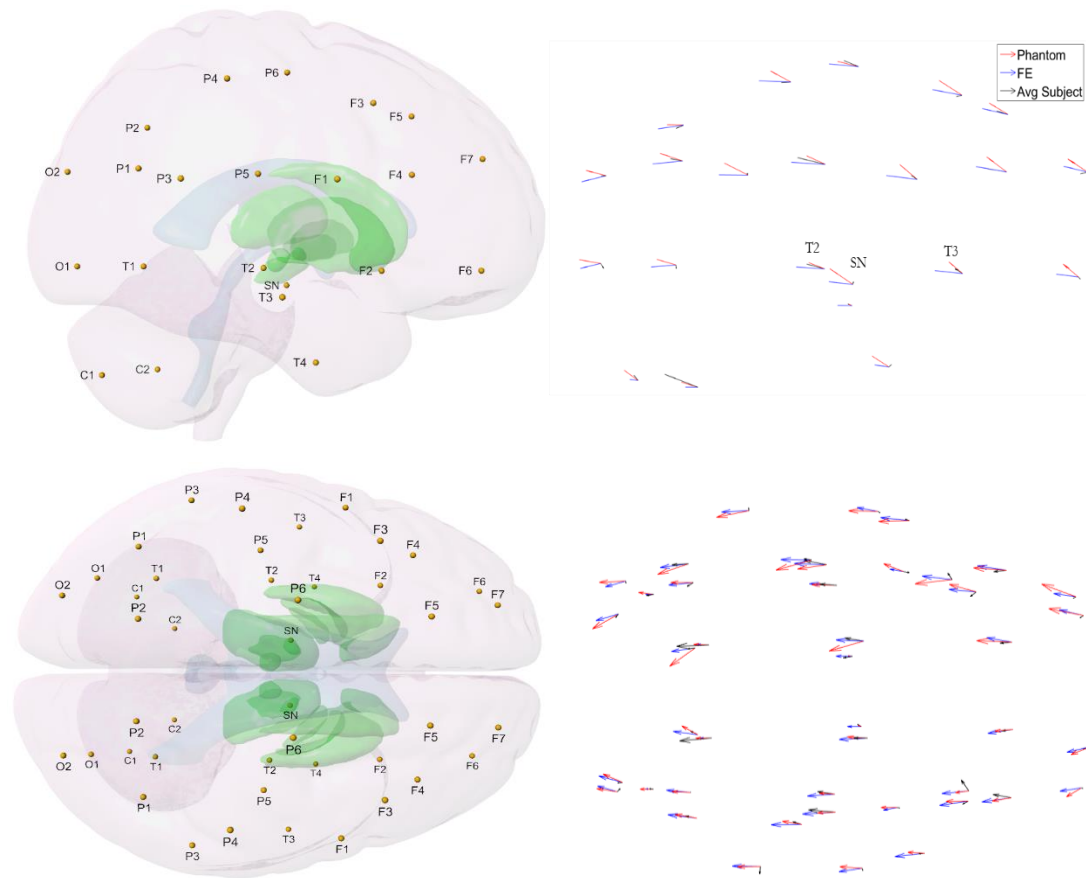


Figure 67 – Marker distribution throughout the brain, as used in the phantom study. The top image shows only the right-hand side for clarity. The bottom image shows a transverse view of both sides. The marker designation was based on the approximate anatomical location: C - Cerebellum, O - Occipital, P - Parietal, T - Temporal, F - Frontal, SN - Substantia nigra. Green regions show structures of the basal ganglia, clinically relevant to Parkinson’s disease. Left images reproduced from doctoral thesis of Matthew Potts; currently unpublished. Displacement vectors have been scaled by a factor of 10 relative to the brain.

By using points defined in the phantom, comparison of all three methods was possible. The vector plots of these three sets of results are also shown in Figure 67. Regions most relevant to DBS are likely to be SN, T2 and F2; these are highlighted on the lateral image. In general, good alignment was achieved between the FE and phantom studies, with the subject data being more similar in regions more distant from the boundary, as was previously the case. Full details of the marker displacements for each data set are given in Table 5-10.

Table 5-10 – Components of the marker displacement in the phantom, FE and subject data.

Marker	Phantom			FE			Subject		
	X	Y	Z	X	Y	Z	X	Y	Z
R-C1	0.00	0.39	-0.33	-0.01	0.24	-0.03	-0.01	0.12	-0.17
C2	0.01	0.47	-0.17	0.01	0.35	0.00	0.10	0.94	-0.42
O1	-0.10	0.60	-0.12	-0.19	0.57	0.16	-0.10	-0.09	0.16
O2	-0.28	0.57	-0.17	-0.22	0.69	0.20	0.01	0.15	0.01
P1	-0.12	0.64	-0.25	-0.11	0.85	0.09	-0.07	0.35	-0.07
P2	-0.29	0.47	-0.01	-0.11	0.72	0.12	-0.12	0.22	0.11
P3	0.01	0.67	-0.39	-0.01	0.82	-0.01	0.25	0.02	-0.06
P4	-0.10	0.57	-0.36	0.01	0.90	-0.04	-0.08	0.27	0.02
P5	0.02	0.53	-0.28	0.06	0.96	-0.07	-0.08	0.79	-0.22
P6	-0.04	0.59	-0.17	0.04	0.83	-0.09	0.00	0.41	-0.20
T1	-0.03	0.54	-0.18	-0.07	0.70	0.07	-0.01	-0.01	0.12
T2	-0.03	0.45	-0.20	0.06	0.80	-0.06	-0.08	0.50	-0.15
T3	-0.05	0.65	-0.51	0.11	0.68	-0.08	0.08	-0.02	-0.08
T4	0.00	0.47	-0.35	0.09	0.40	-0.06	0.01	-0.08	-0.08
SN	-0.04	0.10	-0.05	0.00	0.41	-0.01	-0.07	0.12	-0.05
F1	-0.03	0.49	-0.48	0.12	0.87	-0.12	0.02	0.17	-0.13
F2	0.06	0.39	-0.38	0.09	0.78	-0.10	-0.36	0.22	-0.16
F3	0.01	0.65	-0.48	0.14	0.84	-0.18	0.10	0.17	0.05
F4	0.11	0.56	-0.49	0.14	0.86	-0.17	-0.11	0.54	-0.11
F5	0.06	0.53	-0.37	0.13	0.73	-0.19	0.05	0.32	-0.11
F6	0.29	0.43	-0.42	0.11	0.62	-0.09	0.02	-0.05	0.08
F7	0.26	0.56	-0.43	0.18	0.68	-0.19	0.08	0.21	0.06
L - C1	-0.07	0.45	-0.08	0.00	0.24	-0.04	0.04	0.21	-0.16
C2	-0.02	0.45	-0.07	-0.01	0.36	0.00	0.04	0.94	-0.47
O1	0.04	0.77	0.16	0.19	0.59	0.15	0.07	-0.01	0.08
O2	0.49	0.76	0.37	0.22	0.66	0.19	0.12	0.09	-0.05
P1	0.35	0.90	0.08	0.13	0.83	0.10	0.04	0.49	-0.12
P2	0.60	0.74	0.27	0.11	0.69	0.11	0.03	0.22	-0.11
P3	0.22	0.95	-0.19	0.05	0.80	0.02	-0.10	0.01	-0.03
P4	0.33	1.04	-0.27	-0.02	0.90	-0.06	-0.04	0.23	-0.17
P5	0.14	0.85	-0.17	-0.04	0.94	-0.06	-0.15	0.67	-0.08
P6	0.33	1.01	-0.14	-0.04	0.81	-0.09	-0.10	0.56	-0.02
T1	0.00	0.66	0.04	0.08	0.72	0.07	0.13	0.19	0.01
T2	-0.02	0.73	-0.13	-0.05	0.80	-0.06	-0.04	0.50	-0.11
T3	-0.02	0.85	-0.33	-0.13	0.61	-0.08	0.04	-0.07	-0.05
T4	-0.26	0.58	-0.29	-0.08	0.40	-0.06	0.04	-0.17	-0.23
SN	-0.02	0.13	0.01	-0.01	0.48	0.01	0.05	0.27	0.00
F1	0.03	0.90	-0.38	-0.10	0.85	-0.11	-0.05	0.13	-0.02
F2	-0.25	0.78	-0.43	-0.08	0.79	-0.11	0.16	0.17	-0.17
F3	0.14	1.08	-0.52	-0.12	0.88	-0.16	-0.22	0.13	-0.13
F4	-0.08	0.96	-0.61	-0.14	0.85	-0.18	0.05	0.38	-0.04
F5	-0.05	1.03	-0.48	-0.15	0.74	-0.20	0.03	0.35	-0.04
F6	-0.42	1.00	-0.60	-0.11	0.65	-0.12	0.05	0.08	0.03
F7	-0.23	1.01	-0.65	-0.19	0.70	-0.20	0.08	0.11	0.05

Biomechanical Analysis of the Final Model

It was previously shown that the developed FE model and identified material parameters offer excellent correlation to the limited cerebral region of the subject data used in calibration 2. As confidence in the subject data was greater in the central regions than near the boundary, it was considered that the mechanical constraints of FEA may indeed offer an improved prediction of the boundary displacements than the subject data itself. As such, analysis of final FE models was undertaken to help understand the biomechanical process of brain shift. In this analysis we first recall the expanded form of Equation 16 in Equation 42:

$$\boldsymbol{\sigma} = \begin{bmatrix} \sigma_{xx} & \sigma_{xy} & \sigma_{xz} \\ \sigma_{yx} & \sigma_{yy} & \sigma_{yz} \\ \sigma_{zx} & \sigma_{zy} & \sigma_{zz} \end{bmatrix} = \begin{bmatrix} \sigma_{hyd} & 0 & 0 \\ 0 & \sigma_{hyd} & 0 \\ 0 & 0 & \sigma_{hyd} \end{bmatrix} + \begin{bmatrix} \tilde{\sigma}_{xx} & \tilde{\sigma}_{xy} & \tilde{\sigma}_{xz} \\ \tilde{\sigma}_{yx} & \tilde{\sigma}_{yy} & \tilde{\sigma}_{yz} \\ \tilde{\sigma}_{zx} & \tilde{\sigma}_{zy} & \tilde{\sigma}_{zz} \end{bmatrix} \quad 42$$

where the hydrostatic stress σ_{hyd} is $\frac{1}{3}tr(\boldsymbol{\sigma})$ and $\boldsymbol{\sigma}$ is the Cauchy stress tensor. The component plots of the Cauchy stress tensor in the prone position are shown in Figure 68.

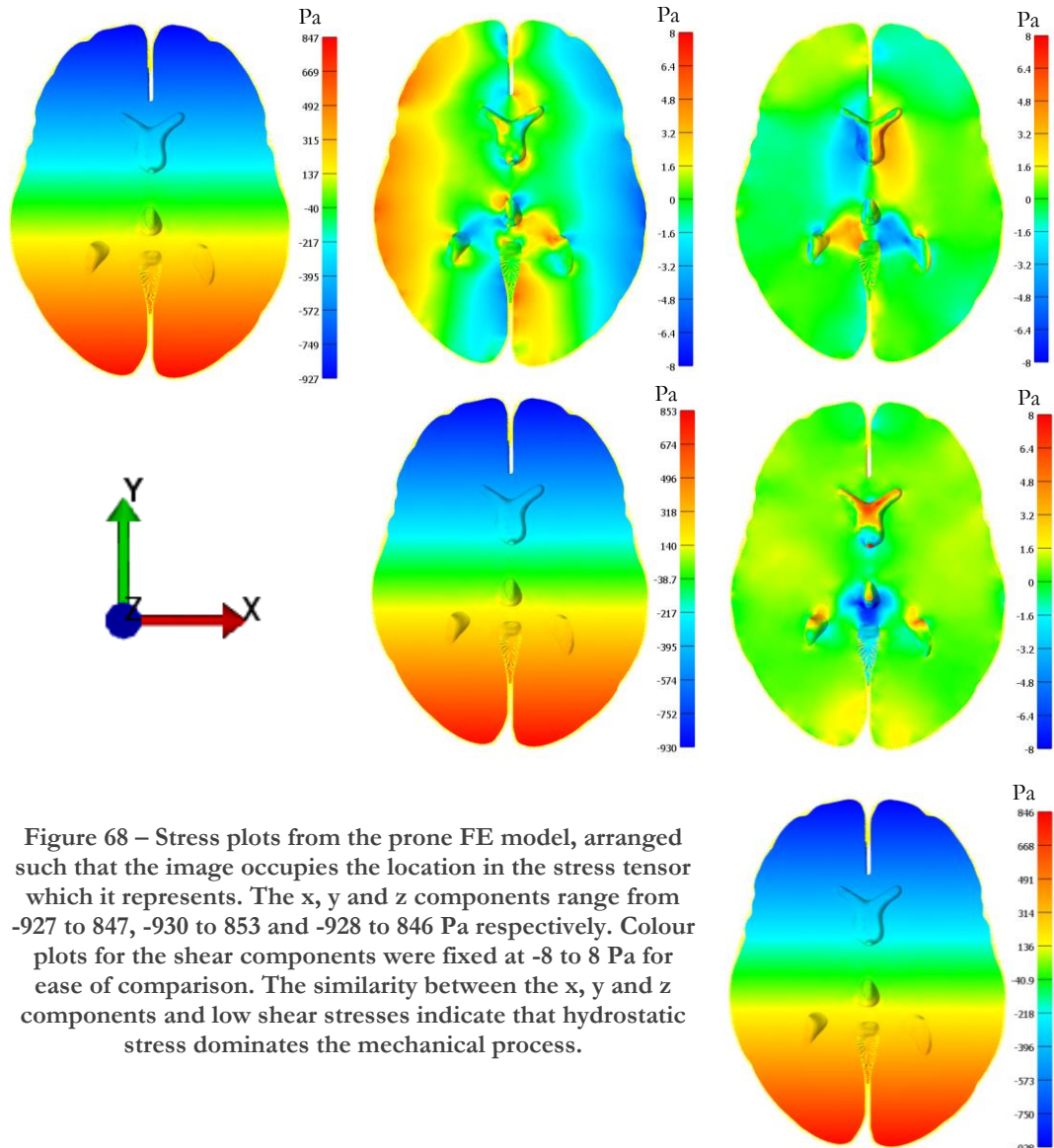


Figure 68 – Stress plots from the prone FE model, arranged such that the image occupies the location in the stress tensor which it represents. The x, y and z components range from -927 to 847, -930 to 853 and -928 to 846 Pa respectively. Colour plots for the shear components were fixed at -8 to 8 Pa for ease of comparison. The similarity between the x, y and z components and low shear stresses indicate that hydrostatic stress dominates the mechanical process.

The pressure distribution follows the same pattern as the x, y and z components ranging from -848 to 928 Pa. Recalling that $p = -\sigma_{hyd}$, this becomes -928 to 848 Pa, values almost identical to the x, y and z components. The same pattern is present in the supine examples given in Figure 69, where the hydrostatic stress ranged from -839 to 947 Pa. Considering this and the comparatively low shear stresses in both cases, we conclude that the deviatoric stress is low throughout the brain area and the mechanical process is dominated by volumetric change within the brain tissue. Figure 69 shows the equivalent plots in the supine position, demonstrating a similar mechanical response.

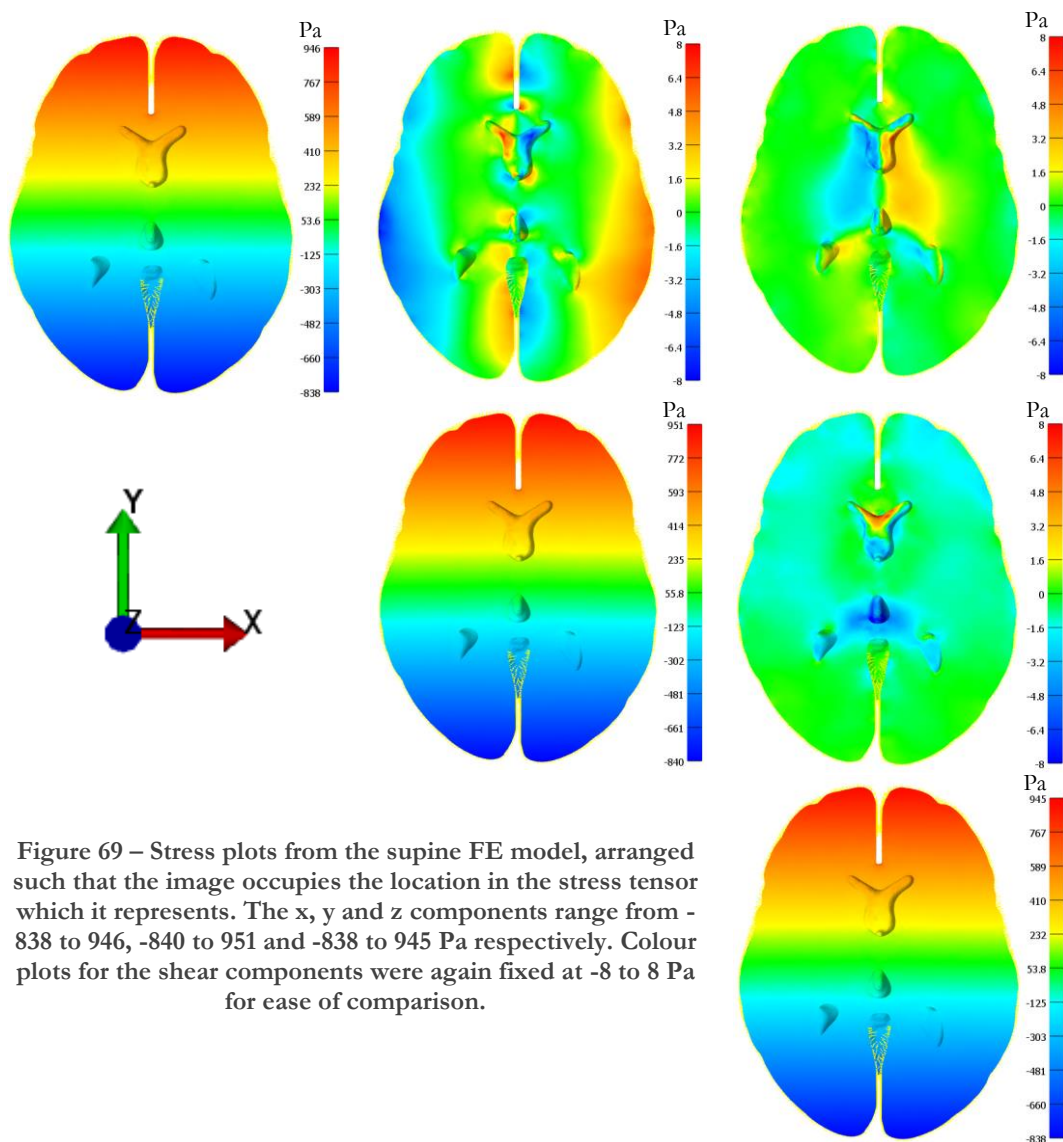


Figure 69 – Stress plots from the supine FE model, arranged such that the image occupies the location in the stress tensor which it represents. The x, y and z components range from -838 to 946, -840 to 951 and -838 to 945 Pa respectively. Colour plots for the shear components were again fixed at -8 to 8 Pa for ease of comparison.

Of the shear stresses, the most interesting is the σ_{xy} component in both cases, which show peaks in regions along the sagittal plane which are close to the dura. This suggests tethering of the surface of the brain with sagging in central unsupported regions as is highlighted in Figure 70.

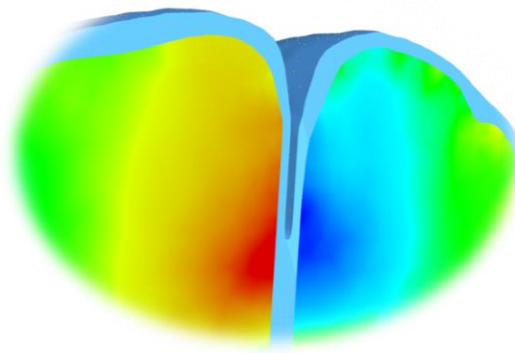


Figure 70 – Zoomed image of the anterior midline region of the supine model, where the PAC region is shown in solid blue. The colour scale shows σ_{xy} component of the Cauchy stress, highlighting a peak near the external boundary of the PAC.

The 1st deviatoric principle stress (Figure 71) was low as expected, with peaks of around 5 Pa in each position. Being the deviatoric component, stresses were sensitive to shape change, with the ventricles and boundary influencing the distribution. In each case, stress was greatest in the top side relative to gravity and around the surface, suggesting this tissue was in mechanical tension due to tethering of the PAC.

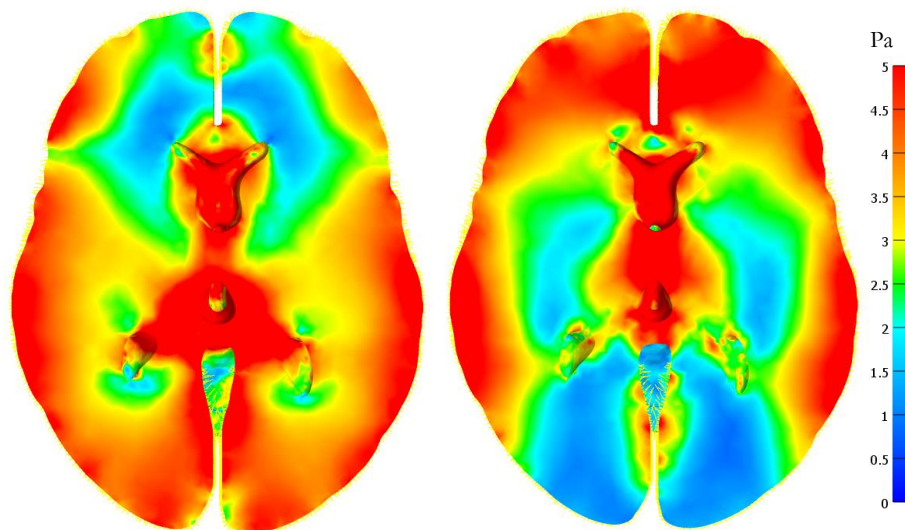


Figure 71 – 1st deviatoric principle stress for the prone [left] and supine [right] FE models.

1st principle strain patterns were similar to the 1st deviatoric principle stresses. Most notably, even in areas of local stress concentration and increased strain, peaks were still in the order of 1%. Volume change in each loading case varied by approximately $\pm 0.7\%$, in a linear manner over the gravitational axis of the brain, mirroring the hydrostatic stress distribution. Whilst this volume change appears negligible it is inextricably linked to the bulk modulus, which has already been shown during sensitivity analysis to be the most significant factor driving brain shift.

The 1st principle strain, shown in Figure 72, suggests that in both the prone and supine cases, strains were greatest in the top region relative to gravity; however, these are relatively small, in the order of 0.5%.

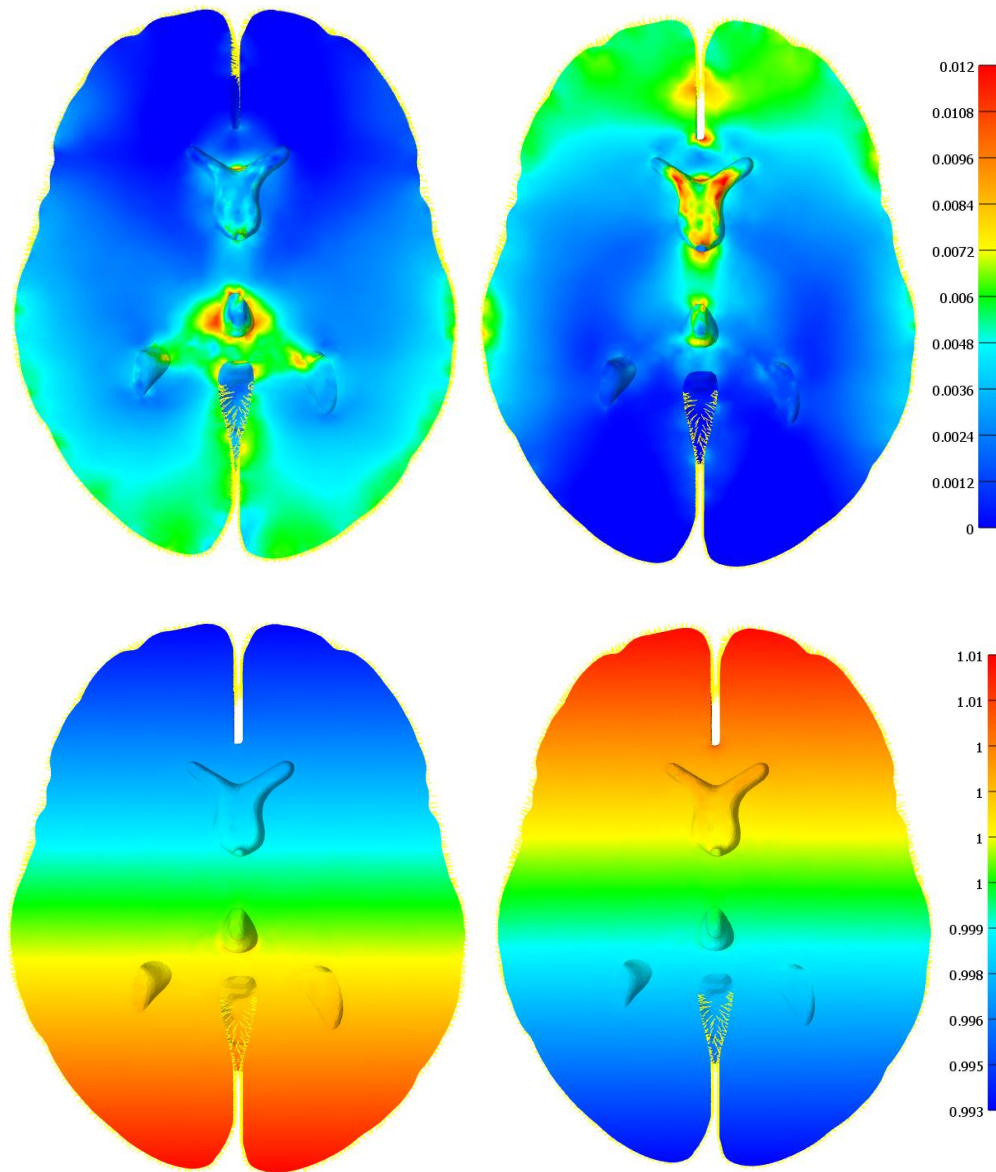


Figure 72 – Sections of the final FE model showing 1st principle strain [top] in the prone [left] and supine [right] positions, elemental Jacobian [bottom] respectively.

Displacements were in the order of 0.1-0.2 mm and up to 0.5 mm on the ‘top’ and ‘bottom’ surfaces respectively. Even though the strains are small, they are sufficient to lead to surgically significant non-rigid displacement. This pattern can also be seen in Figure 73. Also shown is the volume change in the PAC from the neutral to loaded and prone-to-supine reorientations. Regions normal to the loading direction exhibited highest strains, peaking at approximately ± 60 % by volume in some elements.

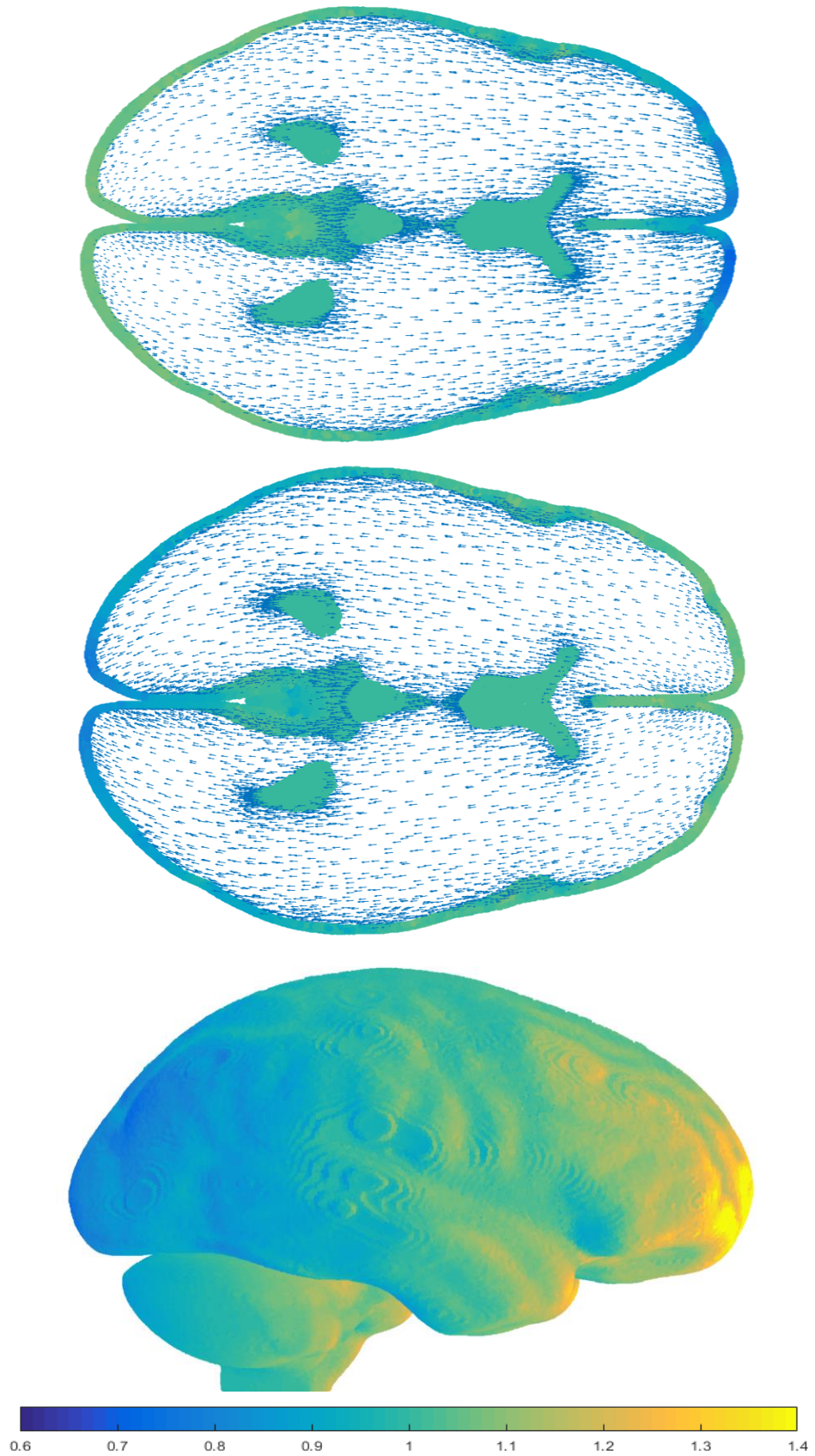


Figure 73 – Neutral to prone [top], neutral to supine [middle] and prone to supine [bottom] displacement fields (scaled by a factor of 10), superimposed with the Jacobian of fluid regions (shown in colour). The prone to supine image treats the prone elemental volume as the starting point rather than calculating J from the neutral position.

As suggested throughout this section, the arachnoid trabeculae appear to tether the surface of the brain to more rigid structures. The force generated by each individual element was very small, with peak forces, predominantly located on gyri, in the order of 0.2 mN. However, as the effective weight of the brain is only 0.5 N a stiff layer is not required to maintain a relatively stationary position of the brain in quasi-static loading. This said, if the PAC was not represented, the 'bottom' surfaces of the brain would come into contact with the skull, leading to larger than expected displacements. The force exerted by the springs over the surface is displayed in Figure 74, which demonstrates tethering on the top surfaces relative to gravity.

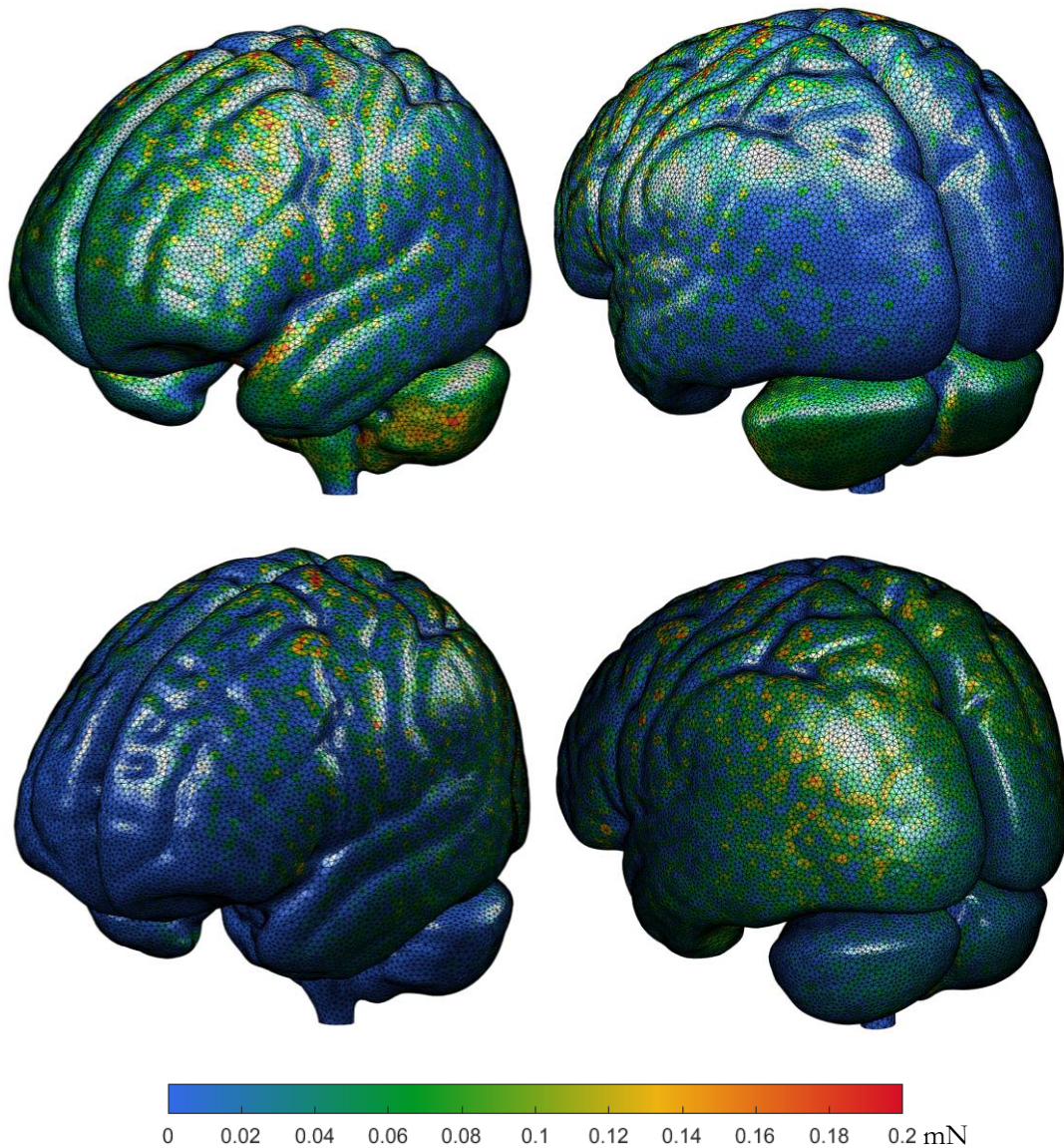


Figure 74 – Prone [top] and supine [bottom] images of the pia mater, where the colour represents the reaction force (mN) in each spring element of the arachnoid trabeculae, averaged over the three nodes of each surface element, not accounting for elemental area.

The pia mater also plays an important mechanical contribution, even though the stiffness suggested by the parametric analysis was lower than expected. As with the trabeculae, the stress is greatest on the 'top' surface, this is shown in Figure 75. The stresses in the pia mater are in a

different order of magnitude to deviatoric stresses in the brain, with levels in the order of 2,000 Pa. This is depicted in Figure 75.

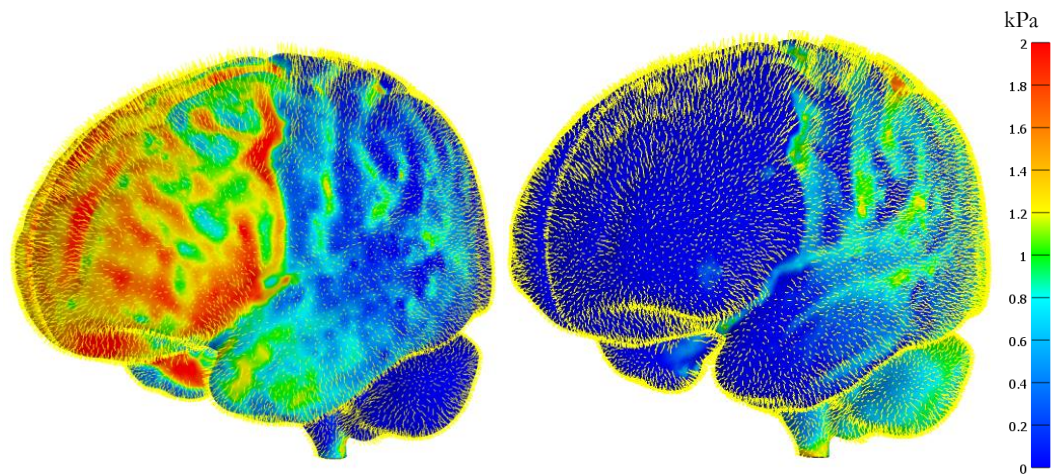


Figure 75 – 1st Principle stress (kPa) in the pia mater, in supine [left] and prone [right] loading.

Surgical Prediction Test Case

Prediction was performed in 6 orientations common to neurosurgery. As a reminder, a modified version of Figure 45 is included below in Figure 76.

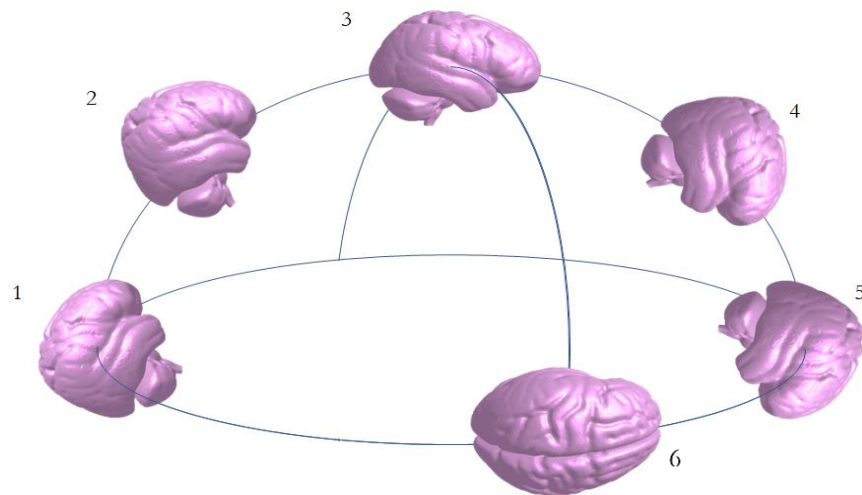


Figure 76 – Modified schematic of the prediction test case positions.

As the right decubitus position was predicted, displacement in the approximate location of the left STN was measured. It was assumed that presurgical imaging is undertaken in the supine position; orientation 1. Displacement between the supine and other orientations is shown in the sagittal and axial planes in the left and right graphs of Figure 77 respectively. As expected, the peak displacement was found between the supine and prone position, with X, Y and Z vector components of 0.00, 0.65 and 0.03 mm respectively. Whilst not the greatest absolute displacement, the decubitus position exhibited the greatest displacement relative to the overall change in load with displacements of 0.31, 0.30 and 0.02 mm.

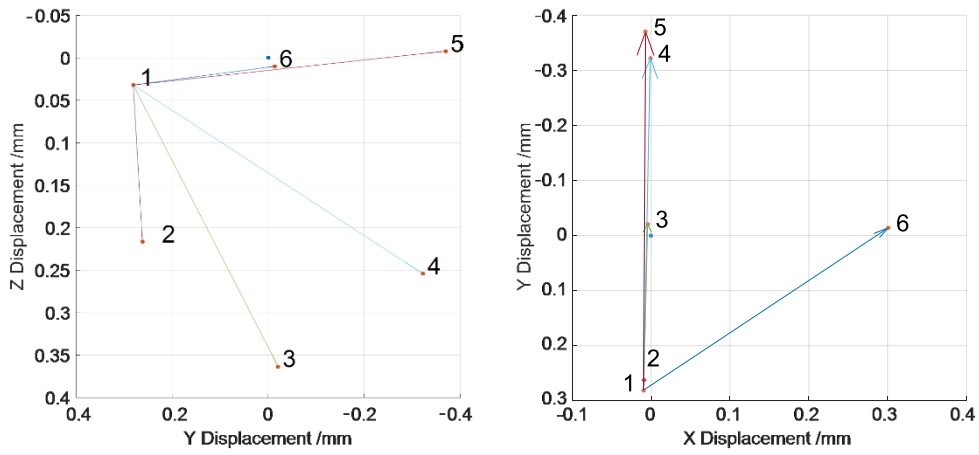


Figure 77 – Sagittal (left) and axial (right) plots illustrating the vector displacements between the supine and other orientations as predicted by the final parameter sets.

Chapter 6: Discussion

It has previously been shown how PBS was identified as a key component of error within stereotactic neurosurgery and the necessary starting point for any future modelling efforts. The model developed according to this finding and results obtained from it, constitute the main contributions of this work. To recap, they can be summarised as:

- The development of the model itself, utilising the state-of-the-art in terms of modelling techniques.
- The identification of material properties through direct use of the adjacent human study, whilst also considering the existing literature.
- A biomechanical analysis, yielding new insight into PBS as well as head modelling and brain shift as a whole.
- A proof of concept test prediction which confirms PBS to be a clinically significant source of potential error in stereotactic neurosurgery.

These key areas will be expanded upon in the following discussion.

Development of the model

As noted in Chapter 3, efforts within computational modelling of stereotactic procedures have so far been limited to ensuring procedure safety. This was achieved through modelling the worst case of CSF loss and adapting the trajectory to avoid a danger region defined as the space between the initial and worst-case final positions. These are certainly useful works to consider clinically, as minimising risk of haemorrhage is desirable, even if it does not lead to improved accuracy. However, the long-term goal of this work is to offer such improvements and therefore required considerably different methods.

Upon review of the literature, discussed in Chapter 2, it was concluded that an improved understanding of the mechanics of small-scale brain movement was required. The study of positional brain shift offered a unique opportunity to directly calibrate and validate the developed model. This was especially important, as to the best of the author's knowledge, PBS had not been the focus of a computational model to date.

Although largely undocumented here, the final model was the result of hundreds of developmental iterations and thousands of computations. Early in this development it became clear that typical methods used in other areas of modelling would not apply in this case. Furthermore, with no previous works to build upon, generation of the model required full manual segmentation in order to meet the requirements of both the computational and phantom study.

When considering geometry, the PAC is often oversimplified or left out entirely in other modelling works. Approaches include direct attachment of the brain to the surface of the skull, sliding contacts or various stages in between (178). As the maximum potential movement in this layer is approximately 2 mm, this may be insignificant compared to the levels of deformation expected and therefore not worth the increased complexity (162).

In the early stages of this study, a transversely-isotropic fibre stiffened layer with a very low bulk modulus was used, with initially positive results. However, mathematical definition of the fibre distribution around three fibre centres in each cerebral hemisphere and the cerebellum led to stiffness discontinuity and erroneous results. In late 2018, the inclusion of FSI into FEBio enabled a new method, where the CSF was modelled as a fluid and the arachnoid trabeculae were included as spring elements spanning the subarachnoid space. These methods have been used separately in other modelling efforts (133, 153, 168, 194), but to the best of our knowledge this is the first implementation where these features have been combined.

Although it was not possible to implement this in Preview directly, it was achieved through manipulation of the ‘.feb’ file in Matlab; a method that would facilitate easy experimentation with different spring distributions in the future. This work would not have been possible without this PAC representation, which provided a stable model capable of converging with the vast majority of material parameter combinations.

There is considerable literature regarding the material properties of the brain in other intracranial structures. However, many groups chose a seemingly arbitrary value to represent the compressibility of the brain (166). Applying these values generated displacements far from the order of magnitude that was expected with PBS. In fact, the literature appeared to be absent of appropriate values for the boundary conditions concerned with this mechanical process. Some groups previously had identified the importance of bulk compressibility and implemented this computationally using consolidation theory (126). However, this implementation was unnecessary due to considering only the equilibrium state. As it became apparent that the bulk modulus of the brain was important to this process, focus of the project moved from one based on assessing the impact of geometric variation, to the understanding of material sensitivity.

It was from this point that the decision to use GEM-SA and undertake sensitivity analysis stemmed. It was felt that determining material parameters applicable to quasi-static loading would not only be necessary to facilitate any continuation of this work, but also to add to the body of knowledge with results being obtained entirely from in-vivo images rather than the usual methods of mechanical testing. These results form one of the major contributions of this work.

Kinematics of Positional Brain Shift

Displacement and deformation of the brain result from the loading of various anatomical structures, each with different geometry and material properties. The methods employed in this study utilise measurements of these patterns to derive said properties. As such, the results are directly linked to this data and rely greatly upon it being a true likeness of what occurs in-vivo. Given that displacement is the input and ultimately the output of the modelling works described here, the results found in the present study are first considered in the context of the other measurements presented in the literature.

PBS measurement in the literature

Whilst the literature on PBS is somewhat limited, past notable contributions include those from Hill (78), Schnaudigel et al. (4), Monea et al. (93) and Mikkonen and Laakso (94). Although the accompanying human study was used directly for calibration of material parameters, the published data must also be considered when assessing the validity of the final parameters. That said, as the human data was not generated as part of this study directly, it will not be the focus of discussion. To recap, Hill was limited by technological limits on image resolution, but concluded that brain shift in PBS was less than 1 mm. Schnaudigel et al. assessed the brain area as a whole with improved resolution using magnetic resonance morphometry. They found brain shift in PBS to be between 0.6-1.3 mm in the sagittal plane which supports the findings of Hill's study when considering the resolution involved. Importantly, they also posed that brain shift is not a rigid body displacement of the brain within the subarachnoid space, but a more complex deformation. Monea et al. presented findings suggesting peak magnitudes at the cortical and ventricular surfaces which were higher than other groups, although displacements were less than 3 mm at the majority of points. A more detailed account of the general direction of movement was also given and is reproduced in Figure 78.

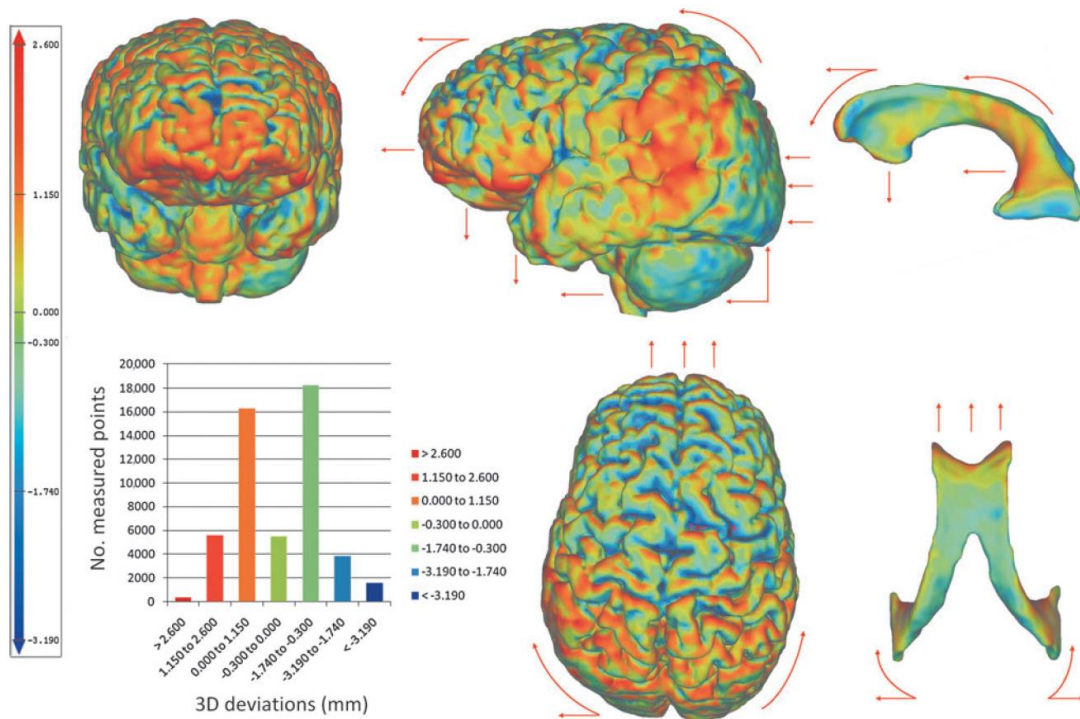


Figure 78 – Cortical and ventricular surface displacement due to reorientation from supine to prone in the sagittal plane. Gross displacement is indicated by the red arrows, with local change corresponding to the colour code. Reproduced from (93).

While this pattern of displacement is interesting, it seems that the level of surface displacements of the levels reported were unlikely, given typical PAC thickness. Most recently, Mikkonen and Laakso reported asymmetrical, predominantly inferior displacement with supine-to-prone repositioning, as is shown in Figure 79.

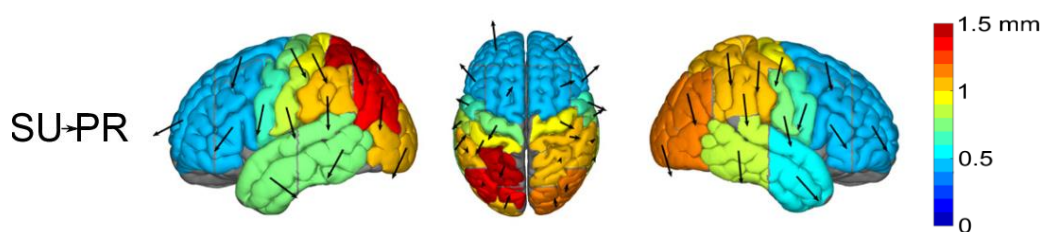


Figure 79 – Surface displacement colour plot resulting from supine-to-prone repositioning. Adapted from (94).

In the gravitational axis, displacement appears to be greater in the anterior regions than the posterior, however the inferior component is significantly larger in magnitude, contradicting both the results of Monea et al. and what one would expect.

Perhaps the most meaningful conclusion from previously reported accounts of PBS is that it is an incredibly difficult phenomenon to measure, with the variation found by different groups probably linked to the methods used more than intrasubject variability itself.

Accompanying in-vivo human study

Whilst much effort was put into making this study as accurate as possible, it appears on balance that the surface displacements found may not be reliable. For example, the section shown in Figure 80 suggests the anterior surface of the brain moves against the direction of gravity when moving to the supine position, whilst the midline region around the falx cerebri displays predominantly lateral movement. A similarly unexpected pattern can be seen in the posterior region.

The registration method employs continuity of displacement to reduce the influence of noise, which may introduce small levels of artificial deformation. Furthermore, it may act to enforce other erroneous displacements, for example those caused by partial volume errors at the boundaries. It is expected that these factors contribute to the unusual displacement pattern shown in Figure 80. Although, these potential sources of error are known, the subject data is still likely to contain some true, local displacement variation, induced by anatomical structures which are not captured in the FE model.

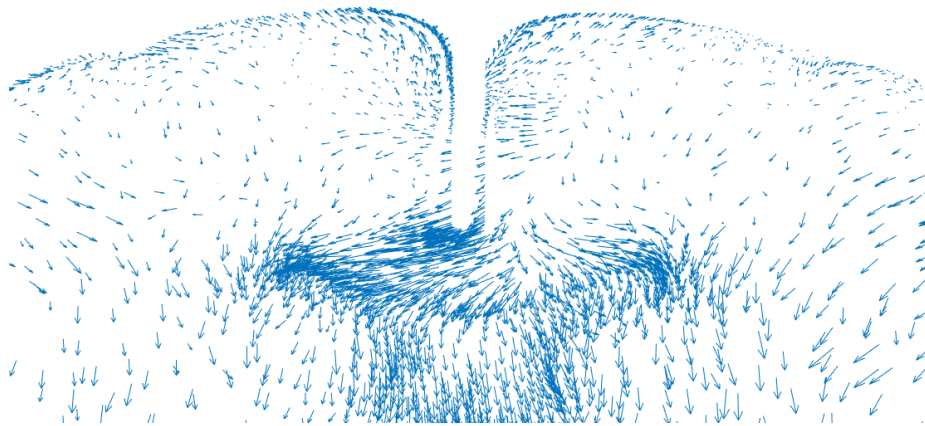


Figure 80 – Anterior transverse section, highlighting the variation in cortical surface displacement in the subject data obtained as part of the accompanying human study.

As previously mentioned, the magnitudes reported in the literature may be questionable. Although, the displacement pattern presented by Monea et al. (93) represents what one would most likely expect. In an effort to avoid the difficulties of generating a 3D deformation field, Tsutsumi et al. (141) instead analysed the movement of cerebral bridging veins and volume change within the PAC on 2D images, again with supine to prone repositioning. Figure 81 illustrates the methodology, where anatomical landmarks were used to help define CSF regions manually. In doing so, this method eliminated the potential error associated with automatic definition of the skull boundaries. Although out of plane motion may impact the measurement, it is likely that this is a good compromise and the results are relatively reliable. Their analysis found that, whilst venous sections remained stationary, the parasagittal frontal convexity underwent a volume change of $17.8\% \pm 11.7\%$ (range 2-43%).

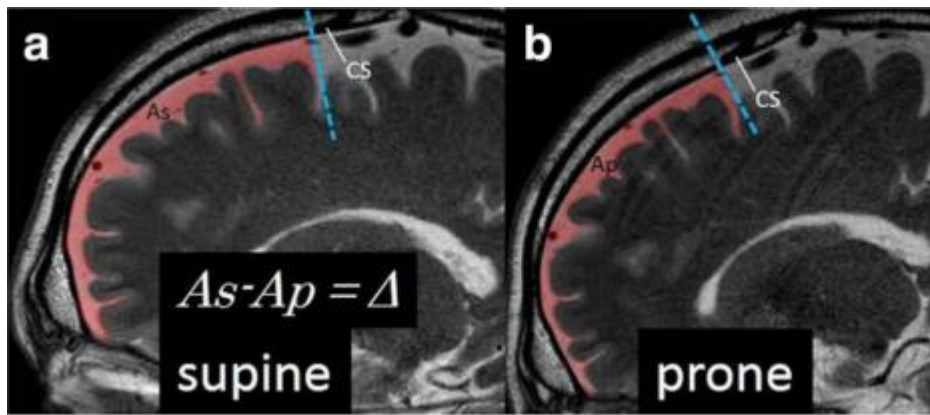


Figure 81 – 2D CSF area measurement in the prone and supine positions, identified by manual tracing of the bright CSF filled region. Reproduced from (141).

It is difficult to equate this volume change to a surface displacement directly as portions of the region considered were not normal to the direction of movement. However, the data strongly suggests that the displacement is predominately in the direction of gravity. Whilst it's understood that age plays an important role in PAC thickness, the patients analysed in this study had a mean age of 46.8 years, suggesting the result is not skewed by only considering young or elderly patients.

Due to the technical difficulty of acquiring volumetric data, it is even more scarce than surface data. Schnaudigel et al. (4) presented the deformation field shown in Figure 82, in which there is a predominately posterior to anterior displacement. The authors also note an inferior component, in their view probably due to bending of the subject's neck in the scanner.

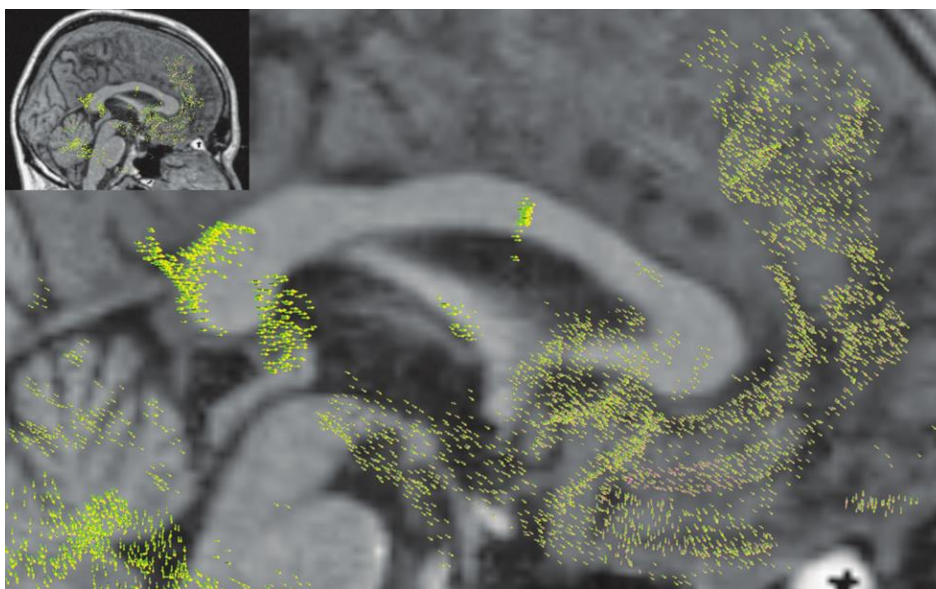


Figure 82 – Midsagittal deformation field with supine to prone repositioning presented by Schnaudigel et al. (4).

An equivalent section from the accompanying human study (Figure 83) shows similar (but oppositely loaded) patterns. However, the pattern does not remain in regions close to the falx cerebri, shown approximately by the black line. More work is required to understand the cause of such an effect, but it should be noted when considering these results.

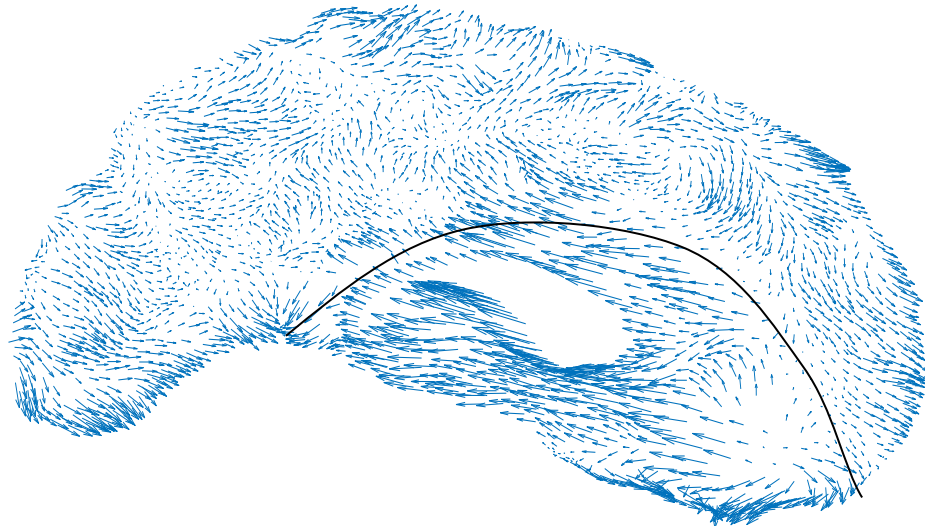


Figure 83 – Subject displacement field from a sagittal plane just off midline (as midline has no limited brain nodes), presented as comparison to Figure 82. Note the displacements depict prone-supine reorientation as opposed to supine-prone. Midbrain/cerebellum is also not shown due to poor results. The black line indicates the approximate inferior boundary of the falx cerebri. Scaled by a factor of 10.

Figure 84, shows a histogram of the sagittal components of the nodal displacements across the cerebrum as a whole, and the limited list >10 mm from the boundary. These represent the data sets used in calibration 1 and calibration 2 respectively. The histogram highlights how the elements close to the boundary produce unexpected results. Although some positive values remain in the middle region subset, these values fall close to the 0.6 to 1.3 mm reported by Schnaudigel et al. (4). Judging by the limited vector field in Figure 82, the lower limit of 0.6 mm may not represent the actual minimum level of displacement, but only the minimum in the regions considered by their analysis. Considering the small numbers of subjects in the human study conducted here, these results are remarkably similar, especially given that the histogram shape may be skewed as nodal data is not weighted by element volume.

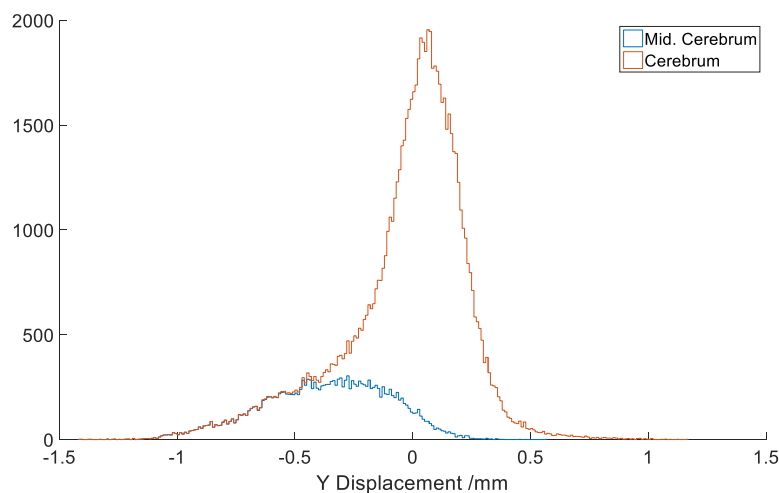


Figure 84 – Histogram of the gravitational component of the nodal displacements in the entire cerebrum vs the reduced cerebral area of the averaged human data set. For reference, Schnaudigel et al. (4) reported displacements between 0.6-1.3 mm.

FE study

The FE model developed in this study was calibrated twice against the human data, once with the entire cerebrum and once with nodes <10 mm from the surface excluded due to the boundary effects in the human data. This yielded distinctly different results, with the sagittal component of the global displacement 0.26 and 0.80 mm for first and second calibrations respectively.

This difference in displacements is shown in Figure 85, again comparing the reduced subset of nodes for each. The initial displacement field resulting from calibration 1 was not able to capture the more significant displacements but was similar in mean magnitude to the whole cerebrum subject data. The displacement field resulting from calibration 2 yielded results more similar to the displacements found by Schnaudigel et al. (4). Although the proportions of the histogram are skewed by using nodal data (not accounting for node density), it provides a more meaningful comparison between the different groups of data within this, the human study and the reported range. Due to differences in reporting, it is difficult to compare to the distribution of displacements found in the other published works. If it is assumed that the general displacements patterns given by Monea et al. in Figure 78 hold true for deeper structures in the brain, there is remarkable similarity to the marker displacements in Figure 67, particularly for the FE and phantom.

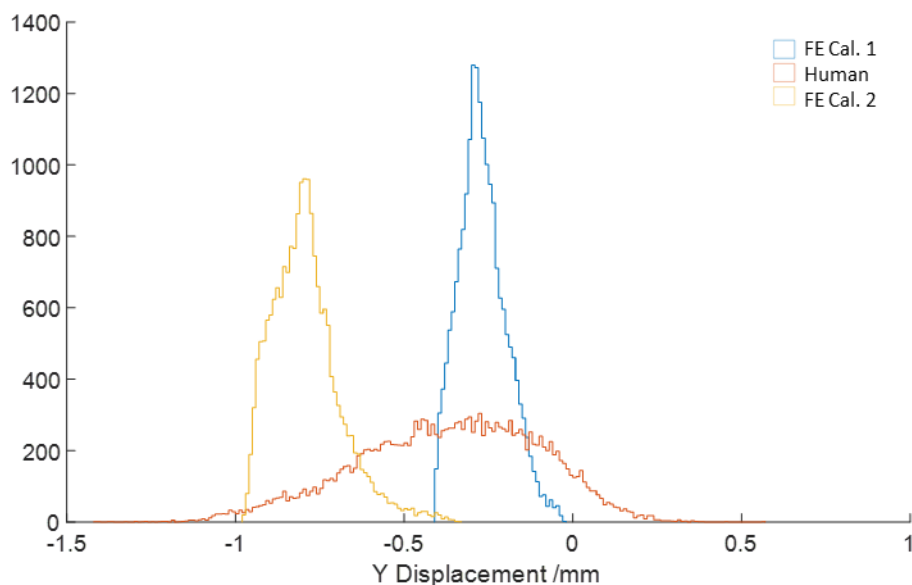


Figure 85 – Sagittal component of the vectors in the reduced ‘middle cerebrum’ nodeset, for both optimisations of the FE model and the human data. Change of the material parameters led to significant change in magnitude of displacement but had little impact on the distribution.

Again, for reference, Schnaudigel et al. (4) reported displacements between 0.6-1.3 mm.

The displacement of the brain surface in the FE results is perhaps best visualised as volume change in the PAC, as was shown in Figure 73. In this figure, the volume change was calculated against the prone elemental volume instead of the neutral position such that results were comparable to the literature. Peak elemental volume changes in the PAC for calibration 2 were in the order of $\pm 60\%$. Further analysis was conducted to compare this to the data from Tsutsumi

et al. (141) more directly. In that study, volume change was measured over a midsagittal region from the anterior to a line defined by the coronal suture. It was estimated that this defined a region approximately equivalent to the anterior third of the brain. Considering only elements in this region, the prone and supine volume was 3,860 and 4,300 mm³, respectively. With reorientation from prone to supine, this equates to a volume change of 11.3% in the FE model, compared to that of 17.8% \pm 11.7% found by Tsutsumi et al. Bearing in mind that the approximation of the region of interest will affect this comparison, the PAC volume change resulting from the calibration 2 falls well within a realistic range. In contrast, calibration 1 yielded a peak volume change in the order of 5%. This indicates that the volume change within the PAC as a whole would be considerably lower than that expected according to Tsutsumi et al.

With confidence that realistic levels of PAC volume change occur in the model generated by the results of calibration 2, we now consider the surface displacement which drives this. Figure 86 shows the surface displacement magnitude of the final model from a number of viewpoints.

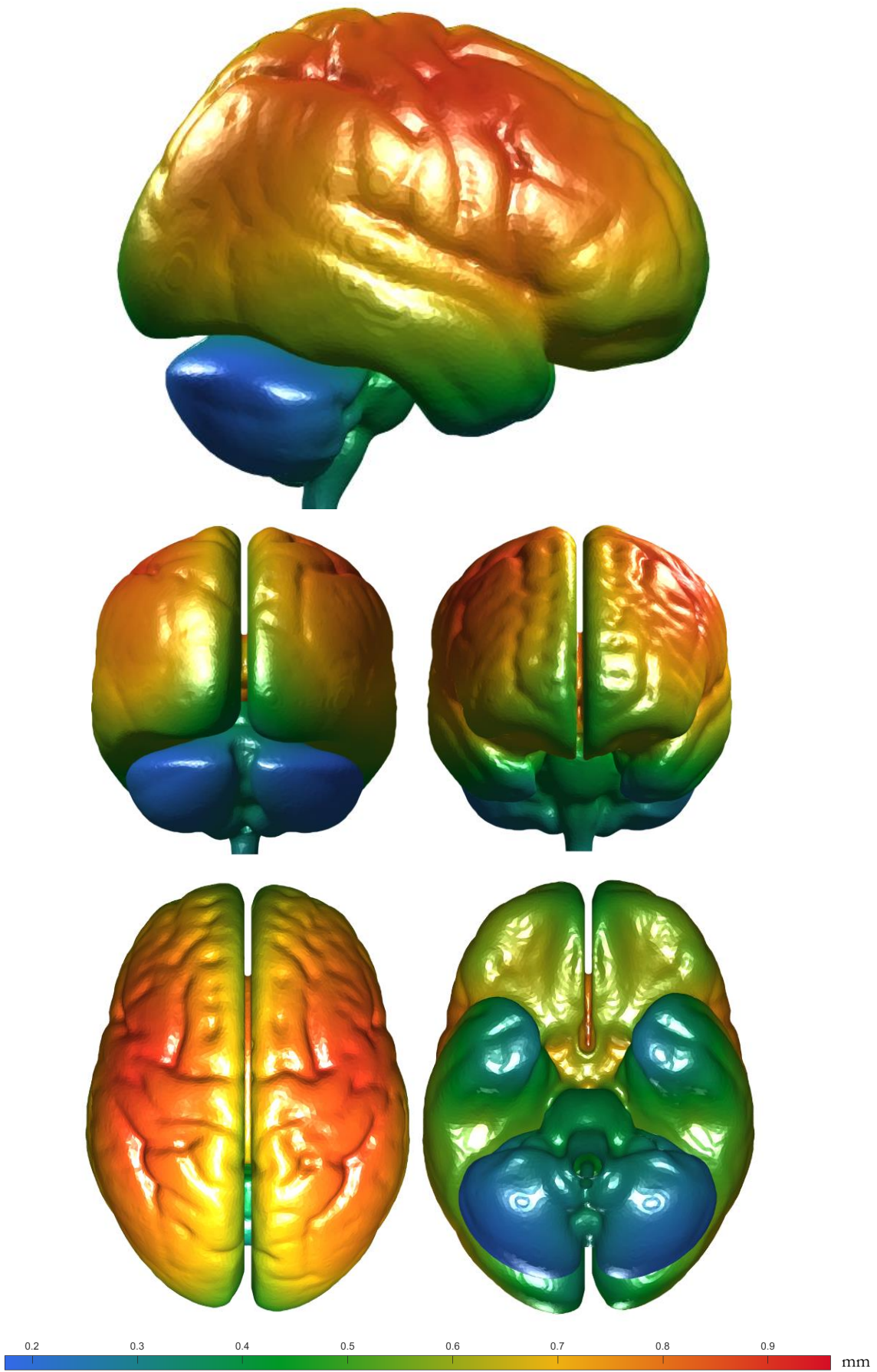


Figure 86 – Surface displacement magnitude in mm from the calibration 2 final FE model.

The anterior and posterior poles of the brain exhibit relatively low displacement, in the order of 0.4 mm. In contrast, the PAC had the greatest volume change in these regions, as the displacements acted normal to the surface. In general, the superior, parasagittal regions experienced the greatest displacements, peaking in the order of 1 mm. Although it is acknowledged that the model did not incorporate the relatively stiff bridging veins which are present in this region. The relatively constrained and geometrically complex inferior regions moved the least, with the cerebellum indicated to be most stable. This is likely an underestimation as no neck bend was simulated in the model and this is known to induce cerebellar movement (195). Surface displacement patterns can be inferred by the displacement vectors; sampled across the volume of the brain, as shown in Figure 87. In general, there is remarkable similarity between the FE model, the trends annotated by Monea et al. (93) in Figure 78 and the phantom study, but not with Mikkonen and Laakso (94), shown in Figure 79. However, all MR studies are impacted by an unknown quantity of image distortion. This has a potentially significant impact on the measured displacement field.

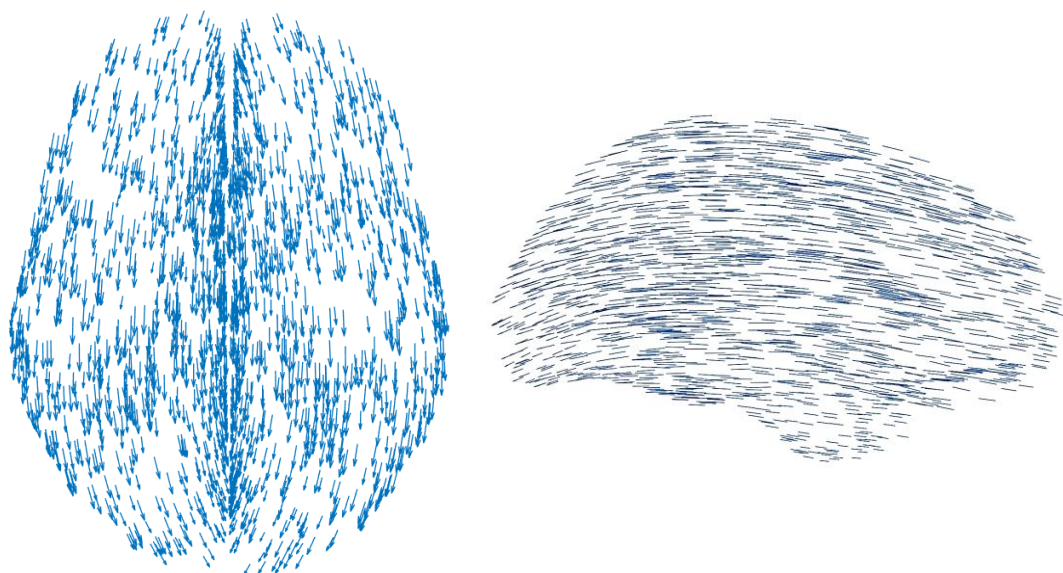


Figure 87 – Vector plot of displacement induced with prone-to-supine reorientation across the volume of the cerebrum, shown from superior [left] and lateral [right] viewpoints. Arrows are intended to show the displacement pattern and have been scaled by a factor of 10 for clarity.

The intention of this work was to highlight a likely set of material parameters over which realistic displacements can be achieved. When considering the accompanying human study, the published data and all the associated limitations, it appears that the displacement field generated with the material parameters found in calibration 2 fits with what could be expected within a typical person. In the future, should more patient data become available and the boundary issue with the image processing be resolved, the methods here could be readily applied and used to generate enough data for form a more statistically significant representation of variation across a wider population. However, in the context of this study that is not possible, and the results generated here are instead intended to present a realistic example.

Material Parameters and Sensitivity

Due to uncertainty in the validity across the entire volume of the validation data, calibration was performed over the whole cerebrum and a subset where the exterior nodes were removed, leading to two parameter sets. In excluding such significant portions of the volumetric displacement data, the author concedes that this raises questions about the validity of using any of it. However, upon comparison to other literature, confidence was established that the second set was likely to represent the displacement pattern of a typical person. In this section, we consider the parameter identification method and compare the results obtained to the literature. To recap, the parameters found are re-presented in Table 6-1.

Table 6-1 – Material parameters identified after calibration with the entire cerebrum and reduced volume.

Parameter	Calibration 1	Calibration 2
Bulk modulus /Pa	187,000	127,000
'Shear modulus' /Pa	1,580	1,250
Exponential coefficient	-1	-16.9
Pia Young's modulus /Pa	254,000	250,000
Spring constant /N/m	10.4	0.5

Brain

The brain itself has received considerably more attention in the literature than any of the surrounding structures. Numerous constitutive models have been developed to capture its unique properties, each better or worse at doing so in specific loading scenarios. These can use as few as three, but as many as 20 material parameters (10). As mentioned in Chapter 3, the material parameters which can be identified for any model are normally only valid for the specifics of loading and constraint in which they were obtained. As such, when choosing a constitutive model, one should carefully consider the physiological process at hand (10).

When choosing the constitutive model to study PBS, the desired outcome was first considered. This was namely to understand displacement throughout the brain with reorientation relative to a supine position. After some initial investigation, it was concluded that equilibrium would be reached in a relatively short time ($\sim < 10$ minutes); although measurement could not be made in a shorter time than this due to practicalities of MR imaging. This settling time contradicted one previous report (4). The source of this discrepancy has not yet been identified, but it was felt that even if the brain had not completely settled over this time frame, any further displacement would be negligible. Within surgery it is certain that the time between final fix of head orientation and the beginning of the procedure would be greater than 10 minutes and therefore only the equilibrium shift is clinically relevant.

Time dependency does not need to be considered in the constitutive model when only concerned with the equilibrium displacement. This reduces the number of parameters needed to characterise the material response. This was important, as it is difficult to achieve a meaningful fit with a highly parameterised model when inverse modelling with equilibrium in-vivo displacement data

alone. It was also assumed that displacements would be relatively small and other considerations such as tissue preconditioning would not apply.

The Ogden constitutive model is often suggested when considering the elastic response of brain tissue (10). Although there will always be debate, a lack of clear consensus about a better alternative makes it difficult to conclude that it is not a good option. Furthermore, the relatively simple formulation with as few as three material parameters and successful implementation in some of the prominent studies within the field (112, 117) provided sufficient grounds to use the Ogden model for this study.

Ogden coefficient - c_1

The original formulation by Ogden has been modified by many groups over the years. Such additions considered the time dependant response (112) and material compressibility (115). Some small manipulation of these models is often required to compare the results across different studies. Equation 43 gives the strain energy function as is used in FEBio:

$$\psi = \sum_{i=1}^N \frac{c_i}{m_i^2} (\tilde{\lambda}_1^{m_i} + \tilde{\lambda}_2^{m_i} + \tilde{\lambda}_3^{m_i} - 3) + U(J) \quad 43$$

Here, i allows up to 6 sets of parameters to be defined. This has been shown to improve the fit of experimental data, especially under complex loading regimes such as combined shear and compression/tension (11, 118). However, given the small strains expected, a one term was used here and compared to the literature.

Studies 1-3 of Table 6-2 all use the same formulation, whereas study 4 uses one more similar to the original Ogden version (116). For ease of manipulation, some parameters have had their symbol changed from the original manuscripts. In 1-3, μ is defined to be equivalent to the classical shear modulus according to linear theory (98, 119). Considering first that $\alpha = 2\alpha_0$, this shear modulus relates to C_0 , according to $\mu = \frac{C_0\alpha}{2}$.

Table 6-2 – Literature values for material parameters of the time-independent, one-term, Ogden strain energy density function.

Study	Formulation	Parameter values
1) Miller and Chinzei (112).	$\psi = \frac{2\mu}{\alpha^2}(\lambda_1^\alpha + \lambda_2^\alpha + \lambda_3^\alpha - 3)$	$\mu = 842 \text{ Pa}$ $\alpha = -4.7$
2) Prange and Margulies (117)	$\psi = \frac{2\mu}{\alpha^2}(\lambda_1^\alpha + \lambda_2^\alpha + \lambda_3^\alpha - 3)$	$\mu = 296 \text{ Pa}$ $\alpha = 0.0323$
3) Budday et al. (119)	$\psi = \frac{2\mu}{\alpha^2}(\lambda_1^\alpha + \lambda_2^\alpha + \lambda_3^\alpha - 3)$	$\mu = 350 \text{ to } 1,430 \text{ Pa}$ $\alpha = -25.3 \text{ to } -19.0$
4) Mihai et al. (11)	$\psi = \frac{C_0}{2\alpha_0}(\lambda_1^{2\alpha_0} + \lambda_2^{2\alpha_0} + \lambda_3^{2\alpha_0} - 3)$	$C_0 = -93.9 \text{ Pa}$ $\alpha_0 = -4.0250$ $\mu = 378 \text{ Pa}$ $\alpha = -8.05$

With the format presented in Table 6-2, and formula used in FEBio, a simple conversion is possible: $c_1 = 2\mu$ and $m_1 = \alpha$. As mentioned previously, the quantity c_1 in the results section was referred to as the shear modulus, whereas c_1 is actually two times this quantity. Therefore, calibrations 1 and 2 yielded shear modulus values of 790 and 625 Pa, respectively. The values found here show notable similarity to the results of mechanical testing in the literature. This is especially the case when considering the known levels of variation that exists both between subjects, and regionally over the brain volume.

The regional analysis by Budday et al. (119) considered samples from the corpus callosum, corona radiata, basal ganglia and the cortex. The model was fit to combined loading, yielding mean shear modulus values of 350, 660, 700 and 1,430 Pa, respectively. Without calculating the exact volumetric ratios within the brain, it can safely be said that the corpus callosum is very small in volume compared to the other regions. If these figures are representative of the rest of the brain, an average value would likely be towards the higher end.

When comparing the results of this study to others, it must be remembered that the brain was modelled as an isotropic, homogeneous body, with no inclusion of the cerebral vasculature. Therefore, the stiffness found is likely to be a slight overestimate compared to mechanical testing on samples with no vasculature. Interestingly, calibration 2 did not consider the cortex, which is known to be twice as stiff as the other structures (119), with the obtained value dropping by over 150 Pa compared to calibration 1. Much future work would be required to determine if this is just a coincidence. If not, this result supports the mechanical testing data and also shows the method to be potentially sensitive to regional property change.

The final sensitivity plots of Figure 64 show variation in the order of 0.01 mm due to full range (0 to 1500 Pa) variation of the shear modulus. This suggests that the shear modulus is not a highly influential variable in PBS, and that the impact of regional variation or anisotropy might be limited. On the other hand, the combination of a lack of sensitivity and a result which is very much in line with the literature is extremely encouraging evidence towards the efficacy of the experimental method developed here.

Ogden coefficient - m_1

The exponential coefficient m_1 , often referred to as α , was identified in calibration 2. This parameter functions to scale the stresses as the stretch changes, allowing models to capture the complex non-linear behaviour that is often found experimentally. The effect of this is illustrated in Figure 88, which shows the impact of variation in the value of α on the second derivative of the strain energy function (instantaneous deviatoric stiffness), with μ at a value of 750 Pa.

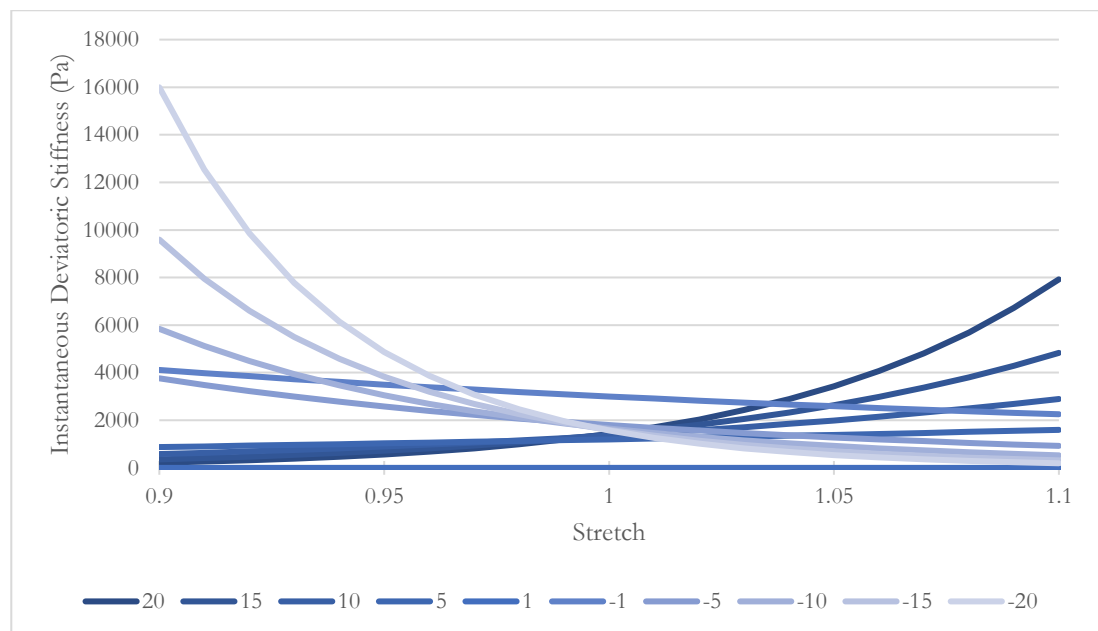


Figure 88 – Plot demonstrating the effect of exponential coefficient variation on the instantaneous deviatoric stiffness, using a realistic corresponding shear modulus.

There are two key things to note from this. Firstly, at small stretches, variation in the value of this coefficient has a small impact on the deviatoric stiffness. This effect is almost negligible when considering variation over a range of -5 to -15, for example. Secondly, it illustrates the reason most groups have identified the parameter to be negative for the brain, as testing has shown the tissue to have increasingly greater stiffness in compression and reducing stiffness in tension (119).

In calibration 1, this coefficient was found to have no effect on the result, probably due to the very small average strains involved. In the calibration 2, a value of -16.9 was identified, falling very much in the range of commonly reported values in the literature. Sensitivity was significant after the initial iteration obtained more realistic parameter ranges for the bulk modulus.

Bearing in mind that μ and α should not be interpreted alone, but together, the identified combination of 625 Pa and -16.9, respectively, represent a realistic approximation of whole brain behaviour.

Bulk Modulus

It is now well established that the incompressibility assumption is only valid in certain circumstances (10, 115). During mechanical testing, Budday et al. (119) found a clear pre-conditioning effect over three consecutive cycles. After soaking the sample with phosphate-buffered saline solution for 60 minutes, they found the impact of pre-conditioning to effectively disappear. This suggests that the effect is down to fluid loss, rather than damage to the tissue itself, further emphasising the influence of relative volume change.

When not interested in the time-dependant modelling of consolidation theory, the bulk modulus and Poisson's ratio can be used to account for volume change within a material. Conversion between the quantities is only valid with certain measures of stiffness and at small strains, but this is the case with PBS. The bulk modulus was determined to be 127 kPa in the final model. With the shear modulus of 625 Pa, the Poisson's ratio ν can be found according to Equation 44:

$$\nu = \frac{3k - 2\mu}{2(3k + \mu)} \quad 44$$

yielding a result of 0.497. Assessment of the bulk modulus directly in the literature has been limited. Values for the bulk modulus in the order of 40,000 Pa ($\nu \sim 0.4$) were initially reported (127, 131, 132), but are thought to be incorrect due to methodological assumptions. In direct consolidation testing of real human tissue, Franceschini et al. determined a drained Poisson's ratio of 0.496 (115), with full consolidation occurring with volumetric strain in the order of 3%.

The lack of attention given to the bulk modulus in most modelling implementations initially gave the suggestion that it was an unimportant factor purely required for mathematical stability in modelling. It quickly became clear that it is arguably the most influential factor in PBS, at least when varied over commonly used ranges. With a bulk modulus in the order of 500,000 Pa ($\nu \sim 0.499$) and up, brain shift is limited to small scale, rigid body displacement. On the other hand, much lower values lead to unrealistically large displacements. The obtained value of 0.497 strongly supports the findings of Franceschini et al. (115); especially when considering that the volumetric strains found here peaked at 0.7%, suggesting full consolidation was not achieved. Although the difference between 0.499 and 0.497/0.496 is small in terms of Poisson's ratio, it is very large in terms of bulk modulus and this study confirms that in confined loading scenarios such as PBS it is very influential.

Whilst is unlikely that local anisotropy would impact PBS significantly (119), regional variation of bulk properties might offer interesting insight into local displacement patterns, especially when considering the non-equilibrium state at a similar strain rate to that studied here.

Arachnoid trabeculae

The arachnoid trabeculae have probably received the least attention of all the intracranial structures and have been all but ignored until recently. The method employed utilised thousands of discrete spring elements, spaced in a relatively consistent pattern across the surface of the brain. The stiffness of the structure as a whole depends on the stiffness of each element and various geometric details. Using the quantities detailed in Table 6-3, the calculation provided in Equation 45 allows conversion of the spring constant obtained in the material study to an approximate value for the Young's modulus of the layer.

Table 6-3 – Parameter values used in the calculation of the layer stiffness of the PAC.

Symbol	Quantity	Value
σ	Tensile stress	N/A
ε	Tensile strain	N/A
F	Reaction force	N/A
A_{spring}	Area per spring	N/A
Δx	Change in spring length	N/A
A_{total}	Total surface area	0.083 m ³
x	Original spring length	0.0021 m
a	Spring constant	0.5 N/m
$n_{springs}$	Number of springs	38,000
E	Young's Modulus	480 Pa

Some of the quantities are not actually needed in the final calculation as they cancel out or can be decomposed to simpler components. This derivation is summarised in Equation 45:

$$\therefore E = \frac{\sigma}{\varepsilon} = \frac{\frac{F}{A}}{\frac{\Delta x}{x}} = \frac{Fx}{A_{spring} \cdot \Delta x} = \frac{a \cdot \Delta x \cdot x}{\frac{A_{total}}{n_{springs}} \cdot \Delta x} = \frac{n_{springs} \cdot a \cdot x}{A_{total}} \quad 45$$

As the spring elements only offer stiffness in tension, the value obtained here also only applies in tension. The resulting average stiffness is only dependant on four quantities: the number of springs, spring constant, average PAC thickness and total surface area of the brain. The conversion yielded a equivalent Young's modulus of approximately 480 Pa.

In comparison, direct measurement by Jin et al. (60, 97, 134, 135) estimated the minimum tensile stiffness to be in the order of 61 kPa, increasing with increasing strain rate. Mazumder et al. (136) used inverse modelling methods based on indentation of sheep brain. The schematic in Figure 89 represents the physical test, which generated a load displacement curve as the indenter was progressed into the tissue through a cavity in the skull.

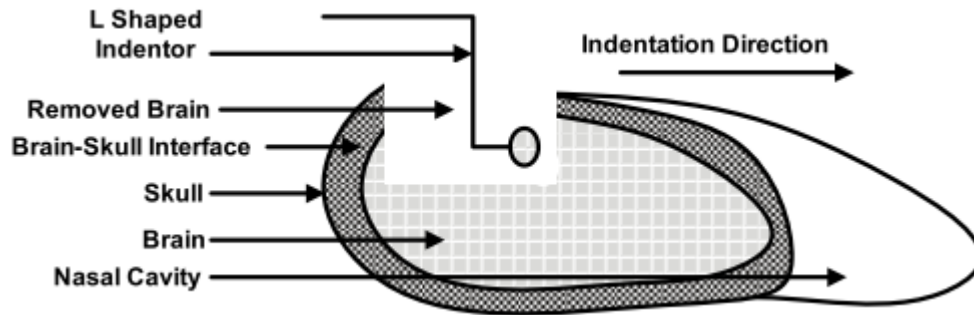


Figure 89 – Schematic of the experimental set-up used by Mazumder et al., adapted from (136). Brain displacement was measured by tracking markers placed into the brain tissue with X-ray images. Inverse modelling involved the generation of a homogeneous brain structure, attached to the rigid skull with approximately 5,000 spring elements, 0.3 mm in length, representing the estimated thickness of the PAC. Results suggested a stiffness of the ‘brain-skull interface’ of $11.45 \text{ Nmm}^{-1}/\text{mm}^2$. For ease of comparison, this was converted to meters, yielding a value of $11,450,000,000 \text{ N m}^{-1}/\text{m}^2$.

Results from the current study were also converted to these units. Considering the spring constant: $a = 0.5 \text{ N m}^{-1}$ per spring, and the total springs per unit area: $38,000/0.083 = 460,000$ springs/ m^2 , the equivalent stiffness is the product of these two quantities, yielding a value of $230,000 \text{ N m}^{-1}/\text{m}^2$. If the stiffness obtained by Mazumder et al. was applied to the same geometry used in this study, the ratios of known values found here can be used to calculate an equivalent tensile Young’s modulus of approximately 24 MPa. These results are summarised in Table 6-4.

Table 6-4 – Comparison of the difference between value found for the tensile stiffness of the PAC found in the present study and the literature.

Study	Approx. Young’s Modulus /Pa	Factor of difference
Present	480	1
Jin et al. (97)	61,000	127
Mazumder et al. (136)	24,000,000	48,000

Whilst considering that these calculations are an approximation, a significant discrepancy exists between the results, particularly with those by Mazumder et al. When considering the implementation of this value, Wang et al. (178) commented:

“[the Mazumder et al. experiment was] ... conducted under loads compatible with neurosurgery in a direction tangential to the skull ... [therefore containing] ... very limited information about the brain-skull interface stiffness in direction normal to the skull ...”

This is a particularly interesting comment, as the two papers share a number of co-authors, but this limitation is not mentioned in the paper by Mazumder et al. itself, aside from a caution in extrapolating this sheep data to humans. To add to this, assuming the calculations are sufficiently accurate, it is unlikely that a fluid layer sparsely populated with fibrous strands and vessels is likely

to have a stiffness of 24 MPa; greater than what some consider to be the stiffness of the dense, fibrous dura mater (14). In fact, the solid volume fraction of subarachnoid space has been shown to be as low as 13.8 % in some regions, although normally more in the region of 30 % (196). Considering this, and as the authors of the paper itself have later stated that the result is inapplicable to normal stiffness, using a spring stiffness/distribution of $11.45 \text{ Nmm}^{-1}/\text{mm}^2$ is not advisable.

The differences between the present results and those of Jin et al. (97) are more difficult to explain. One factor might be strain rate; Jin et al. used rates of 0.22 s^{-1} to 49 s^{-1} . If a very crude approximation of the present results is taken, assuming that elements undergo a strain of 0.1 over a period representing 5 minutes (300 s), the resulting strain rate is over 600 times slower than that used experimentally by Jin et al. The PAC does not appear to be as sensitive to strain rate as some other intracranial soft tissues (97, 119), probably due to its relatively sparse solid distribution in its drained state. However, the experimental results do suggest greater stiffness at higher strain rates, possibly explaining some part of the difference.

Another source of the deviation might be in the experimental method itself. Testing out-of-plane tensile properties on thin, membranous structures is inherently difficult, as each side must be bonded to the testing rig, in this case using cyanoacrylate. Whilst care was taken to ensure that there was no adhesion of the sides, it would prove extremely difficult to ensure this did not happen to any extent with such a delicate, thin structure.

Finally, immature bovine tissue was obtained for this mechanical testing. Little information about the details of testing is known, as the full paper could not be obtained. Assuming similar methods to other experiments in their series were used, the initial thickness, x , of the PAC samples was only $24 \mu\text{m}$. Engineering strain, ϵ , was calculated for all samples, such that $\epsilon = \frac{\Delta x}{x}$, with peak strains of approximately 0.3. It is inferred from this that the total extension in the tissue, Δx , was only in the order of $8 \mu\text{m}$. When using engineering stress and strain to calculate the Young's modulus, results are highly sensitive to the initial thickness that is defined. At such small scales, ensuring accuracy in these measurements is difficult, especially when attempting to capture the gradual engagement of numerous material fibres. In a later paper, this gradual fibre recruitment is considered in a proposed constitutive model, developed to capture the unique behaviour of the PAC. As such, it is difficult to have confidence that the values obtained for large strains in a thin bovine layer are applicable to the adult human with small strains.

With the other studies considered, the results of the present study must also be critically assessed. Volume change in the PAC was actually marginally lower than the average found by Tsutsumi et al. (141). When also considering the sensitivity analysis of the spring stiffness, the curve did not reach a minima before the lowest value of 0.5 N/m . therefore, it appears that the results of the

present study may still be an overestimate, although more data is required to give confidence in this finding.

The mean elemental surface area, which relates directly to the spring distribution and therefore stiffness, was relatively consistent at $1.3 \pm 0.5 \mu\text{m}^2$, with no apparent regional bias. Of course, this study is open to the same error resulting from the use of an average initial thickness, however in this case it is directly measurable to a high degree of confidence. Anatomically, the design used did not incorporate bridging veins individually, which are of considerably greater stiffness than the combined stiffness of distributed arachnoid trabeculae (18). Therefore, the obtained value for trabeculae is potentially an overestimate of what would be expected with no bridging veins and instead represents a combination of all structures within the PAC.

Whilst it is difficult to rebuke the results of direct mechanical testing, the results found here indicate that the PAC stiffnesses indicated by Jin et al. (97) and especially by Mazumder et al. (136) are overestimates, potentially by a significant margin. If employed in this model, this level of stiffness would lead to an immobile brain surface, which is known not to be the case in PBS (141). That said, care should be taken when applying the stiffness found in the present study to higher strain-rate loading scenarios. It is also critical to remember that this value was found using a combined model with spring representation of the PAC and FSI modelling of the CSF. In this case, the CSF supported all but $\sim 0.5 \text{ N}$ of the weight of the brain in total. If this was not included, the optimum value of the spring stiffness would have been considerably higher, and the mechanics of the deformation would have changed. It should be noted that similar spring representations have been used in the past, but intentionally defined to be a higher value due to the lack of a fluid component in the model (153, 194). Values obtained with this adjustment were not considered in this analysis.

On this basis, it is recommended that if using a spring connector representation of the PAC with combined FSI in quasi-static loading, a spring stiffness of $230,000 \text{ N m}^{-1}/\text{m}^2$ or equivalent Young's modulus of 480 Pa should be used.

Pia mater

The pia mater is often included in high-strain-rate models, but with inconsistent parameter values and thickness, with some suggesting stiffness of 10 MPa (109, 161, 178). The results of the present study suggested a much lower value. In fact, this value was so much lower that the range defined for the training models was insufficient to capture a minima, with the lowest value within the range being 250 kPa . This may be in part due to the boundary effects once again, as the pia mater lines the surface of the brain. However, it is suspected that it plays an important mechanical role in limiting the non-rigid deformation of the brain.

In identifying an approximate value of 250 kPa, this study presents a finding contrary to what is commonly implemented in the literature. A greater understanding of displacement at the boundaries is required before more confidence can be had in the value.

Dura mater

The dura mater was not included in the parametric study, its expected stiffness was initially found to have a negligible influence on the displacement field when considering sagittal reorientation. This was reassessed within the analysis of the surgical prediction test case and as such not discussed here.

Model Derived Mechanics of Positional Brain Shift

As this is, to the best of the author's knowledge, the first computational analysis of positional brain shift, it is difficult to compare the results found here to the literature. Once again, works from adjacent fields are not applicable. For example, low acceleration impacts have been shown to generate near-rigid body displacement, with greater accelerations inducing non-rigid deformation (197). That said, apparent rigid body displacements were reported to be in the order of 4-5 mm. However, this is not conducive with typical SAS thickness and is therefore unlikely. Further studies on the mechanics of high strain rate brain deformation have suggested mechanisms which are unlikely to apply here (198).

Based on the results found in this study, the mechanical role of the intracranial structures is considered. Although displacements are small, PBS displays a complex pattern, that is not just rigid body translation. The dura mater is a relatively thick layer with high stiffness. Under the loads induced by gravity, deformation in this layer was negligible, apart from when loaded laterally. On this basis, the dura mater should be included when considering higher loads, or with non-sagittal loading.

The most influential component stabilising the brain is the CSF, which generates a buoyancy force almost entirely counteracting the weight of the brain. The remaining physical stabilisation on the surface of the brain comes from the arachnoid trabeculae. The surface displacement is indicative of the rigid body component of displacement. In a typical person, this may account for approximately 0.5 mm of translation when reorienting from supine to prone. When analysed from a neutral position, it was shown that stretch of the arachnoid trabeculae is only in the order of 0.1 – 0.2 mm, on the side in tension. The relatively even displacement on the sagittal extremes stem predominantly from the trabeculae which are compressed in the initial loaded orientation returning to a more neutral position in the second loading orientation. This concept is represented schematically in Figure 90.

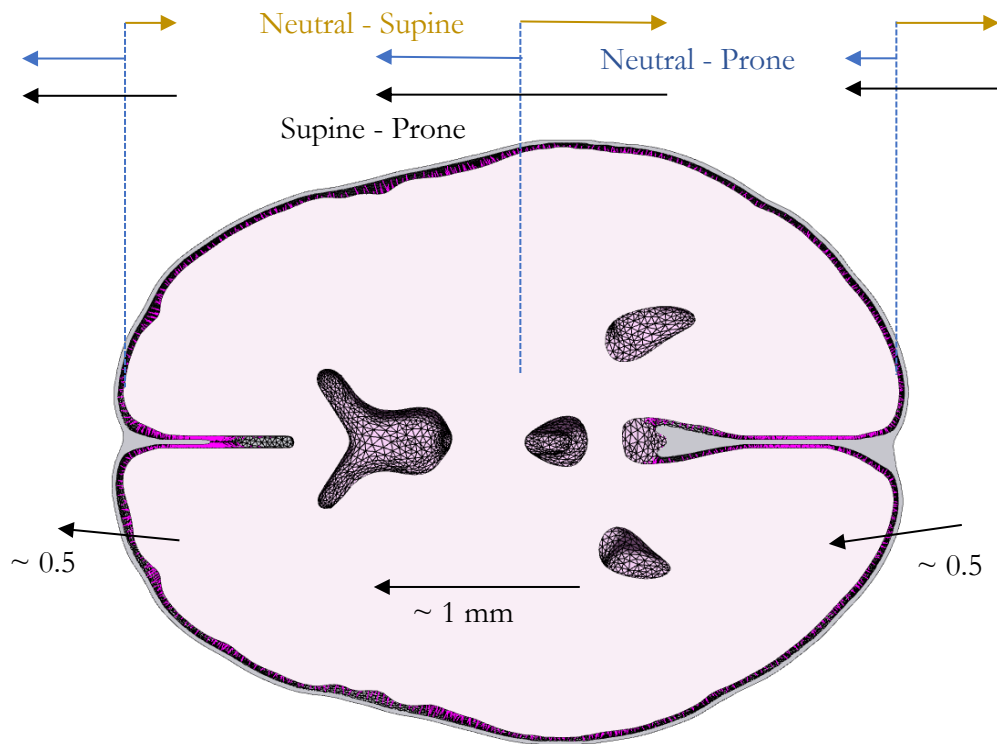


Figure 90 – Schematic representation of the extension and compression of the PAC in neutral – prone/supine and the resulting supine – prone displacement.

Although the stiffness of the PAC was found to be very low in tension, it is still critical to stabilise the brain position, as left unattached it would sink towards the surface of the skull. Displacement in superior regions of the brain are greater than inferior regions. This is likely due to increased thickness of the subarachnoid space near the superior sagittal sinus. This difference in displacement generates a component of rotation in the sagittal plane.

The pia mater is in direct contact with the arachnoid trabeculae. In this model, a lower stiffness than expected of 250 kPa yielded the best results. This was surprising given the thickness used here was orders of magnitude lower than other works (178). The results suggest that a stiffer pia mater is responsible for distributing stress across the surface of the brain, but also in limiting the stretch of brain along the gravitational axis and in doing so, reducing stress on the brain itself.

That said, stress in the brain tissue has almost negligible deviatoric components when compared to volumetric equivalents. In reorientation, a fluid pressure head develops over its depth. Whilst the interstitial fluid itself and blood are highly incompressible on their own, the results suggest that fluid redistributes throughout the bulk of the brain. This redistribution is the source of the non-rigid deformation, which presented as increased deformation in the deeper structures of the brain. In this quasi-static scenario, a bulk modulus of 127 kPa best represented the displacement seen in the subject data. However, it is fully acknowledged that the potential intersubject variability in this figure could be significant.

The small deviatoric stresses in the brain corroborate the findings of the sensitivity analysis, which showed relatively low sensitivity to the shear modulus. Although the model used did not incorporate any regional property variation or local anisotropy, this low sensitivity indicates that the displacement field would not be significantly impacted by this additional detail anyway.

Implications for Modelling

The purpose of continuing to develop constitutive models and further characterise soft tissues is to enable more realistic and accurate computational models. Therefore, it is useful to briefly consider how the in-vivo identification of material parameters and mechanical analysis of PBS presented here may impact future works.

Brain

In some areas of research, such as the study of infusions to the brain, a non-linear poroelastic material model is necessary (159). This thesis is also not the first to discuss the potential importance of the bulk modulus itself (129). This level of complexity is not always essential, and it is accepted that in some areas of modelling the impact of bulk modulus is likely to be negligible (162). However, the value of bulk modulus used is often varied inexplicably (129). An in-depth review of the literature in (130) reports values for the Poisson's ratio to be $0.4 \leq \nu \leq 0.495$. Due to the number of these studies that have obtained acceptable results with such varying values, it cannot be said that all future works should consider the value determined in the present work. On the other hand, if one is considering loading in the order of minutes to hours, like the majority of neurosurgical cases, it is likely that the bulk modulus could play an important role in the mechanics of the deformation. With the impact in PBS in the order of tenths of millimetres, this is especially the case as the research community strives for increasingly accurate models.

The Ogden coefficients identified here add to an already well documented area of research (11, 112, 119). Whilst not necessarily offering a new assessment of the values, it was instead encouraging to show the methodology developed here was able to so accurately reproduce commonly accepted results based on MR data alone. Probably more significant a finding is the lack of sensitivity to the deviatoric stiffness parameters seen in PBS. This would suggest that complex dispersions of anisotropic tissue are potentially unnecessary; however, this is said with caution, as the premise of this work is based on ever improving accuracy.

Pia-arachnoid complex

Arguably the most significant contribution of this study is the implementation of a full spring/FSI representation of the PAC and identification of the representative layer stiffness. Studies concerning TBI are generally more concerned with the PAC and bridging vessels, but have often relied on the work of Jin et al. (97) for defining the stiffness of trabecular components (133).

If the findings of this study prove correct, this level of stiffness is an overestimate. Due to the methods of modelling often used, this may not have been apparent in previous studies (153, 194). For example, if the PAC is modelled with spring connectors but no FSI or other representation of the CSF layer, the important mechanical role of the CSF will instead be taken solely by the springs in the model. This would mean that the impact of the overestimated spring stiffness will be counteracted by unrealistically high loading, leading to similar overall displacement. This would greatly impact the distribution of stress on the surface of the brain, which is the main area of interest.

Intuitively, it seems logical that a layer of similar stiffness to the brain tissue would contribute to energy absorption in impact scenarios, reducing the forces experienced by the surface of the brain. As such, the contrary exists for a layer with considerably higher stiffness, presenting an evolutionary disadvantage. This explanation would support the PAC stiffness values obtained in this study; however, it is important to note that this is speculation and is not the author's area of knowledge.

This concept was recently demonstrated by Scott et al. (133), who found that a spring connector model was not able to distribute loads efficiently over the surface of the brain. Instead, it was found that representing the PAC as a solid transversely isotropic layer, with regional stiffness calibrated to regional trabecular volume fraction, yielded a more representative stress distribution. Whilst discussing their results, it was considered that the impact of CSF in this interaction would be minimal. However, it would be very interesting to repeat the tests with the combined spring/FSI model, a spring distribution representative of trabecular volume fraction and stiffness of the order found in the present study. Again, if PAC stiffness is lower than previously reported, it may be demonstrable that the CSF layer is in fact the most important mechanical contribution, and the trabeculae may act in a secondary role to stabilise the impact. Recent works implementing FSI layers have shown promising results (168); however, publications using this method are still limited.

On this basis, it is proposed that modelling the brain-skull interface as a tied contact, sliding contact, or anything in-between (178) may not be advisable in all circumstances. With increasing computational power, combined spring/FSI models or similar should be considered, where possible. Whilst the mechanism of deformation between quasi-static and impact scenarios are likely driven by poroelastic and viscoelastic responses, respectively, it is likely that this improved representation of the PAC will benefit all brain model studies.

Recap: Objectives

1. Understand the key factors involved in brain shift, and which should be considered in the FE model.
2. Develop a FE model incorporating key anatomical structures (which can also be used for the phantom model).
3. Investigate the material sensitivity of brain shift and the mechanics of the process using human data and the FE model.
 - i. There is no conclusion in the literature about the magnitude or displacement pattern seen in sagittal reorientation PBS.
 - ii. The likely displacement pattern in a typical person involves surface displacement which is greater in superior regions, away from supporting structures and sagittal poles. Displacement is greatest in deeper structures, in the order of 1 mm, suggesting a non-rigid deformation.
 - iii. Material parameters were identified using statistical methods. Results indicated that the deviatoric stiffness of the brain is less important than compressibility and that the arachnoid trabeculae are less stiff than has previously been reported in the literature.
4. Predict a test-case of displacements in a clinically relevant region that could be used as a pre-operative adjustment.

Surgical Prediction Test Case

To address the potential future applications, simulations were run with the final material parameters in a series of 6 orientations. These positions represented what is commonly seen in surgery, based both on the literature available and the author's experience. Displacement in the STN was analysed as it is a common target location for DBS procedures (33).

Throughout development it was found that inclusion of the dura mater increased computational time and made negligible impact to the displacements found in sagittal reorientation. The first intention of the test case was to reassess the assumption and confirm it held true. Comparison of model results with the dura included and excluded, with the final material parameters, showed discrepancies in the order of 20 μm , a result which was still considered to be negligible.

Although not tested in the early stages, it was suspected that due to its geometry, the dura may play a more important role in coronal plane reorientation. Figure 91 shows a view of the dura from inside the intracranial cavity with all other structures removed. The arrows indicate displacement induced from neutral to right decubitus orientation, peaking in the order of 0.35 mm.

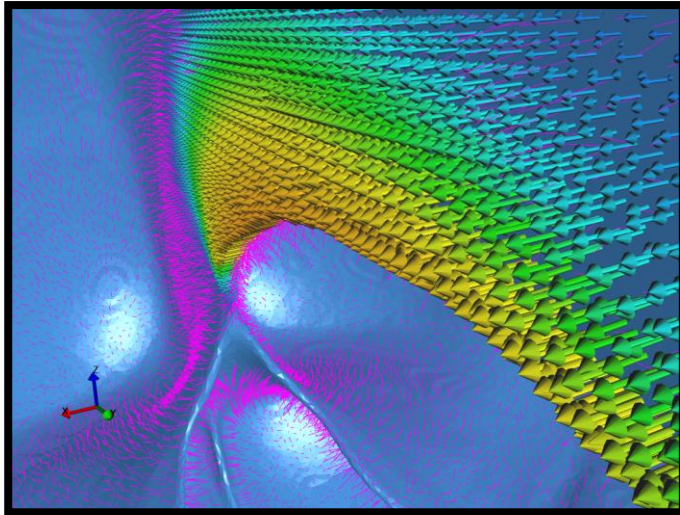


Figure 91 – Interior view along the midline of the falx cerebri and cranial dura mater, showing the displacement (peak 0.35 mm) induced from neutral to right decubitus reorientation.

Whilst the displacement is small, it is well within the order of magnitude considered to be significant and therefore is an important inclusion when considering non-sagittal reorientation.

Test case displacement in the STN indicated supine to prone displacement of up to 0.65 mm in the direction of gravity. A typical electrode has a diameter of 1.27 mm (199), meaning an implantation might have a radial error of half the electrode width itself with an implantation trajectory normal to this displacement. To put this into context, not correcting for this magnitude of brain shift could almost double the targeting error in state-of-the-art systems (6). Reorientation from supine to semi-supine positioning is commonplace in the literature, with some groups advocating this approach to limit brain shift (29, 200). When 45° from horizontal, the STN was displaced by approximately 0.2 mm to the inferior. Interestingly, this is a similar magnitude to the difference in accuracy between iMRI systems and the best performing systems not using this technology (6).

Finally, the test case supported previous reports which found greater displacement with lateral reorientation compared to sagittal (4, 93). This is potentially explained by the finding that the falx cerebri only undergoes significant deformation when not loading along its long axis. Mechanically this is logical, as its second moment of area is considerably higher when loaded in the sagittal plane. However, it is still meaningful to confirm what was expected.

Although this final example of a test case is brief, it utilises all that has been presented in this thesis whilst demonstrating the future potential of this method.

Recap: Objectives

1. Understand the key factors involved in brain shift, and which should be considered in the FE model.
2. Develop a FE model incorporating key anatomical structures (which can also be used for the phantom model).
3. Investigate the material sensitivity of brain shift and the mechanics of the process using human data and the FE model.
4. Predict a test-case of displacements in a clinically relevant region that could be used as a pre-operative adjustment.
 - i. A test case was computed, considering the effects of six orientations on PBS in the STN; a typical target in stereotactic neurosurgery.
 - ii. Of the positions tested, supine-to-prone reorientation led to the greatest displacement around 0.7 mm. Orientation change as little as 45° rotation in the sagittal plane still induced meaningful displacement.

Limitations

The model developed as part of this study has a number of simplifications and limitations. Geometrically, the model required smoothing at the segmentation phase, both to allow for creation of the physical phantom and to increase the computational stability. The area most affected by this was the surface of the brain, where in some regions the gyri and sulci were difficult to distinguish. However, it must be noted that as the MNI 152 data set used was obtained in the supine position, PBS might explain the reduced extent of these features on the posterior brain compared to the anterior.

Whilst care was taken to follow the true shape as consistently as possible, Boolean shape change functions were needed to ensure minimum thickness in some structures. This practice is common in modelling (133) and the remaining geometry still shows visual likeness to the MR images from which it was based. A considerable assumption applied to both the geometry and loading, was the ‘neutral’, unloaded state, employed as a starting point for all simulations. This took the form of a relatively even thickness PAC layer and loading from neutral to prone and neutral to supine independently. This was justified, as imaging in an unloaded state is not possible and accurate segmentation of a loaded state would then encounter issues in defining pre-stresses in the structure. Estimating these pre-stresses would arguably be more of an estimation than the neutral position used here. In future, experiments such as inclusion of pre-stresses in the spring elements would be interesting. However, if the model is able to recreate in-vivo displacement without this accounted for, it may be an unnecessary complication.

The use of spring elements is not new, but also not very common (133, 136, 153). To the best of the author’s knowledge, this study is like others in using straight 2D springs to represent the

complex trabeculae. Exceptions come in studies like that of Scott et al. (133), where multiscale models were used to characterise solid elements. Studies such as this have shown that good results can be achieved if the stress/strain response is appropriate, mitigating the impact of the geometric representation itself. That said, much could be done in the future to experiment with different distributions. For the brain an Ogden model, popular with much of the literature, was used here. As only an equilibrium state was concerned, it was felt that a single-phase representation was acceptable, although this is understood to be a simplification. A further limitation is the use of homogenous brain tissue. Whilst the literature has not found statistically significant levels of anisotropy, there is strong support for regional differences in stiffness which were not included in this model (119).

Whilst the methods used here proved to yield remarkably positive results, this study is still significantly limited by the sample size analysed and uncertainty surrounding the true nature of PBS in humans. With only three subjects, statistical analysis of the resulting material properties has largely not been possible, meaning reported values cannot necessarily be considered to represent the population as a whole.

One of the most significant limitations of MR based measurements is image distortion, due to non-linearity in the gradient fields when acquiring the images (53). This distortion can be a significant source of error. For example, during development of the human study methodology, images not corrected for distortion yielded displacement in the brain of up to 8 mm, a magnitude which we now consider to be a gross overestimate. Whilst all MR images used in the present study were corrected for image distortion, it cannot for said for certain that this correction is 100 % accurate and that no artefact remains.

Chapter 7: Conclusions

The clinical effectiveness of stereotactic neurosurgery is directly related to the achieved proximity of the surgical device to the anatomical target. Significant investment is being made to improve the accuracy of the surgical systems, but efforts to mitigate the impact of brain shift have been relatively limited. Upon reviewing the literature, positional brain shift, induced by reorientation of the head, was identified as a potentially significant source of surgical error. It was decided that understanding PBS through computational methods would be the primary focus of this thesis.

A bespoke, biofidelic head model was generated from the MNI 152 dataset, such that the geometry was representative of an average person. Upon reviewing the literature, material and geometric representations of the relevant intracranial soft tissues were identified, with the intention of combining multiple state-of-the-art features. For the brain, the Ogden constitutive model is widely accepted and was used in this work in its commonly apply single term, single phase formulation. This was chosen in the expectation that the bulk modulus could be used as surrogate for fluid redistribution from the base matrix of brain tissue, as is the case in the mathematical representation of consolidation theory. The other intracranial soft tissues were modelled using commonly accepted constitutive models from the literature.

When looking at FE implementations from other types of neurosurgery, it became clear that the dominant boundary conditions in open neurosurgical cases differed greatly from the constrained case of PBS. In fact, more insight was gained through looking at previous models used for head impacts, identifying the brain-skull interface as a key structure in need of improvement in most models. The model developed for this study used FSI functionality within FEBio in conjunction with spring elements, in what is thought to be first full implementation of its kind.

After overcoming notable difficulties associated with 3-dimensional elastic registration, the displacement fields of human prone-supine reorientation generated by Stefano Zappalá were used in identification of material parameters. GEM-SA, free-to-use emulation software, was trained with a set of 60 parameter sets with values defined by the space filling Latin Hypercube algorithm over an initial range estimated from the literature. From this, estimate levels of error from combinations of parameters not tested could be generated, allowing for the identification of optimal parameter sets. Similar techniques employing GEM-SA to derive material parameters for biomechanical models have not been identified in the literature, yet the technique has great potential for future application.

Results for the brain Ogden parameters of μ , α and k yielded values of 675 Pa, -16.9 and 127,000 Pa. Values in the order of 250,000 Pa and 480 Pa were obtained for the in-plane stiffness of the pia mater and out-of-plane stiffness of the pia arachnoid complex (PAC) respectively. The values found for μ and α fall in line with mechanical testing of the literature to a remarkable

degree, especially considering that derivation was based entirely on the fitting of the model to the measured displacement fields. Converting the bulk modulus to Poisson's ratio yielded a value of 0.497. When compared to the most trustworthy literature value of 0.496 (115), this is once again a significant result. Whilst the obtained value is very close to the mathematical definition of incompressibility ($\nu = 0.5$), it represents high levels of compressibility in terms of soft tissues. Most importantly, this finding has shown that with the enclosed-cranium and quasi-static loading, displacement fields are highly sensitive to the bulk modulus and a value cannot be chosen arbitrarily as is often the case. Although only the equilibrium case is considered here, future work could incorporate a biphasic model when time-dependant calibration data becomes available.

The out-of-plane Young's modulus calculated for the PAC was notably different from values available in the literature. It may be the case that experimental assumptions in the literature may have led to overestimates of this stiffness, therefore further testing should be carried out to confirm this. Should further work confirm the value derived here, this finding represents a marked change in what has previously been accepted and is arguably the single most significant finding of this work. However, in practical terms it is important to note that a stiffness of this level is only applicable when the CSF is accounted for in a model through the use of FSI.

The derived material parameters were used in a final model which formed the basis of a kinetic and biomechanical analysis. Examining stress components in the brain tissue confirmed that the process of PBS is dominated by hydrostatic stress, with redistribution of fluid leading to displacement within the tissue. As such, deviatoric stiffness within the tissue offers relatively little support. A rigid body component of displacement was also identified. Tensile forces in the spring elements were concentrated in upper elements relative to gravity in each loading position. Even with the surprisingly low stiffness, the spring elements experience very low strains in tension, due to support of the brain coming almost entirely from the buoyancy force of the CSF. As such, surface displacement was almost entirely due to compression on the lower surfaces in each orientation, with respect to gravity.

The resulting displacement field showed peaks in the order of 1 mm in central structures, with surface displacements in the order of 0.5 mm. Although small, these surface displacements corresponded to volume changes in the order of $\pm 50\%$ in the anterior and posterior poles. These levels corresponded with 2D measurements reported in the literature, further supporting the validity of the method. In clinically relevant regions, such as the STN, displacement was found to peak at 0.65 mm when transitioning from supine to prone but was clinically significant with all orientation changes. As such this confirms PBS as a considerable source of error in stereotactic neurosurgery and provides a basis for a possible correction that could be incorporated into surgical planning systems in the future.

Whilst intended to focus upon stereotactic neurosurgery, the findings of this study have direct implications elsewhere. For example, the thickness of the subarachnoid space is known to influence the results of transcranial magnetic stimulation, presenting a direct application for a model of this kind (94). In other areas of head modelling, the success of the combined spring/FSI representation of the PAC was such that it should be strongly considered by those moving forward.

More than anything, this thesis highlights the great difficulty involved in any computational modelling of biological tissues. Regardless of this, great progress has been made in the development of a computational tool able to derive material parameters based on in-vivo data and predict brain displacements in orientations which would be otherwise immeasurable. With refinement, this could offer a meaningful reduction to surgical expense with improved patient outcome.

Future work

Although much work has gone into developing a model that is as realistic as possible, the main effort has been focused on developing a methodology capable of obtaining material parameters. With this process now established, future work could focus on addressing some of the limitations of the model discussed.

Firstly, it is accepted that the surface of both the brain and skull in the model are unrealistically smooth. In the future, it would be interesting to re-segment these structures. In particular the surface of the brain, including more detail of the gyri and sulci. One reason for this smoothing was due to the presence of significant vessels typically run along sulci. It is foreseeable that inclusion of these vessels may impact the mechanics of motion.

Another obvious area for future work is in the distribution of arachnoid trabeculae. In this study, this was kept constant and based purely on the mesh distribution generated on the surface of the brain. Variations including the number of spring elements per node, offering potential changes in shear/normal stiffness could be investigated along with regional variation in spring distribution or stiffness. Whilst potentially interesting, this work would require a significant improvement on the validation data currently available. Finally, the geometry of subarachnoid space and cerebral ventricles has already been identified by some as a potentially important factor in determining the magnitude of brain shift. Initially, three different segmentations were generated each with a different PAC thickness, but due to practical limitations testing was not carried out on each. With use of a realistic set of material parameters, as has been identified in this study, geometric variation of these structures could advance our understanding of the importance of morphological changes that are well understood to occur over time.

It was identified early in this project that CSF loss is a key factor in brain shift. Given the unpredictability of the lost volume, it was not realistic to try and model this directly. That said, cohesive functions are now available in FEBio which would enable separation from the skull along the relatively weak dural border cells. Basic implementations of this, not presented here, have been promising. Combining this with the spring/FSI model currently implemented could provide an entirely new avenue of use.

Throughout this thesis, much comparison has been made to modelling efforts in tangential fields. Surgical modelling is largely focussed on craniotomies, which involve substantially different boundary conditions. The model could be applied to impact scenarios with relatively few changes; namely update of the material properties to incorporate strain-rate dependency and use of an explicit FE solver. That said, PBS as it has been analysed here is a source of error in a number of different fields, one prime example being non-invasive brain stimulation. With orientation effecting the strength of intracranial stimulation by as much as 10 % (94), prediction methods developed here could feed directly into the FE models used in this adjacent field.

Whilst the potential to advance and re-apply the model is exciting, the next area of focus would be bridging the gap between this initial investigation into the underlying mechanics and the future clinical implementation. The first step would involve repeating the process developed here with more human data. A larger sample size would yield the exciting opportunity to assess changes in the material properties of the brain against patient variables such as age or gender. This method has the notable benefit over ex-vivo mechanical testing in not relying on donated tissues. Patient specific simulation is not the goal; however, if such relationships were established a more tailored prediction of brain shift may be relatively simple to implement.

For example, if age was found to significantly influence brain shift (due to changes in material properties or geometry), individual models could be generated, representing the mean of each decade of life. Each model could then be used to populate a displacement library, in a similar sense to what was shown in the surgical prediction test case. At the time of surgery, the surgeon would input the patient age and orientation during the procedure. Using a method already developed by Stefano Zappalá, this displacement field could then be used to morph the MRI to the settled position, allowing the surgical plan to be based on position of the brain at the time of surgery.

If this system successfully improved the accuracy of device location in the anatomical target, there would be notable clinical benefits. However, in updating the entire MRI, informed trajectory planning, avoiding the future position of blood vessels would also be possible, improving the safety of the procedure. Whilst the work presented here is of academic interest, an implementation such as this would offer true patient benefit for years into the future.

References

1. Mtui E., Gruener G., Dockery P., FitzGerald M. J. T. FitzGerald's clinical neuroanatomy and neuroscience e-book: Elsevier; 2015.
2. Faria C., Erlhagen W., Rito M., De Momi E., Ferrigno G., et al. Review of robotic technology for stereotactic neurosurgery. *IEEE Rev Biomed Eng.* 2015;8:125-137.
3. Renishaw. Neuroinspire surgical planning software for stereotactic procedures. [Video]. Accessed 3/5/19. Available from: <https://www.renishaw.com/en/neuroinspire-neurosurgical-planning-software--8244>.
4. Schnaudigel S., Preul C., Ugur T., Mentzel H. J., Witte O. W., et al. Positional brain deformation visualized with magnetic resonance morphometry. *Neurosurgery.* 2010;66(2):376-384.
5. Elias W. J., Fu K. M., Frysinger R. C. Cortical and subcortical brain shift during stereotactic procedures. *Journal of Neurosurgery.* 2007;107(5):983-988.
6. Li Z., Zhang J.-G., Ye Y., Li X. Review on factors affecting targeting accuracy of deep brain stimulation electrode implantation between 2001 and 2015. *Stereot Funct Neuros.* 2016;94(6):351-362.
7. Kleiven S., Hardy W. N. Correlation of an fe model of the human head with local brain motion--consequences for injury prediction. *Stapp Car Crash J.* 2002;46:123-144.
8. Darling T., Muthuswamy J., Rajan S. D. Finite element modeling of human brain response to football helmet impacts. *Comput Methods Biomech Biomed Engin.* 2016;19(13):1432-1442.
9. Wittek A., Hawkins T., Miller K. On the unimportance of constitutive models in computing brain deformation for image-guided surgery. *Biomech Model Mechanobiol.* 2009;8(1):77-84.
10. de Rooij R., Kuhl E. Constitutive modeling of brain tissue: Current perspectives. *Appl Mech Rev.* 2016;68(1).
11. Mihai L. A., Budday S., Holzapfel G. A., Kuhl E., Goriely A. A family of hyperelastic models for human brain tissue. *J Mech Phys Solids.* 2017;106:60-79.
12. De Boer H. H., Van der Merwe A. E., Soerdjbalie-Maikoe V. V. Human cranial vault thickness in a contemporary sample of 1097 autopsy cases: Relation to body weight, stature, age, sex and ancestry. *Int J Legal Med.* 2016;130(5):1371-1377.
13. Lynnerup N., Astrup J. G., Sejrsen B. Thickness of the human cranial diploe in relation to age, sex and general body build. *Head Face Med.* 2005;1(13).
14. De Kegel D., Vastmans J., Fehervary H., Depreitere B., Vander Sloten J., et al. Biomechanical characterization of human dura mater. *J Mech Behav Biomed Mater.* 2018;79:122-134.
15. Peterson J., Dechow P. C. Material properties of the human cranial vault and zygoma. *Anat Rec A Discov Mol Cell Evol Biol.* 2003;274(1):785-797.

16. Snyder S. R. Troubled mind: The lowdown on increased icp. 2012. Accessed 10/4/19. Available from: <https://www.emsworld.com/article/10624283/troubled-mind-lowdown-increased-icp>.
17. Haines D. E., Harkey H. L., Al-Mefty O. The “subdural” space: A new look at an outdated concept. *Neurosurgery*. 1993;32(1):111-120.
18. Famaey N., Ying Cui Z., Umuhire Musigazi G., Ivens J., Depreitere B., et al. Structural and mechanical characterisation of bridging veins: A review. *J Mech Behav Biomed Mater*. 2015;41:222-240.
19. Morton D. A., Foreman K. B., Albertine K. H. *Gross anatomy: The big picture*. New York, NY: McGraw-Hill Education; 2011.
20. Hartmann P., Ramseier A., Gudat F., Mihatsch M. J., Polasek W. Normal weight of the brain in adults in relation to age, sex, body height and weight. *Pathologe*. 1994;15(3):165-170.
21. Sheikhzadi A., Sadr S. S., Ghadyani M. H., Taheri S. K., Manouchehri A. A., et al. Study of the normal internal organ weights in tehran's population. *J Forensic Leg Med*. 2010;17(2):78-83.
22. Cameron J. *Physical properties of tissue. A comprehensive reference book*, edited by francis a. Duck. *Medical Physics*. 1991;18(4):834-834.
23. Levin E., Muravchick S., Gold M. I. Density of normal human cerebrospinal fluid and tetracaine solutions. *Anesth Analg*. 1981;60(11):814-817.
24. Miyagi Y., Shima F., Sasaki T. Brain shift: An error factor during implantation of deep brain stimulation electrodes. *J Neurosurg*. 2007;107(5):989-997.
25. Goriely A., Geers M. G., Holzapfel G. A., Jayamohan J., Jerusalem A., et al. Mechanics of the brain: Perspectives, challenges, and opportunities. *Biomech Model Mechanobiol*. 2015;14(5):931-965.
26. Abbott N. J. Evidence for bulk flow of brain interstitial fluid: Significance for physiology and pathology. *Neurochem Int*. 2004;45(4):545-552.
27. Kramer D. R., Halpern C. H., Danish S. F., Jaggi J. L., Baltuch G. H. The effect of intraventricular trajectory on brain shift in deep brain stimulation. *Stereotact Funct Neurosurg*. 2012;90(1):20-24.
28. Winkler D., Tittgemeyer M., Schwarz J., Preul C., Strecker K., et al. The first evaluation of brain shift during functional neurosurgery by deformation field analysis. *J Neurol Neurosurg Ps*. 2005;76(8):1161-1163.
29. Takumi I., Mishina M., Hironaka K., Oyama K., Yamada A., et al. Simple solution for preventing cerebrospinal fluid loss and brain shift during multitrack deep brain stimulation surgery in the semisupine position: Polyethylene glycol hydrogel dural sealant capping: Rapid communication. *Neurol Med Chir (Tokyo)*. 2013;53(1):1-6.
30. Miyagi Y. S., K., Kishimoto, J. and Chen, X. . Supine position for the prevention of brain shift in dbs surgery: Technical note and novel hypothesis “water in the inverted cup” mechanism. *Austin Neurosurg Open Access*. 2015;2(1).
31. Hunsche S., Sauner D., Maarouf M., Poggenborg J., Lackner K., et al. Intraoperative x-ray detection and mri-based quantification of brain shift effects subsequent to implantation of

the first electrode in bilateral implantation of deep brain stimulation electrodes. *Stereotact Funct Neurosurg.* 2009;87(5):322-329.

32. Falowski S., Ooi Y. C., Smith A., Metman L. V., Bakay R. A. E. An evaluation of hardware and surgical complications with deep brain stimulation based on diagnosis and lead location. *Stereot Funct Neuros.* 2012;90(3):173-180.

33. Kalia S. K., Sankar T., Lozano A. M. Deep brain stimulation for parkinson's disease and other movement disorders. *Curr Opin Neurol.* 2013;26(4):374-380.

34. Baizabal Carvallo J. F., Mostile G., Almaguer M., Davidson A., Simpson R., et al. Deep brain stimulation hardware complications in patients with movement disorders: Risk factors and clinical correlations. *Stereotact Funct Neurosurg.* 2012;90(5):300-306.

35. Wichmann T., DeLong M. R. Deep brain stimulation for movement disorders of basal ganglia origin: Restoring function or functionality? *Neurotherapeutics.* 2016;13(2):264-283.

36. Richter E. O., Hoque T., Halliday W., Lozano A. M., Saint-Cyr J. A. Determining the position and size of the subthalamic nucleus based on magnetic resonance imaging results in patients with advanced parkinson disease. *J Neurosurg.* 2004;100(3):541-546.

37. Hamani C., Saint-Cyr J. A., Fraser J., Kaplitt M., Lozano A. M. The subthalamic nucleus in the context of movement disorders. *Brain.* 2004;127:4-20.

38. Khan M. F., Mewes K., Gross R. E., Skrinjar O. Assessment of brain shift related to deep brain stimulation surgery. *Stereotact Funct Neurosurg.* 2008;86(1):44-53.

39. Pallavaram S., Dawant B. M., Remple M. S., Neimat J. S., Kao C., et al. Effect of brain shift on the creation of functional atlases for deep brain stimulation surgery. *Int J Comput Assist Radiol Surg.* 2010;5(3):221-228.

40. Datteri R., Pallavaram S., Konrad P. E., Neimat J. S., D'Haese P. F., et al. Potential predictors for the amount of intra-operative brain shift during deep brain stimulation surgery. *Medical Imaging 2011: Visualization, Image-Guided Procedures, and Modeling; 2011. Proc. SPIE 7964.*

41. Halpern C. H., Danish S. F., Baltuch G. H., Jaggi J. L. Brain shift during deep brain stimulation surgery for parkinson's disease. *Stereotact Funct Neurosurg.* 2008;86(1):37-43.

42. Nazzaro J. M., Lyons K. E., Honea R. A., Mayo M. S., Cook-Wiens G., et al. Head positioning and risk of pneumocephalus, air embolism, and hemorrhage during subthalamic deep brain stimulation surgery. *Acta Neurochir.* 2010;152(12):2047-2052.

43. Southwell D. G., Narvid J. A., Martin A. J., Qasim S. E., Starr P. A., et al. Comparison of deep brain stimulation lead targeting accuracy and procedure duration between 1.5- and 3-tesla interventional magnetic resonance imaging systems: An initial 12-month experience. *Stereotact Funct Neurosurg.* 2016;94(2):102-107.

44. Inomed. Deep brain stimulation - dbs - isis mer - stereotactic surgery [Video]. 2015. Accessed 15/6/16. Available from: <https://www.youtube.com/watch?v=7ftnWyMETtk>.

45. Hartmann C. J., Fliegen S., Groiss S. J., Wojtecki L., Schnitzler A. An update on best practice of deep brain stimulation in parkinson's disease. *Therapeutic Advances in Neurological Disorders.* 2019;12:1-20.

46. Cui Z., Pan L., Song H., Xu X., Xu B., et al. Intraoperative mri for optimizing electrode placement for deep brain stimulation of the subthalamic nucleus in parkinson disease. *J Neurosurg.* 2016;124(1):62-69.
47. Seijo F., Alvarez de Eulate Beramendi S., Santamarta Liebana E., Lozano Aragonese B., Saiz Ayala A., et al. Surgical adverse events of deep brain stimulation in the subthalamic nucleus of patients with parkinson's disease. The learning curve and the pitfalls. *Acta Neurochir (Wien).* 2014;156(8):1505-1512.
48. Blomstedt P., Bjartmarz H. Intracerebral infections as a complication of deep brain stimulation. *Stereot Funct Neuros.* 2012;90(2):92-96.
49. Boviatsis E. J., Stavrinou L. C., Themistocleous M., Kouyialis A. T., Sakas D. E. Surgical and hardware complications of deep brain stimulation. A seven-year experience and review of the literature. *Acta Neurochir (Wien).* 2010;152(12):2053-2062.
50. Vergani F., Landi A., Pirillo D., Cilia R., Antonini A., et al. Surgical, medical, and hardware adverse events in a series of 141 patients undergoing subthalamic deep brain stimulation for parkinson disease. *World Neurosurg.* 2010;73(4):338-344.
51. Jiang C., Mo X., Dong Y., Meng F., Hao H., et al. An experimental study of deep brain stimulation lead fracture: Possible fatigue mechanisms and prevention approach. *Neuromodulation.* 2015;18(4):243-248.
52. Samura K., Miyagi Y., Okamoto T., Hayami T., Kishimoto J., et al. Short circuit in deep brain stimulation. *J Neurosurg.* 2012;117(5):955-961.
53. Seibert T. M., White N. S., Kim G. Y., Moiseenko V., McDonald C. R., et al. Distortion inherent to magnetic resonance imaging can lead to geometric miss in radiosurgery planning. *Pract Radiat Oncol.* 2016;6(6):319-328.
54. Starr P. A., Markun L. C., Larson P. S., Volz M. M., Martin A. J., et al. Interventional mri-guided deep brain stimulation in pediatric dystonia: First experience with the clearpoint system. *J Neurosurg Pediatr.* 2014;14(4):400-408.
55. von Langsdorff D., Paquis P., Fontaine D. In vivo measurement of the frame-based application accuracy of the neuromate neurosurgical robot. *J Neurosurg.* 2015;122(1):191-194.
56. Hartkens T., Hill D. L., Castellano-Smith A. D., Hawkes D. J., Maurer C. R., Jr., et al. Measurement and analysis of brain deformation during neurosurgery. *IEEE Trans Med Imaging.* 2003;22(1):82-92.
57. Petersen E. A., Holl E. M., Martinez-Torres I., Foltynie T., Limousin P., et al. Minimizing brain shift in stereotactic functional neurosurgery. *Neurosurgery.* 2010;67(3):213-221.
58. Ivan M. E., Yarlagadda J., Saxena A. P., Martin A. J., Starr P. A., et al. Brain shift during bur hole-based procedures using interventional mri. *Journal of Neurosurgery.* 2014;121(1):149-160.
59. Bilger A., Duriez C., Cotin S. Computation and visualization of risk assessment in deep brain stimulation planning. *Stud Health Technol Inform.* 2014;196:29-35.
60. Jin X., Yang K. H., King A. I. Mechanical properties of bovine pia-arachnoid complex in shear. *J Biomech.* 2011;44(3):467-474.

61. Sloty P. J., Kamp M. A., Wille C., Kinfe T. M., Steiger H. J., et al. The impact of brain shift in deep brain stimulation surgery: Observation and obviation. *Acta Neurochir (Wien)*. 2012;154(11):2063-2068.
62. Bijsterbosch J. D., Lee K. H., Hunter M. D., Wilkinson I. D., Farrow T., et al. The effect of head orientation on subarachnoid cerebrospinal fluid distribution and its implications for neurophysiological modulation and recording techniques. *Physiol Meas*. 2013;34(3):9-14.
63. Toyoda K., Urasaki E., Umeno T., Sakai W., Nagaishi A., et al. The effectiveness of the stereotactic burr hole technique for deep brain stimulation. *Neurol Med-Chir*. 2015;55(9):766-772.
64. Patel N. K., Plaha P., Gill S. S. Magnetic resonance imaging-directed method for functional neurosurgery using implantable guide tubes. *Neurosurgery*. 2007;61(5):358-365.
65. Sharim J., Pezeshkian P., DeSalles A., Pouratian N. Effect of cranial window diameter during deep brain stimulation surgery on volume of pneumocephalus. *Neuromodulation*. 2015;18(7):574-578.
66. Vogel T. W., Dlouhy B. J., Howard M. A. Don't take the plunge: Avoiding adverse events with cranial perforators clinical article. *Journal of Neurosurgery*. 2011;115(3):570-575.
67. Martin A. J., Larson P. S., Ostrem J. L., Keith Sootsman W., Talke P., et al. Placement of deep brain stimulator electrodes using real-time high-field interventional magnetic resonance imaging. *Magn Reson Med*. 2005;54(5):1107-1114.
68. van den Munckhof P., Contarino M. F., Bour L. J., Speelman J. D., de Bie R. M., et al. Postoperative curving and upward displacement of deep brain stimulation electrodes caused by brain shift. *Neurosurgery*. 2010;67(1):49-53; .
69. Azmi H., Machado A., Deogaonkar M., Rezai A. Intracranial air correlates with preoperative cerebral atrophy and stereotactic error during bilateral stn dbs surgery for parkinson's disease. *Stereot Funct Neuros*. 2011;89(4):246-252.
70. Patel N. K., Heywood P., O'Sullivan K., Love S., Gill S. S. Mri-directed subthalamic nucleus surgery for parkinson's disease. *Stereotact Funct Neurosurg*. 2002;78(3-4):132-145.
71. Pollo C., Vingerhoets F., Pralong E., Ghika J., Maeder P., et al. Localization of electrodes in the subthalamic nucleus on magnetic resonance imaging. *J Neurosurg*. 2007;106(1):36-44.
72. Coenen V. A., Abdel-Rahman A., McMaster J., Bogod N., Honey C. R. Minimizing brain shift during functional neurosurgical procedures - a simple burr hole technique that can decrease csf loss and intracranial air. *Cent Eur Neurosurg*. 2011;72(4):181-185.
73. Peters R. Ageing and the brain. *Postgrad Med J*. 2006;82(964):84-88.
74. Pereira J. L., B A. S., Sharim J., Yazdi D., DeSalles A. A., et al. Lateralization of the subthalamic nucleus with age in parkinson's disease. *Basal Ganglia*. 2016;6(2):83-88.
75. Contarino M. F., Bot M., Speelman J. D., de Bie R. M., Tijssen M. A., et al. Postoperative displacement of deep brain stimulation electrodes related to lead-anchoring technique. *Neurosurgery*. 2013;73(4):681-688; .
76. Obuchi T., Katayama Y., Kobayashi K., Oshima H., Fukaya C., et al. Direction and predictive factors for the shift of brain structure during deep brain stimulation electrode implantation for advanced parkinson's disease. *Neuromodulation*. 2008;11(4):302-310.

77. Lalys F., Haegelen C., D'Albis T., Jannin P. Analysis of electrode deformations in deep brain stimulation surgery. *Int J Comput Assist Radiol Surg.* 2014;9(1):107-117.
78. Hill D. L. G., Maurer C. R., Maciunas R. J., Barwise J. A., Fitzpatrick J. M., et al. Measurement of intraoperative brain surface deformation under a craniotomy. *Neurosurgery.* 1998;43(3):514-526.
79. Villalobos J., Fallon J. B., McNeill P. M., Allison R. K., Bibari O., et al. Preclinical evaluation of a miniaturized deep brain stimulation electrode lead. *Conf Proc IEEE Eng Med Biol Soc;* 2015 Aug.
80. Fiegele T., Feuchtner G., Sohm F., Bauer R., Anton J. V., et al. Accuracy of stereotactic electrode placement in deep brain stimulation by intraoperative computed tomography. *Parkinsonism Relat Disord.* 2008;14(8):595-599.
81. Parittotokkaporn T., Thomas D. G., Schneider A., Huq E., Davies B. L., et al. Microtextured surfaces for deep-brain stimulation electrodes: A biologically inspired design to reduce lead migration. *World Neurosurg.* 2012;77(3-4):569-576.
82. Zrinzo L., van Hulzen A. L. J., Gorgulho A. A., Limousin P., Staal M. J., et al. Avoiding the ventricle: A simple step to improve accuracy of anatomical targeting during deep brain stimulation. *Journal of Neurosurgery.* 2009;110(6):1283-1290.
83. Falowski S., Ghods A. J., Bakay R. A. E. Displacement of a deep brain stimulator lead during placement of an additional ipsilateral lead. *Neuromodulation.* 2013;16(1):41-45.
84. Sadeghi Y., Pralong E., Knebel J. F., Vingerhoets F., Pollo C., et al. Bilateral deep brain stimulation: The placement of the second electrode is not necessarily less accurate than that of the first one. *Stereotact Funct Neurosurg.* 2015;93(3):160-167.
85. Amirnovin R., Williams Z. M., Cosgrove G. R., Eskandar E. N. Experience with microelectrode guided subthalamic nucleus deep brain stimulation. *Neurosurgery.* 2006;58(1):96-102.
86. Chrastina J., Novak Z., Balaz M., Riha I., Bockova M., et al. The role of brain shift, patient age, and parkinson's disease duration in the difference between anatomical and electrophysiological targets for subthalamic stimulation. *Brit J Neurosurg.* 2013;27(5):676-682.
87. Petraglia F. W., 3rd, Farber S. H., Han J. L., Verla T., Gallis J., et al. Comparison of bilateral vs. Staged unilateral deep brain stimulation (dbs) in parkinson's disease in patients under 70 years of age. *Neuromodulation.* 2016;19(1):31-37.
88. Poon C. C., Irwin M. G. Anaesthesia for deep brain stimulation and in patients with implanted neurostimulator devices. *Br J Anaesth.* 2009;103(2):152-165.
89. Asha M. J., Kausar J., Krovvidi H., Shirley C., White A., et al. The effect of dopaminergic therapy on intraoperative microelectrode recordings for subthalamic deep brain stimulation under ga: Can we operate on patients 'on medications'? *Acta Neurochir (Wien).* 2016;158(2):387-393.
90. Cala L. A., Thickbroom G. W., Black J. L., Collins D. W., Mastaglia F. L. Brain density and cerebrospinal fluid space size: Ct of normal volunteers. *AJNR Am J Neuroradiol.* 1981;2(1):41-47.

91. Agartz I., Marions O., Saaf J., Wahlund L. O., Wetterberg L. Visual rating of magnetic resonance images of human cerebrospinal fluid spaces and white brain matter: Relation to sex and age in healthy volunteers. *Magn Reson Imaging*. 1992;10(1):135-142.
92. Bilger A., Dequidt J., Duriez C., Cotin S. Biomechanical simulation of electrode migration for deep brain stimulation. *MICCAI*. 2011;6891:339-346.
93. Monea A. G., Verpoest I., Vander Sloten J., Van der Perre G., Goffin J., et al. Assessment of relative brain-skull motion in quasistatic circumstances by magnetic resonance imaging. *J Neurotrauma*. 2012;29(13):2305-2317.
94. Mikkonen M., Laakso I. Effects of posture on electric fields of non-invasive brain stimulation. *Phys Med Biol*. 2019;64(6):065019.
95. Sillay K. A., Kumbier L. M., Ross C., Brady M., Alexander A., et al. Perioperative brain shift and deep brain stimulating electrode deformation analysis: Implications for rigid and non-rigid devices. *Ann Biomed Eng*. 2013;41(2):293-304.
96. Joldes G. R., Wittek A., Miller K. Real-time nonlinear finite element computations on gpu - application to neurosurgical simulation. *Comput Methods Appl Mech Eng*. 2010;199(49-52):3305-3314.
97. Jin X., Mao H., Yang K. H., King A. I. Constitutive modeling of pia-arachnoid complex. *Ann Biomed Eng*. 2014;42(4):812-821.
98. Holzapfel G. A. Nonlinear solid mechanics: A continuum approach for engineering science. *Meccanica*. 2002;37(4):489-490.
99. Maas S., Rawlins D., Weiss J., Ateshian G. *Febio: Finite elements for biomechanics. Theory manual 2.7*. 2018.
100. Mullins L. Softening of rubber by deformation. *Rubber Chemistry and Technology*. 1969;42(1):339-362.
101. Maas S. A., Ellis B. J., Ateshian G. A., Weiss J. A. *Febio: Finite elements for biomechanics*. *J Biomech Eng*. 2012;134(1).
102. Treloar L. R. G. The elasticity of a network of long-chain molecules. I. *Transactions of the Faraday Society*. 1943;39(0):36-41.
103. Treloar L. R. G. The elasticity of a network of long-chain molecules—ii. *Transactions of the Faraday Society*. 1943;39(0):241-246.
104. Treloar L. R. G. The elasticity of a network of long-chain molecules.—iii. *Transactions of the Faraday Society*. 1946;42(0):83-94.
105. Feng Y., Abney T. M., Okamoto R. J., Pless R. B., Genin G. M., et al. Relative brain displacement and deformation during constrained mild frontal head impact. *J R Soc Interface*. 2010;7(53):1677-1688.
106. Ateshian G. A., Ellis B. J., Weiss J. A. Equivalence between short-time biphasic and incompressible elastic material responses. *J Biomech Eng-T Asme*. 2007;129(3):405-412.
107. Madhukar A., Ostojja-Starzewski M. Finite element methods in human head impact simulations: A review. *Ann Biomed Eng*. 2019;49(9):1832-1854.

108. Miller K., Wittek A., Joldes G. Biomechanics of the brain for computer-integrated surgery. *Acta Bioeng Biomech.* 2010;12(2):25-37.
109. Ghajari M., Hellyer P. J., Sharp D. J. Computational modelling of traumatic brain injury predicts the location of chronic traumatic encephalopathy pathology. *Brain.* 2017;140(2):333-343.
110. Rashid B., Destrade M., Gilchrist M. D. Mechanical characterization of brain tissue in tension at dynamic strain rates. *J Mech Behav Biomed Mater.* 2014;33:43-54.
111. Miller K., Chinzei K. Constitutive modelling of brain tissue: Experiment and theory. *J Biomech.* 1997;30(11-12):1115-1121.
112. Miller K., Chinzei K. Mechanical properties of brain tissue in tension. *J Biomech.* 2002;35(4):483-490.
113. Miga M. I., Sun K., Chen I., Clements L. W., Pheiffer T. S., et al. Clinical evaluation of a model-updated image-guidance approach to brain shift compensation: Experience in 16 cases. *Int J Comput Assist Radiol Surg.* 2016;11(8):1467-1474.
114. Paulsen K. D., Miga M. I., Kennedy F. E., Hoopes P. J., Hartov A., et al. A computational model for tracking subsurface tissue deformation during stereotactic neurosurgery. *IEEE Trans Biomed Eng.* 1999;46(2):213-225.
115. Franceschini G., Bigoni D., Regitnig P., Holzapfel G. A. Brain tissue deforms similarly to filled elastomers and follows consolidation theory. *J Mech Phys Solids.* 2006;54(12):2592-2620.
116. Ogden R. W. Large deformation isotropic elasticity - correlation of theory and experiment for incompressible rubberlike solids. *Proc R Soc Lon Ser-A.* 1972;326(1567):565-584.
117. Prange M. T., Margulies S. S. Regional, directional, and age-dependent properties of the brain undergoing large deformation. *J Biomech Eng.* 2002;124(2):244-252.
118. Mihai L. A., Chin L., Janmey P. A., Goriely A. A comparison of hyperelastic constitutive models applicable to brain and fat tissues. *J R Soc Interface.* 2015;12(110):0486.
119. Budday S., Sommer G., Birkl C., Langkammer C., Haybaeck J., et al. Mechanical characterization of human brain tissue. *Acta Biomater.* 2017;48:319-340.
120. Shafieian M., Laksari K., Darvish K., Crandall J. Development of a constitutive model for brain tissue under multiaxial loading. 2012 IRCOBI Conference Proceedings - International Research Council on the Biomechanics of Injury; 2012.
121. Budday S., Sommer G., Haybaeck J., Steinmann P., Holzapfel G. A., et al. Rheological characterization of human brain tissue. *Acta Biomaterialia.* 2017;60:315-329.
122. Zappala S. B., N., Kusmia, S., Wu, J., Evans, S. Jones, D., Marshall, D. Ten minutes for the brain to settle: An in-vivo investigation of positional brain shift [abstract]. International Society for Magnetic Resonance in Medicine 27th Annual Meeting & Exhibition; 11-16 May 2019; Montreal, Canada. 2019.
123. Biot M. A. General theory of three-dimensional consolidation. *Journal of Applied Physics.* 1941;12(2):155-164.
124. Terzaghi K. Theoretical soil mechanics. New York: Wiley and Sons, Inc.; 1943.

125. Hakim S., Venegas J. G., Burton J. D. The physics of the cranial cavity, hydrocephalus and normal pressure hydrocephalus: Mechanical interpretation and mathematical model. *Surg Neurol.* 1976;5(3):187-210.
126. Miga M. I., Paulsen K. D., Hoopes P. J., Kennedy F. E., Hartov A., et al. In vivo modeling of interstitial pressure in the brain under surgical load using finite elements. *J Biomech Eng-T Asme.* 2000;122(4):354-363.
127. Sahar A H. G. M., Ransohoff J. Experimental hydrocephalus: Cerebrospinal fluid formation and ventricular size as a function of intraventricular pressure. *Journal of the Neurological Sciences.* 1970;11(1):81-91.
128. Bower A. F. *Applied mechanics of solids.* Boca Raton: CRC Press; 2009.
129. Ganpule S., Daphalapurkar N. P., Cetingul M. P., Ramesh K. T. Effect of bulk modulus on deformation of the brain under rotational accelerations. *Shock Waves.* 2018;28(1):127-139.
130. Morin F., Chabanas M., Courtecuisse H., Payan Y. Biomechanical modeling of brain soft tissues for medical applications. *Biomechanics of Living Organs: Hyperelastic Constitutive Laws for Finite Element Modeling.* 2017:127-146.
131. Flexner L. B., Clark J. H., Weed L. H. The elasticity of the dural sac and its contents. *American Journal of Physiology-Legacy Content.* 1932;101(2):292-303.
132. Tenti G. S., S.; Drake, J. M. . Brain biomechanics: Steady-state consolidation theory of hydrocephalus. *Canadian Applied Mathematics Quarterly* 1999;7(1):111-124.
133. Scott G. G., Margulies S. S., Coats B. Utilizing multiple scale models to improve predictions of extra-axial hemorrhage in the immature piglet. *Biomech Model Mechanobiol.* 2016;15(5):1101-1119.
134. Jin X., Lee J. B., Leung L. Y., Zhang L., Yang K. H., et al. Biomechanical response of the bovine pia-arachnoid complex to tensile loading at varying strain-rates. *Stapp Car Crash J.* 2006;50:637-649.
135. Jin X., Ma C., Zhang L., Yang K. H., King A. I., et al. Biomechanical response of the bovine pia-arachnoid complex to normal traction loading at varying strain rates. *Stapp Car Crash J.* 2007;51:115-126.
136. Mazumder M. M., Miller K., Bunt S., Mostayed A., Joldes G., et al. Mechanical properties of the brain-skull interface. *Acta Bioeng Biomech.* 2013;15(2):3-11.
137. Zhang L., Bae J., Hardy W. N., Monson K. L., Manley G. T., et al. Computational study of the contribution of the vasculature on the dynamic response of the brain. *Stapp Car Crash J.* 2002;46:145-164.
138. Saboori P., Sadegh A. Material modeling of the head's subarachnoid space. *Sci Iran.* 2011;18(6):1492-1499.
139. Saboori P., Sadegh A. Histology and morphology of the brain subarachnoid trabeculae. *Anat Res Int.* 2015;2015.
140. Cipolla M. J. *The cerebral circulation.* San Rafael, Calif.: Morgan & Claypool Life Sciences; 2010.

141. Tsutsumi S., Ono H., Yasumoto Y. Immobile cerebral veins in the context of positional brain shift: An undescribed risk factor for acute subdural hemorrhage. *Surg Radiol Anat.* 2017;39(10):1063-1067.
142. Ramo N. L., Troyer K. L., Puttlitz C. M. Viscoelasticity of spinal cord and meningeal tissues. *Acta Biomater.* 2018;75:253-262.
143. Aïmedieu P., Grebe R. Tensile strength of cranial pia mater: Preliminary results. *J Neurosurg.* 2004;100(1):111-114.
144. Wang F., Han Y., Wang B., Peng Q., Huang X., et al. Prediction of brain deformations and risk of traumatic brain injury due to closed-head impact: Quantitative analysis of the effects of boundary conditions and brain tissue constitutive model. *Biomech Model Mechanobiol.* 2018.
145. Chen I., Coffey A. M., Ding S., Dumpuri P., Dawant B. M., et al. Intraoperative brain shift compensation: Accounting for dural septa. *IEEE Trans Biomed Eng.* 2011;58(3):499-508.
146. Melvin J. W., McElhaney J. H., Roberts V. L. Development of a mechanical model of the human head - determination of tissue properties and synthetic substitute materials. *SAE International*; 1970.
147. Galford J. E., McElhaney J. H. A viscoelastic study of scalp, brain, and dura. *J Biomech.* 1970;3(2):211-221.
148. van Noort R., Black M. M., Martin T. R., Meanley S. A study of the uniaxial mechanical properties of human dura mater preserved in glycerol. *Biomaterials.* 1981;2(1):41-45.
149. van Noort R., Martin T. R., Black M. M., Barker A. T., Montero C. G. The mechanical properties of human dura mater and the effects of storage media. *Clin Phys Physiol Meas.* 1981;2(3):197-203.
150. Wolfenbarger Jr. L., Zhang Y., Adam B.-L. T., Homsy D., Gates K., et al. Biomechanical aspects on rehydrated freeze-dried human allograft dura mater tissues. *Journal of Applied Biomaterials.* 1994;5(3):265-270.
151. Sacks M. S., Jimenez Hamann M. C., Otano-Lata S. E., Malinin T. I. Local mechanical anisotropy in human cranial dura mater allografts. *J Biomech Eng.* 1998;120(4):541-544.
152. McGarvey K. A., Lee J. M., Boughner D. R. Mechanical suitability of glycerol-preserved human dura mater for construction of prosthetic cardiac valves. *Biomaterials.* 1984;5(2):109-117.
153. Coats B., Eucker S. A., Sullivan S., Margulies S. S. Finite element model predictions of intracranial hemorrhage from non-impact, rapid head rotations in the piglet. *Int J Dev Neurosci.* 2012;30(3):191-200.
154. Miga M. I., Roberts D. W., Kennedy F. E., Platenik L. A., Hartov A., et al. Modeling of retraction and resection for intraoperative updating of images. *Neurosurgery.* 2001;49(1):75-84.
155. Wittek A., Kikinis R., Warfield S. K., Miller K. Brain shift computation using a fully nonlinear biomechanical model. *Med Image Comput Comput Assist Interv.* 2005;8:583-590.
156. Miga M. I. Computational modeling for enhancing soft tissue image guided surgery: An application in neurosurgery. *Ann Biomed Eng.* 2016;44(1):128-138.

157. Bilger A., Bardinete E., Fernandez-Vidal S., Duriez C., Jannin P., et al. Intra-operative registration for stereotactic procedures driven by a combined biomechanical brain and csf model. *Lect Notes Comput Sc.* 2014;8789:76-85.
158. Hamze N., Bilger A., Duriez C., Cotin S., Essert C. Anticipation of brain shift in deep brain stimulation automatic planning. *Conf Proc IEEE Eng Med Biol Soc*; 2015 Aug.
159. Li X., von Holst H., Kleiven S. Influences of brain tissue poroelastic constants on intracranial pressure (icp) during constant-rate infusion. *Comput Methods Biomech Biomed Engin.* 2013;16(12):1330-1343.
160. Siegkas P., Sharp D. J., Ghajari M. The traumatic brain injury mitigation effects of a new viscoelastic add-on liner. *Scientific reports.* 2019;9(1).
161. Kleiven S. Predictors for traumatic brain injuries evaluated through accident reconstructions. *Stapp Car Crash J.* 2007;51:81-114.
162. Dutta-Roy T., Wittek A., Miller K. Biomechanical modelling of normal pressure hydrocephalus. *J Biomech.* 2008;41(10):2263-2271.
163. Chen Y., Fan Z., Ji S., Muenzer J., An H., et al. Patient-specific biomechanical modeling of ventricular enlargement in hydrocephalus from longitudinal magnetic resonance imaging. *Med Image Comput Comput Assist Interv.* 2013;16(Pt 3):291-298.
164. Keshtgar M. Evaluating the effectiveness of cranial molding for treatment of positional plagiocephaly using finite element analysis. 2015.
165. Tse K. M., Piang Lim S., Tan V. B. C., Lee H. A review of head injury and finite element head models. *American Journal of Engineering, Technology and Society.* 2014;1:28-52.
166. Dixit P., R. Liu G. A review on recent development of finite element models for head injury simulations. *Archives of Computational Methods in Engineering.* 2016;24.
167. Giordano C., Kleiven S. Connecting fractional anisotropy from medical images with mechanical anisotropy of a hyperviscoelastic fibre-reinforced constitutive model for brain tissue. *Journal of the Royal Society, Interface.* 2014;11(91).
168. Zhou Z., Li X., Kleiven S. Fluid-structure interaction simulation of the brain-skull interface for acute subdural haematoma prediction. *Biomech Model Mechanobiol.* 2019;18(1):155-173.
169. Chen Y., Ostoja-Starzewski M. Mri-based finite element modeling of head trauma: Spherically focusing shear waves. *Acta Mechanica.* 2010;213:155-167.
170. Roth S., Raul J. S., Ludes B., Willinger R. Finite element analysis of impact and shaking inflicted to a child. *Int J Legal Med.* 2007;121(3):223-228.
171. Viano D. C., Casson I. R., Pellman E. J., Zhang L., King A. I., et al. Concussion in professional football: Brain responses by finite element analysis: Part 9. *Neurosurgery.* 2005;57(5):891-916.
172. Takhounts E., Ridella S., Hasija V., Tannous R., Quinn Campbell J., et al. Investigation of traumatic brain injuries using the next generation of simulated injury monitor (simon) finite element head model. 2008;52:1-31.

173. Migueis G., Fernandes F., Ptak M., Ratajczak M., Alves de Sousa R. Detection of bridging veins rupture and subdural haematoma onset using a finite element head model. *Clinical Biomechanics*. 2019;63:104-111.
174. Fernandes F., Alves de Sousa R. J., Ptak M. Development of a new finite element human head model. Head injury simulation in road traffic accidents. Cham: Springer International Publishing; 2018. p. 25-39.
175. Claessens M., Sauren F., Wismans J. Modeling of the human head under impact conditions: A parametric study. *SAE Technical Papers*. 1997:315-328.
176. Ji S. B., Zhao W., Ford J. C., Beckwith J. G., Bolander R. P., et al. Group-wise evaluation and comparison of white matter fiber strain and maximum principal strain in sports-related concussion. *J Neurotraum*. 2015;32(7):441-454.
177. Lee C.-H., Han I. S., Lee J. Y., Phi J. H., Kim S.-K., et al. Analysis of a bleeding mechanism in patients with the sylvian arachnoid cyst using a finite element model. *Child's Nervous System*. 2014;30(6):1029-1036.
178. Wang F., Han Y., Wang B. Y., Peng Q., Huang X. Q., et al. Prediction of brain deformations and risk of traumatic brain injury due to closed-head impact: Quantitative analysis of the effects of boundary conditions and brain tissue constitutive model. *Biomech Model Mechan*. 2018;17(4):1165-1185.
179. Iwamoto M., Nakahira Y., Kimpara H. Development and validation of the total human model for safety (thums) toward further understanding of occupant injury mechanisms in precrash and during crash. *Traffic Inj Prev*. 2015;16:36-48.
180. Zoghi-Moghadam M., Sadegh A. M. Global/local head models to analyse cerebral blood vessel rupture leading to asdh and sah. *Comput Methods Biomech Biomed Engin*. 2009;12(1):1-12.
181. Wittek A., Miller K., Kikinis R., Warfield S. K. Patient-specific model of brain deformation: Application to medical image registration. *J Biomech*. 2007;40(4):919-929.
182. Roberts D. W., Hartov A., Kennedy F. E., Miga M. I., Paulsen K. D. Intraoperative brain shift and deformation: A quantitative analysis of cortical displacement in 28 cases. *Neurosurgery*. 1998;43(4):749-758.
183. Miga M. I., Sinha T. K., Cash D. M., Galloway R. L., Weil R. J. Cortical surface registration for image-guided neurosurgery using laser-range scanning. *IEEE Trans Med Imaging*. 2003;22(8):973-985.
184. Miller K., Wittek A., Joldes G., Horton A., Dutta-Roy T., et al. Modelling brain deformations for computer-integrated neurosurgery. *International Journal for Numerical Methods in Biomedical Engineering*. 2010;26(1):117-138.
185. Clatz O., Delingette H., Bardinet E., Dormont D., Ayache N. Patient-specific biomechanical model of the brain: Application to parkinson's disease procedure. *Surgery Simulation and Soft Tissue Modeling, Proceedings*. 2003;2673:321-331.
186. Marc K., O'Hagan T. The gem software. 2017. Accessed 24/1/19. Available from: <http://www.tonyohagan.co.uk/academic/GEM/>.
187. O'Hagan T. Bayesian analysis of computer code output: A tutorial. *Reliability Engineering & System Safety*. 2006;91:1290-1300.

188. Bayes T. An essay towards solving a problem in the doctrine of chances. 1763. MD Comput. 1991;8(3):157-171.
189. MathWorks. Gaussian process regression models. 2018. Accessed 08/3/19. Available from: <https://uk.mathworks.com/help/stats/gaussian-process-regression-models.html>.
190. Frydrychowski A. F., Szarmach A., Czaplewski B., Winklewski P. J. Subarachnoid space: New tricks by an old dog. PLoS One. 2012;7(5):1-15.
191. Chafi M. S., Karami G., Ziejewski M. Biomechanical assessment of brain dynamic responses due to blast pressure waves. Ann Biomed Eng. 2010;38(2):490-504.
192. Holmes M., Parker N., Povey M. Temperature dependence of bulk viscosity in water using acousticspectroscopy. Journal of Physics Conference Series. 2011;269.
193. Moerman K. Gibbon: The geometry and image-based bioengineering add-on. The Journal of Open Source Software. 2018;3:506.
194. Pasquesi S. A., Margulies S. S. Measurement and finite element model validation of immature porcine brain-skull displacement during rapid sagittal head rotations. Front Bioeng Biotechnol. 2018;6:16.
195. Ji S., Zhu Q., Dougherty L., Margulies S. S. In vivo measurements of human brain displacement. Stapp Car Crash J. 2004;48:227-237.
196. Scott G. G., Coats B. Microstructural characterization of the pia-arachnoid complex using optical coherence tomography. Ieee T Med Imaging. 2015;34(7):1452-1459.
197. Zou H., Schmiedeler J. P., Hardy W. N. Separating brain motion into rigid body displacement and deformation under low-severity impacts. Journal of Biomechanics. 2007;40(6):1183-1191.
198. Namjoshi D. R., Good C., Cheng W. H., Panenka W., Richards D., et al. Towards clinical management of traumatic brain injury: A review of models and mechanisms from a biomechanical perspective. Dis Model Mech. 2013;6(6):1325-1338.
199. Kahan J., Papadaki A., White M., Mancini L., Yousry T., et al. The safety of using body-transmit mri in patients with implanted deep brain stimulation devices. Plos One. 2015;10(6).
200. Kajita Y., Nakatsubo D., Kataoka H., Nagai T., Nakura T., et al. Installation of a neuromate robot for stereotactic surgery: Efforts to conform to japanese specifications and an approach for clinical use-technical notes. Neurol Med Chir (Tokyo). 2015;55(12):907-914.

Appendix A

Model parameter values

Set	Brain - k	Brain - c_1	Brain - m_1	Pia - E	Spring - α
1	376017	1475	-21.64	4067797	4.25
2	106186	611	-6.41	6864407	11.45
3	881949	865	-3.95	9915255	16.95
4	763898	560	-25.08	8898305	9.33
5	443475	2543	-13.29	14745763	17.38
6	662712	52	-11.81	2288136	19.49
7	780763	1373	-19.19	1779662	18.22
8	460339	153	-2.97	11440678	11.02
9	241102	1068	-8.37	3559323	0.86
10	494068	1678	-26.07	3050848	25.00
11	89322	1221	-22.63	508475.5	8.48
12	831356	357	-28.53	8135594	19.92
13	865085	1729	-19.68	9152543	20.34
14	21864	2593	-20.17	10423729	13.56
15	645847	814	-9.85	5338984	5.94
16	848220	662	-27.05	2033899	7.63
17	342288	2339	-23.12	7627119	10.18
18	966271	1	-18.69	8644068	16.53
19	561525	3000	-14.27	1271187	4.67
20	983136	2695	-20.66	15000000	9.75
21	527797	204	-24.10	5084746	24.15
22	898814	2949	-6.90	4576272	2.55
23	291695	1628	-18.20	14491525	0.43
24	190508	1983	-1.98	11694915	21.61
25	797627	1424	-26.56	12457627	3.82
26	257966	1780	-5.92	12203390	7.21
27	224237	2187	-9.36	762712.8	21.19
28	747034	408	-15.75	12711865	0.01
29	696441	1831	-17.22	1525425	5.52
30	123051	1526	-4.44	4830509	19.07
31	38729	1272	-10.83	254238.3	8.06
32	156780	916	-16.24	13474576	23.73
33	409746	458	-24.59	4322035	11.87
34	730169	1170	-1.00	3305086	13.14
35	72458	2492	-12.80	5847458	2.13
36	595254	2238	-29.02	1016950	12.29
37	578390	2441	-15.25	3813560	14.83
38	5000	967	-11.32	13728814	3.40
39	139915	2034	-29.51	11949153	5.09

40	949407	2746	-22.14	5593221	12.72
41	308559	255	-16.73	2796611	2.97
42	207373	103	-23.61	10677966	6.79
43	932542	2390	-7.39	13220339	22.46
44	679576	2848	-7.88	9661017	1.70
45	359153	2644	-4.93	10932204	14.41
46	628983	1882	-3.46	14237288	15.68
47	612119	2797	-17.71	7881356	22.04
48	510932	1119	-28.03	10169492	18.65
49	1000000	2136	-12.31	7118645	6.36
50	915678	1018	-10.34	2542374	23.31
51	173644	763	-25.58	9406780	22.88
52	426610	1577	-8.86	1	13.99
53	392881	1323	-1.49	6101696	8.90
54	55593	509	-30.00	7372882	1.28
55	325424	2085	-27.54	13983051	15.26
56	477203	713	-5.42	6355933	17.80
57	274831	2288	-21.15	6610170	20.76
58	713305	306	-14.76	12966102	24.58
59	814492	2898	-2.47	8389831	16.11
60	544661	1933	-13.78	11186441	10.60

Solution parameters used in FEBio

```
<Control>
  <time_steps>100</time_steps>
  <step_size>0.01</step_size>
  <max_refs>25</max_refs>
  <max_ups>4</max_ups>
  <diverge_reform>1</diverge_reform>
  <reform_each_time_step>1</reform_each_time_step>
  <dtol>0.001</dtol>
  <vtol>0.001</vtol>
  <ftol>0.001</ftol>
  <etol>0.01</etol>
  <rtol>0</rtol>
  <lstol>0.9</lstol>
  <min_residual>1e-020</min_residual>
  <rhoi>0</rhoi>
  <qnmethod>1</qnmethod>
  <time_stepper>
    <dtmin>0.01</dtmin>
    <dtmax lc="1"></dtmax>
    <max_retries>25</max_retries>
    <opt_iter>10</opt_iter>
  </time_stepper>
  <analysis type="dynamic"/>
  <plot_level>PLOT_MUST_POINTS</plot_level>
  <output_level>OUTPUT_FINAL</output_level>
</Control>
```